TECHNISCHE
UNIVERSITÄT
DARMSTADT

From Hot to Cold, from Dense to Dilute
– Renormalization Group Studies of Strongly-Interacting Matter –

vom Fachbereich Physik
der Technischen Universität Darmstadt

zur Erlangung des Grades
Doctor rerum naturalium
(Dr. rer. nat.)

genehmigte Dissertation von
Martin Pospiech, M.Sc.
aus Frankfurt am Main

Referent: Prof. Dr. rer. nat. Jens Braun
Korreferent: Prof. Dr. rer. nat. Robert Roth

Tag der Einreichung: 17. September 2019
Tag der Prüfung: 11. November 2019

Darmstadt 2019
D17

From Hot to Cold, from Dense to Dilute
– Renormalization Group Studies of Strongly-Interacting Matter –

Von Heiß zu Kalt, von Dicht zu Dünn
– Renormierungsgruppenstudien von Stark-Wechselwirkender Materie –

Genehmigte Dissertation von Martin Pospiech aus Frankfurt am Main.

Zusammenfassung

Wir untersuchen stark-wechselwirkende fermionische Materie unter Verwendung funktionaler Renormierungs-gruppentechniken (RG). Im ersten Teil dieser Arbeit untersuchen wir relativistische, heiße und dichte Quark-materie, wobei wir uns auf den Mechanismus der spontanen Symmetriebrechung in der Quantenchromodyna-mik (QCD) mit zwei masselosen Quark-Flavours konzentrieren. Zu diesem Zweck betrachten wir zunächst *Nambu–Jona-Lasinio*-artige Modelle, die als effektive Niederenergiebeschreibung der QCD dienen. Wir arbeiten die Be-deutung der *Fierz*-Vollständigkeit in diesen Studien heraus, analysieren die Fixpunktstruktur, studieren die RG-Flüsse der Vier-Fermionen-Kopplungen und bestimmen die Phasenstruktur bei endlicher Temperatur und quark-chemischem Potenzial, wobei der Einfluss verschiedener Trunkierungen untersucht wird. Mit Hilfe einer *Fierz*-vollständigen Vier-Quark-Basis studieren wir anschließend die Auswirkung von Eichfreiheitsgraden auf die ther-mische Phasengrenze und erforschen die Phasenstruktur von QCD mit zwei masselosen Quark-Flavours. Wir stellen fest, dass sich die Phasengrenze signifikant verändert, sobald *Fierz*-unvollständige Ansätze verwendet wer-den. Darüber hinaus deuten unsere *Fierz*-vollständigen Studien darauf hin, dass die Dynamik bei niedrigem quark-chemischem Potenzial vorwiegend durch einen nicht-*Gaußschen* Fixpunkt kontrolliert wird, wodurch sichergestellt wird, dass die Niederenergiephysik von chiralen Freiheitsgraden dominiert wird. Im Bereich großer quarkchemi-scher Potenziale finden wir darüber hinaus starke Hinweise für die Entstehung eines chiralen Diquark-Kondensats.

Im zweiten Teil untersuchen wir Bindungseigenschaften nicht-relativistischer fermionischer Systeme mit weni-gen Teilchen am Temperaturnullpunkt unter Verwendung eines funktionalen Renormierungsgruppenzuganges zur Dichtefunktionaltheorie (DFT-RG). Wir geben eine kurze Einführung zur DFT und den bekannten *Kohn-Sham*-Gleichungen (KS), diskutieren die Herleitung der DFT-RG-Flussgleichung und betrachten ein eindimensionales Kernmodell als Beispiel. Mit dem Ziel die Genauigkeit der trunkierten DFT-RG-Gleichungen zu verbessern, stellen wir eine Optimierung des Startpunktes des RG-Flusses auf Grundlage der KS-Gleichungen vor. Die Anwendbarkeit des neu entwickelten Ansatzes studieren wir mittels Systeme quasi-eindimensionaler, dipolarer Fermionen, die in einer harmonischen Falle konfiniert sind. Für bis zu fünf Teilchen berechnen wir Grundzustandsenergien für ver-schiedene Wechselwirkungsstärken und testen dabei die jeweilige Leistungsfähigkeit unterschiedlichster Trunkie-rungen. In niedrigster Ordnung stellen wir fest, dass unser neuer Ansatz für attraktive Wechselwirkungen am besten abschneidet. Repulsive Wechselwirkungen sind damit aber nur eingeschränkt zugänglich. Wir beobachten weiter-hin, dass die relative Abweichung zum exakten Resultat mit zunehmender Teilchenzahl kleiner wird.

Abstract

We study the nature of strongly-interacting fermion matter by employing functional Renormalization Group (RG) techniques. In the first part of this thesis, we examine relativistic hot and dense quark matter focusing on the mechanism of spontaneous symmetry breaking in Quantum Chromodynamics (QCD) with two massless quark flavors. To this end, we consider *Nambu–Jona-Lasinio*-type (NJL) models serving as effective low-energy descriptions of QCD. We highlight the significance of *Fierz* completeness in such studies, analyze the fixed-point structure, study the RG flows of the four-fermion couplings, and explore the phase structure at finite temperature and quark chemical potential where we investigate the influence of different truncations. Using a *Fierz*-complete four-quark basis, we then study the impact of gauge degrees of freedom on the thermal phase boundary and explore the phase structure of chiral two-flavor QCD. We find that the phase boundary is significantly altered when *Fierz*-incomplete ansätze are considered. Moreover, our *Fierz*-complete studies suggest that the dynamics at low quark chemical potential is predominantly controlled by a non-*Gaussian* fixed point, ensuring that the low-energy physics is governed by chiral degrees of freedom. For the regime at large quark chemical potential, we find strong indications for the formation of a chiral diquark condensate.

In the second part, we study bound-state properties of non-relativistic few-fermion systems at zero temperature using a functional Renormalization Group approach to Density Functional Theory (DFT-RG). We give a short introduction to DFT and the famous *Kohn-Sham* (KS) equations, discuss the derivation of the DFT-RG flow equation, and study a one-dimensional nuclear model as an introductory example. To improve the precision of the truncated DFT-RG equations, we propose an improvement based on the KS equations optimizing the starting point of the RG flow. As a feasibility study for this new development, we consider a system of quasi-one-dimensional dipolar fermions confined in a harmonic trap. For up to $N = 5$ particles, we compute ground-state energies for various interaction strengths and let different truncations compete against each other. Within our approximation, our KS-optimized DFT-RG method performs best for attractive interaction strengths but appears to be less suited in the repulsive regime of our benchmark system. Compared to exact results, we observe that the relative deviation decreases for higher particle numbers.

Contents

Chapter 1

Introduction

Strongly-interacting fermionic systems play an essential role in nature where a special interest is attached to those which can assume non-trivial ground states as a consequence of dynamics on microscopic scales. The physical behavior of a quantum system is then often governed by new effective degrees of freedom composed of constituents of the underlying theory. Below a transition temperature, for instance, it is energetically favorable for fermions to form *Cooper* pairs [1] in *Bardeen-Cooper-Schrieffer*-type (BCS) superconductors [2, 3] accompanied by the emergence of a gap in the excitation spectrum. Such non-trivial ground-state configurations are often related to various phenomena, which can be noticeable on macroscopic scales, e.g., the electric resistance vanishes identically in the superconducting phase. In many cases, the transition between two phases dominated by distinct degrees of freedom has then its origin in the spontaneous breakdown of a continuous global symmetry of the underlying theory.

Spontaneous symmetry breaking mechanisms also play an important role in Quantum Chromodynamics (QCD) [4–7], the fundamental theory of the strong interaction, describing the intricate interplay between quarks [8] and gluons. An intriguing aspect of QCD is its non-Abelian gauge structure which implies gluonic self-interactions already on the level of the classical action and gives rise to several phenomena. For instance, QCD is asymptotically free [6, 7] meaning that the theory is weakly coupled at large momentum scales. Therefore, given a sufficiently high temperature $T \gtrsim 130\,\mathrm{MeV}$ [9–13], about a hundred thousand times hotter than the core of the sun, quarks and gluons appear as a quasi-ideal gas known as the Quark-Gluon Plasma (QGP) [14]. It is expected that the QGP was the predominant state of matter in the very early universe $t \lesssim 10^{-5}\,\mathrm{s}$ [15], shortly after the Big Bang. Below a critical temperature, however, QCD matter appears to be dominated by hadronic bound states like protons and neutrons in which the fundamental degrees of freedom, the quarks, are confined [16, 17]. In correspondence to BCS theory, the formation of new effective degrees of freedom is accompanied by the emergence of a gap, now a mass gap, so that the quarks acquire a comparably large so-called constituent mass being responsible for a major part of the observable mass in the universe. As it turns out, fluctuation effects in the strong gauge sector [18–23] are the main driving force of this physical mechanism which is known as spontaneous chiral symmetry breaking.

Even though QCD provides us with the fundamental description of hadrons and their interplay in our universe, a direct investigation of the symmetry breaking patterns and critical phenomena at finite baryon density appears to be challenging. In particular, since QCD becomes strongly coupled at low momentum scales, the use of perturbation theory is limited. On the other hand, at non-zero densities lattice QCD approaches are plagued by the infamous sign problem [24]. In the past decades, therefore, *Nambu–Jona-Lasinio*-type (NJL) models [25, 26] and related quark-meson (QM) models mainly guided our understanding of the QCD phase diagram and the underlying symmetry breaking patterns. NJL-type models indeed became a useful tool to study the low-energy regime of QCD [27–30]. The phase structure of QCD at densities of several times of normal nuclear density $n_0 = 0.16\,\mathrm{fm}^{-3}$ is of special interest as these studies suggest that the low-energy regime is governed by new types of degrees of freedom which are called diquarks [28, 31–35]. The symmetry breaking mechanism which is then expected to occur in QCD at large density is of the *Anderson*-type [36–39]. As a consequence, some gluons would acquire an effective so-

called *Meissner* mass [40, 41] implying that the strong interaction becomes short-ranged. Since this phenomenon is well-known from conventional BCS-type superconductors, in QCD, this state of matter is referred to as a color superconductor [42, 43].

Hadronic matter far beyond normal nuclear density may also be observable in nature. For instance, it is expected that deconfined or exotic QCD matter could exist in the interior of neutron stars, the very compact remnants of supernova explosions of massive stars beyond $M \gtrsim 8\,M_\odot$, see Refs. [44, 45] for reviews. Since they represent the most compact stellar objects in the universe besides black holes, neutron stars are intriguing laboratories for the study of dense nuclear matter. In recent years, new experimental efforts have therefore been made to better understand the composition of neutron stars in order to constrain the equation of state of hadronic matter. At the moment, there are several promising complementary experiments ongoing. For example, from measurements of gravitational wave signals of binary neutron stars in the premerger phase, the tidal deformability of the compact objects can be extracted [46–49] from which the equation of state can be constrained. An alternative approach is tested by the orbital-based X-ray *Neutron star Interior Composite ExploreR* (NICER) [50–53] which aims at a direct measurement of the mass-radius relation of neutron stars. At the same time, it is also an exciting era for theoretical studies of matter under extreme conditions. For instance, chiral Effective Field Theory (χEFT) [54–58] as a systematic framework based on an expansion in low-energy degrees of freedom provides us with a reliable description of the equation of state in the regime of normal nuclear density. Perturbative QCD [59–62], on the other hand, may be well suited for 70 to 100 times of the nuclear density where QCD becomes weakly coupled. However, the intermediate density regime of the equation of state still remains challenging to access.

In the first part of the present thesis, we therefore aim at an improvement of our present knowledge of the phase structure at finite temperature and quark chemical potential. To this end, we consider the functional Renormalization Group [63, 64] to investigate two-flavor QCD in the chiral limit. In particular, we study the RG flow of the four-fermion correlation functions, the fixed-point structure, and the symmetry breaking patterns of hot and dense baryonic matter using *Fierz*-complete ansätze for the scale-dependent four-fermion vertices in the effective action.

In the second part of the thesis, we discuss bound-state properties of one-dimensional non-relativistic few-fermion systems at zero temperature using a Renormalization Group inspired approach to Density Functional Theory (DFT-RG) [65, 66]. In our study, we aim at an enhancement of the convergence properties of the truncated DFT-RG flow equations by considering a *Kohn-Sham*-improved starting point for the RG flow.

In the past years, our understanding of light- and medium mass nuclei has been significantly put forward due to the use of chiral effective field theory interactions [67–78] and the development of improved many-body methods like the In-Medium Similarity Renormalization Group (IMSRG) [79–84], many-body perturbation theory [85–88], self-consistent Green's function approaches [74, 89–91], or coupled-cluster theory [92–97]. Density Functional Theory (DFT), on the other hand, appears to be the most practicable many-body technique in the regime of heavy nuclei [98] where impressive theoretical efforts have also been made in order to investigate the nuclear chart over a wide range of mass number in the last decades. One example for this successful work is the UNEDF/NUCLEI SciDAC collaboration employing large truncations for the nuclear energy density functional to predict binding energies for several hundred nuclei, see Refs. [99–102].

Originally, the starting point for DFT is the famous *Hohenberg-Kohn* (HK) theorem [103, 104] which guarantees, in principle, the existence of a universal energy density functional. The consequences are far-reaching as the complexity of a given many-body problem with $3N$ degrees of freedom is considerably reduced due to the fact that the density is characterized by three coordinates. Unfortunately, the HK theorem only states the existence of the energy density functional but does not provide any "recipe" for its computation. For the latter, one then often chooses a global ansatz relying on phenomenological considerations in conventional DFT studies.

Starting from microscopic principles, the DFT-RG framework provides an evolution equation for the two-particle-point-irreducible (2PPI) effective action allowing for a systematic computation of the HK energy density functional, see Refs. [105–107] for reviews and Refs. [65, 66] for the seminal works. In this framework, the density plays the role of an effective bosonic composite field describing the dynamics of the underlying fermionic degrees of

freedom. An intriguing feature of the DFT-RG approach is that *exchange-correlation* effects are naturally included which usually turns out to be most challenging in DFT. In recent years, the DFT-RG framework has been put forward in various works. For example, the feasibility of this approach was tested successfully in studies of $(0 + 0)$-, $(0 + 1)$-, $(1 + 1)$- and $(2 + 1)$-dimensional field theories with various two-body interactions, e.g., see Refs. [108–114]. The DFT-RG scheme provides a microscopic and systematic approach to DFT. As it turns out, however, the previously employed expansion of the energy density functional in terms of density correlation functions entails rather slow convergence properties for interactions studied up to now. A first step towards an improved ansatz for the 2PPI evolution equation was considered in Ref. [113] relying on a splitting of the effective action into a *mean-field* and a fluctuation part which is then RG evolved by the corresponding RG flow equation. The ground-state energy results for a $(0 + 0)$-dimensional toy model seem promising, even though the feasibility of this scheme for higher dimensions still needs to be investigated because of the increasing computational complexity.

In this work, we shall also present an improvement scheme for the DFT-RG approach. To this end, we initialize the RG flow at a starting point associated with a system of non-interacting fermions in an external KS potential which we obtain from solving the KS equations self-consistently. In this context, the KS single-particle states can be interpreted as an optimized basis for the particular problem under consideration. This approach may also be compared to advances in other methods such as many-body perturbation theory [85–88, 115] where a suitably chosen reference system can improve ground-state energy results notably.

The present thesis is organized as follows: We begin in Chap. 2 with a general overview of the theoretical tools we employ throughout this work. In particular, we discuss the basics of thermal field theory and outline the connection between the *Eulidean* path integral and the partition function. We further derive the *Wetterich* equation and present some frequently employed approximation schemes for the scale-dependent effective action. In Sec. 2.3, we discuss the basic aspects of non-Abelian local gauge invariance from which we motivate the famous QCD Lagrangian. We further give an introduction to the mechanism of spontaneous chiral symmetry breaking and discuss how its onset can be studied by considering four-fermion correlation functions. In Sec. 2.3.3, we show the importance of *Fierz* completeness for the predictive power of four-fermion theories, and discuss in Sec. 2.3.4 the phase structure of two-flavor QCD at finite temperature and quark chemical potential as it is found in previous NJL model studies.

In Chap. 3, we present key results from our studies of the symmetry breaking patterns in hot and dense quark matter. We begin in Sec. 3.1 with the study of a one-flavor and one-color NJL-type model at leading order of the derivative expansion using two different parametrizations for a *Fierz*-complete four-fermion basis. We study the vacuum fixed-point structure and explore the one-flavor and one-color phase diagram at finite temperature and fermion chemical potential. From the observed dominance pattern, i.e., the relative strengths of the scale-dependent four-fermion couplings, we discuss the emerging symmetry breaking patterns in the low-energy regime. We compare different regularization schemes, a *covariant* one and a non-*covariant* one, and discuss their influence on physical observables. In Sec. 3.2, we then study the phase structure of an NJL model with two massless quark flavors and N_c colors at finite temperature and quark chemical potential. We introduce a ten-channel *Fierz*-complete basis of four-quark interactions obeying a global $SU(N_c) \times SU(2)_L \times SU(2)_R \times U(1)_V$ symmetry and study the phase boundary of the NJL model in analogy to Sec. 3.1. Additionally, we investigate the impact of $U(1)_A$-symmetric initial conditions on the critical temperature and the underlying symmetry breaking patterns. Inspired by the observed dominances, we study the fixed-point structure of a *Fierz*-incomplete two-channel approximation and analyze the RG flow at finite temperature and quark chemical potential. In Sec. 3.3, we investigate QCD with two massless quark flavors. By including the ten-channel *Fierz*-complete four-quark basis from the previous section and the quark-gluon three-point vertex in the effective action, we study the phase structure of QCD and compare our findings with the results from Sec. 3.2. In Sec. 3.4, we discuss how the present findings may help to constrain the equation of state of isospin-symmetric nuclear matter.

In Chap. 4, we study systems of one-dimensional identical fermions using the DFT-RG framework. In Sec. 4.1, we outline the main statements of the famous *Hohenberg-Kohn* theorem representing the foundation of Density Functional Theory. In Sec. 4.2, we further introduce the general idea of the *Kohn-Sham* (KS) approach to DFT and discuss the self-consistent KS equations. Moreover, we give an overview about a few approximation schemes for the *exchange-correlation* functional which encodes all non-trivial information on the interacting N-particle system. In Sec. 4.3, we present a Renormalization Group approach to DFT where we discuss the derivation of the DFT-RG flow equation for the 2PPI effective action. As an introductory example, we study a one-dimensional nuclear toy model where we compute ground-state properties of different few-body systems. We further propose a novel improvement for the DFT-RG framework where we use a system of non-interacting fermions in a KS potential as a starting point for the DFT-RG flow. In Sec. 4.4, we test this improvement scheme by studying a system of quasi-one-dimensional fermions in a harmonic trap which interact via a dipolar-type two-body interaction. For this, we compute the ground-state energy for up to $N = 5$ particles as a function of the dipolar coupling strength where we consider different truncations for the DFT-RG flow equations. As a benchmark, we use results from an exact diagonalization approach.

1.1   List of Publications

The present dissertation was written solely by the author. Nevertheless, most of the presented results rely on works which were done together with my collaborators in the past years. Some of these works are already published or exist as preprints. In the following list, we shall give an overview of the publications and where they appear within this work:

  (i) "Fierz-complete NJL model study: fixed points and phase structure at finite temperature and density"
      with Jens Braun and Marc Leonhardt
      In: Phys. Rev. **D96** (2017), 076003
      E-print: arXiv:1705.00074 [hep-ph]
      Large parts of this publication underlie Sec. 3.1 and the appendices B, C, and E.

 (ii) "Fierz-complete NJL model study. II. Toward the fixed-point and phase structure of hot and dense two-flavor QCD"
      with Jens Braun and Marc Leonhardt
      In: Phys. Rev. **D97** (2018), 076010
      E-print: arXiv:1801.08338 [hep-ph]
      Many aspects of this article are discussed in Sec. 3.2 and in the appendices B and E.

(iii) "Fierz-complete NJL model study III: Emergence from quark-gluon dynamics"
      with Jens Braun and Marc Leonhardt
      E-print: arXiv:1909.06298 [hep-ph]
      Some results of this article are presented in Sec. 3.3.

 (iv) "Symmetric nuclear matter from the strong interaction"
      with Marc Leonhardt, Benedikt Schallmo, Jens Braun, Christian Drischler, Kai Hebeler, and Achim Schwenk
      E-print: arXiv:1907.05814 [nucl-th]
      In Sec. 3.4, we give a short overview of this very recent publication.

  (v) "Formation of Selfbound States in a One-Dimensional Nuclear Model – A Renormalization Group based Density Functional Study"
      with Sandra Kemler and Jens Braun
      In: J. Phys. **G44** (2016), 015101
      E-print: arXiv:1606.04388 [nucl-th]

Parts from the introduction to the DFT-RG framework and selected results from this article underlie our discussion in Sec. 4.3.

In the bibliography, these articles can also be found in Refs. [54, 110, 116–118], respectively.

Part I

Relativistic Hot and Dense Strong-Interaction Matter

Chapter 2

Theoretical Background

In this chapter, we introduce the essential theoretical tools which we employ throughout the first part of the present work. At the beginning of this chapter, we start with an overview of the general ideas of thermal Quantum Field Theory from a path integral perspective by working within the so-called *Matsubara* formalism. Here, we also discuss how a finite particle density can be realized in relativistic Quantum Field Theories in *Euclidean* spacetime.

In the second section, we then show the general derivation of the famous *Wetterich* equation, which is a functional Renormalization Group equation for the quantum effective action. For the latter, we shall briefly discuss two frequently employed expansion schemes which are predominantly used to study critical behavior in quantum systems in a nonperturbative fashion.

We further outline the concepts of non-Abelian local gauge invariance in Subsec. 2.3.1 and discuss the mechanism of spontaneous chiral symmetry breaking in Subsec. 2.3.2. In this context, we introduce the theory of the strong interaction as a part of the Standard Model of particle physics. This theory, the famous QCD, is a non-Abelian gauge theory and describes the interplay of fermionic quark and bosonic gluon degrees of freedom. In Subsec. 2.3.4, we discuss the conjectured phase diagram of hot and dense two-flavor QCD, which is until today especially based on model considerations at least at high densities. We emphasize that the first chapter shall only serve as a brief reminder. For a detailed discussion on the various subjects, we refer to the references we shall give in this chapter.

2.1 Characteristics of Thermal Quantum Field Theory

In this section, we wish to give a short overview of our approach to thermal Quantum Field Theory, which is based on an *Euclidean* path integral formalism. As already indicated in the introduction, this section intends to give the reader an impression of the theoretical concepts we employ in the first part of this work. Therefore, we rather concentrate on some terminology and definitions, where we avoid to dig too deep into the various details. Note that the following introduction is mainly based on Refs. [119–123]. Moreover, we use natural units $\hbar = c = k_{\mathrm{B}} = 1$ throughout the entire thesis.

An essential property of the path integral is its relation to statistical physics. Here, the partition function $\mathcal{Z}$ is the main theoretical object which contains all non-trivial information about the many-body quantum system under consideration. The statistical partition function can be written as

$$\mathcal{Z} = \mathrm{Tr}\, \mathrm{e}^{-\beta H}\,, \tag{2.1}$$

where $\beta = 1/T$ is the inverse temperature. From the partition function in statistical physics we can then compute thermal expectation values for any observable O via

$$\langle O \rangle = \frac{\mathrm{Tr}[\mathrm{e}^{-\beta H} O]}{\mathrm{Tr}[\mathrm{e}^{-\beta H}]}\,. \tag{2.2}$$

Here, the expectation value can be associated with a physical observable, such as the magnetization, which can give valuable insights into the underlying microscopic dynamics as we shall see below.

From a field-theoretical point of view, the same expression for the statistical partition function Eq. (2.1) can be derived by considering the transition amplitude, e.g., for a bosonic Quantum Field Theory with a classical action $S_\mathrm{M}[\phi]$ defined for a *Minkowski*-type spacetime geometry. In particular, the transition amplitude describes the propagation from a field state $|\phi_a\rangle$ at time $t = 0$ to a state $|\phi_b\rangle$ at some final time $t = t_\mathrm{f}$:

$$\langle\phi_b|\,\mathrm{e}^{-\mathrm{i}Ht_\mathrm{f}}\,|\phi_a\rangle \sim \mathcal{N} \int_{\phi(0,x)=\phi_a(x)}^{\phi(t_\mathrm{f},x)=\phi_b(x)} \mathcal{D}\phi\,\mathrm{e}^{\mathrm{i}S_\mathrm{M}[\phi]}\,, \tag{2.3}$$

with a proper normalization constant $\mathcal{N}$. We now perform a so-called *Wick* rotation turning the real time axis onto the imaginary one by imposing $\tau = \mathrm{i}t$. Further, we assume that the system ends up again in the state ϕ_a after a time $t_\mathrm{f} = -\mathrm{i}\beta$. The transition amplitude can then be related to the statistical partition function Eq. (2.1) by summing over all states ϕ_a. Note that the bosonic field ϕ has now to obey periodic boundary conditions $\phi(0, x) = \phi(\beta, x)$ and the imaginary time variable τ is confined on a finite (periodic) interval $\tau \in (0, \beta]$. For a system of fermions, however, the compactified temporal box has to be antiperiodic to ensure *Pauli*'s principle. For instance, for a fermionic field type $\psi(\tau, x)$, the boundary condition $\psi(0, x) = -\psi(\beta, x)$ has to be fulfilled which is a consequence of the *Pauli* exclusion principle on the level of the path integral, see, e.g., Ref. [124]. Due to the compactification of the time direction, we find discretized so-called *Matsubara* modes in the energy spectrum where we have $\omega_n = 2n\pi T$ for bosons and $\nu_n = (2n+1)\pi T$ for fermions, see also App. A. Note that another convenient property of the imaginary time formalism is that our originally *Minkowskian* spacetime metric $g_{\mu\nu} = \eta_{\mu\nu} = \mathrm{diag}(-1, +1, +1, +1)$ becomes *Euclidean* $g_{\mu\nu} = \delta_{\mu\nu} = \mathrm{diag}(+1, +1, +1, +1)$ which simplifies computations on a technical level in many cases. Nevertheless, we have to handle theoretical objects which are sensitive to the underlying spacetime geometry with some care, e.g., the properties of the *Euclidean Dirac* matrices as well as of *Euclidean* spinor fields [125] do slightly change, see also App. B.

Now, we can write down the *Euclidean* path integral or the statistical partition function, respectively:

$$\mathcal{Z} \sim \mathcal{N} \int \mathcal{D}\phi\,\mathrm{e}^{-S_\mathrm{E}[\phi]}\,, \tag{2.4}$$

where S_E denotes the so-called *Euclidean* classical action. Note that this object requires a suitable regularization. For the moment, however, we ignore the latter issue and move the discussion concerning a proper regularization to Sec. 2.2. There, within the non-perturbative functional Renormalization Group framework, a regulator is added to the classical action on the level of the path integral. The so-called scale-dependent partition function $\mathcal{Z}_k$ is then the starting point for the derivation of the *Wetterich* equation.

Since we work throughout the present thesis in the imaginary time formalism, we assume from now that all mathematical objects are defined for a *Euclidean* spacetime geometry, i.e., $S[\phi] \equiv S_\mathrm{E}[\phi]$. We add that the so-defined *Euclidean* path integral has the further advantage to have a well-defined (positive semidefinite) probability measure, which is an essential property for many lattice studies of Quantum Field Theories. However, by considering a finite particle density, the positivity of the probability measure can again be spoiled as we shall discuss at the end of this chapter.

We add that the finite temperature T enters our studies as an external parameter which can be seen as a heat-bath distinguishing the temporal and spatial components of the *Euclidean* spacetime. From this, it is clear that the *Poincaré* symmetry of relativistic QFT's is broken at finite temperature, see Sec. 3.1 for a detailed discussion.

From the so-defined partition function (2.4), it is straightforward to define the n-point correlation functions of a quantum theory under consideration where the correlation functions are basically the expectation values of the fluctuating fields which enter the classical action. Note, the "one-point" correlation function $\langle\phi\rangle$ is associated with the expectation value of the fluctuating quantum field itself. We further stress that the correlation functions carry

all non-trivial information of a quantum system under consideration. For example, from the spectrum of the two-point function, we can compute possible two-body bound states and resonances. To derive the n-point correlation function in an efficient way, it is convenient to attach an external source J to the fluctuation field ϕ. This is in analogy to the situation in statistical physics where one introduces an external magnetic field H in *Ising*-type models to compute, e.g., the magnetization M, which can be related to the classical field from above, by taking derivatives of the free energy with respect to the external field H. In the same spirit, we define the so-called source-dependent partition function

$$\mathcal{Z}[J] = \int \mathcal{D}\phi \, \mathrm{e}^{-S_{\mathrm{E}}[\phi] + \int_\chi J_\phi(\chi)\phi(\chi)} \equiv \mathrm{e}^{W[J]} \,, \tag{2.5}$$

where we have defined the *Euclidean Schwinger* functional $W[J]$ which is the generating functional of the so-called connected correlation functions. Moreover, we use the shorthand notation $\chi \equiv (\tau, x)$. From this, we can derive the connected n-point correlation function by just performing functional derivatives with respect to the external source $J(x)$ and setting the source to zero subsequently:

$$\langle \phi(\chi_1)\phi(\chi_2)\dots\phi(\chi_n)\rangle_{\mathrm{c}} = \left(\frac{\delta}{\delta J_\phi(\chi_1)} \frac{\delta}{\delta J_\phi(\chi_2)} \cdots \frac{\delta}{\delta J_\phi(\chi_n)} \ln Z[J] \right)_{J_\phi=0} \,, \tag{2.6}$$

where $\langle\dots\rangle_{\mathrm{c}}$ indicates that only contributions which are associated with connected correlation functions are considered. For example, the connected two-point function reads

$$\left(\frac{\delta}{\delta J_\phi(\chi_1)} \frac{\delta}{\delta J_\phi(\chi_2)} W[J] \right)_{J_\phi=0} = \langle \phi(\chi_1)\phi(\chi_2)\rangle - \langle\phi(\chi_1)\rangle \langle\phi(\chi_2)\rangle \,. \tag{2.7}$$

Using the *Schwinger* functional $W[J]$, we can now define the quantum effective action $\Gamma[\phi_{\mathrm{cl}}]$ which has the so-called classical field ϕ_{cl} as its fundamental degree of freedom. To compute $\Gamma[\phi_{\mathrm{cl}}]$, we apply the functional equivalent of a *Legendre* transformation for the generating functional $W[J]$. This is again in complete analogy to statistical physics where the different thermodynamical ensembles are connected by means of conventional *Legendre* transformations. Then, the quantum effective action reads (e.g. see Ref. [126]):

$$\Gamma[\phi_{\mathrm{cl}}] = \sup_J \left(-W[J] + \int_\chi J(\chi)\phi_{\mathrm{cl}}(\chi) \right) \,. \tag{2.8}$$

Note that the supremum guarantees that the effective action is convex. For instance, we have for any value of the classical field ϕ_{cl} a unique source $J = J_{\mathrm{sup}}$ so that the convexity of the effective action can be ensured, see, e.g., Refs. [127–129].

To study the regime of quark matter at finite density, we need to introduce a chemical potential μ entering the theory as an external *Lagrange* multiplier in the partition function. Since we consider two different types of massless quark flavors, i.e., up and down quarks, we also need two separate types of chemical potentials for each fermion flavor. Therefore, we add to the fermionic classical action $S[\bar{u}, u, \bar{d}, d]$, which encodes the dynamics of our massless quarks, the following expression:

$$S[\bar{u}, u, \bar{d}, d] \to S[\bar{u}, u, \bar{d}, d] + \mathrm{i}\mu_u \int \mathrm{d}^4 x \, (u^\dagger u) + \mathrm{i}\mu_d \int \mathrm{d}^4 x \, (d^\dagger d) \,, \tag{2.9}$$

where we used that the particle density operator associated with a quark flavor $q = u, d$ can be expressed via $n \sim (q^\dagger q)$, see also Ref. [125] for a review on spinors in *Euclidean* spacetime. Note that, for each quark flavor q, the particle number N_q is conserved, where the corresponding particle number operator can be written as $\int \mathrm{d}^3 x \, (q^\dagger q)$. This conservation law can be traced back to a preserved symmetry by virtue of the famous *Noether* theorem. The

underlying symmetry which gives rise to the particle conservation is the $U(1)_V$ symmetry which is exactly realized in QCD, see Sec. 2.3.2 for a more detailed discussion.

The two different quark chemical potentials, which are associated with the up- and down-quark density, can be rewritten using the following transformation:

$$\mu_q = \frac{1}{2}(\mu_u + \mu_d), \qquad\qquad \mu_I = \frac{1}{2}(\mu_u - \mu_d), \qquad\qquad (2.10)$$

where μ_q is the quark chemical potential, and μ_I denotes the isospin chemical potential. Loosely speaking, μ_q can be interpreted as the "amount" of baryonic matter compared antimatter. On the other hand, the "amount" of up to down quarks is controlled by the isospin chemical potential μ_I. Using the transformation above, we can write the classical action in terms of a collective fermion field $\psi = (u, d)^T$, which stores both flavor types simultaneously. Using the latter notation, the classical action from Eq. (2.9) can be written as

$$S[\bar{\psi}, \psi] \to S[\bar{\psi}, \psi] + \mathrm{i}\mu_q \int \mathrm{d}^4x \, (\bar{\psi}\gamma_0\psi) + \mathrm{i}\mu_I \int \mathrm{d}^4x \, (\bar{\psi}\gamma_0\tau_3\psi), \qquad (2.11)$$

with the diagonal *Pauli* matrix τ_3. Note that for our computations in the present work, we concentrate on so-called isospin-symmetric matter where an equal number of up and down quarks is assumed. In this case, the chemical potentials associated with the up and down quarks are identical $\mu_u = \mu_d$ so that the isospin chemical potential vanishes $\mu_I = 0$. For convenience, we shall therefore write throughout this work $\mu \equiv \mu_q$ where we implicitly assume no imbalance between the number of up and down quarks. However, for various astrophysical applications like the description of dense neutron-rich matter ($\mu_I \neq 0$), which most likely exists in the core of neutron stars, see, e.g., Refs. [44, 45, 58], the approximation $\mu_I = 0$ can only be a first step towards a better understanding of the nature of dense QCD matter from microscopic interactions. We further stress that we neglect any strange quark degrees of freedom within our studies. The latter may also have a significant impact on the physics of neutron stars, see, e.g., Refs. [130, 131] for studies considering strange quark degrees of freedom in their derivation of the equation of state of dense hadronic matter. Nevertheless, our first-principle study of isospin-symmetric matter with two quark flavors may already provide us with some constraints for the nuclear equation of state and can give us insights about the nature of matter at high baryonic density, see Sec. 3.4 for a discussion.

2.2   The Functional Renormalization Group

In this section, we introduce our main framework to study QCD in the strongly-coupled *infrared* (IR) regime. Since QCD is asymptotically free, the strong interaction becomes weak in the limit of large momenta [6, 7]. At low momentum scales, however, the gauge interaction becomes strong and inaccessible with conventional perturbative methods. In the present work, we therefore employ the functional Renormalization Group (fRG) to study the long-range and low-momentum physics of QCD. For instance, let us consider a Quantum Field Theory that is defined on a microscopic high-momentum scale $k = \Lambda$ in the *ultraviolet* (UV). As we shall see, the Renormalization Group (RG) flow can then provide us with information on the *infrared* behavior of the theory by successively resolving quantum fluctuations. From this, we can determine whether the theory exhibits, e.g., critical behavior giving rise to long-range correlation effects and a possible finite mass gap, see our discussion in Sec. 2.3.2. In particular, the main idea of the Renormalization Group relies on a coarse-graining procedure where one usually studies the scaling behavior of the theory's associated correlation functions by varying a dimensionful scaling parameter. The corresponding RG flow is then mostly driven by fluctuation effects and dominated by (scale-invariant) non-trivial fixed points of the underlying theory space. Note that alone the mere existence of critical fixed points can be of great importance for the *infrared* behavior of a theory and may point to new physics in the low-energy regime.

Historically, a perhaps rather descriptive view on the Renormalization Group goes back to *Kadanoff* [132]. He constructed a coarse-graining prescription by employing a reframing procedure of a two-dimensional lattice of

atomic particles with spin sitting on different lattice sites of a grid. By gathering particles in block-type structures and deriving, e.g., the averaged spin of such a block, one effectively defines a certain type of RG transformation. Repeating this aforementioned procedure several times, we create new blocks which are assembled again from old spin-block structures. The so-defined block-spin transformation then allows for a study of the long-range behavior of, e.g., *Ising*-type models, to understand the scaling relation of the magnetization as a function of the temperature close to the critical *Curie* temperature.

Further developments in the understanding of the Renormalization Group were made by *Callan* and *Symanzik* who studied the dependence of the two-point function by varying the renormalized mass parameter of a theory, see Ref. [133, 134] for the famous *Callan-Symanzik* Renormalization Group equation. A closely related view on the Renormalization Group goes back to *Wilson* who proposed to integrate out quantum fluctuations piecewise within so-called momentum shells, see Ref. [135]. For this, one usually starts with a microscopic theory in the limit of large momenta which can be described best using high-energy degrees of freedom such as quarks and gluons. By successively integrating out the high-momentum modes, we approach the *infrared* theory which is possibly dominated by effective low-energy degrees of freedom such as mesons or nucleons, see Refs. [136, 137] and also Ref. [138] for a review of *Wilson's* work. Since the regulator function $R_k(p^2)$ appearing in the *Wetterich* equation we shall discuss below only slices out momenta around $p \sim k$, where k defines our continuous RG scale, the functional RG can be seen as a direct representation of *Wilson's* idea.

2.2.1 Derivation of the Wetterich Equation

The *Wetterich* equation was derived in 1992, see Refs. [63, 64], and corresponds to a *Wilson*-type Renormalization Group. By successively integrating out quantum fluctuations momentum shell by momentum shell, the *infrared* physics is approached by starting from a microscopic action in the *ultraviolet*. In the last decades, the *Wetterich* and related Renormalization Group equations, were successfully applied in various fields of physics ranging from, e.g., the description of turbulence in continuum mechanics [139–145] to a theory of quantum gravity [146–157] in the sense of an asymptotic safety scenario originally proposed by *Weinberg* [158]. The main object of the *Wetterich* equation is the scale-dependent coarse-grained effective action Γ_k with an RG-scale parameter k. For Γ_k, we require:

$$\lim_{k \to \Lambda} \Gamma_k = S \,, \qquad\qquad \lim_{k \to 0} = \Gamma \,, \qquad\qquad (2.12)$$

which means that at an *ultraviolet* RG-cutoff scale $k = \Lambda$ we recover the microscopic classical action S. In the *infrared* limit $k \to 0$, however, we find the full quantum action Γ which includes all quantum effects. As we have mentioned above, the *Wetterich* equation interpolates between the microscopic physics at high momenta and small length scales and the macroscopic physics at low momenta and large length scales. In this spirit, it can be compared to a theoretical microscope resolving physics on different length or momentum scales, respectively. We add that a further convenient property of the *Wetterich* equation is that it only deals with fully *dressed* renormalized n-point functions.

Let us now discuss the derivation of the *Wetterich* equation. To this end, we need to regularize the partition function $\mathcal{Z}[J]$ from the previous section by inserting a proper scale-dependent regulator $R_k(p)$ implementing the technical details of the aforementioned momentum shell integration. For this, we define the regularized partition function [63, 159] which reads

$$\mathcal{Z}_k[J] \sim \mathcal{N} \int_\Lambda \mathcal{D}\Phi \, \mathrm{e}^{-(S[\Phi] + \Delta S_k[\Phi]) + J^T \cdot \Phi} \sim \mathrm{e}^{W_k} \,, \qquad\qquad (2.13)$$

where we introduced the super field $\Phi = (\psi^T, \bar\psi, A_\mu^a, \phi)^T$. The latter contains different quantum field types such as boson, fermion and gauge fields. Here, the fermion fields are *Grassmann*-valued and carry internal color as well as flavor degrees of freedom. Depending on the theory, there can be other quantum fields as well, e.g., ghost fields for theories of the *Yang-Mills* type [5, 160] which we shall discuss in Sec. 2.3.1. From Eq. (2.13), we see that each

field is accompanied by an external source term of the form $J^T = (\bar{J}_\psi, -J^T_{\bar{\psi}}, J^a_{A,\mu}, J_\phi)$. The different sources inherit the field properties of their corresponding quantum fields, i.e. source terms coupled to fermion fields are also anticommuting *Grassmann* fields and carry the same internal quantum numbers. The matrix-valued regulator function is included in $\Delta S_k[\Phi]$ which reads:

$$
\begin{aligned}
\Delta S_k[\Phi] &= \frac{1}{2}\Phi^T \cdot R_k \cdot \Phi \\
&= \frac{1}{2}\int \frac{\mathrm{d}^D q}{(2\pi)^D} \left(\bar{\psi}(q)R_{\psi,k}(q)\psi(q) - \psi^T(-q)R^T_{\psi,k}(-q)\bar{\psi}^T(-q) \right. \\
&\qquad\qquad \left. + A^a_\mu(-q)R^{ab,\mu\nu}_{A,k}(q)A^b_\nu(q) + \phi(-q)R_{\phi,k}(q)\phi(q) \right),
\end{aligned}
\tag{2.14}
$$

with the regulator matrix R_k. For further details on our conventions, we also refer to App. A. Note that we shall discuss the regulator R_k and its properties at the end of this section. From Eq. (2.13), the derivation of the *Wetterich* equation can be performed by computing the derivative of the coarse-grained *Schwinger* functional $W_k[J]$ with respect to the RG-scale parameter k:

$$
\partial_k W_k[J] = -\langle \partial_k \Delta S_k[\Phi]\rangle_{k,J} = -\frac{1}{2}(\partial_k R_k)_{mn}\langle \Phi^T_m \Phi_n\rangle_{k,J}.
\tag{2.15}
$$

Here, the indices m, n shall reflect the matrix structure of the expression above. In the next step, we substitute the structure above with the full connected two-point function $W^{(1,1)}_k \equiv \langle \Phi \cdot \Phi^T\rangle_{\mathrm{c}}$ which can be obtained by taking the second functional derivative of $W_k[J]$ with respect to the source J:

$$
W^{(1,1)}_k[J] = \frac{\overrightarrow{\delta}}{\delta J^T}W_k[J]\frac{\overleftarrow{\delta}}{\delta J} = \langle \Phi \cdot \Phi^T\rangle_{k,J} - \langle \Phi\rangle_{k,J}\cdot\langle \Phi^T\rangle_{k,J}.
\tag{2.16}
$$

Note that this is done in complete analogy to Eq. (2.7) from the previous section. With the connected two-point correlation function at hand, we can write for Eq. (2.15):

$$
\partial_k W_k[J] = -\frac{1}{2}\mathrm{STr}\left[(\partial_k R_k)\cdot W^{(1,1)}_k\right] + \partial_k \Delta S_k[\Phi_{\mathrm{cl}}],
\tag{2.17}
$$

where we introduced the classical field $\Phi_{\mathrm{cl}} = \langle\Phi\rangle$. In principle, the classical field Φ_{cl} entering the scale-dependent effective action can, in general, also depend on the RG-scale parameter k. The latter then allows for a continuous transition from high- to low-energy degrees of freedom [22, 159, 161–164]. Since such an extension lies beyond the scope of the present work, however, we neglect any k-dependence of the classical field. For convenience, we moreover introduced a shorthand notation for functional derivatives acting on a functional $F[h]$:

$$
F^{(n,m)} = \underbrace{\frac{\overrightarrow{\delta}}{\delta h^T}\cdots\frac{\overrightarrow{\delta}}{\delta h^T}}_{n-\mathrm{times}} F[h] \underbrace{\frac{\overleftarrow{\delta}}{\delta h}\cdots\frac{\overleftarrow{\delta}}{\delta h}}_{m-\mathrm{times}}.
\tag{2.18}
$$

According to Eq. (2.18), we take derivatives with respect to the super fields Φ and J from the right (row vectors) and derivatives with respect to transposed super fields Φ^T and J^T from the left (column vectors)[1] so that the propagator $W^{(1,1)}_k$ becomes matrix-valued in field space as it is already the case for the regulator matrix R_k.

The coarse-grained effective average action is again defined by using the functional equivalent of a *Legendre* transformation of the generating functional $W_k[J]$ (see also the definition in Eq. (2.8)):

$$
\Gamma_k[\Phi_{\mathrm{cl}}] = \sup_J \left(J^T \cdot \Phi_{\mathrm{cl}} - W_k[J]\right) - \Delta S_k[\Phi_{\mathrm{cl}}].
\tag{2.19}
$$

---

[1]In case of purely bosonic theories there is no need to distinguish between left and right derivatives. The *Grassmann* nature of the fermionic fields, however, requires a careful treatment of the antisymmetric field subspaces.

Again, we introduced the supremum condition for the first part of the equation to ensure convexity. However, compared to Eq. (2.8), there is now a regulator term $\sim \Delta S_k$ present in the definition of the coarse-grained effective action Γ_k. Thus, any non-convexities appearing at finite k originate from the regulator part ΔS_k which is removed for $k \to 0$ by construction, see our discussion below. Therefore, in case of $J = J_{\text{sup}}$, it is ensured that $\Gamma = \Gamma_{k=0}$ is convex in any case. From here, we shall now always tacitly assume that a source J is chosen such that the supremum requirement in Eq. (2.19) is fulfilled. From Eq. (2.19), we further deduce:

$$
\begin{aligned}
\frac{\overrightarrow{\delta}}{\delta \Phi_{\text{cl}}^T}(\Gamma_k[\Phi_{\text{cl}}] + \Delta S_k[\Phi_{\text{cl}}]) &= \left(\frac{\overrightarrow{\delta} J^T}{\delta \Phi_{\text{cl}}^T} \cdot \Phi_{\text{cl}} + J - \frac{\overrightarrow{\delta} J^T}{\delta \Phi_{\text{cl}}^T} \cdot \frac{\overrightarrow{\delta} W_k[J]}{\delta J^T} \right) \\
&= J \, .
\end{aligned}
$$

(2.20)

By taking the second functional derivative with respect to the classical field from the right, we find:

$$
\frac{\overrightarrow{\delta}}{\delta \Phi_{\text{cl}}^T}(\Gamma_k[\Phi_{\text{cl}}] + \Delta S_k[\Phi_{\text{cl}}]) \frac{\overleftarrow{\delta}}{\delta \Phi_{\text{cl}}} \cdot W_k^{(1,1)}[J] = \mathbb{1}_{\text{FS}} \, \delta(x - x') \, .
$$

(2.21)

with the identity operator $\mathbb{1}_{\text{FS}}$ of the underlying field space. Taking the k derivative of Eq. (2.19) and inserting our result from Eq. (2.17), we find

$$
\partial_k \Gamma_k[\Phi_{\text{cl}}] = \frac{1}{2}\text{STr}\left[(\partial_k R_k) \cdot W_k^{(1,1)}[J]\right] \, .
$$

(2.22)

We use our result from Eq. (2.21) to obtain the final form of the famous *Wetterich* equation:

$$
\partial_t \Gamma_k[\Phi_{\text{cl}}] = \frac{1}{2}\text{STr}\left(\frac{\partial_t R_k}{\Gamma_k^{(1,1)}[\Phi_{\text{cl}}] + R_k} \right) = \frac{1}{2} \, \otimes\!\!\bigcirc \, ,
$$

(2.23)

with the dimensionless scale derivative $\partial_t = k \, \partial_k$. The crossed circle in the diagram on the right-hand side shall underscore the regulator insertion we perform via $\partial_t R_k$. Moreover, the super trace reflects the nature of our field space containing both antisymmetric (fermionic) and symmetric (bosonic) field subspaces. Therefore, in case of an antisymmetric subspace an additional minus sign is added. We also observe that the *Wetterich* equation has a simple one-loop structure. However, by no means this shall indicate that only one-loop contributions in the sense of perturbation theory are present in the *Wetterich* equation (2.23). On the contrary, it contains an arbitrary number of perturbative loop orders, see, e.g. Ref. [165] for an explicit example at two-loop order.

As already mentioned, the *Wetterich* equation can be understood as an interpolation prescription between the microscopic theory and its corresponding macroscopic counterpart where the latter then gives us a direct access to the physical ground state. This can be illustrated by drawing the theory space of a Quantum Field Theory which is spanned by the renormalized couplings associated with the operator structures entering the theory under consideration. In Fig. 2.1, we therefore show two exemplary RG trajectories depicted as grayish lines and associated with different regularization and/or truncation schemes connecting the effective action at some initial scale $k = \Lambda$ and the full quantum effective action at $k = 0$ (arrows point towards the *infrared* direction). Here, the initial conditions are fixed at the high-momentum scale $k = \Lambda$ which are given, e.g., from known experimental constraints or measurements. We emphasize that the trajectories are dominated by fixed points (blue dots) of the theory for which the beta functions of the renormalized couplings vanish. Note that these fixed points in theory space mark theories which are scale invariant, i.e., the averaged action Γ_k remains constant for any value of k.

We demand for $k \to 0$ that the regulator is removed so that observables in the *infrared* physics do not depend on the regulator choice. However, because of necessary truncations which have to be made and due to the fact that
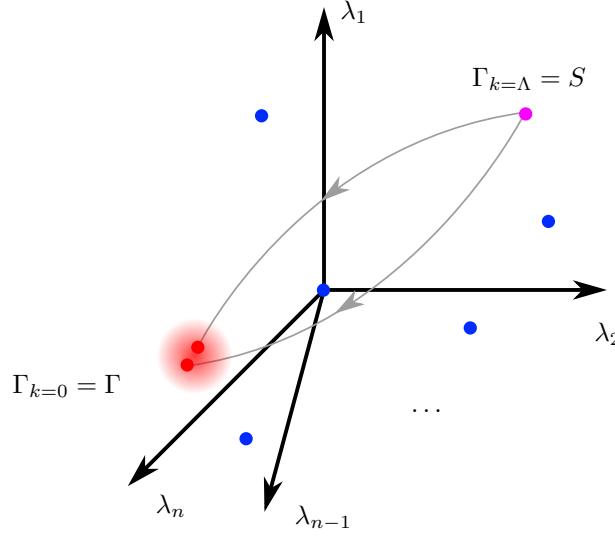
Figure 2.1: Illustrated is the theory space spanned by the couplings $\{\lambda_i\}$ which correspond to the operators entering a given ansatz for the coarse-grained effective action. The fixed points of the theory are depicted as blue dots. The *Wetterich* equation interpolates between the bare action $\Gamma_{k=\Lambda} = S$ in the *ultraviolet* and the full quantum effective action in the *infrared* $\Gamma_{k=0} = \Gamma$. Depending on the employed regulator and used truncations, however, RG flows are not necessarily unique as illustrated by the two grayish trajectories. Because of necessary truncations, moreover, the trajectories may end up at different points in the *infrared*.

a complete integration down to $k = 0$ can become very challenging if possible at all[2], the regulator function has, nevertheless, an impact on results. Therefore, it is desirable in any case that the influence of the regulator choice is mild, i.e., the *infrared* physics should not change drastically.

Let us now discuss the regulator function which we have inserted in the path integral in more detail. Even though the choice of the regulator is free, there are some minimal and necessary requirements the latter has to fulfill to ensure, e.g., the imposed boundary conditions Eq. (2.12). The three minimal requirements are (see Ref. [63]):

(i) The regulator remains finite in the limit of vanishing four-momenta:

$$\lim_{q^2/k^2 \to 0} R_k(q) > 0 \,. \tag{2.24}$$

(ii) It diverges suitably for $k \to \infty$ to ensure that the quantum effective average action Γ_k approaches the classical action S in the *ultraviolet*:

$$\lim_{k^2 \to \infty} R_k(q) \to \infty \,. \tag{2.25}$$

(iii) It vanishes in the limit $k \to 0$ so that the regulator function is removed in the *infrared*:

$$\lim_{k^2/q^2 \to 0} R_k(q) = 0 \,. \tag{2.26}$$

For example, an exponential regulator $R_k(p)$ and its scale derivative $\partial_t R_k(p)$ as a function of the momentum are depicted in Fig. 2.2. We find that the regulator acts in the *infrared* regime as an effective mass (i). For momenta around $p^2 \sim k^2$, the scale derivative of the regulator only cuts out a small momentum band which illustrates the

---

[2]A spontaneous breakdown of a continuous symmetry can be indicated by a divergence of the RG flow at a finite critical scale $k = k_{\mathrm{cr}}$, see our discussion in Sec. 2.3.2
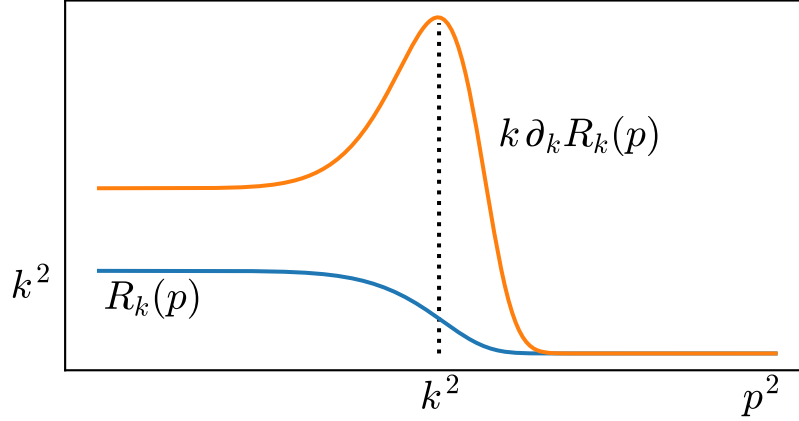
Figure 2.2: The figure shows an exemplary regulator function. For the regularization of any *infrared* divergences, the regulator is finite for $p \to 0$ which corresponds to a mass-like term in the propagator. The scale derivative of the regulator peaks at $p^2 \sim k^2$ implementing the *Wilsonian* momentum shell integration. For high momenta $p^2 > k^2$, the derivative of the regulator renders the propagator finite in the *ultraviolet*.

aforementioned *Wilsonian* momentum shell idea. Moreover, it renders the *ultraviolet* regime finite as it goes to zero for large momenta so that high-momentum modes are suppressed. All three requirements Eqs. (2.24)-(2.26) are necessary but may not be sufficient for certain theories. The regulator should further not, e.g., introduce an artificial breaking of fundamental symmetries of a quantum theory under consideration. Otherwise, an inappropriate regulator choice can significantly spoil the *infrared* physics. In worst case scenarios, certain regulator artifacts can not even be distinguished from real physics which can then lead to false conclusions, see Sec. 3.1.3 where we demonstrate how an uncareful regulator choice can alter results considerably. Therefore, we demand an extended set of "weak"/"convenience" requirements:

(iv) The regulator does not violate the chiral symmetry (see Sec. 2.3.2) of the kinetic term in the fermionic action.

(v) It does not introduce an artificial breaking of *Poincaré* invariance and, in particular, it preserves *Poincaré* invariance in the limit $T \to 0$ and $\mu \to 0$.

(vi) It respects the invariance of relativistic theories under the transformation $\mu \to -\mu$.

(vii) It ensures that the regularization of the loop diagrams is local in terms of temporal and spatial momenta at any finite value of the RG scale k.

The last requirement aims at all types of regulators which only act on spatial momenta and leave the temporal direction unregularized. These types of regulators have other technical advantages which we shall discuss in Sec. 3.1.3. However, they come along with the drawback to be incompatible with the *Wilsonian* momentum shell idea: For each infinitesimally small RG step δk, all temporal momenta contribute simultaneously. Therefore, one rather cuts out small cylindrical shells with an infinite cylinder height of the four-dimensional momentum space, instead of integrating out small spherical slices.

For an analytical treatment of the *Wetterich* equation, it is more convenient to write Eq. (2.23) in a slightly different mathematical form:

$$\partial_t \Gamma_k[\Phi_{\mathrm{cl}}] = \frac{1}{2} \mathrm{STr}\, \tilde{\partial}_t \ln \left\{ \Gamma_k^{(1,1)}[\Phi_{\mathrm{cl}}] + R_k \right\} , \tag{2.27}$$

with a modified scale derivative $\tilde{\partial}_t = \partial_t R_k \frac{\partial}{\partial R_k}$ which shall indicate that the derivative only acts on the regulator R_k. Moreover, the two-point function can be decomposed:

$$\Gamma_k^{(1,1)}[\Phi_{\text{cl}}] + R_k = \mathcal{P}_k + \mathcal{F}_k \,, \tag{2.28}$$

where we have split the two-point function $\Gamma^{(1,1)}[\Phi_{\text{cl}}]$ into a field-independent inverse propagator part $\mathcal{P}_k$ which is basically the two-point function evaluated at $\Phi_{\text{cl}} = 0$, and in a field-dependent fluctuation part $\mathcal{F}_k$. We now consider the series representation of the logarithmic function $\ln(1 + x)$ for the expression in Eq. (2.27):

$$
\begin{aligned}
\partial_t \Gamma_k[\Phi_{\text{cl}}] &= \frac{1}{2}\text{STr}\,\tilde{\partial}_t \ln\left(\mathcal{P}_k + \mathcal{F}_k\right) \\
&= \frac{1}{2}\text{STr}\,\tilde{\partial}_t \ln \mathcal{P}_k + \frac{1}{2}\text{STr}\,\tilde{\partial}_t \sum_{n=1}^{\infty} \frac{(-1)^{n-1}}{n}\left(\mathcal{P}_k^{-1}\mathcal{F}_k\right)^n \,,
\end{aligned}
\tag{2.29}
$$

with the propagator matrix $\mathcal{P}_k^{-1}$. Since $\mathcal{F}_k$ does not depend on the regulator, the scale derivative only acts on $\mathcal{P}_k$-type terms. Using the reformulation of the *Wetterich* equation above, one usually compares the right- and left-hand side of Eq. (2.29) in terms of contracted operator structures to deduce the beta functions corresponding to the renormalized couplings appearing in a given ansatz for the effective action.

Throughout the first part of our present study, we use existing software packages to compute the RG flow equations for our different quantum systems we shall introduce in the upcoming sections. For the derivation of the symbolic flows, we use the software package *DoFun* [166]. For the computation of traces in finite-dimensional vector spaces (*Dirac* space, $SU(N)$ space for color and flavor degrees of freedom), we employ the package *Form-Tracer* [167] which is based on the *FORM* library [168]. In the next subsection, we shall briefly discuss different expansion schemes which are frequently employed in non-perturbative functional Renormalization Group studies.

2.2.2 Approximations and Expansion Schemes

In the last section, we have introduced an exact evolution equation for the effective average action Γ_k with the convenient property that it is exact at one-loop order. Nevertheless, we also mentioned that, in principle, arbitrarily high loop orders are included and contribute to the RG flow. Moreover, from the structure of the *Wetterich* equation (2.29), we can readily see that an arbitrary n-point function, in general, also depends on the $(n + 1)$- and $(n + 2)$-point function building up an infinite tower of coupled differential equations. Therefore, interactions other than those originally considered in the effective action at some UV initial scale Λ can be generated dynamically. In particular, all operators which are compatible with the underlying symmetries may appear on the right-hand side of Eq. (2.29). It can therefore be important to anticipate at least certain fluctuation-induced operators in an ansatz for the effective action as we shall discuss in detail in Sec. 2.3.2. Our discussion above underscores the requirement to tailor efficient expansion and appropriate truncation schemes which should be both manageable and provide reasonably well results already at low expansion order covering the relevant physics of the quantum system under consideration.

Let us now briefly review some expansion schemes used in theoretical calculations. Here, the probably most frequently employed ansatz is an expansion in powers of a small dimensionless parameter $\alpha \lesssim 1$. Besides using a small dimensionless coupling constant, one can also expand a theory in $1/N$, where N can be the number of color or flavor degrees of freedom. Other schemes perform an expansion for a small anomalous dimension η or use so-called hard-thermal-loop perturbation theory for studies at finite temperature, see, e.g., Refs. [169–171] for early works and Refs. [172, 173] for reviews.

Nevertheless, we emphasize that it is far from being trivial to find efficient expansion schemes which are valid over a wide range of parameter sets and scales. Especially, if one tries to resolve inherently non-perturbative phenomena, e.g., the physics close to a phase transition. Moreover, it would be desirable if an expansion scheme is systematic in the sense that higher-order contributions improve the findings from lower orders. Unfortunately, the

radius of convergence of a given expansion can be small so that this might not necessarily be the case. In the following, we discuss two frequently used expansion schemes for the effective average action which are often employed in RG studies. Note that the following discussion mostly relies on the review in Ref. [174]:

- *Derivative expansion:* We expand the effective average action (or any other functional of interest) by counting the number of derivatives:

$$\Gamma_k[\phi] = \int \mathrm{d}^D x \left(U_k(\phi^2) + \frac{1}{2} Z_k(\phi^2)(\partial_\mu \phi)^2 + \frac{1}{4} Y_k(\phi^2)(\phi\,\partial_\mu\phi)^2 + \mathcal{O}(\partial^4) \right) , \qquad (2.30)$$

with a bosonic field denoted by ϕ. Here, the next higher order of the *derivative expansion* [175–178] would contain four derivatives $\mathcal{O}(\partial^4)$. At leading order of the *derivative expansion*, the so-called wave-function renormalizations Z_k is set to one and Y_k as well as all further complicated momentum dependencies of the n-point correlation functions are dropped. The latter type of simplification is then also known as the so-called *Local Potential Approximation* (LPA). Let us now briefly discuss how critical behavior can be studied using a *derivative expansion*. For this, we start with the remark that a critical inverse propagator of the type

$$\Gamma_k^{(2)} \sim p^2 (p^2 + k^2)^{-\eta/2} , \qquad (2.31)$$

with anomalous dimension η, can be non-analytic in the momentum structure. The key ingredient why the *derivative expansion* is not doomed to fail in this case, can be explained from the observation that for any finite $k \gtrsim 0$, the limit $p^2 \to 0$ is well defined. Even further, due to the mass-like behavior of the regulator R_k, long-range modes in the *infrared* regime are suppressed. Since the scale derivative of the regulator $\partial_t R_k$ also suppresses high-momentum modes $p^2 \gg k^2$, the propagator remains finite in any case. From this discussion, we see that even an expansion about $p^2 = 0$ should yield reasonable results. However, we emphasize that this is a consequence of the necessary regulator properties Eqs. (2.24)-(2.24) which has to be fulfilled.

- *Expansion in n-point correlation functions:* We write the effective action in terms of n-point functions $\Gamma^{(n)}$ coupled to powers of the field:

$$\Gamma_k[\phi] = \Gamma_k[\phi_{0,k}] + \sum_{n=1}^{N} \int \mathrm{d}^D x_1 \cdots \int \mathrm{d}^D x_N \left[\frac{1}{n!} \Gamma_k^{(n)}[\phi_{0,k}]\Big((\phi - \phi_{0,k}) \ldots (\phi - \phi_{0,k}) \Big) \right], \quad (2.32)$$

where $\Gamma^{(n)}$ denotes the n-th functional derivative with respect to the classical field ϕ. Note that $\Gamma^{(n)}$ depends, in general, on N spacetime coordinates which are not displayed to improve the readability. We further emphasize that the expansion is performed around the k-dependent ground state $\phi_{0,k}$ so that $\Gamma^{(1)}[\phi_{0,k}] = 0$, by construction. Using such an expansion, it is possible to keep track of the interacting ground state for any finite value of k. By taking arbitrary derivatives of the expansion above, we obtain a coupled set of differential equations for the various n-point correlation functions depending on the $(n + 1)$- and $(n + 2)$-correlation function. From this, the aforementioned infinite tower of differential equations is very obvious. The main idea behind this scheme relies on the assumption that higher-order correlation functions have a smaller impact on observables of interest for certain scales. Therefore, a truncated number of n-point correlation functions still allows to model the relevant properties of the system under investigation. Based on an expansion in n-point functions, there are other schemes which try to include the effect of dropped correlation functions partially. For example, with the *Blaizot, Méndez-Galain* and *Wschebor* (BMW) approximation, it is, in principle, possible to close the tower of flow equations, see Refs. [179, 180] for details.

Aside from the *derivative expansion* and the *expansion in n-point correlation functions*, there are other frequently employed schemes, e.g., an *expansion in the canonical dimension*, see Ref. [174]. In the first part of this thesis, we use a *derivative expansion* in leading order to study hot and dense quark matter, where we consider the RG flow of effective four-quark interactions. The latter appears to be crucial for our study of the chiral phase transition, see

our discussion in Sec. 2.3.2. In our study of non-relativistic fermion matter, we employ an *expansion in n-point correlation functions* where our fundamental degree of freedom is the density $\rho \sim \langle \psi^\dagger \psi \rangle$ and not the classical field $\langle \phi \rangle$. Therefore, we expand our functional in terms of *n-density correlation functions* which is, nevertheless, in complete analogy to the *expansion in n-point* functions which we have introduced above.

2.3 Phases of QCD and Spontaneous Symmetry Breaking

In this section, we shall give a brief overview of QCD, the theory of the strong interaction. Due to properties like asymptotic freedom, i.e., the theory becomes weakly coupled for large momentum-scales as discovered by *Gross*, *Wilczek* and *Politzer* [6, 7], non-Abelian gauge theories like QCD still attract a tremendous scientific interest as they represent our best understanding of the particles and their interplay in our universe so far.

The quantum fields, which enter QCD as fundamental degrees of freedom are quarks and gluons. In QCD, the up and the down quark are the two lightest quarks in of the theory. Compared to its constituent quark mass, they have a comparably small but finite so-called current quark mass $m_\psi \approx 2-5\,\mathrm{MeV}$. The latter does not stem from QCD itself but rather has its origin in the electroweak sector of the Standard Model of particle physics. QCD with only two flavors can further be considered to obey an approximate global $SU(2)_L \times SU(2)_R \times U(1)_V \times U(1)_A$ symmetry. As we shall see, this symmetry can break spontaneously. As a consequence, the three pions $\vec{\pi} = \{\pi^-, \pi^0, \pi^+\}$ would be massless if chiral two-flavor symmetry were exact. Even though they acquire a finite mass because of the explicit chiral symmetry breaking due to the finite current quark mass, they are still by far the lowest-lying states in the meson spectrum, i.e., the pion triplet has an averaged mass of $m_\pi \approx 138\,\mathrm{MeV}$ where the next higher-lying kaon multiplet has an averaged mass of $m_K \approx 495\,\mathrm{MeV}$, see Ref. [181]. The pions are so-called (pseudo) *Nambu-Goldstone* bosons and can be seen as an example for the prediction of the famous *Nambu-Goldstone* theorem [182–184]. The main statement of the latter theorem is that we find massless *Nambu-Goldstone* modes (bosons) in the theory's energy spectrum for each broken generator of the underlying continuous global symmetry group. It is important to emphasize that the *Nambu-Goldstone* theorem only holds for continuous symmetries. For instance, there are no *Nambu-Goldstone* bosons present for spontaneously broken discrete symmetries, e.g., for theories which obey a discrete Z_2 symmetry with $\phi(x) \to -\phi(x)$. Chiral symmetry is only realized approximately in the underlying QCD Lagrangian. Throughout the present thesis, for simplicity, we work in the so-called chiral limit $m_\psi \to 0$. At least in the vacuum, chiral symmetry is then spontaneously broken in the ground state of the theory. From this, it follows that the *Nambu-Goldstone* modes are massless in our case. The breakdown of chiral symmetry also comes along with the formation of a finite mass gap in the quark propagator giving rise to a dynamically generated and comparably large constituent quark mass $m_\psi \approx 300\,\mathrm{MeV}$ as we shall see in Sec. 2.3.2. The latter is then responsible for a significant amount of the observable mass created through the spontaneous breakdown of chiral symmetry that occurred in the early universe.

For large densities, however, various model studies [28, 31–35] predict a tremendously rich QCD phase diagram accompanied by a large variety of different symmetry breaking patterns. Here, the probably most interesting prediction is a phase rather dominated by so-called diquark degrees of freedom than by mesonic ones [32, 33]. The underlying quark-quark pairing mechanism shares several similarities to the conventional theory of superconductivity initially developed by *Bardeen*, *Cooper*, and *Schrieffer* [2, 3], which is the reason why this state of matter is often referred as a color superconductor [42, 43]. We shall discuss these aspects in more detail in the subsections 2.3.2 and 2.3.4.

We structure the present section as follows: we begin with a short introduction to non-Abelian gauge theories starting from the requirement of local gauge invariance. To satisfy the latter, we find that the inclusion of gauge bosons is required which can be identified with gluons for a $SU(3)$ gauge theory like QCD. After that, we discuss two-flavor QCD at vanishing current quark mass in the chiral limit. We review the spontaneous breakdown of chiral symmetry induced by strong gauge dynamics and analyze the consequences for the *infrared* physics. In this context, we also discuss the influence of gauge degrees of freedom on the fixed-point structure of the effective four-fermion

vertices playing an essential role in the mechanism of spontaneous chiral symmetry breaking. Finally, we briefly discuss the conjectured QCD phase diagram at finite temperature and quark chemical potential.

2.3.1   Non-Abelian Local Gauge Invariance and the QCD Lagrangian

We discuss the principles of local gauge symmetry and outline the quantization of non-Abelian gauge theories. For this, we work along the lines of standard textbooks such as Refs. [126, 185, 186]. Local gauge invariance is the defining property for all gauge theories. There are two important types of gauge theories. On the one hand, for example, we have Abelian gauge theories, e.g., Quantum Electrodynamics (QED), where the generators of the underlying gauge group commute. On the other hand, we also have non-Abelian gauge theories, e.g., QCD or the *Glashow-Salam-Weinberg* (GSW) theory of the electroweak force, where the generators do not commute. In the present subsection, we shall see that for both types of gauge theories, the requirement of local gauge invariance implies the existence of gauge bosons like photons or gluons.

  We begin with the definition of the fermionic matter field $\psi(x)$ appearing in N_c different states[3]. For this, we define the column vector

$$\psi(x) \equiv \begin{pmatrix} \psi_1(x) & \psi_2(x) & \dots & \psi_{N_c}(x) \end{pmatrix}^T , \tag{2.33}$$

with $N_c = 3$ in case of QCD. We further define the local gauge transformation $U(x) \in SU(N_c)$ for the fermion field:

$$\psi(x) \rightarrow U(x)\psi(x) = \mathrm{e}^{\mathrm{i}\theta^a(x)T^a}\psi(x) , \tag{2.34}$$

with the real-valued generalized rotation angles $\theta^a(x)$ and the infinitesimal hermitian generators T^a of the underlying *Lie* group $SU(N_c)$ obeying the $(N_c^2 - 1)$-dimensional *Lie* algebra

$$\left[T^a, T^b \right] = \mathrm{i} f^{abc} T^c , \tag{2.35}$$

with the antisymmetric structure constants f^{abc} in the fundamental representation [187]. For a $SU(2)$ (spin-1/2) gauge group, e.g., the structure constants are the entries of the three-dimensional totally antisymmetric *Levi-Civita* symbol $f^{abc} = \varepsilon^{abc}$. In case of the color $SU(3)$ gauge group, however, the structure constants are rather involved, see, e.g., Ref. [126]. Note that for a local transformation it is crucial that we allow for the rotation angles $\theta^a(x)$ to depend on the spacetime coordinates as well.

  We now require local gauge invariance of the equations of motion corresponding to a theory under consideration. Let us therefore consider the infinitesimal version of the $SU(N_c)$ transformation (2.34) which reads:

$$\psi \rightarrow \psi + \mathrm{i}\theta^a(x)T^a\,\psi(x) + \mathcal{O}(\theta^2) , \qquad\qquad \bar{\psi} \rightarrow \bar{\psi} - \mathrm{i}\theta^a(x)\bar{\psi}(x)\,T^a + \mathcal{O}(\theta^2) . \tag{2.36}$$

where we denote the N_c infinitesimal rotation angles by $\theta^a(x)$ and use that $(T^a)^\dagger = T^a$. In general, the Lagrangian $\mathcal{L}$ of a given theory also entails derivatives acting on the fermion fields, e.g, a kinetic term of the form $T_{\mathrm{kin}} \sim \bar{\psi}(x)\gamma^\mu\partial_\mu\psi(x)$. Under the local transformation (2.34), we find for the field derivative

$$\partial_\mu\psi(x) \rightarrow \partial_\mu\psi(x) + \mathrm{i}(\partial_\mu\theta^a(x))T^a\,\psi(x) + \mathrm{i}\theta^a(x)T^a\,(\partial_\mu\psi(x)) + \mathcal{O}(\theta^2) . \tag{2.37}$$

We immediately see that the infinitesimal local rotation in Eq. (2.36) just corresponds to a linear shift. In this case, it makes no difference if the transformation was local or global, i.e., the rotation angles can be considered to be constants for all spacetime points. However, we recognize that this is not true for Eq. (2.37) as the derivative also acts on the rotation angle $\theta^a(x)$ itself. To compensate the contribution $\sim \partial_\mu\theta^a(x)$, in the following we introduce a

---

[3]For simplicity, we neglect further internal degrees of freedom at this point.

new bosonic field type.

For the theory underlying this new bosonic gauge field $A_\mu^a(x)$ with $a = 1, \ldots, (N_c^2 - 1)$, we require again local gauge invariance. Since we wish to define a transformation rule similar to Eq. (2.36), i.e., we have a matrix T^a acting on a vector $\psi(x)$, we use the adjoint representation of the $SU(N_c)$. Here, the generators in the adjoint representation t^a are represented by $(N_c^2 - 1, N_c^2 - 1)$ matrices which are defined via the group structure constants f^{abc}:

$$(t^a)_{bc} = -\mathrm{i} f^{abc} \,. \tag{2.38}$$

Since the commutation relation is independent of the representation, we have for the generators in the adjoint representation:

$$\left[t^a, t^b\right] = \mathrm{i} f^{abc}\, t^c \,. \tag{2.39}$$

The local $SU(N_c)$ gauge transformation for the gauge field $A_\mu(x) \equiv A_\mu^a(x) T^a$ for finite rotation angles $\theta^a(x)$ can be written as

$$A_\mu(x) \rightarrow A_\mu^\theta(x) \equiv U(x) A_\mu(x) U^{-1}(x) - \frac{\mathrm{i}}{\bar{g}} \left(\partial_\mu U(x)\right) U^{-1}(x) \,, \tag{2.40}$$

where we have introduced a bare gauge coupling constant $\bar{g}$. In case of QCD, we shall relate $\bar{g}$ to the strong coupling. Using the adjoint representation, the gauge transformation for infinitesimal $\theta^a(x)$ reads:

$$
\begin{aligned}
A_\mu^{\theta,a}(x) &= A_\mu^a(x) + \frac{1}{\bar{g}} \partial_\mu \theta^a(x) + \theta^c(x)(t^c)_{ab}\, A_\mu^b(x) \\
&= A_\mu^a(x) + \frac{1}{\bar{g}} \partial_\mu \theta^a(x) + f^{abc} A_\mu^b(x) \theta^c(x) \\
&= A_\mu^a + \frac{1}{\bar{g}} D_\mu \theta^a(x) \,.
\end{aligned}
\tag{2.41}
$$

Here, we have introduced the so-called *covariant* derivative

$$D_\mu = \partial_\mu - \mathrm{i}\bar{g} A_\mu^a(x) T^a \,. \tag{2.42}$$

Using the definition from above, we find that the gauge transformation of $(D_\mu \psi)$ is proportional to $\theta^a(x)$, as desired:

$$
\begin{aligned}
D_\mu \psi(x) &\rightarrow D_\mu \psi(x) + \mathrm{i}\theta^a(x) \left(T^a \partial_\mu \psi - \bar{g} f^{abc} A_\mu^c T^b \psi - \mathrm{i}\bar{g} A_\mu^b T^b T^a \psi\right) + \mathcal{O}(\theta^2) \\
&= D_\mu \psi(x) + \mathrm{i}\theta^a(x) T^a D_\mu \psi(x) + \mathcal{O}(\theta^2) \,.
\end{aligned}
\tag{2.43}
$$

Note, the so-defined *covariant* derivative has the same transformation behavior as it is the case for the matter field ψ itself. Thus, as a "cooking recipe" to set up a locally gauge invariant theory, one has to replace all conventional four-derivatives acting on matter fields by their *covariant* counterparts $\partial_\mu \rightarrow D_\mu$.

From our discussion above, let us now consider a gauge-invariant kinetic term for the quarks. For this, we assume that the $N_f = 2$ quark flavors (up, down) encoded in a matter field ψ carry $N_c = 3$ different color charges (red, blue, green). Correspondingly, antiquarks carry anticolors (antired, antiblue, antigreen). Following the "cooking recipe" from the discussion above, a gauge-invariant kinetic term for the quarks in *Euclidean* spacetime is given by

$$\mathcal{L}_{(\bar{\psi}\psi)} = \bar{\psi}(\mathrm{i}\gamma_\mu D_\mu + \mathrm{i} M_f)\psi \,, \tag{2.44}$$

with a mass matrix M_f, which we set to zero in the chiral limit $M_f \rightarrow 0$.

In general, the gauge field A_μ^a is dynamical, too. A local gauge transformation of a possible kinetic term $\sim \partial_\mu A_\mu^a$

then generates again contributions like $\partial_\mu \partial_\nu \theta^a(x)$. This problem can be solved, by considering the commutator relation of the *covariant* derivative D_μ, which yields (e.g. see Ref. [185])

$$[D_\mu, D_\nu] = -i\bar{g} F^a_{\mu\nu} T^a \,, \tag{2.45}$$

with the non-Abelian field strength tensor

$$F^a_{\mu\nu} = \partial_\mu A^a_\nu - \partial_\nu A^a_\mu + \bar{g} f^{abc} A^b_\mu A^c_\nu \,. \tag{2.46}$$

Eq. (2.46) shows an important feature of non-Abelian gauge theories. Due to the non-Abelian structure of the gauge group $SU(N_c)$, we now obtain a term $g f^{abc} A^b_\mu A^c_\nu$ in the field tensor $F^a_{\mu\nu}$, which does not appear in Abelian gauge theories. As a consequence, the gauge fields become self-interacting. Let us now compute the transformation of the field strength tensor $F^a_{\mu\nu}$. We find:

$$F^a_{\mu\nu} \rightarrow F^a_{\mu\nu} - f^{abc} \theta^b(x) F^c_{\mu\nu} \,. \tag{2.47}$$

As desired, the transformation of $F^a_{\mu\nu}$ is just linear in $\theta^a(x)$.

Together with the field strength tensor (2.46), we can now construct the Lagrangian of chiral two-flavor QCD [4–7]:

$$\mathcal{L}^{(N_f=2)}_{\chi\text{QCD}} = \bar{\psi}(i\gamma_\mu D_\mu)\psi + \frac{1}{4} F^a_{\mu\nu} F^a_{\mu\nu} \,. \tag{2.48}$$

As a non-Abelian gauge theory, QCD has several remarkable properties. For example, due to color confinement [16, 17], bound states assembled of quarks always appear as color singlets which have a net zero color charge. A meson, for instance, consists of a quark and an antiquark where both carry opposite color charges, i.e., the antiquark carries the anticolor which corresponds to the color of the quark. For baryonic bound states, which are composed of three quarks, each quark carries a different color so that the net color charge of the three-body bound state is still zero. By trying to separate a quark spatially, the potential energy in the generated color flux tube increases until it breaks and a new quark-antiquark pair is created, see, e.g., Refs. [188, 189]. As a consequence, the quarks are always confined in a color singlet state.

The purely gluonic term $\sim F^a_{\mu\nu} F^a_{\mu\nu}$ in Eq. (2.48) corresponds to the famous *Yang-Mills* theory [5]. As already indicated, the *Yang-Mills* Lagrangian contains fundamental three- and four-boson self-interactions which are already present on the level of the classical action. However, we emphasize that there are other choices possible to define gauge-invariant Lagrangians from the field strength tensor $F^a_{\mu\nu}$. As one can show, chiral two-flavor QCD as defined in Eq. (2.48) is simultaneously invariant under charge $\mathcal{C}$ and parity $\mathcal{P}$ transformations. Nevertheless, one may also consider a term violating $\mathcal{P}$ and $\mathcal{CP}$ which is given by

$$\mathcal{L}_\theta \sim \theta \, \varepsilon_{\mu\nu\lambda\sigma} F^a_{\mu\nu} F^a_{\lambda\sigma} \,, \tag{2.49}$$

with a parameter θ and the antisymmetric *Levi-Civita* symbol in four dimensions $\varepsilon_{\mu\nu\lambda\sigma}$. Interestingly, experimental tests of QCD suggests that the parameter θ has to be surprisingly small $\theta \lesssim 10^{-9}$, see Refs. [190, 191]. This observation alone may not be an issue since QCD could be a theory where the discrete $\mathcal{CP}$ symmetry is exactly realized. However, as a consequence of the topologically non-trivial quantum vacuum structure of QCD, there are gauge configurations possible so that terms like (2.49) are generated by QCD itself [192–194]. Therefore, it is not clear why $\mathcal{CP}$ should not be badly broken. Thus, the main question of the so-called strong $\mathcal{CP}$ problem is, why the parameter θ should be small at all. For this, there exists a possible solution proposed by *Peccei* and *Quinn* in 1977 [195]. To resolve the strong $\mathcal{CP}$ problem, they introduced a new chiral $U(1)$ symmetry, which can break spontaneously. They showed that for the interacting ground state the theory then assumes, the $\mathcal{CP}$ symmetry is dynamically conserved since the "angle" θ becomes small, see Ref. [196] for a review.

We end this very brief overview of the strong $\mathcal{CP}$ problem with the remark that the non-trivial ground state of the *Peccei-Quinn* theory is associated with a new hypothetical particle, the axion. Since the discovery that the observable amount of matter in the universe seems to be insufficient to explain astrophysical observations, e.g., the anomalous rotation curve of spiral galaxies [197, 198], the axion became a possible candidate for cold dark matter, see, e.g., Ref. [199] for a review. In general, cold dark matter is a collective expression for the invisible matter at thermal energies which can only be measured due to its gravitational influence. Dark matter further appears to be hidden since it is expected to interact only weakly with conventional electromagnetic radiation. Since the prediction of the axion, there were various experiments proposed and already ongoing [200, 201] to find the axion solving the strong $\mathcal{CP}$ problem and to understand the nature of cold dark matter.

Up to this point, we discussed non-Abelian gauge theories on a classical level. Since we are interested in the quantum theory of the strong interaction, we wish to revisit the quantization process of non-Abelian theories. To be more specific, we concentrate on the gauge fixing procedure on the level of the functional field integral. Originally, when one tried to compute quantum corrections to scattering amplitudes, several issues were encountered in non-Abelian gauge theories, questioning the applicability of the latter at first sight. The problems could be resolved when one recognized that the application of the path integral method for gauge theories also includes an integration over an infinite number of equivalent gauge configurations. From the discussion above, we know that we can always employ a gauge transformation to the gauge field A_μ^a so that the Lagrangian (2.48) is left invariant. Using Eq. (2.41), the redundant gauge orbits can be illustrated. For this, let us assume that $A_\mu^a = 0$. In this case, we still have non-vanishing gauge-equivalent modes $\propto \partial_\mu \theta^a(x)$ accounting to the functional field integral. In that sense, it is necessary to find a way to properly fix the gauge avoiding an overcounting of gauge orbits in the path integral.

A solution for this problem was found by *Faddeev* and *Popov* who presented a method to define a gauge-fixed functional field integral, see Ref. [160]. To this end, it is necessary to introduce the following identity

$$1 = \int \mathcal{D}\theta \, \delta \left(G[A(\theta)] \right) \, \det \left(\frac{\delta G[A^\theta]}{\delta \theta} \right) , \tag{2.50}$$

with the transformed gauge field A^θ and a gauge-fixing condition $G[A]$ at our disposal. Obviously, for all gauge-fixing functionals $G[A]$ which are linear in θ, the functional derivative in the *Jacobi* determinant does not depend on the rotation angle. Clearly, this is also the case for the functional determinant itself. For example, we employ as a *covariant* gauge condition, see, e.g., Ref. [126]:

$$G[A] = \partial_\mu A_\mu^a(x) - \omega^a(x) , \tag{2.51}$$

where $\omega^a(x)$ denotes an arbitrary scalar function.

Let us now insert the identity (2.50) in a purely gluonic path integral with the *Yang-Mills* Lagrangian $\mathcal{L}_{\mathrm{YM}}$:

$$\begin{aligned} \mathcal{Z}[0] \sim \int \mathcal{D}A \, \mathrm{e}^{-\int \mathcal{L}_{\mathrm{YM}}[A]} &= \int \mathcal{D}\theta \int \mathcal{D}A \, \mathrm{e}^{-\int \mathcal{L}_{\mathrm{YM}}[A]} \delta \left(G[A(\theta)] \right) \det \left(\frac{\delta G[A(\theta)]}{\delta \theta} \right) \\ &= \int \mathcal{D}\theta \int \mathcal{D}A \, \mathrm{e}^{-\int \mathcal{L}_{\mathrm{YM}}[A]} \delta \left(G[A(\theta)] \right) \det \left(\frac{1}{\bar{g}} \, \partial_\mu D_\mu \right) . \end{aligned} \tag{2.52}$$

By introducing a new fermionic field type, the determinant term can be rewritten:

$$\det \left(\frac{1}{\bar{g}} \, \partial_\mu D_\mu \right) = \int \mathcal{D}\bar{c} \, \mathcal{D}c \, \mathrm{e}^{-\int \bar{c}(\partial_\mu D_\mu)c} . \tag{2.53}$$

Here, the fields $\bar{c}$ and c are the infamous so-called *Faddeev-Popov* ghosts. Further, the inverse coupling $1/\bar{g}$ has already been absorbed in the field normalization of the ghost fields. We now integrate over all $\omega(x)$ where we use the properties of the functional delta distribution in Eq. (2.52) which just picks one representative from the desired

gauge condition. For convenience, we add a *Gaussian* weighting function to the integrand of the ω integration giving only a contribution to the integral normalization:

$$
\begin{aligned}
\mathcal{Z}[0] \quad &\sim \quad \int \mathcal{D}\omega \int \mathcal{D}\theta \int \mathcal{D}A\,\mathcal{D}\bar{c}\,\mathcal{D}c\, \mathrm{e}^{-\int (\mathcal{L}_{\mathrm{YM}}[A] + \bar{c}(\partial_\mu D_\mu)c)} \delta\left(\partial_\mu A_\mu^a(x) - \omega^a(x)\right) \mathrm{e}^{-\int \frac{(\omega^a(x))^2}{2\xi}} \\
&= \quad \mathcal{N}(\xi) \int \mathcal{D}\theta \int \mathcal{D}A\,\mathcal{D}\bar{c}\,\mathcal{D}c\, \mathrm{e}^{-\int (\mathcal{L}_{\mathrm{YM}}[A] + \bar{c}(\partial_\mu D_\mu)c)} \mathrm{e}^{-\int \frac{(\partial_\mu A_\mu^a)^2}{2\xi}}\,,
\end{aligned}
\tag{2.54}
$$

with an (unimportant) normalization factor $\mathcal{N}(\xi)$ and a gauge parameter ξ. Since a gauge transformation is a linear shift which is followed by a rotation, one can show that the measure remains preserved under infinitesimal gauge transformations $\mathcal{D}A(\theta) = (\mathcal{D}A(\theta))'$. As a consequence, the integral over the rotation angle $\int \mathcal{D}\theta$ can be computed trivially where we absorb the resulting constant in the normalization $\mathcal{N}(\xi)$ of the functional field integral. Eventually, we find for the gauge-fixed path integral

$$
\mathcal{Z}[0] \quad \sim \quad \int \mathcal{D}A\,\mathcal{D}\bar{c}\,\mathcal{D}c\, \mathrm{e}^{-\int \left(\mathcal{L}_{\mathrm{YM}}[A] + \bar{c}(\partial_\mu D_\mu)c + \frac{1}{2\xi}(\partial_\mu A_\mu^a)^2\right)}\,.
\tag{2.55}
$$

In actual computations, the parameter ξ can be used to control some details of the employed gauge. For *covariant linear gauges* (2.51), two choices are employed very frequently

$$
\xi = \begin{cases} 0\,, & \text{for } \textit{Landau} \text{ gauge}\,, \\ 1\,, & \text{for } \textit{Feynman-t'Hooft} \text{ gauge}\,. \end{cases}
\tag{2.56}
$$

In our present work, we shall employ for technical reasons *Feynman-t'Hooft* gauge, see Sec. 3.3.

We end this section with some remarks. The ghost fields emerging from the *Jacobi* determinant in Eq. (2.53) transform in the adjoint representation of the $SU(N_c)$ group. For the latter, one obtains $(N_c^2 - 1)$ *Faddeev-Popov* ghost fields which are present in non-Abelian gauge theories. In the Abelian case, however, they can be completely removed, e.g., in case of QED. Even though they appear as *Grassmann*-valued fermion fields, they should by no means be considered as real particles, i.e., ghost fields do not obey the famous spin-statistics theorem and do only appear as internal lines, see, e.g., Ref. [186]. Instead, they should be seen as a convenient way to define a gauge-fixing condition in the functional field integral.

In our discussion, we have assumed that in order to fix the gauge uniquely, it suffices to use the divergence of the gauge field $\partial_\mu A_\mu^a$. Unfortunately, this is not necessarily the case as found by *Gribov* [202]. For further readings to the influence of *Gribov* copies, we refer to the reviews Refs. [203, 204].

The emergence of the unphysical ghost fields is accompanied by new questions, e.g., it is not clear if the so-defined gauge-fixing procedure holds for non-perturbative studies. Further, as a consequence of our gauge-fixing procedure, the *Faddeev-Popov* Lagrangian in Eq. (2.55) is not gauge invariant anymore. Nevertheless, gauge invariance should hold at least for physical observables such as correlation functions. Otherwise, physics could be changed by just varying the gauge. We note that these questions can be resolved by studying the so-called *Becchi-Rouet-Stora-Tyutin* (BRST) symmetry [205–207]. Indeed, one can show that the aforementioned gauge-fixed *Faddeev-Popov* Lagrangian in the path integral (2.55) is invariant under global BRST symmetry transformations. The *Noether* theorem then implies the existence of both a conserved charge and current associated with the BRST symmetry. In fact, the existence of so-called *Slavnov-Taylor* identities (STI) [208, 209] can be seen as a consequence of BRST charge conservation where the STI's are non-trivial relations linking the theory's different correlation functions. They can be therefore interpreted as a non-Abelian extension of the famous *Ward-Takahashi* identity (WTI) in, for example, QED. However, a detailed discussion of the topics above is not needed and would go beyond the scope of the present thesis. For further readings, we therefore refer to the literature given above.

2.3.2 Chiral Symmetry and Spontaneous Chiral Symmetry Breaking

The mechanism of spontaneous symmetry breaking plays a crucial role in the understanding of a wide range of physical phenomena. The breakdown of a continuous (global) symmetry comes along with a phase transition from a phase where the symmetry remains intact, to a phase where the symmetry is spontaneously broken in the ground state. This is then indicated by an order parameter σ which assumes a finite value $\sigma \neq 0$ in the symmetry broken regime. To be more specific, consider a theory described by a Lagrangian $\mathcal{L}$ which is invariant under a global symmetry transformation[4]. This symmetry is broken spontaneously if the ground state of the given theory obeys a "lower" symmetry than the corresponding Lagrangian itself. In this subsection, we shall focus on the spontaneous breakdown of the global $SU(2)_L \times SU(2)_R \times U(1)_V \times U(1)_A$ symmetry of QCD with two massless quark flavors. Note, however, the axial $U(1)_A$ is, actually, not a real symmetry of QCD on the quantum level. As we shall discuss below, it is anomalously broken due to instanton effects [192–194].

In the introduction of this section, we discussed that the *Nambu-Goldstone* theorem predicts the emergence of massless *Nambu-Goldstone* modes in case of the breakdown of a continuous symmetry. Instead of a spontaneous breaking of a global symmetry, there also exists the possibility of a "spontaneous breakdown" of a continuous local gauge symmetry by virtue of a *Anderson-Higgs*-type mechanism, see Refs. [36–39]. Briefly speaking, a gauge field A_μ can acquire a dynamically generated *Meissner* mass [41] rendering the gauge interaction short-ranged. For this, one usually considers order parameters which are not gauge invariant, possibly indicating the spontaneous breakdown of the local gauge symmetry. Here, it is essential to emphasize that a local symmetry cannot break in nature [212]. In fact, the choice of a specific gauge-fixing condition already yields an explicit and not spontaneous breaking of the theory's gauge symmetry. In such a gauge-fixed theory, a spontaneous breakdown then occurs for the corresponding global and not for the local symmetry. Nevertheless, we emphasize that the choice of an order parameter which is gauge dependent can be a useful trick to find, e.g., new quantum phases, and to deduce gauge invariant observables as a consequence. One example for an Abelian *Anderson-Higgs*-type mechanism can be found in condensed-matter physics. In superconductors, one can observe that the magnetic field is expelled from the interior of the latter in the superconducting phase. This is known as the *Meissner-Ochsenfeld* effect [41] which is a direct consequence of the *Anderson-Higgs* mechanism in the following sense: the effective *Meissner* mass appearing in the photon propagator of QED yields a screening of the electromagnetic force within the superconductor.

Let us now discuss the chiral two-flavor symmetry of QCD in more detail. The QCD Lagrangian for two flavors in the chiral limit can be written as

$$\mathcal{L}_{\text{QCD}}^{(N_f=2)} = \frac{1}{4}\, F_{\mu\nu}^a F_{\mu\nu}^a + \bar{u}^L \mathrm{i}\slashed{D} u^L + \bar{u}^R \mathrm{i}\slashed{D} u^R + \bar{d}^L \mathrm{i}\slashed{D} d^L + \bar{d}^R \mathrm{i}\slashed{D} d^R \,, \qquad (2.57)$$

with the *covariant* derivative $\slashed{D} = \gamma_\mu D_\mu$ which we have introduced in Eq. (2.42). Above, we used the transformation $\psi^L = \frac{1}{2}(1 - \gamma_5)\psi$, and $\psi^R = \frac{1}{2}(1 + \gamma_5)\psi$, to decompose the fermionic spinor fields u and d appearing in the usual kinetic term $T \sim (\bar{u}\mathrm{i}\slashed{D}u + \bar{d}\mathrm{i}\slashed{D}d)$, into their left- and right-handed components, see also Ref. [125]. Then, the different chirality doublets can be rotated separately, leaving the Lagrangian $\mathcal{L}_{\chi\text{QCD}}^{(N_f=2)}$ invariant under chiral two-flavor transformations:

$$\begin{pmatrix} u^L \\ d^L \end{pmatrix} \to g_L \begin{pmatrix} u^L \\ d^L \end{pmatrix} \,, \qquad\qquad \begin{pmatrix} u^R \\ d^R \end{pmatrix} \to g_R \begin{pmatrix} u^R \\ d^R \end{pmatrix} \,, \qquad (2.58)$$

where the rotations g_L and g_R are associated with the *Lie* groups $SU(2)_L$ and $SU(2)_R$, respectively, see, e.g., Ref. [186]. Note that this is impossible if a finite current quark mass $\sim (m_u\, \bar{u}u + m_d\, \bar{d}d)$ is present, mixing left- and right-handed fields in our QCD Lagrangian. For actual studies, it appears to be most convenient to rewrite the

---

[4]In fact, for having a real global symmetry present in a quantum theory under consideration, it is not sufficient that only the classical Lagrangian $\mathcal{L}$ is invariant under the specific symmetry operation. It also requires the invariance of the path integral measure. Otherwise, *Adler-Bell-Jackiw*-type anomalies [210, 211] can potentially break symmetries on the quantum level which would be present on the classical one.

transformation Eq. (2.58) in the following form:

$$SU(2)_L \times SU(2)_R : \quad \psi \to e^{(i\alpha^a T^a + i\gamma_5 \beta^b T^b)} \psi, \qquad \text{where} \quad \psi = \begin{pmatrix} u \\ d \end{pmatrix}. \tag{2.59}$$

Here, the generators T^a (see App. B) belong to the fundamental representation of the $SU(2)$ *Lie* algebra. Moreover, α^a and β^b are real-valued (global) rotation angles associated with the different group generators. Driven by strong gauge dynamics, the chiral $SU(2)_L \times SU(2)_R$ symmetry[5] can dynamically break, see our discussion at the end of this section.

The complete symmetry group of the Lagrangian (2.57) is an $U(2)_L \times U(2)_R$ which is usually decomposed into $SU(2)_L \times SU(2)_R \times U(1)_V \times U(1)_A$. The rotation of the spinors under $U(1)_V$ and $U(1)_A$ transformations can be written as

$$U(1)_V : \quad \psi \mapsto e^{i\alpha} \psi, \qquad\qquad U(1)_A : \quad \psi \mapsto e^{i\gamma_5 \alpha} \psi. \tag{2.60}$$

From *Noether*'s theorem, we know that there exists a conserved charge as well as a conserved current for each continuous symmetry. For our chiral symmetry group, we then have the following conserved covariant currents:

$$j_\mu^a = \bar{\psi} T^a \gamma_\mu \psi, \qquad j_\mu^{5a} = \bar{\psi} T^a \gamma_\mu \gamma_5 \psi, \qquad j_\mu = \bar{\psi} \gamma_\mu \psi, \qquad j_\mu^5 = \bar{\psi} \gamma_\mu \gamma_5 \psi. \tag{2.61}$$

The charge operator $\int d^3x\, \psi^\dagger \psi = N_R + N_L$, where N_R and N_L denote the number operators of the right- and left-handed fermion fields, corresponds to the vector current j_μ and is associated with the baryon number. Since the $U(1)_V$ symmetry is exactly realized in QCD, the baryon number is conserved. Note that this remains true, even at the level of the corresponding quantum theory. However, it is expected that baryon conservation is violated in QCD as a part of the Standard Model, i.e. when electroweak interactions are also considered. Here, the baryon number is not conserved since the vector $U(1)_V$ symmetry is broken through *Adler-Bell-Jackiw* anomalies [193, 194]. Therefore, it might be possible in nature that processes like the annihilation of protons and neutrons occur. In reality, however, baryon number violating processes play a negligible role and are extremely unlikely, i.e., it may not happened once within the entire life span of the universe, see Ref. [213].

Let us now discuss anomalies in more detail. In QCD, the axial $U(1)_A$ symmetry is anomalously broken at the level of the quantum theory because of instanton-mediated vacuum transitions. Experimentally, this can be seen, e.g., from the absence of parity partners in the meson spectrum [214] and the absence of a ninth light *Nambu-Goldstone* boson [215]. In Sec. 2.3.1, we have already indicated that gauge-invariant terms such as Eq. (2.49) are, in principle, allowed to exist in *Yang-Mills* theory. In fact, in 1975 *Belavin* et al. [192] showed the existence of quasi-particle solutions of *Yang-Mills* theory. These so-called instanton solutions [193, 194] describe topologically non-trivial vacuum configurations stemming from non-vanishing surface terms such as

$$\Delta N = \int d^4x\, \partial_\mu j_\mu^A = \frac{\bar{g}^2}{32\pi^2} \epsilon_{\mu\nu\alpha\beta} \int d^4x\, F_{\mu\nu}^a F_{\alpha\beta}^a, \tag{2.62}$$

where we introduced the so-called (gauge-dependent) *Chern-Simons* current

$$j_\mu^A = \frac{\bar{g}^2}{16\pi^2} \epsilon_{\mu\nu\alpha\beta} \, \mathrm{Tr} \left(A_\nu F_{\alpha\beta} + \frac{2i\bar{g}}{3} A_\nu A_\alpha A_\beta \right), \tag{2.63}$$

with the topological winding number $\Delta N \in \mathbb{Z}$ in Eq. (2.62). Further, we used the abbreviation $F_{\mu\nu} \equiv F_{\mu\nu}^a T^a$ and $A_\mu \equiv A_\mu^a T^a$. In this case, the winding number ΔN can be related to topologically distinct vacuum states, see

---

[5]This is sometimes also referred as the $SU(2)_V \times SU(2)_A$ symmetry group which is, technically speaking, not completely correct. The $SU(2)_A$ is not an actual group as it is not closed. Since $\gamma_5 \gamma_5 = \mathbb{1}$, a multiple application of an $SU(2)_A$ transformation may generate an element which is part of $SU(2)_V$.

Refs. [213, 215] for details. The anomalous breaking of the axial $U(1)_A$ comes into play from the observation that the divergence of the current j_μ^5 in Eq. (2.61) is, up to a multiplicative constant, equivalent to the aforementioned non-vanishing surface term of $\partial_\mu j_\mu^A$:

$$\partial_\mu j_\mu^5 = \frac{N_f \bar{g}^2}{16\pi^2} \, \epsilon_{\mu\nu\alpha\beta} F_{\mu\nu}^a F_{\alpha\beta}^a \, , \tag{2.64}$$

where the so-called *Adler-Bell-Jackiw* term can be computed, for example, from a triangle diagram at one-loop order including vector- as well as axial-vector currents, see also Refs. [211, 213, 215]. Originally, this particular triangle diagram appeared conspicuous as it seemed to be impossible to find a suitable regularization scheme so that chiral symmetry and gauge symmetry were conserved simultaneously. From a functional field integral point of view, the *Adler-Bell-Jackiw* contribution Eq. (2.64) can also be computed from the path integral measure which appears to be not invariant under $U(1)_A$ transformations, see Ref. [216]. Using (2.62) and (2.64), we can construct a divergenceless current from j_μ^A and j_μ^5:

$$J_\mu^A = j_\mu^5 - 2N_f j_\mu^A \, . \tag{2.65}$$

Since the divergence of this current has to vanish by construction, the corresponding charge has to be conserved:

$$0 \stackrel{!}{=} \int \mathrm{d}^3 x \, J_0^A = (N_R - N_L) - 2N_f N \, , \tag{2.66}$$

where we used that $\int \mathrm{d}^3 x \, j_0^5 = (N_R - N_L)$. This identity can be associated with the difference between the number of right- and left-handed particles. Again, N denotes the winding number of the gauge field. From Eq. (2.66), one can see why the $U(1)_A$ symmetry is anomalously broken: By considering transitions between two topologically distinct vacuum states by changing the winding number N, it is necessary to simultaneously adjust the fermion chirality $(N_R - N_L)$ so that the charge associated with J_μ^A remains conserved. For instance, consider that there is a vacuum transition from $N \to (N+1)$. Then, one can show that there exists a net movement, e.g., from right-handed energy states moving an energy level upwards and from left-handed energy states moving an energy level downwards, respectively. Since this is done for all flavor types, the net change of the chirality is $2N_f \Delta N$.

Note that this example was presented for the gauge condition $A_0 = 0$, see Ref. [213]. In this case, the instantons are associated with tunneling paths between distinct vacuum configurations which are identified with different topological winding numbers. One can also find gauges where a unique vacuum state exists. Here, the tunneling path starts and ends at the same point. Nevertheless, the main statement that the instanton-mediated vacuum transition alters the chirality remains intact. In our studies, we shall mostly consider an explicit breaking of the anomalous $U(1)_A$ symmetry as it is the case in QCD. For this, we implement this breaking on the level of the four-quark correlation functions as we shall discuss in Sec. 3.2.

Let us now discuss the spontaneous breakdown of the $SU(2)_L \times SU(2)_R$ symmetry. For this, let us consider an effective model of four-quark interactions which can be motivated from the *Wilsonian* RG in the following sense: at one-loop order in QCD, four-quark vertices are dynamically generated as a consequence of strong gauge dynamics, see the box diagram $\sim g^4$ in Fig. 2.3. Due to the so-induced effective four-fermion interactions, new types of diagrams become possible which then also contribute to the RG running of the effective four-quark vertex, e.g., triangle-type diagrams $\sim g^2 \lambda$ are generated which are built from quark-gluon as well as from four-quark vertices. In our present work, we shall focus on the four-quark sector generated in QCD. The latter is of great importance since it already provides us with essential information on the mechanism of spontaneous chiral symmetry breaking. From a *Wilsonian* perspective, we can then think of the QCD high-momentum modes to be already integrated out.

To better understand the relation between four-quark theories and the mechanism of spontaneous chiral symmetry breaking, we consider a purely fermionic model. In this case, we only consider the four-quark diagram $\propto \lambda^2$ in Fig. 2.3. Note that we shall also study these so-called *Nambu-Jona-Lasinio*-type (NJL) models [25, 26] at finite
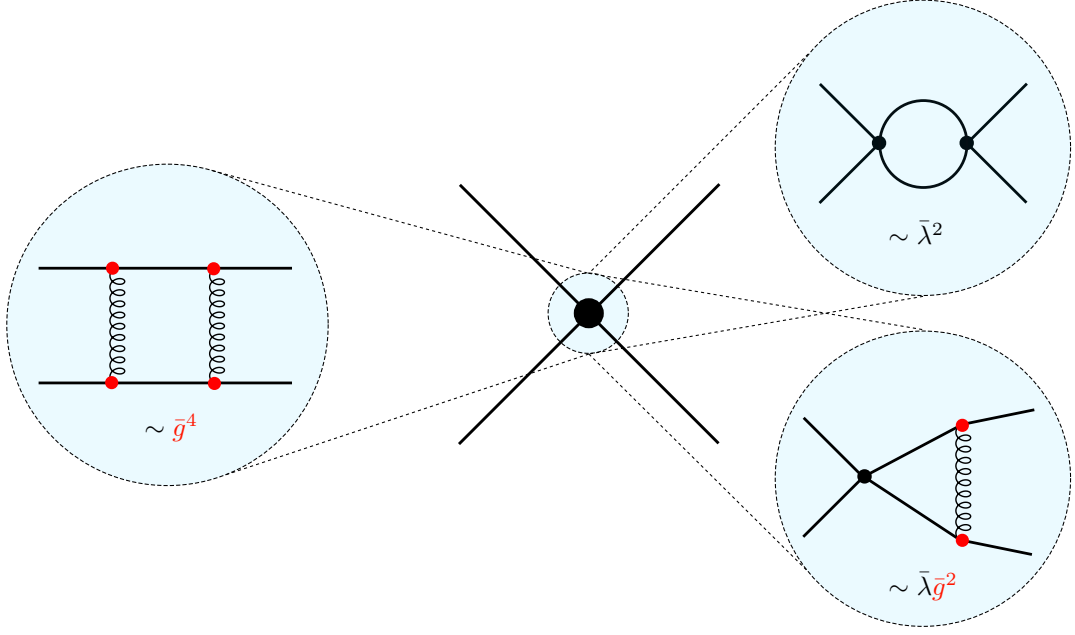
Figure 2.3: The figure schematically illustrates the four-fermion diagrams which contribute to the RG running of the four-fermion vertex (black dots) by considering four-quark and quark-gluon interactions in an ansatz for the effective action. At large momentum scales, so-called box diagrams on the left-hand side are generated from quark-gluon interactions (red dots) at one-loop order from first principles. Once the four-quark vertex is generated, two additional types of diagrams also contribute to the running of the four-quark vertex, see the diagrams on the right-hand side.

temperature and quark chemical potential in Secs. 3.1 and 3.2. In the pre-QCD era, NJL models were invented to study chiral symmetry breaking in particle physics based on an analogy to superconductivity from condensed-matter physics. When QCD was developed, and one recognized that the fundamental constituents of baryonic matter are quarks, NJL models were successfully reemployed to analyze the low-energy dynamics of QCD. As the gauge coupling increases for low-momentum scales rendering QCD non-perturbative, model studies have become an essential tool to explore key features of the strong interaction within mathematically feasible theories, e.g., to study spontaneous chiral symmetry breaking or the confinement/deconfinement phase transition in *Polyakov*-loop extended low-energy models, see, e.g., Refs. [217–227]. However, we also note that NJL models in four spacetime dimensions are defined with an explicit UV cutoff Λ as an additional parameter as they are perturbatively nonrenormalizable. Note that nonperturbative studies further indicate that they are also not nonperturbatively renormalizable (see, e.g., Refs. [228, 229]). In case of four spacetime dimensions, we shall therefore always consider the UV cutoff Λ as well as the regularization scheme as a part of the NJL model itself.

To see why NJL models can help to guide our understanding of the mechanism of spontaneous chiral symmetry breaking, let us consider the following classical action S_{NJL} associated with a one-channel NJL-type model in four spacetime dimensions:

$$S_{\mathrm{NJL}}[\bar{\psi}, \psi] = \int \mathrm{d}^4 x \left\{ (\bar{\psi} \mathrm{i} \partial\!\!\!/ \psi) + \frac{1}{2} \bar{\lambda}_{(\sigma\text{-}\pi)} \left[(\bar{\psi}\psi)^2 - (\bar{\psi}\gamma_5 \tau_i \psi)^2 \right] \right\}, \tag{2.67}$$

with the *Pauli* matrices τ_i and the dimensionful scalar-pseudoscalar coupling $\bar{\lambda}_{(\sigma\text{-}\pi)}$. Note that the corresponding dimensionless scalar-pseudoscalar coupling is defined as $\lambda_{(\sigma\text{-}\pi)} \sim \bar{\lambda}_{(\sigma\text{-}\pi)}/\Lambda^{D-2}$ where D denotes the number of spacetime dimensions. This action is invariant under global $SU(3)$ gauge transformations and under chiral $SU(2)_L \times SU(2)_R \times U(1)_V$ transformations which we have defined in Eqs. (2.59)-(2.60). The partition function

associated with this NJL model reads:

$$\mathcal{Z}[0] \sim \int \mathcal{D}\psi \, \mathcal{D}\bar{\psi} \, \mathrm{e}^{-S_{\mathrm{NJL}}[\bar{\psi},\psi]} \, . \tag{2.68}$$

The purely fermionic path integral above can be rewritten in terms of auxiliary bosonic fields. For this, we insert the following identity in the partition function Eq. (2.68),

$$1 = \mathcal{N} \int \mathcal{D}\sigma \, \mathcal{D}\pi_i \, \mathrm{e}^{-\int \mathrm{d}^4 x \, \frac{1}{2} \, \bar{m}^2_{(\sigma\text{-}\pi)}(\pi_i^2 + \sigma^2)} \, , \tag{2.69}$$

with the auxiliary fields σ and π_i, a normalization constant $\mathcal{N}$, and a parameter $\bar{m}^2_{(\sigma\text{-}\pi)}$ which remains arbitrary for the moment.[6] In the next step, we perform the linear field shift

$$\sigma \to \sigma + \frac{\mathrm{i}\bar{h}_{(\sigma\text{-}\pi)}}{\bar{m}^2_{(\sigma\text{-}\pi)}} \, (\bar{\psi}\psi) \, , \qquad\qquad \pi_i \to \pi_i + \frac{\mathrm{i}\bar{h}_{(\sigma\text{-}\pi)}}{\bar{m}^2_{(\sigma\text{-}\pi)}} \, (\bar{\psi}\gamma_5\tau_i\psi) \, , \tag{2.70}$$

which leaves the value of the path integral unchanged. Above, we have introduced a new *Yukawa*-type coupling denoted by $\bar{h}_{(\sigma\text{-}\pi)}$. Our partition function then reads

$$\mathcal{Z}[0] \sim \int \mathcal{D}\sigma \, \mathcal{D}\pi_i \, \mathcal{D}\psi \, \mathcal{D}\bar{\psi} \, \mathrm{e}^{-S[\bar{\psi},\psi,\sigma,\pi_i]} \, , \tag{2.71}$$

with the partially bosonized classical action

$$S[\bar{\psi},\psi,\sigma,\pi_i] = \int \mathrm{d}^4 x \, \left\{ \bar{\psi}\mathrm{i}\slashed{\partial}\psi + \mathrm{i}\bar{h}_{(\sigma\text{-}\pi)}\,\bar{\psi}(\sigma + \gamma_5\tau_i\pi_i)\psi + \frac{1}{2}\,\bar{m}^2_{(\sigma\text{-}\pi)}(\sigma^2 + \pi_i^2) \right\} \, . \tag{2.72}$$

Here, we made the choice:

$$\bar{\lambda}_{(\sigma\text{-}\pi)} \overset{!}{=} \frac{\bar{h}^2_{(\sigma\text{-}\pi)}}{\bar{m}^2_{(\sigma\text{-}\pi)}} \, , \tag{2.73}$$

so that the four-quark vertex is "removed" by construction: we substitute the scalar-pseudoscalar coupling $\bar{\lambda}_{(\sigma\text{-}\pi)}$ with the mass-like parameter $\bar{m}^2_{(\sigma\text{-}\pi)}$ and the new *Yukawa*-type coupling $\bar{h}^2_{(\sigma\text{-}\pi)}$.

The partial bosonization we have performed above is known as a *Hubbard-Stratonovich* (HS) transformation [230, 231] where we exchange our fermionic four-quark vertex for a *Yukawa*-type interaction with the associated *Yukawa* coupling $\bar{h}_{(\sigma\text{-}\pi)}$. The bosonic auxiliary fields σ and π_i now mediate the interaction between the quarks within this new type of effective field theory. We further point to $\bar{m}^2_{(\sigma\text{-}\pi)}$ which can now be interpreted as an explicit "screening" mass term of the bosonic fields σ and π_i. Note also that chiral symmetry is still present in our transformed action (2.72). For the boson fields it is now manifested in terms of an $O(N_f^2)$ rotational symmetry, e.g., see Refs. [232, 233].

It is now straightforward to show that once the field σ has a non-vanishing field expectation value, the quark fields acquire an effective fermion mass. For this, we compute the classical equations of motion from the partially bosonized classical action (2.72):

$$\frac{\delta S}{\delta\bar{\psi}}\bigg|_{\sigma=\langle\sigma\rangle,\pi_i=0} = (\mathrm{i}\slashed{\partial} + \mathrm{i}m_\psi)\psi(x) \, , \tag{2.74}$$

with $m_\psi = \bar{h}_{(\sigma\text{-}\pi)}\langle\sigma\rangle$, see also Ref. [228] for details. Here, we assumed that the field σ acquires a finite field expectation value $\langle\sigma\rangle \sim \langle\bar{\psi}\psi\rangle \neq 0$. Because of the non-vanishing fermion mass, it is clear that chiral symmetry

---

[6]In principle, the choice of the auxiliary fields is at our disposal. The important point is that the four-quark vertex is "removed" in the following and we ensure that the integral measure is positive semidefinite.

can be broken spontaneously if such a non-trivial ground state exists, i.e., if $\langle\sigma\rangle \neq 0$. The important message here is that the expectation value $\langle\bar{\psi}\psi\rangle$ can be used as an order parameter for spontaneous chiral symmetry breaking as it indicates the emergence of a finite fermion mass. The remaining question is, under which circumstances such a non-trivial ground state may exist. We shall answer this question below.

The functional integral (2.71) can further be computed by splitting the boson fields into a background and a fluctuation part $\phi = \bar{\phi} + \delta\phi$. We now perform a so-called *mean-field* approximation, i.e., we neglect all bosonic fluctuations of the type $\delta\phi$. Since the fermion fields $\bar{\psi}$ and ψ only appear as bilinears, we can compute the functional field integral for the fermion fields straightforwardly. As a consequence of the *mean-field* approximation, the bosonic field integral becomes also trivial. The effective action computed in a *mean-field* approximation then reads

$$\Gamma_{\mathrm{MF}}[\bar{\sigma}, \bar{\pi}_i] = \int \mathrm{d}^4x \left\{ \frac{1}{2}\, \bar{m}_{(\sigma\text{-}\pi)}^2 \left(\bar{\sigma}^2 + \bar{\pi}_i^2\right) \right\} - \mathrm{Tr} \ln \left\{ \mathrm{i}\slashed{\partial} + \mathrm{i}\bar{h}_{(\sigma\text{-}\pi)} \left(\bar{\sigma} + \gamma_5\tau_i\bar{\pi}_i\right) \right\} , \tag{2.75}$$

where we use

$$\mathrm{Tr}\, \mathcal{O} = \mathrm{tr}_{\mathrm{D,F,C}} \int \mathrm{d}^4x \, \langle x| \, \mathcal{O} \, |x\rangle , \tag{2.76}$$

with the trace $\mathrm{tr}_{\mathrm{D,F,C}}$ running over *Dirac*, flavor, and color space.

We now assume that the bosonic background fields are constant.[7] We minimize Eq. (2.75) with respect to $\bar{\sigma}$ and evaluate that expression at the physical ground state $\langle\sigma\rangle$. We emphasize that we could also minimize Γ_{MF} with respect to any other field direction as they are all equivalent as a reason of chiral symmetry. The minimization of the *mean-field* effective action yields

$$\langle\sigma\rangle = 8N_c \frac{\bar{h}_{(\sigma\text{-}\pi)}^2}{\bar{m}_{(\sigma\text{-}\pi)}^2} \int \frac{\mathrm{d}^4p}{(2\pi)^4} \frac{\langle\sigma\rangle}{p^2 + \bar{h}_{(\sigma\text{-}\pi)}^2\langle\sigma\rangle^2} , \tag{2.77}$$

where we find a so-called gap equation[8] for the homogeneous ground state $\langle\sigma\rangle$. Here, we point to the fermion mass $m_\psi^2 = \bar{h}_{(\sigma\text{-}\pi)}^2 \langle\sigma\rangle^2$ appearing in the denominator of the gap equation (2.77) above. We further see that the fermionic four-quark coupling $\bar{\lambda}_{(\sigma\text{-}\pi)} = \bar{h}_{(\sigma\text{-}\pi)}^2/\bar{m}_{(\sigma\text{-}\pi)}^2$ appears on the right-hand side of the gap equation (2.77). Depending on the value of the four-quark coupling $\bar{\lambda}_{(\sigma\text{-}\pi)}$, one can prove that Eq. (2.77) has, besides the trivial solution $\langle\sigma\rangle = 0$, a non-trivial solution $\langle\sigma\rangle \neq 0$ signaling the spontaneous breakdown of chiral symmetry, see, e.g., Ref. [27, 228] for details. As one can show, for $\lambda_{(\sigma\text{-}\pi)} < \lambda_{(\sigma\text{-}\pi)}^{\mathrm{crit.}}$, the theory remains in the chirally symmetric phase, where for $\lambda_{(\sigma\text{-}\pi)} > \lambda_{(\sigma\text{-}\pi)}^{\mathrm{crit.}}$ chiral symmetry is broken spontaneously. Note that the value of the critical four-quark coupling $\lambda_{(\sigma\text{-}\pi)}^{\mathrm{crit.}} = \bar{\lambda}_{(\sigma\text{-}\pi)}^{\mathrm{crit.}}\Lambda^2$ depends on the employed regularization scheme, see also our discussion in Chap. 3. In Fig. 2.4, we show the corresponding *Ginzburg-Landau*-type potential $U(\bar{\sigma}, \bar{\pi}_i)$ [234], where $\Gamma_{\mathrm{MF}} = \int \mathrm{d}^4x\, U(\bar{\sigma}, \bar{\pi}_i)$. On the left-hand side of Fig. 2.4, we show the order-parameter potential in case of a vanishing expectation value $\langle\sigma\rangle = 0$ where the illustration of the order-parameter potential on the right-hand of the figure corresponds to a non-trivial ground state associated with $\langle\sigma\rangle \neq 0$. In case of a scenario where the symmetry is spontaneously broken, we observe by studying the potential $U(\bar{\sigma}, \bar{\pi}_i)$ that there is an infinite number of energetically equivalent minima along the valley of the order-parameter potential which are all connected by means of chiral rotations. Since there is no preference in our chiral model, one minimum is randomly assumed. The situation would be different, if chiral symmetry was broken by, e.g., a term linear in $\sim \bar{\sigma}$. The order-parameter potential would be then deformed in a way such that a unique ground state could possibly exist.

If we expanded the order potential about the non-trivial ground state in case of broken chiral symmetry, we would find one massive and three massless bosons. According to the *Nambu-Goldstone* theorem, we can identify these massless modes with the three *Nambu-Goldstone* modes associated with the three broken generators of the axial part of the $SU(2)_L \times SU(2)_R$ group. The massless pion modes can moreover be interpreted as a motion along

---

[7]In general, the bosonic fields are highly nonlocal. For our present discussion, however, it suffices to neglect the spacetime dependencies.

[8]Note that we have not regularized this expression so far. In any quantitative computation, a proper regulator has to be considered.
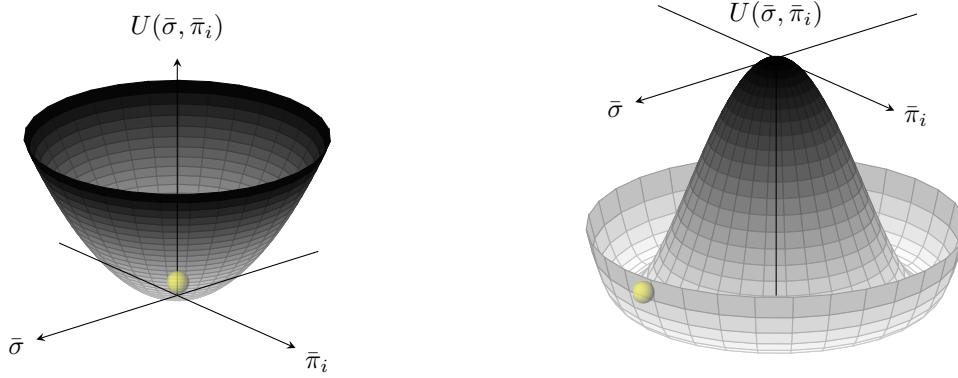
Figure 2.4: *Ginzburg-Landau*-type order-parameter potential for a vanishing order parameter $\langle\bar{\psi}\psi\rangle = 0$ (left) and for a finite order parameter value $\langle\bar{\psi}\psi\rangle \neq 0$ associated with a non-trivial ground state (right) indicating a spontaneous breakdown of chiral symmetry. We can also see that the curvature of the potential at its origin is positive $\bar{m}^2_{(\sigma\text{-}\pi)} > 0$ in case of $\langle\bar{\psi}\psi\rangle = 0$. For $\langle\bar{\psi}\psi\rangle \neq 0$, the curvature at the origin switches its sign $\bar{m}^2_{(\sigma\text{-}\pi)} < 0$ in case of a second-order phase transition. For a first-order phase transition it tends to zero but remains positive.

the valley of the "*Mexican hat*" on the right-hand side of Fig. 2.4. Within this picture, the massive sigma mode can then be understood as a motion perpendicular to the valley. Eventually, we emphasize that chiral symmetry is only broken for the interacting ground state $\langle\sigma\rangle \neq 0$. On the level of the original action, it is preserved in any case which leaves its imprint from the possibility to rotate one ground state into another one.

From the partially bosonized theory, we have seen that a non-trivial ground state can exist. Further, given that a finite expectation value for the condensate $\langle\bar{\psi}\psi\rangle$ exists, the quark fields acquire a finite constituent mass and chiral symmetry breaks spontaneously. Using the identity given in Eq. (2.73), we can relate the curvature $\bar{m}^2_{(\sigma\text{-}\pi)}$ of the order potential in the bosonized picture to the four-fermion coupling $\bar{\lambda}_{(\sigma\text{-}\pi)}$. As a consequence, we can formulate a criterion for spontaneous chiral symmetry breaking already on the level of the four-fermion theory, see Ref.[228]:

> A rapidly increasing or diverging four-fermion coupling $\lambda_{(\sigma\text{-}\pi)}$ indicates the onset of spontaneous chiral symmetry breaking,

$$m^2_{(\sigma\text{-}\pi)} \sim \frac{1}{\lambda_{(\sigma\text{-}\pi)}} \to 0\,, \tag{2.78}$$

> where $m^2_{(\sigma\text{-}\pi)}$ is the curvature at the origin of the *Ginzburg-Landau* potential and corresponds to the bosonic curvature mass, respectively. In particular, a divergence of the four-fermion coupling then signals a change in the sign of the curvature at the origin of the *Ginzburg-Landau*-type order-parameter potential.

Following the discussion above, we now have a criterion at hand to study spontaneous chiral symmetry breaking in four-fermion theories.

So far, we discussed the mechanism of spontaneous chiral symmetry breaking within a purely fermionic NJL-type model (2.67). In the next step, we discuss how spontaneous chiral symmetry breaking can be triggered by gluon dynamics in QCD, see Refs. [21, 22, 235]. To this end, we also consider gluonic degrees of freedom entering our four-quark theory below. We use the criterion for the onset of spontaneous chiral symmetry breaking defined in Eq. (2.78) and study the RG running of the dimensionless and renormalized four-quark coupling λ when gauge degrees of freedom come into play. For simplicity, we assume that only one four-quark channel is present, e.g, the scalar-pseudoscalar channel in Eq. (2.67). Note that the four-quark coupling does now depend on the RG scale k,
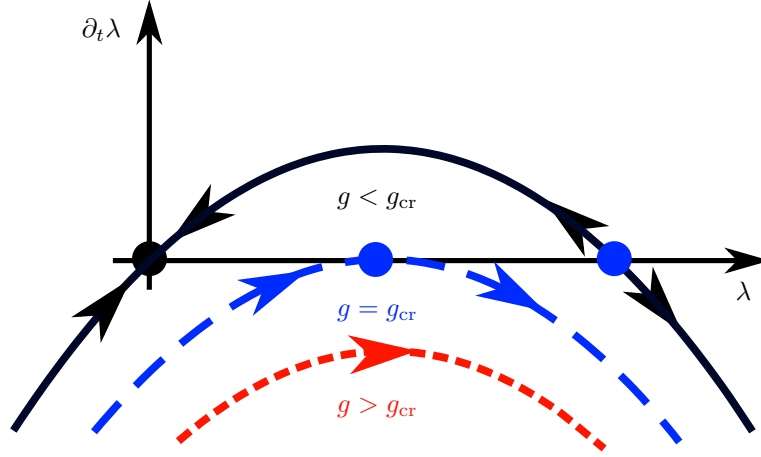
Figure 2.5: Typical four-fermion beta function including gauge degrees of freedom (arrows shall indicate the direction of the RG flow towards the *infrared*). For an increasing gauge coupling g, the parabola is shifted downwards so that the *Gaussian* (black dot) and non-*Gaussian* (blue dot) fixed point merge for a critical value of the gauge coupling $g = g_{\rm cr}$, see the blue curve. For $g > g_{\rm cr}$, the parabola is not controlled by fixed points anymore, see the red curve. This graphic has been adapted from Ref. [21].

see also our detailed discussion in Chap. 3. We now consider all four-quark diagrams discussed in Fig. 2.3, i.e., we also include box- and triangle-type 1PI diagrams. A typical beta function associated with the four-quark vertex then reads

$$\beta_\lambda \equiv \partial_t \lambda = (D-2)\lambda - a_1 \lambda^2 - a_2 \lambda g^2 - a_3 g^4 \,, \tag{2.79}$$

with a dimensionless four-quark coupling $\lambda \sim \bar{\lambda} k^{D-2}$ and a dimensionless gauge coupling $g \sim \bar{g} k^{D/2-2}$ where D defines again the number of spacetime dimensions. The coefficients a_i are independent on the RG scale k but may depend on other external parameters such as temperature or chemical potential, see also Sec. 3.3. For simplicity, let us now assume that $a_i > 0$. The beta function for this one-channel approximation is sketched in Fig. 2.5. For this, let us briefly recall the qualitative scaling behavior of the strong running gauge coupling, see, e.g., Refs. [20, 23, 236, 237] for studies using functional RG methods. At large scales $k \gg 1\,\mathrm{GeV}$, the strong coupling g is found to be rather weak and asymptotically free in the limit $k \to \infty$. By going to lower scales, however, the value of the strong coupling increases so that the *infrared* physics become strongly coupled.

Let us now assume that we start in the perturbative regime of QCD where $g \ll 1$. The solid black curve in Fig. 2.5 then depicts this situation for the four-quark beta function. Here, we find an IR-attractive *Gaussian* fixed point which we display in black and an IR-repulsive non-*Gaussian* fixed point λ^* which we depict in blue. If we started with $\lambda^{\rm (UV)} = 0$ or at least $\lambda^{\rm (UV)} < \lambda^*$, we would never find that the system becomes critical as it would always be governed by the attractive *Gaussian* fixed point. By lowering the scale, the value of the strong coupling increases. The parabola is then shifted downwards, turning the *Gaussian* fixed point into a non-*Gaussian* fixed point. By further increasing the gauge coupling, both non-*Gaussian* fixed points approach each other. Eventually, for a critical value of the strong coupling $g = g_{\rm cr}$, the fixed points merge, see the blue dashed curve. Given that a critical value of the gauge coupling is exceeded $g > g_{\rm cr}$, the parabola is not controlled by any real-valued fixed points anymore. In this setting, any value of λ yields a rapidly increasing four-fermion coupling driving the system towards criticality in any case, see the red dotted curve. From the criterion formulated in Eq. (2.78), we can then relate the rapidly increasing/diverging four-quark coupling λ to the onset of spontaneous (chiral) symmetry breaking as discussed above. Note that the mechanism above takes place at zero temperature and is solely driven by gluonic degrees of freedom. In Sec. 3.3.1, we shall discuss what might change when thermal fluctuations come into play.

So far, we focused on spontaneous chiral symmetry breaking in QCD. However, for QCD at finite temperature and chemical potential, various symmetry breaking patterns are expected to occur. In Sec. 2.3.4, we therefore present a selection of different QCD matter states from model studies, where we concentrate on the two-flavor case. Since the different phases of QCD are again associated with non-trivial ground states, the general arguments above still hold, i.e., the onset of spontaneous global symmetry breaking is again indicated by a rapidly increasing/diverging four-fermion coupling. Note that within the truncations used in the present work, the true nature of the ground state in the broken regime is inaccessible. Nevertheless, the four-fermion flows in the symmetric regime can potentially provide us with additional information about the regime governed by spontaneous symmetry breaking as we shall discuss in Chap. 3.

2.3.3 Mean-Field Ambiguity and Fierz Completeness

In the previous section, we have seen how we can study the phenomenon of spontaneous chiral symmetry breaking by employing NJL-type four-fermion models. We have already indicated that it is usually not sufficient to consider only one four-fermion channel in the effective action for a theory under investigation. In this section, we shall see why this is the case. For this, let us consider an NJL-type model without any color or flavor degrees of freedom. Further, we assume that the effective action is invariant under global $U(1)_V \times U(1)_A$ symmetry transformations. Moreover, we consider only one four-fermion channel of the scalar-pseudoscalar type:

$$\Gamma[\bar{\psi}, \psi] = \int \mathrm{d}^4 x \left\{ Z_\psi (\bar{\psi} \mathrm{i} \partial\!\!\!/ \psi) + \frac{1}{2} Z_\sigma \bar{\lambda}_\sigma \left[(\bar{\psi}\psi)^2 - (\bar{\psi}\gamma_5\psi)^2 \right] \right\} , \tag{2.80}$$

with a vertex renormalization Z_σ and a wave-function renormalization Z_ψ. Note that we work throughout this thesis in the so-called pointlike limit of the four-point correlation functions in the effective action:

$$\bar{\lambda}_j (\bar{\psi}\mathcal{O}_j\psi)^2 = \lim_{\{p_k \to 0\}} \bar{\psi}_a(p_1)\bar{\psi}_b(p_2)\Gamma^{(2,2)}_{j,abcd}(p_1, p_2, p_3, p_4)\psi_c(p_3)\psi_d(p_4) , \tag{2.81}$$

where a, b, c, d shall denote spinor indices. We therefore neglect all non-trivial momentum information which would be encoded in the four-fermion correlation functions. In the discussion below, the pointlike four-fermion interactions shall play an essential role.

We now employ the *Wetterich* equation (2.29) to derive the running of the renormalized scalar-pseudoscalar coupling. From this, we readily find expressions like

$$\mathrm{STr}\left(\mathcal{P}_k^{(-1)} \mathcal{F}_k \mathcal{P}_k^{(-1)} \mathcal{F}_k \right) \sim Z_\sigma \bar{\lambda}_\sigma \, \mathrm{tr_D} \left(\gamma_\mu \psi \bar{\psi} \gamma_\mu \psi \bar{\psi} \right) \times \mathrm{const.} + \ldots . \tag{2.82}$$

where the trace on the right-hand side shall only run over *Dirac* space. The vector-type channel $(\bar{\psi}\gamma_\mu\psi)^2$ appearing in (2.82) is a result of quantum fluctuations stemming from the right-hand side of the *Wetterich* equation (2.23). In fact, our finding would account to the running of a fictitious vector coupling $\bar{\lambda}_V$. This is an example that all channels which are compatible with the underlying symmetries can appear. However, we have no vector-like channel present in the truncation above. To this end, we can try to rewrite the vector-type interaction by means of so-called *Fierz* transformations (see App. B). In general, *Fierz* transformations correspond to a non-trivial rearrangements of indices in the fermionic tensor structures of the four-fermion vertices. Together with the antisymmetry requirement implemented by the *Grassmann*-valued fermion fields, one can find various identities for the different interaction channels, see Ref. [238] for a detailed discussion. Note that the possible reorderings of the fermion fields would be more restricted if we considered momentum dependencies of the four-fermion vertex beyond the pointlike limit. For the vector channel, e.g., one finds the following *Fierz* identity:

$$(\bar{\psi}\gamma_\mu\psi)^2 = (\bar{\psi}\gamma_\mu\gamma_5\psi)^2 - 2\left[(\bar{\psi}\psi)^2 - (\bar{\psi}\gamma_5\psi)^2 \right] . \tag{2.83}$$

We see that we may rewrite the vector channel again into a scalar-pseudoscalar channel which comes at the cost of introducing an additional axial-vector contribution. In particular, we deduce that the model we have defined in Eq. (2.80) is incomplete with respect to *Fierz* transformations, i.e., in the one-channel approximation it is impossible to map all four-fermion channels appearing on the right-hand side of the *Wetterich* equation onto the original ansatz (2.80). This implies that we would have to make further approximations and neglect vector-type or axial-vector-type couplings in a one-channel calculation. Even worse, any approximation would not be unique since *Fierz*-identities could always be used to reshuffle contributions from one channel to another. This issue appears for all types of so-called *Fierz*-incomplete ansätze including at least quartic fermion couplings and is known as the *Fierz* ambiguity.

However, by considering *Fierz*-complete ansätze, this problem can be resolved. Indeed, in case of our simple toy model at vanishing temperature and quark chemical potential defined by Eq. (2.80), it would be sufficient to add a vector-type or axial-vector-type channel to take care of all different four-fermion interactions appearing as a result of fluctuation effects. The overall strategy to avoid *Fierz* ambiguities in four-fermion theories can now be formulated as follows:

(i) Find all possible four-fermion interactions which are compatible with the underlying symmetries of the theory under consideration.

(ii) Derive all *Fierz* identities for the four-fermion channels found above and reduce the number of invariant channels by the number of obtained non-trivial *Fierz* identities.

The second requirement ensures that a *Fierz*-complete ansatz does not contain more channels than necessary to set up the entire underlying theory space. Otherwise, we would get an overcomplete *Fierz* basis so that information would be distributed over multiple channels. The latter is not a real flaw since all crucial information on quantum fluctuations is still encoded in the overcomplete *Fierz* basis. Nevertheless, computations are simplified considerably when the number of channels is reduced.

Fortunately, the reduction of the channels by means of *Fierz* identities can be mapped to a problem in linear algebra. By unfolding the antisymmetrized quartic tensor structures appearing in the four-fermion channels, they can be represented as large column vectors. For this, we can compute numerically the rank of the basis matrix which provides us the "ideal" number of basis elements required for a *Fierz*-complete basis.

Even though we mostly work in the purely fermionic sector where the *Fierz* ambiguity is under control, we wish to add some words of caution in situations where one may be interested in low-energy observables. In the last section, we have used a *Hubbard-Stratonovich* transformation to partially bosonize our one-channel model and made a *mean-field* approximation where we ignored all types of bosonic fluctuations. Unfortunately, the price we need to pay for this is to bring back the *Fierz* ambiguity which is then also known as the so-called *mean-field* ambiguity [162, 239].

The reason why this is the case, can be understood as follows: *Fierz* identities tell us that there are generic redundancies in our quartic couplings. For example, we could add in Eq. (2.80) a vector $(\bar{\psi}\gamma_\mu\psi)^2$ and an axial-vector $(\bar{\psi}\gamma_\mu\gamma_5\psi)^2$ channel with the corresponding couplings $\bar{\lambda}_V$ and $\bar{\lambda}_A$, respectively. This ansatz would then be overcomplete as discussed above. Following Refs. [162, 239], we may introduce an unphysical parameter γ into our ansatz reflecting the free choice of the *Fierz* basis:

$$\bar{\lambda}_\sigma = \bar{\lambda}'_\sigma - 2\gamma\bar{\lambda}'_V\,, \qquad \bar{\lambda}_V = (1-\gamma)\bar{\lambda}'_V\,, \qquad \bar{\lambda}_A = \gamma\bar{\lambda}'_V\,. \tag{2.84}$$

Physical observables of all kinds, however, must not be effected by any value of γ as it just corresponds to an alternative basis choice. Loosely speaking, the parameter γ just adds a complicated zero to our ansatz. If one now performs a *Hubbard-Stratonovich* transformation and computes the functional field integral within a *mean-field* approximation, one may find again a non-trivial vacuum state. For this, we can compute a critical four-fermion coupling[9] $\bar{\lambda}^{\mathrm{crit}}_{\sigma,\Lambda}$, for which the curvature $\bar{m}^2_\sigma$ switches its sign signaling the onset of spontaneous chiral symmetry

---

[9]Note that the value of the critical four-fermion coupling also depends on the particular cutoff scheme.

breaking. Let us further assume that we are only interested in the curvature associated with the mass of the scalar $\bar{\sigma}$ and pseudoscalar $\bar{\pi}_i$ background fields. Therefore, we set the other composite fields, which are associated with the vector and axial-vector couplings, to zero $V_\mu = A_\mu = 0$. Using the analogue of Eq. (2.73), one finds for the value of the critical four-fermion coupling

$$\bar{\lambda}_{\sigma,\Lambda}^{\text{crit}} = \frac{\bar{h}_{\sigma,\Lambda}^2}{\bar{m}_{\sigma,\Lambda}^2} = C_\Lambda \,. \tag{2.85}$$

However, using Eq. (2.84), we find

$$\bar{\lambda}_{\sigma,\Lambda}^{\prime\,\text{crit}} = C_\Lambda + 2\gamma\bar{\lambda}_{V,\Lambda}' \,, \tag{2.86}$$

which depends on the unphysical parameter γ, see Ref. [239] for a detailed discussion. This underscores that there is again the *Fierz* ambiguity present at the level of the *mean-field* approach. By making any choice for γ we could, in principle, obtain arbitrary values for $\bar{\lambda}_{\sigma,\Lambda}^{\prime\,\text{crit}}$ and $\bar{m}_{\sigma,\Lambda}^2$, respectively. The reason why a *mean-field* study still may work is the following: for sufficiently small values of the vector coupling $\bar{\lambda}_{V,\Lambda}'$, the influence on $\bar{\lambda}_{\sigma,\Lambda}^{\prime\,\text{crit}}$ may be not too strong, see Ref. [162].

One may wonder why this ambiguity is present in the partially bosonized study at all. The problem can be traced back to the *mean-field* choice we made at the bosonization scale Λ. In *mean-field* theory, we ignore all bosonic fluctuations $\sim \delta\phi$. In particular, we neglect contributions such as

$$\partial_t\bar{\lambda}_i \sim \sum_{nm} a_{nm}\,\bar{h}_n^2\bar{h}_m^2 \sim \quad\vdots\quad\vdots\quad , \tag{2.87}$$

where $\bar{h}_m$ denote different *Yukawa*-type couplings associated with quark-meson interaction channels and a_{nm} are coefficients which correspond to the one-loop diagrams above, see also Refs. [22, 228, 239]. It is obvious that there is a back-coupling from the mesonic to the fermionic sector. This observation can be linked to *mean-field* studies in the following way: Even though we tried to get rid of the fermionic degrees of freedom by performing a *Hubbard-Stratonovich* transformation, for any infinitesimal RG step $\Lambda \to \Lambda - \delta k$ they are generated again by virtue of bosonic box diagrams as shown in Eq. (2.87). As a consequence, they contribute to the running of the four-fermion beta function.

The good news is that this problem can be resolved by employing dynamical bosonization techniques which has been put forward in Refs. [22, 159, 161–164] and successfully applied in various QCD-type studies, see, e.g., Refs. [23, 235, 240–242]. The basic idea of this method relies on a continuous transition from fermionic to composite bosonic operators by also considering bosonic fluctuations as shown above. For such a powerful extension, the classical fields of the bosonic operators in the *Wetterich* equation (2.23) has then to become scale-dependent as well $\Phi \to \Phi_k$.

As indicated above, in our present study, we investigate the mechanism of spontaneous symmetry breaking by starting the RG flow in the (chirally) symmetric regime. To describe the dynamics close to the phase transition line, we employ four-fermion theories as discussed above. Since we consider *Fierz*-complete ansätze, there is no kind of *Fierz* ambiguity present in our truncations. Nevertheless, we shall also discuss the consequences of *Fierz*-incomplete ansätze for NJL-type models and their impact on physical observables like the chiral phase boundary. As we do not include mesonic degrees of freedom in our studies in Chap. 3, we neglect any scale dependence of the classical field. In future works, however, it is inevitable to use dynamical hadronization techniques, at least if one is interested in computing low-energy observables such as quark and meson masses in the (chirally) broken regime.
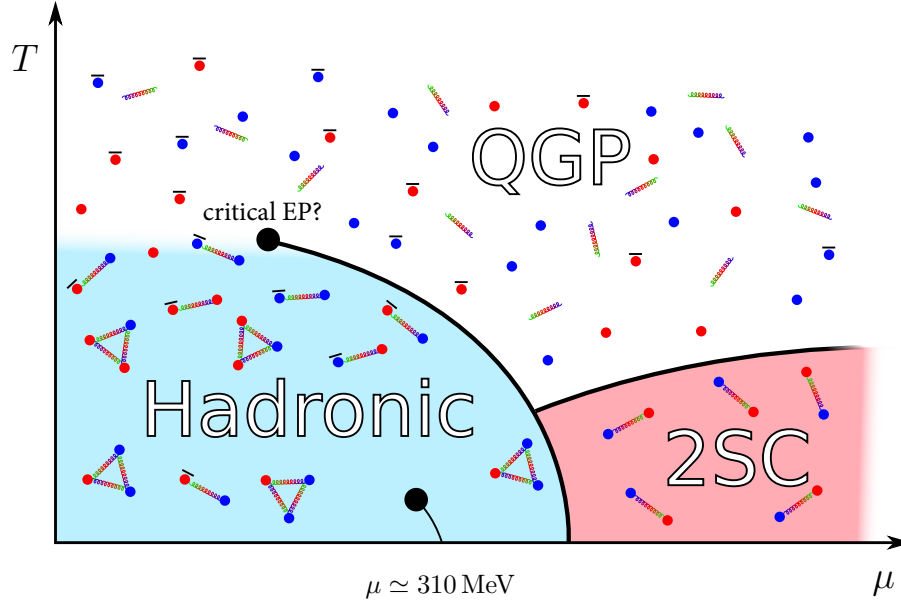
Figure 2.6: Sketch of the conjectured two-flavor QCD phase diagram at finite temperature T and quark chemical potential μ from model considerations, see Ref. [254] for a review. At vanishing current quark mass and quark chemical potential, the *crossover* at finite temperature might become a second-order phase transition, see, e.g., Ref. [232]. If this is the case, the critical endpoint (EP) would then turn into a so-called tricritical point, separating the second- from the first-order phase transition line, see main text for details.

2.3.4 Conjectured Phases of Two-Flavor QCD

In this subsection, we discuss the conjectured QCD phase diagram at finite temperature T and quark chemical potential μ. First, we begin with the remark that our current knowledge of the QCD phase diagram at finite chemical potential is mostly based on model studies since lattice QCD methods are plagued by the infamous sign problem, see, e.g., Ref. [24]. Briefly speaking, due to the inclusion of a finite chemical potential, the measure of the corresponding *Euclidean* path integral is no longer positive semidefinite. To surmount the sign problem, there are several attempts presently ongoing. For example, one may employ an imaginary chemical potential and perform an analytic continuation towards the real chemical potential axis, see, e.g., Refs. [243–245]. Unfortunately, this approach is limited to $\mu/T \lesssim 1$. A promising alternative approach is the *Complex-Langevin* (CL) method, which is based on stochastic quantization [246, 247]. The latter has already been successfully applied for QCD at finite temperature and quark chemical potential as well as for ultracold gases in several works [248–252] and may provide us with more insights into the dynamics underlying the QCD phase diagram in future studies, see Ref. [253] for the current status of the CL framework.

Let us now discuss the conjectured QCD phase diagram from model considerations. Note that in many cases, the employed models are related to those of the NJL type we have discussed in the last subsection. We begin with the QCD phase diagram with two quark flavors, i.e., up and down, and neglect all quark flavors with larger current quark masses, i.e., strange, charm, bottom and top quarks. For our first discussion, we assume that both light quark flavors have a small but finite current masses $m_{u,d} \gtrsim 0$. We know from Sec. 2.3.2 that chiral symmetry is then explicitly broken. Using the aforementioned parameters for the quark masses, the phase diagram of QCD may look similar to Fig. 2.6, see Refs. [254–256] for reviews. For very high temperatures $T \gg T_{\mathrm{cr}} \simeq 130\,\mathrm{MeV}$, see Ref. [9, 10] for recent lattice studies, the quarks and gluons are found in a deconfined state, the so-called Quark-Gluon Plasma (QGP). Since quantum fluctuations are strongly suppressed due to the large thermal screening mass in the propagators at high temperature, the QGP can be seen, in a first approximation, as a free quantum gas consisting of quarks and

gluons, see, e.g., Refs. [257–259]. By lowering the temperature, one expects at zero quark chemical potential $\mu = 0$ a *crossover* at a pseudocritical temperature of $T_{\mathrm{cr}} \simeq 132\,\mathrm{MeV}$ [9, 10] where the light quarks gradually condense to form hadronic bound states, see the light-blue regime in Fig. 2.6. At non-zero quark chemical potential, however, a first-order phase transition line at finite temperature separating the QGP from a phase dominated by a finite gap is expected. The latter then implies the existence of a critical endpoint of the first-order transition line at finite temperature and quark chemical potential. Nevertheless, the existence as well as the position of this critical endpoint is still a subject of theoretical, see, e.g., Refs. [227, 260–266], and ongoing experimental works, see, e.g., Ref. [267]. Inside the hadronic phase at zero temperature, there is a first-order liquid-gas phase transition of nuclear matter [268–271] at a quark chemical potential of $\mu \simeq 310\,\mathrm{MeV}$. Moreover, at finite temperature the associated first-order transition line ends in a critical endpoint. This is comparable to the conjectured endpoint of the first-order transition line separating the QGP from condensed hadronic matter.

Before we study the regime of large quark chemical potential and low temperature, let us first discuss the limit of vanishing current quark masses $m_{u,d} \to 0$. Here, we have a situation as described in Sec. 2.3.2 where the QCD Lagrangian obeys chiral symmetry. In the chiral limit, it is argued that the *crossover* at finite temperature and zero chemical potential could become a second-order phase transition [232]. However, recent lattice QCD results, see, e.g., Refs. [272–275], indicate that the thermal phase transition at vanishing quark chemical potential could also be first order. Therefore, the true nature of the phase transition is still not settled and remains an open question. Nevertheless, if there exists a second-order phase transition at $\mu = 0$, the expected critical endpoint might turn into a tricritical point. Note that we shall also assume in our NJL-type and QCD studies in the next chapter that the up and down quarks have a vanishing current quark mass.

Let us turn to the expected state of matter at large quark chemical potential. Here, *mean-field* studies suggest that it becomes favorable for up and down quarks of different colors to form *Cooper*-type pairs, so-called diquarks, as it is the case in the *Bardeen-Cooper-Schrieffer* (BCS) theory of superconductivity, see, e.g. Refs. [32, 33, 42, 43] and for rather general overviews Refs. [28, 35, 254]. In Fig. 2.6, the so-called color superconducting (2SC) phase is highlighted using a light-red color tone. We emphasize that the 2SC phase has been found to be favorable in case of two massless quark flavors as well as for small finite current quark masses for the up and down quarks. The phase transition line between the hadronic state and the 2SC phase is likely to be first order where the transition between the QGP and the 2SC phase is expected to be second order, see, e.g., Refs. [28, 276]. In contrast to the hadronic phase, within the 2SC phase, the chiral symmetry remains likely to be intact [277]. For example, this is true for a diquark condensate of the form

$$\delta^l \sim \langle \mathrm{i}\bar{\psi}^C \gamma_5 \epsilon_f \varepsilon_c^l \psi \rangle \,, \tag{2.88}$$

with $\epsilon_f \equiv \epsilon_f^{(\alpha,\beta)}$ and $\varepsilon_c^l \equiv \varepsilon_c^{l(m,n)}$ which are antisymmetric tensors in flavor and color space, respectively. Further, we have introduced the conjugated fields $\psi^C = \mathcal{C}\bar{\psi}^T$ and $\bar{\psi}^C = \psi^T \mathcal{C}$ with the charge conjugation operator $\mathcal{C} = \mathrm{i}\gamma_2\gamma_0$. A diquark which corresponds to a δ^l-type condensate is a $J^P = 0^+$ state and is predominantly preferred by one-gluon exchange diagrams [277] and instanton-induced strong correlations [215, 278] by model studies [33, 278] at high densities. The formation of a $J^P = 0^+$ diquark condensate is then accompanied by a spontaneous breakdown of the global $U(1)_V$ symmetry implying the violation of the baryon number. At the same time, one also expects a spontaneous breaking of the (global) $SU(3)$ color gauge symmetry by virtue of the *Anderson-Higgs* mechanism. As indicated in the introduction of this section, the 2SC order parameter Eq. (2.88) signaling the onset of spontaneous local symmetry "breaking", is not gauge invariant. Nevertheless, it appears to be legitimate to utilize non-gauge invariant order parameters to achieve a basic overview of the phase structure and the underlying symmetry breaking patterns. In that sense, we shall also employ this type of order parameter in our studies. However, we emphasize that the associated diquark gap in the energy spectrum is indeed a gauge invariant quantity as one can show, see Ref. [28]. Still, the exact nature of the phase dominated by diquark degrees of freedom is not completely understood. For instance, quark-quark bound states other than 0^+-type diquarks, i.e., states with non-vanishing spin, are also discussed by various authors and may also exist for different parameter settings, see, e.g., Ref. [28] for

an overview.

So far, we concentrated on the phase diagram of two-flavor QCD. Let us now briefly discuss the QCD phase diagram if a strange quark with a non-vanishing current quark mass comes into play. For this, at large quark chemical potential, there is another state of matter discussed in the light of diquark-type bound states. Within the so-called *Color-Flavor-Locking* (CFL) phase [33, 35], the chiral symmetry is spontaneously broken as it is the case in the hadronic phase. Nevertheless, within the CFL phase, there is still a BCS-type pairing of quarks ongoing with all three flavor and color degrees of freedom involved. The latter then form spinless *Cooper* pairs with vanishing center-of-mass momentum $\vec{q} = 0$. Note further that the mass of the strange quark does also have an essential influence on the expected order of the phase transition line separating the deconfined QGP from the gapped matter states. For instance, we have already seen that a vanishing current quark mass for the up and down quark may crucially alter the type of the finite temperature phase transition at zero quark chemical potential. This is also the case for a finite strange quark mass, where the order of the phase transition line at vanishing quark chemical potential is still not completely understood. Here, the famous Columbia plot, see, e.g., Refs. [273, 279], gives an overview of the expected nature of the phase transition at finite temperature and zero chemical potential as a function of the light and strange quark mass.

We end this very brief summary of the QCD phase diagram at finite quark chemical potential with the remark that we discussed by far not all possible phases which are expected to emerge within dense QCD matter. In particular, we only considered QCD matter at zero isospin chemical potential. At non-vanishing isospin chemical potential, for example, one expects in analogy to a *Fulde-Ferrell-Larkin-Ovchinnikov*-type (FFLO) superconductor [280, 281] where the *Cooper* pairs carry a finite center-of-mass momentum $\vec{q}$, the possible existence of a corresponding crystalline color superconducting state in QCD [34, 282, 283]. As one would expect it for a FFLO-type superconductor of atomic matter, the order parameter of a color crystal condensate would then acquire a modulation in position space.

We emphasize that aside from usual hadronic matter, there are still experimental verifications missing for any of the discussed types of exotic matter states at large μ. Due to the sign problem which we have mentioned at the beginning of this section, an exploration of the dense QCD regime using conventional lattice methods also turns out to be less feasible. Therefore, in our present work, we employ the functional Renormalization Group which allows us to study the (T, μ) plane over a wide range of temperature and quark chemical potential including fluctuation effects beyond a *mean-field* approximation.

Chapter 3

Phases and Fixed-Points of Strong-Interaction Matter

In this chapter, we study the phase diagram of strong-interaction matter in the plane spanned by the temperature T and the quark chemical potential μ. We begin in Sec. 3.1 with a *Fierz*-complete one-flavor and one-color NJL-type model study. Here, we discuss the fixed-point structure of the corresponding vacuum theory and analyze the running of the four-fermion couplings. At finite temperature and fermion chemical potential, we then compute the phase diagram from two different *Fierz*-complete approaches, showing that the resulting phase boundaries are unique. On the other hand, we shall see that this is not the case for *Fierz*-incomplete basis choices. In the end, we discuss the impact of different types of regularization schemes from a technical point of view.

In Sec. 3.2, we then present a *Fierz*-complete NJL study with two flavors and three colors. We discuss the critical phase boundary in the (T, μ) plane, where we compare different *Fierz*-incomplete basis sets with our ten-channel *Fierz*-complete approach. Further, we analyze the fixed-point structure and analyze the pseudo fixed-point behavior under a variation of the temperature and quark chemical potential for a two-channel approximation. The pseudo fixed-point structure then provides us with further valuable insight into the dynamics underlying the observed symmetry breaking patterns.

We finally study in Sec. 3.3 the phase boundary of two-flavor QCD by employing the *Fierz*-complete basis from the previous section. Further, we consider dynamical gluon degrees of freedom so that the four-quark interactions are generated automatically from the RG running of the strong coupling. We discuss the phase diagram and compare the QCD study with our NJL model from Sec. 3.3. Eventually, we give an outlook to future studies on the equation of state for isospin-symmetric strong-interaction matter based on this work.

3.1 Nambu–Jona-Lasinio: One Flavor and One Color

We begin our first study with a purely fermionic NJL model at finite temperature and fermion chemical potential, see Ref. [116] for the original paper. For simplicity, we study massless fermions with no further internal degrees of freedom like color or flavor ($N_f = N_c = 1$). These type of chiral theories have already been investigated intensively for different truncations and approximations, see, e.g., Refs. [162, 228, 284]. In our study, we investigate the underlying mechanisms of spontaneous chiral symmetry breaking by employing a *Fierz*-complete ansatz. Since there are no flavor degrees of freedom present in our study below, the chiral $U(2)_L \times U(2)_R$ symmetry in QCD is replaced by a residual global $U(1)_A \times U(1)_V$ symmetry obeying the following transformation rules for the spinor fields ψ and $\bar{\psi}$:

$$U(1)_A \quad : \qquad \bar{\psi} \mapsto \bar{\psi}\, \mathrm{e}^{\mathrm{i}\gamma_5\alpha}, \qquad \psi \mapsto \mathrm{e}^{\mathrm{i}\gamma_5\alpha}\psi\,, \tag{3.1}$$

and

$$U(1)_V \quad : \qquad \bar{\psi} \mapsto \bar{\psi}\, \mathrm{e}^{-\mathrm{i}\alpha}, \qquad \psi \mapsto \mathrm{e}^{\mathrm{i}\alpha}\psi\,. \tag{3.2}$$

Here, α denotes in both cases a real-valued "rotation angle" as we have discussed in Sec. 2.3.2. Recall that the $U(1)_V$ symmetry is related to the conservation of the fermion number.

The classical action in *Euclidean* spacetime which is invariant under Eqs. (3.1) and (3.2) is given by

$$S[\bar{\psi},\psi] \;\; = \;\; \int_0^\beta \mathrm{d}\tau \int \mathrm{d}^3 x \left\{ \bar{\psi}(\mathrm{i}\slashed{\partial} - \mathrm{i}\mu\gamma_0)\psi + \frac{1}{2}\bar{\lambda}_\sigma \left[(\bar{\psi}\psi)^2 - (\bar{\psi}\gamma_5\psi)^2 \right] \right\}. \tag{3.3}$$

Here, the scalar-pseudoscalar four-fermion interaction appearing in the classical action carries similar quantum numbers like the σ-meson and the pions, which we have discussed in Sec. 2.3.2. Nevertheless, the NJL-type model we consider in this section is drastically simplified as we neglect color and flavor degrees of freedom. In the study below, the onset of the spontaneous breakdown of the chiral $U(1)_A$ symmetry is signaled by the formation of the condensate $\langle \bar{\psi}\psi \rangle$ which serves as an order parameter. To distinguish the breakdown of the chiral $U(1)_A$ from a breakdown of the $U(1)_V$ symmetry we further consider the order parameter $\langle \psi^T \mathcal{C}\gamma_5\psi \rangle$ with $\mathcal{C} = \mathrm{i}\gamma_2\gamma_0$ associated with a difermion-type condensate. The latter can be compared to diquark-type condensates in QCD matter which we expect to exist at large quark chemical potential, see our discussion in Sec. 2.3.4. Below, we shall discuss how difermion-type four-fermion correlation functions can be included in our present study and how they are related to conventional "fermion-antifermion-type" four-fermion interactions by means of *Fierz* transformations.

Due to the external heat bath and the finite chemical potential, some symmetries of the vacuum theory underlying Eq. (3.3) are broken explicitly. Since we distinguish the temporal direction of spacetime by considering a finite temperature and fermion chemical potential, the *(Euclidean) Poincaré* symmetry is broken. Due to the finite fermion chemical potential, we further break the invariance under discrete charge conjugations $\mathcal{C}$. Note that the classical action is still invariant under discrete time $\mathcal{T}$ and parity $\mathcal{P}$ transformations. One may wonder, why our QFT is not invariant under $\mathcal{CPT}$ as one might expect. For this, we emphasize that a prerequisite for the famous $\mathcal{CPT}$ theorem is *Lorentz* invariance (cf. Ref. [126]), which is violated by introducing, e.g., a fermion chemical potential.

As an ansatz for our effective action Γ, we have to consider the most general action which satisfies the symmetries underlying our theory. We already know from our "recipe" in Sec. 2.3.3 that we have also to include four-fermion channels other than $\left[(\bar{\psi}\psi)^2 - (\bar{\psi}\gamma_5\psi)^2 \right]$ as the *Wetterich* equation (2.23) dynamically generates all types of four-fermion interaction which are compatible with the symmetries. For instance, we also need to take vector-type $(\bar{\psi}\gamma_\mu\psi)^2$ and axial-vector-type $(\bar{\psi}\gamma_\mu\gamma_5\psi)^2$ four-fermion channels into account. In leading order (LO) of the derivative expansion, see also Sec. 2.2.2, we then find six channels which are invariant under $U(1)_V \times U(1)_A$ transformations:

$$\begin{aligned}
\Gamma_{\mathrm{LO}}[\bar{\psi},\psi] = \int_0^\beta \mathrm{d}\tau \int \mathrm{d}^3 x \Big\{ &\bar{\psi}(Z^\| \mathrm{i}\gamma_0\partial_0 + Z^\perp \mathrm{i}\gamma_i\partial_i - Z_\mu \mathrm{i}\mu\gamma_0)\psi \\
&+ \frac{1}{2}Z_\sigma \bar{\lambda}_\sigma (S-P) - \frac{1}{2}Z_V^\| \bar{\lambda}_V^\| \left(V_\| \right) - \frac{1}{2}Z_V^\perp \bar{\lambda}_V^\perp \left(V_\perp \right) - \frac{1}{2}Z_A^\| \bar{\lambda}_A^\| \left(A_\| \right) \\
&\hspace{4cm} - \frac{1}{2}Z_A^\perp \bar{\lambda}_A^\perp \left(A_\perp \right) - \frac{1}{2}Z_T^\| \bar{\lambda}_T^\| \left(T_\| \right) \Big\}. \tag{3.4}
\end{aligned}$$

The scale-dependent dimensionless vertex renormalizations are denoted by Z_σ, $Z_V^\|$, $Z_V^\perp$, $Z_A^\|$, $Z_A^\perp$, and $Z_T^\|$ where the dimensionful bare couplings are defined as $\bar{\lambda}_\sigma$, $\bar{\lambda}_V^\|$, $\bar{\lambda}_V^\perp$, $\bar{\lambda}_A^\|$, $\bar{\lambda}_A^\perp$ and $\bar{\lambda}_T^\|$. The abbreviations we use in Eq. 3.4 for

the six four-fermion channels are:

$$
\begin{aligned}
(S - P) &\equiv (\bar{\psi}\psi)^2 - (\bar{\psi}\gamma_5\psi)^2\,, & \left(T_{\parallel}\right) &\equiv (\bar{\psi}\sigma_{0i}\psi)^2 - (\bar{\psi}\sigma_{0i}\gamma_5\psi)^2\,, \\
\left(V_{\parallel}\right) &\equiv (\bar{\psi}\gamma_0\psi)^2\,, & \left(V_{\perp}\right) &\equiv (\bar{\psi}\gamma_i\psi)^2\,, \\
\left(A_{\parallel}\right) &\equiv (\bar{\psi}\gamma_0\gamma_5\psi)^2\,, & \left(A_{\perp}\right) &\equiv (\bar{\psi}\gamma_i\gamma_5\psi)^2\,.
\end{aligned}
\tag{3.5}
$$

Furthermore, because of the explicit breaking of the *Poincaré* symmetry, we separately renormalize in Eq. (3.4) the temporal $Z^{\parallel}$ and spatial $Z^{\perp}$ spacetime components of the fermionic wave function. Nevertheless, the leading order of the derivative expansion corresponds to treat the four-fermion vertices in the pointlike limit, see Eq. (2.81). As a consequence, the running of the wave-function renormalizations become trivial, as we shall discuss below. We further identify in Eq. (3.4) the renormalization function corresponding to the fermion chemical potential by Z_{μ}. At vanishing temperature, we have $Z_{\mu}^{-1} = Z^{\parallel} = Z^{\perp}$ for $Z_{\mu}\mu < m_f$. The fermion (pole) mass, possibly generated in the *infrared*, is here denoted by $m_f = \bar{m}_f/Z^{\perp}$, where $\bar{m}_f$ describes the bare fermion mass. The relation between the wave-function renormalization $Z^{\perp}$ and the renormalization function of the chemical potential Z_{μ} is a consequence of the *Silver-Blaze* property of QFT's at zero temperature and finite chemical potential, see Refs. [285–288] and our discussion in Ref. [116].

Since our present ansatz (3.4) is overcomplete, we can reduce the number of basis elements by using *Fierz* identities, see App. B.3.1. In case of the six four-fermion channels in Eq. (3.5), we only find three to be linear independent at finite temperature and chemical potential. In our case, we therefore employ the following *Fierz*-complete ansatz:

$$
\begin{aligned}
\Gamma_{\mathrm{LO}}[\bar{\psi},\psi] = \int_0^{\beta} \mathrm{d}\tau \int \mathrm{d}^3x \,\Big\{ &\bar{\psi}(Z^{\parallel}\mathrm{i}\gamma_0\partial_0 + Z^{\perp}\mathrm{i}\gamma_i\partial_i - Z_{\mu}\mathrm{i}\mu\gamma_0)\psi \\
&+ \frac{1}{2}Z_{\sigma}\bar{\lambda}_{\sigma}(S-P) - \frac{1}{2}Z_V^{\parallel}\bar{\lambda}_V^{\parallel}\left(V_{\parallel}\right) - \frac{1}{2}Z_V^{\perp}\bar{\lambda}_V^{\perp}\left(V_{\perp}\right)\,.
\end{aligned}
\tag{3.6}
$$

Of course, the choice of the three channels above is not unique. In this study, we demonstrate this by considering a second *Fierz*-complete basis which shall be of the difermion-type. Obviously, the values of the scale-dependent couplings then depend on the the particular choice of the *Fierz* basis. However, the crucial feature of a *Fierz*-complete basis is that physical observables are basis independent, e.g., the critical temperature is invariant under arbitrary *Fierz* transformations if a *Fierz*-complete basis is used, see our discussion in Sec. 3.1.2. We emphasize that this is not the case for any *Fierz*-incomplete basis.

In principle, the ansatz (3.6) would also receive contributions from higher order fermion self-interactions, e.g., from eight-fermion interactions. As it turns out, however, eight-fermion correlation functions do not couple to the four-fermion sector at this order of the derivative expansion and are therefore not included, see Ref. [228] for details.

Note that the pointlike limit does not provide us with any information on the momentum structure of the correlation functions encoding the underlying mass spectrum of the theory. The onset of the formation of a finite condensate associated with spontaneous symmetry breaking is then signaled by diverging four-fermion couplings at some finite critical RG scale $k = k_{\mathrm{cr}}$, see our criterion in Sec. 2.3.2. The divergence in a four-fermion channel then indicates that the curvature at the origin of the corresponding *Ginzburg-Landau* potential (see Fig. 2.4) tends to zero so that a non-trivial ground state may be assumed. In the leading order of the derivative expansion in our purely fermionic formulation of Γ, we cannot study the theory within a regime where at least one symmetry is broken spontaneously. Nevertheless, we can start our RG flow in the symmetric regime, e.g., at high temperatures, where it is expected that the symmetries underlying our theory remain intact. By lowering the temperature at a given value of the chemical potential, we then find a critical temperature T_{cr} below which the pointlike limit breaks down. From this, we can deduce an upper bound for the critical phase transition line $T_{\mathrm{cr}}(\mu)$ separating the gapped from the ungapped regime. In former studies, this line of argumentation has already been successfully applied for gauge theories, see Refs. [19–21]. From a phenomenological point of view, however, the meaning of the critical temperature can be manifold. In particular, the critical temperature cannot be related to the breakdown of a spe-

cific symmetry. As we shall see, the divergence in one four-fermion channel automatically triggers divergences in all other four-fermion channels. Therefore, the true nature of the condensate forming in the *infrared* is difficult to assess in the present study. Nevertheless, we employ a technique which allows for a first estimate of the forming ground state as we shall discuss in the next subsection.

A divergence in the four-fermion couplings serves as an indicator for the breakdown of the pointlike limit and signals the onset of spontaneous symmetry breaking. However, the criterion might be not sufficient. To be more specific, symmetry restoration mechanisms might still exist in the deep *infrared*, e.g., quantum fluctuations could restore the symmetry at low scales. If the physical phase transition is of first-order, a divergence in the four-fermion couplings may only hint to a region of metastability. In this case, a liquid-gas-type phase transition which is expected to be of first order cannot be reliably resolved using our present ansatz. Phase transitions which are of second order can in principle be readily detected within our framework, e.g., the color superconducting phase transition is expected to be of second order, see our discussion in Sec. 2.3.4.

Let us further discuss the regularization scheme we use throughout this study. For the latter, we employ a four-dimensional exponential regulator respecting the *Poincaré* symmetry of the theory in the vacuum limit $T \to 0$ and $\mu \to 0$, see also App. C. This is an essential property as we find that the *Fierz*-complete vacuum beta functions with two channels [162, 228] can be recovered straightforwardly from our *Fierz*-complete beta functions (E.1)-(E.3) at finite temperature and fermion chemical potential. Therefore, *covariance* can be restored in the vacuum. Since vacuum observables are usually used to fix the theory's parameters in the *ultraviolet*, it is desirable for any regularization scheme to have a consistent vacuum limit. Note that this is not necessarily the case for spatial regularization schemes where we find a broken *Poincaré* symmetry of the theory even in the vacuum limit.

In the next subsection, we discuss the limit of vanishing temperature and chemical potential. By studying the fixed-point structure and the RG flows associated with the four-fermion beta functions, we can analyze the nature of the condensates which are expected to form in the *infrared*. At finite temperature and fermion chemical potential, we then expect, at least at low fermion chemical potential, the formation of a finite chiral condensate $\sigma \sim \langle \bar{\psi}\psi \rangle$, breaking the axial $U(1)_A$ symmetry.

3.1.1   Vacuum Theory and Fixed Points

Before we discuss the full *Fierz*-complete NJL model at finite temperature and fermion chemical potential, we begin with the discussion of the corresponding vacuum theory, where $T \to 0$ and $\mu \to 0$. In this limit, a *Fierz*-complete ansatz is given by just two linear independent four-fermion channels [162, 228]. As a first step, it is required that we discuss the renormalization of the ansatz (3.6). For this, we can rewrite our bare four-fermion couplings $\bar{\lambda}_i = \{\bar{\lambda}_\sigma, \bar{\lambda}_V^\parallel, \bar{\lambda}_V^\perp\}$ with the renormalization functions $Z_i = \{Z_\sigma, Z_V^\parallel, Z_V^\perp\}$ into dimensionless renormalized couplings

$$\lambda_i = \frac{Z_i k^2 \bar{\lambda}_i}{(Z^\perp)^2} \,, \tag{3.7}$$

where we used the field redefinition

$$\psi \to \psi \, (Z^\perp)^{-\frac{1}{2}} \,, \qquad\qquad \bar{\psi} \to \bar{\psi} \, (Z^\perp)^{-\frac{1}{2}} \,. \tag{3.8}$$

The leading order of the derivative expansion implies that we treat the four-fermion vertices in the pointlike limit. As a consequence, the flow equations associated with the wave-function renormalizations of the fermion propagator vanish identically $\partial_t Z^\parallel = \partial_t Z^\perp = 0$. Note that the corresponding anomalous dimensions $\eta^\perp = -\partial_t \ln Z^\perp$ and $\eta^\parallel = -\partial_t \ln Z^\parallel$ are then equal to zero. Therefore, the wave-function renormalizations remain constant and independent on k where we choose $Z^\perp = Z^\parallel = 1$ at the initial RG scale.

Let us now discuss the *Fierz*-complete set of beta functions in the vacuum limit. For our *covariant* regularization
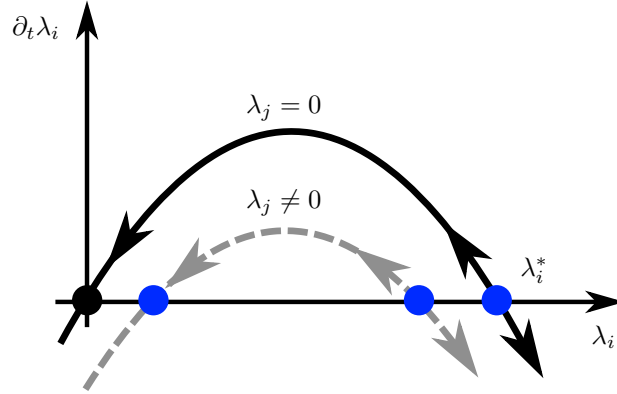
Figure 3.1: Typical four-fermion beta function $\partial_t \lambda_i$ in the vacuum as a function of the coupling λ_i. We also display the *Gaussian* fixed point in black and the non-*Gaussian* fixed points in blue. The grayish dotted parabola depicts the influence of more than one channel which can lift the beta function upwards or downwards. With this shift, the former *Gaussian* fixed point turns into a non-*Gaussian* one. Possibly, there are non-trivial critical values for λ_j so that the beta function is not controlled by any real-valued fixed point anymore.

scheme (see also App. C), we obtain:

$$\partial_t \lambda_\sigma \quad = \quad \beta_{\lambda_\sigma} = 2\lambda_\sigma - 8v_4 \left(\lambda_\sigma^2 + 4\lambda_\sigma \lambda_V + 3\lambda_V^2 \right), \tag{3.9}$$

$$\partial_t \lambda_V \quad = \quad \beta_{\lambda_V} = 2\lambda_V - 4v_4 \left(\lambda_\sigma + \lambda_V \right)^2, \tag{3.10}$$

with $v_4 = 1/(32\pi^2)$. Note that we assume $\lambda_V^\parallel = \lambda_V^\perp$ in (3.6) which holds at zero temperature and chemical potential. We emphasize again that up to some numerical constants which depend on the particular regularization scheme, our beta functions agree with literature calculations, see Refs. [162, 228].

As a first analysis, we start with a *Fierz*-incomplete one-channel truncation. For this, we set in Eq. (3.9) the coupling $\lambda_V = 0$ by hand. The remaining flow equation for the chiral scalar-pseudoscalar four-fermion channel then reads

$$\partial_t \lambda_\sigma \quad = \quad \beta_{\lambda_\sigma} = 2\lambda_\sigma - 8v_4\lambda_\sigma^2, \tag{3.11}$$

which has a non-*Gaussian* fixed point at $\lambda_\sigma^* = 8\pi^2$. The latter is *infrared* repulsive as it turns out from a stability analysis

$$\Theta := -\left.\frac{\partial \beta_\sigma}{\partial \lambda_\sigma}\right|_{\lambda_\sigma^*} = 2, \tag{3.12}$$

with the positive critical exponent Θ governing the scaling behavior of physical observables close to the fixed point λ_σ^*. We can compute the scale dependence of the four-fermion coupling in this one-channel approximation exactly:

$$\lambda_\sigma(k) = \frac{\lambda_\sigma^{(\mathrm{UV})}}{\left(\frac{\Lambda}{k}\right)^\Theta \left(1 - \frac{\lambda_\sigma^{(\mathrm{UV})}}{\lambda_\sigma^*}\right) + \frac{\lambda_\sigma^{(\mathrm{UV})}}{\lambda_\sigma^*}}, \tag{3.13}$$

where $\lambda_\sigma^{(\mathrm{UV})}$ denotes the starting value of the coupling λ_σ at the UV scale Λ. The situation is illustrated in Fig. 3.1, where we show the shape of a typical beta function in case of vanishing temperature and chemical potential, see the black curve (arrows point towards the *infrared*). We find that if the UV value of the scalar-pseudoscalar coupling $\lambda_\sigma^{(\mathrm{UV})}$ is chosen smaller than the fixed point value $\lambda_\sigma^{(\mathrm{UV})} < \lambda_\sigma^*$, the system is dominated by the *Gaussian* fixed

point of the theory. From Eq. (3.13), it then follows that the flow of the dimensionless renormalized coupling λ_σ tends to zero in the *infrared*. In this case, the theory is ungapped and remains in the symmetric phase. On the other hand, for $\lambda_\sigma^{(\mathrm{UV})} > \lambda_\sigma^*$, a quantum phase transition, i.e., a vacuum phase transition, is triggered and the flow of the scalar-pseudoscalar coupling diverges at some finite critical scale

$$k_{\mathrm{cr}} = \Lambda(\Delta\lambda_\sigma)^{\frac{1}{\Theta}}\theta(\Delta\lambda_\sigma)\,. \tag{3.14}$$

Here, we have introduced the relative distance to the non-*Gaussian* fixed point

$$\Delta\lambda_\sigma = \frac{\lambda_\sigma^{(\mathrm{UV})} - \lambda_\sigma^*}{\lambda_\sigma^{(\mathrm{UV})}}\,. \tag{3.15}$$

From the relation above, we can readily deduce that a finite critical scale k_{cr} can only be found in case of $\Delta\lambda_\sigma > 0$. Since the system is governed by the *Gaussian* fixed point for $\Delta\lambda_\sigma < 0$, the theory remains in the symmetric phase as discussed above.

Note that if there was more than one channel present in our truncation, we would observe that four-fermion channels associated with the couplings λ_j are, in principle, able to move the parabola upwards or downwards, see the dotted gray line in Fig. 3.1. This can be seen from the structure of the beta functions, e.g., in Eq. (3.9) where the running λ_V-coupling can shift the parabola associated with the scalar-pseudoscalar coupling λ_σ. This mechanism is comparable to the impact of the running gauge coupling $\sim g$, as discussed in Sec. 2.3.2. We shall come back to this point when we discuss the effect of gluonic degrees of freedom at the end of this chapter.

The critical scale (3.14) sets the scale for all low-energy observables, which are then functions of the critical scale themselves. As we have discussed in the previous section, a diverging four-fermion coupling λ_σ signals the onset of spontaneous chiral symmetry breaking. Since the four-fermion coupling λ_σ is related to the bosonic curvature mass m_σ^2, see Eq. (2.73), of the corresponding partially bosonized theory via $\lambda_\sigma \sim 1/m_\sigma^2$, a divergence in the λ_σ coupling implies that the curvature tends to zero $m_\sigma^2 \to 0$. However, as we have discussed in Sec. 2.3.2, this criterion may not be sufficient for spontaneous symmetry breaking since there might be symmetry restoration processes occurring in the deep IR regime, see also Refs. [21, 22].

Let us now discuss the flow equations (3.9) and (3.10) which are *Fierz*-complete at vanishing temperature and fermion chemical potential. In general, we can visualize the corresponding theory space by using a stream diagram, see Fig. 3.2. Note that the arrows point again in the direction of the *infrared*. In the vacuum, besides the *Gaussian* fixed point at $\mathcal{F}_0 = (0,0)$, we find two non-*Gaussian* fixed points which have the numerical values $\mathcal{F}_1 = (3\pi^2, \pi^2)$ (blue dot) and $\mathcal{F}_2 = (-32\pi^2, 16\pi^2)$. Note that the values are regularization scheme dependent and correspond to our *covariant* regulator. The critical points describe situations in which the beta functions of our theory vanish. Then, the system shows scale-invariant behavior, i.e., the theory does not change under RG transformations and behaves the same on all length or momentum scales, see also our generalized picture Fig. 2.1 from Chap. 2. Note further that the non-*Gaussian* points are not stable fixed points. Each of them has an *infrared* attractive and repulsive direction.

As initial conditions at the UV scale $k = \Lambda$, we choose in case of more than one channel for the rest of the present study $\lambda_{V_\parallel}^{(\mathrm{UV})} = \lambda_{V_\perp}^{(\mathrm{UV})} = \lambda_V^{(\mathrm{UV})} = 0$. From our coupled set of RG flow equations, these channels are then solely dynamically induced by quantum fluctuations. The remaining free parameter of our theory is, therefore, the UV value of the scalar-pseudoscalar coupling $\lambda_\sigma^{(\mathrm{UV})}$. Indeed, from QCD vacuum studies, see, e.g., Ref. [23], we find that the scalar-pseudoscalar channel is dominantly generated in the RG flow of full QCD. As we eventually aim at a study of QCD, we mimic this situation here and only choose a finite UV value for the scalar-pseudoscalar coupling. We shall come back to this in the next section.

In Fig. 3.2, we show an exemplary RG flow for initial conditions of the type as specified by the magenta dot. From the coupled RG equations, we find (red-colored) critical separatrices slicing the underlying theory space in three domains, which are governed by different fixed points. For this showcase, the magenta starting point lies in
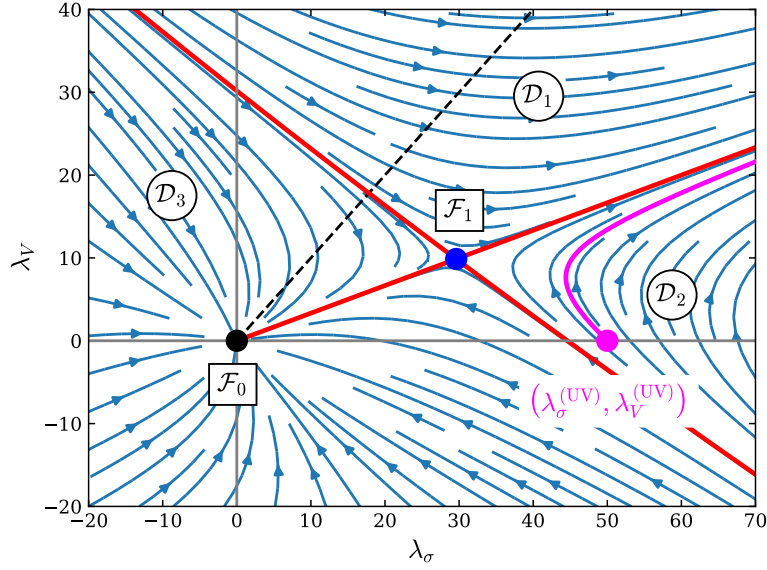
Figure 3.2: The beta functions (3.9) and (3.10) are visualized as a stream plot where the arrows point in the *infrared* direction. The *Gaussian* fixed point ($\mathcal{F}_0$) is shown in black and one of the two non-*Gaussian* fixed points ($\mathcal{F}_1$) in blue. For illustration, we further show an RG trajectory (pink line) which approaches the separatrix (red line) in the *infrared*. The theory space is sliced by the separatrices in three domains $\mathcal{D}_1$, $\mathcal{D}_2$ and $\mathcal{D}_3$. The dominance of the scalar-pseudoscalar channel can be deduced from the relative location of the bisectrix (black dotted line) to the separatrix separating $\mathcal{D}_1$ from $\mathcal{D}_2$.

domain $\mathcal{D}_2$, which is dominated by the repulsive direction of the fixed point $\mathcal{F}_1$. If the system is initialized in this domain, the four-fermion couplings rapidly increase and diverge at a finite critical scale. The magenta trajectory then asymptotically approaches the separatrix in the deep *infrared*. The separatrix which intersect the *Gaussian* and the non-*Gaussian* fixed point $\mathcal{F}_1$ has a smaller gradient than the bisectrix (black dotted line) and points towards the λ_σ direction. From the magenta RG trajectory approaching the latter separatrix, we may then deduce that the scalar-pseudoscalar channel becomes large and dominates the *infrared* regime. The dominance pattern of the competing running couplings can then provide us with information on the symmetry breaking patterns and possible forming condensates at $k \to 0$, see also Refs. [19–21].

Fig. 3.3 illustrates the magenta trajectory from a different perspective. Here, we present the (inverse) flows of the λ_σ and λ_V coupling as a function of the RG scale k. The dominance of the scalar-pseudoscalar channels is, moreover, manifested in $\lambda_\sigma(k) > \lambda_V(k)$ for values k close to the critical scale k_{cr}. On the other hand, the inverse coupling λ_σ^{-1} associated with the curvature of the effective potential, tends "faster" to zero than the competitive coupling λ_V^{-1}. Therefore, we expect the formation of a finite chiral condensate with $\langle \bar{\psi}\psi \rangle \neq 0$. At least for $\lambda_V^{(\mathrm{UV})} = 0$ and $\lambda_\sigma^{(\mathrm{UV})} \in \mathcal{D}_2$, our analysis suggests the onset of spontaneous chiral symmetry breaking in accordance with naive expectation that the ground state is governed by chiral degrees of freedom at $T = \mu = 0$.

We close this subsection with some general comments on the choice of our initial conditions and our dominance analysis from which we infer the nature of the theory's ground state. First, from Fig. 3.2 we deduce that by setting $\lambda_\sigma^{(\mathrm{UV})} = 0$, we still find a dominance in the scalar-pseudoscalar channel, given we choose a sufficiently large starting value for the vector coupling, i.e., the initial value should lie in the domain $\mathcal{D}_1$. In the (deep) *infrared*, one would then observe an RG flow similar to the one we found for our previously employed UV initial condition in the domain $\mathcal{D}_2$. This is an interesting observation in the following sense; the dominance in the scalar-pseudoscalar channel associated with a spontaneously broken chiral symmetry seems to be rather robust and weakly dependent
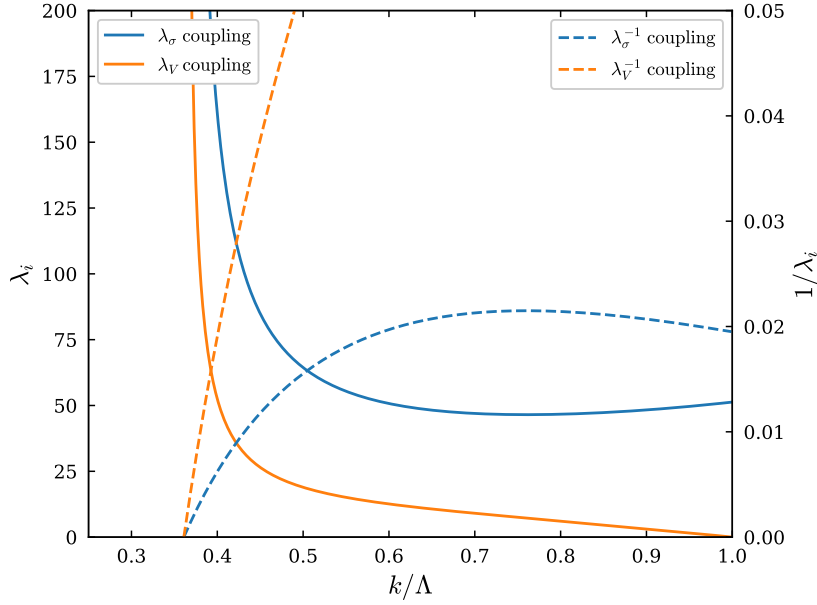
Figure 3.3: RG running of the couplings λ_σ and λ_V for initial conditions as used in Fig. 3.2. Further, we also show the inverse couplings λ_σ^{-1} and λ_V^{-1} as a function of the RG scale k at vanishing temperature and chemical potential. We observe that both couplings rapidly increase and, eventually, diverge at a finite critical scale $k = k_{\mathrm{cr}}$ indicating the onset of spontaneous symmetry breaking.

on the particular choice of UV initial conditions. This statement is true as long as the RG flow starts in $\mathcal{D}_1$ or $\mathcal{D}_2$. Throughout this study, we continue to use this dominance argumentation we employed above. We emphasize that for a quantitative study of the possibly forming condensates in the *infrared*, we would need to study, e.g., at least parts of the momentum structure of the four-fermion correlation functions. Especially in the deep *infrared*, quantum fluctuations could still change the dominance pattern so that vector-type condensates might emerge. Even though it appears to be rather unlikely, a possible vector-like condensate cannot be ruled out using the pointlike limit.

3.1.2 Phase Structure

We discuss the one-flavor and one-color NJL model at finite temperature and fermion chemical potential. In analogy to the previous section, we start again with an analysis of a one-channel approximation only considering a scalar-pseudoscalar channel, before investigating the thermal *Fierz*-complete basis. Again, we obtain the finite-temperature one-channel approximation from the *Fierz*-complete set of equations (E.1)-(E.3) by setting $\lambda_V^{\parallel} = \lambda_V^{\perp} = 0$ by hand. Note that this method yields different beta functions compared to a direct computation starting with an ansatz with only one scalar-pseudoscalar channel. This discrepancy provides an illustrative example of how *Fierz* incompleteness can lead to ambiguities. Even in situations where two different calculations start from an identical *Fierz*-incomplete ansatz, e.g., to derive the beta function of the theory's renormalized couplings, the so-obtained results are usually not unique.

For our studies at finite temperature and chemical potential, as a first step, we shall neglect the running of the renormalization function associated with the fermion chemical potential. For this, we set throughout this work $Z_\mu = 1$. In that case, we find for the running of the scalar-pseudoscalar channel

$$\beta_{\lambda_\sigma} = 2\lambda_\sigma - 16 v_4 \lambda_\sigma^2 \, \mathcal{L}(\tau, \tilde{\mu}_\tau) \,, \tag{3.16}$$

with the temperature- and chemical-potential-dependent function

$$
\begin{aligned}
\mathcal{L}(\tau, \tilde{\mu}_\tau) \;=\; & 3 \left(l_{\perp+}^{(\mathrm{F}),(4)}(\tau, 0, -\mathrm{i}\tilde{\mu}_\tau) + l_{\|+}^{(\mathrm{F}),(4)}(\tau, 0, -\mathrm{i}\tilde{\mu}_\tau) \right) \\
& - l_{\perp\pm}^{(\mathrm{F}),(4)}(\tau, 0, -\mathrm{i}\tilde{\mu}_\tau) - l_{\|\pm}^{(\mathrm{F}),(4)}(\tau, 0, -\mathrm{i}\tilde{\mu}_\tau) \,.
\end{aligned}
\tag{3.17}
$$

The purely fermionic threshold functions $l^{(\mathrm{F}),(4)}$, which correspond to one-loop 1PI diagrams, are defined in App. C. Here, we use again the exponential regularization scheme, which is also discussed in App. C. We further denote the dimensionless temperature by $\tau = T/k$ and the dimensionless chemical potential by $\tilde{\mu}_\tau = \mu/(2\pi T)$. We note that the threshold functions, see Eqs. (C.18)-(C.21), do now depend on the temperature and on the fermion chemical potential. The behavior of the threshold functions under a variation of temperature and chemical potential is essential for the overall dynamics of our thermal NJL model. For this, we shall analyze their influence on the beta functions in more detail at the end of the present section.

In agreement with the one-channel beta function from the previous subsection, we find $\mathcal{L}(0,0) = \frac{1}{2}$ reproducing our result in the vacuum limit Eq. (3.11), as it should be the case. We emphasize again that this would not be possible if we used a spatial regularization scheme. In the next step, we solve Eq. (3.16) analytically, which yields:

$$
\lambda_\sigma(T, \mu, k) = \frac{\lambda_\sigma^{(\mathrm{UV})}}{\left(\frac{\Lambda}{k}\right)^\Theta \left(1 + 4\frac{\lambda_\sigma^{(\mathrm{UV})}}{\lambda_\sigma^*} \mathcal{I}(T, \mu, k)\right)} \,,
\tag{3.18}
$$

with

$$
\mathcal{I}(T, \mu, k) = \frac{1}{\Lambda^2} \int_\Lambda^k \mathrm{d}k' k' \mathcal{L}(\tau', \tilde{\mu}_{\tau'}) \,.
\tag{3.19}
$$

We find for the non-*Gaussian* fixed point $\lambda_\sigma^* = 8\pi^2$, which is again in agreement with our previous vacuum study. As initial conditions for the RG flow equations at finite temperature, we fix the UV value of the scalar-pseudoscalar coupling $\lambda_\sigma^{(\mathrm{UV})}$ so that we reproduce a certain critical temperature at vanishing fermion chemical potential $T_0 = T_{\mathrm{cr}}(\mu = 0)$. To see that the critical temperature and the initial value $\lambda_\sigma^{(\mathrm{UV})}$ are related, let us now define the following necessary condition for spontaneous symmetry breaking at finite temperature and fermion chemical potential:

$$
\lim_{k \to 0} \frac{1}{\lambda_\sigma(T_{\mathrm{cr}}, \mu, k)} = 0 \,.
\tag{3.20}
$$

By using Eq. (3.18), we find from Eq. (3.20) an implicit equation for T_{cr}:

$$
0 = \left(\frac{\lambda_\sigma^*}{\lambda_\sigma^{(\mathrm{UV})}}\right) + 4\,\mathcal{I}(T_{\mathrm{cr}}, \mu, 0) \,.
\tag{3.21}
$$

With Eq. (3.14), we can reformulate Eq. (3.21) to relate the critical scale in the vacuum $k_0 = k_{\mathrm{cr}}(T = 0, \mu = 0)$ and the critical phase transition temperature T_{cr}:

$$
k_0 = \Lambda \left(1 + 4\,\mathcal{I}(T_{\mathrm{cr}}, \mu, 0)\right)^{\frac{1}{\Theta}} \,.
\tag{3.22}
$$

It is clear from our discussion of the one-channel approach in the vacuum that a critical temperature can only be found for $\lambda_\sigma^{(\mathrm{UV})} > \lambda_\sigma^*$.

From Eq. (3.21), we can follow that there exists a one-to-one correspondence between the critical temperature $T_{\mathrm{cr}}(\mu)$ at a given fermion chemical potential and the UV value of the scalar-pseudoscalar channel $\lambda_\sigma^{(\mathrm{UV})}$. Using this
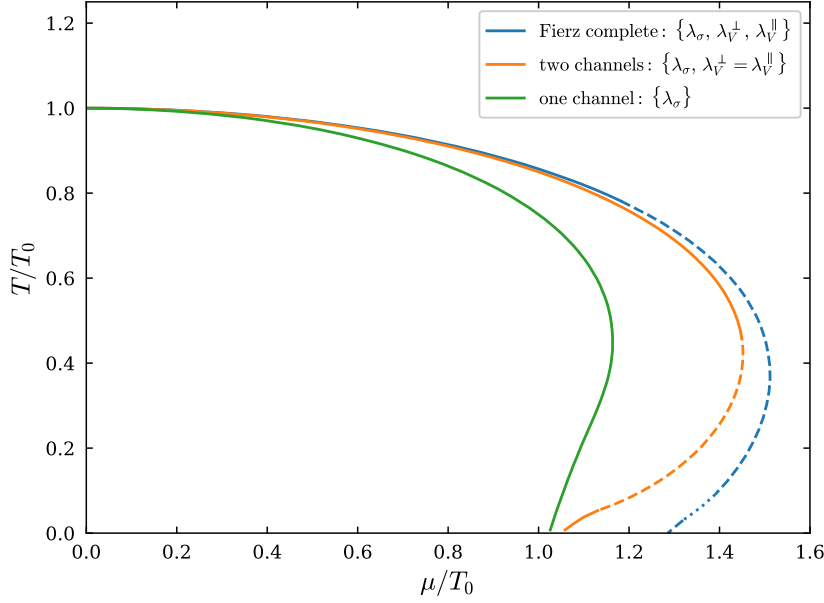
Figure 3.4: Phase boundaries in the (T, μ) plane of our one-flavor and one-color NJL model as it is found from a one-channel (green), two-channel (orange) and *Fierz*-complete ansatz for the effective action, see main text for details.

observation, we can now discuss the scale-fixing procedure for our finite-temperature study where we choose:

$$0 = \left(\frac{\lambda_\sigma^*}{\lambda_\sigma^{(\mathrm{UV})}} \right) + 4\,\mathcal{I}(T_0 = 0.132\Lambda, 0, 0)\,, \tag{3.23}$$

where we use $\Lambda = 1\,\mathrm{GeV}$ as an UV cutoff scale[10] and, therefore, obtain as a critical temperature $T_0 = T_{\mathrm{cr}}(\mu = 0) = 0.132\,\mathrm{GeV}$. Formally, the latter choice is motivated by the critical temperature at vanishing chemical potential found in a recent lattice QCD study [9] considering one massive and two light quark flavors. Recall that we eventually aim at a study of QCD. For an alternative choice for the critical temperature, we refer to the original publication where we used $T_0 = 0.15\,\mathrm{GeV}$. Nevertheless, we find that for both scale-fixing procedures, the qualitative findings remain unchanged. To adjust a critical temperature of $T_{\mathrm{cr}}(\mu = 0) = 0.132\,\mathrm{GeV}$ in our model, we emphasize again that we only tune the $\lambda_\sigma^{(\mathrm{UV})}$ and set all other couplings to zero. The other couplings are then generated dynamically within the RG flow. Note that we use this type of scale fixing in all NJL-type models we study throughout this thesis.

Let us now investigate the phase boundary as it is obtained from a one-channel, a two-channel and a *Fierz*-complete ansatz for the effective action Eq. (3.6). In general, the influence of more than one fermion channel on a beta function can still be explained phenomenologically within the already discussed vacuum picture, see Fig. 3.1. Loosely speaking, the parabola associated with a four-fermion beta function is shifted upwards or downwards in the presence of more than one four-fermion coupling.

In Fig. 3.4 we now present the critical temperature $T_{\mathrm{cr}}(\mu)$ in the (T, μ) plane as obtained from three different truncations. Inside of the depicted curves, we observe that the running four-fermion couplings diverge at a finite critical scale k_{cr} indicating the breakdown of at least one of the symmetries of our model. Outside the phase boundaries, all dimensionless four-fermion couplings tend to zero in the *infrared* limit $\lim_{k \to 0} \lambda_i(k) = 0$ implying that the system remains in a phase with no spontaneously broken symmetry, i.e., no finite gap emerges and the RG flow

---

[10]We have also checked that our results remain unchanged by using RG-consistent larger cutoff scales, see Ref. [276] for a detailed discussion of RG consistency.

in the theory space is dominated by the *Gaussian* fixed point, see Sec. 3.1.1. As indicated in the previous section, we observe that a divergence in one four-fermion channel simultaneously triggers divergences in all other channels.

By comparing the one-channel approximation with our two-channel and *Fierz*-complete three-channel approach, at zero temperature, we find that the phase boundary of our one-channel approximation exhibits a critical fermion chemical potential $\mu_{\mathrm{cr}}/T_0 \approx 1.0$ above no spontaneous symmetry breaking is observed. For the two-channel approach, this critical chemical potential is shifted towards larger values where we find $\mu_{\mathrm{cr}}/T_0 \approx 1.05$. The phase boundary of the *Fierz*-complete ansatz has the largest extent. Here, we observe for the critical fermion chemical potential $\mu_{\mathrm{cr}}/T_0 \approx 1.3$.

Let us now discuss the dominance patterns for the different types of approaches we consider, see Fig. 3.4. By construction, we find for the one-channel ansatz a dominance in the scalar-pseudoscalar channel. For the two-channel approach, we set $\lambda_V^{\parallel} = \lambda_V^{\perp}$ which corresponds to our *Fierz*-complete computation in the vacuum, see also Fig. 3.2. Clearly, the two-channel approximation is still *Fierz* complete at $T = \mu = 0$. We find for $T/T_0 \gtrsim 0.5$ a dominance in the $(S-P)$ channel associated with the breakdown of chiral symmetry. Interestingly, for temperatures $0.5 \gtrsim T/T_0 \gtrsim 0.1$ the dominance pattern changes, now suggesting a vector-like condensate in this regime. The latter condensate indicates that an additional spontaneous breakdown of the *Poincaré* symmetry may be found. Note that this occurs on top of the explicit breaking of *Poincaré* symmetry due to the presence of a finite heat bath and fermion chemical potential. For $T/T_0 \lesssim 0.1$, we find a dominance in the chiral scalar-pseudoscalar channel again. Finally, let us examine the full *Fierz*-complete basis considering all three channels. Here, we encounter a dominance of the $(S - P)$ channel for temperatures $T/T_0 \gtrsim 0.8$. Further, we find in agreement with the two-channel case, a dominance of the $(V_{\parallel})$ and the $(V_{\perp})$ channel. Compared to the two-channel approximation, we observe in the *Fierz*-complete case a significantly larger temperature interval $T/T_0 \lesssim 0.8$ where the vector-type channels appear to be dominant. Over a wide range of the temperature domain, we find that a dominance of the $(V_{\parallel})$ channel associated with a density-type condensate $n \sim \langle \bar{\psi} \mathrm{i} \gamma_0 \psi \rangle$ seems favorable. Only within a small interval of $0.1 \gtrsim T/T_0 \gtrsim 0.02$, we find a dominance of the $(V_{\perp})$ channel. At the end of this analysis, we would like to emphasize again that a dominance in one channel does not necessarily imply that the low-energy regime is governed by the corresponding condensate.

Next, we shall investigate the influence of a different basis set on the phase structure of our model. We shall see that a change of the *Fierz*-complete basis does not alter the phase boundary at all. This is crucial as the particular basis choice should not influence physical observables. The dominance pattern is, however, not unique and can change. In particular, we observe that our presently employed four-fermion basis does not contain a channel which would be sensitive to a possible breakdown of the $U(1)_V$ symmetry. From condensed-matter physics, however, we know that at a sufficiently low temperature and finite chemical potential, a pairing between the interacting fermions of different spin species close to the *Fermi* surface becomes energetically favorable. The associated formation of a BCS-type energy gap [2, 3] in the excitation spectrum is then accompanied with a breakdown of the $U(1)_V$ symmetry. The latter indicates the formation of *Cooper* pairs of two correlated fermions. In Sec. 2.3.4, we already discussed this briefly in case of QCD. There, we argued that the possible pairing mechanisms could be manifold since the quarks also carry more internal degrees as it is the case, e.g., in QED.

To make contact to phenomenology, in the following, we include difermion-type four-fermion channels in our ansatz for the effective action. The difermion condensates, which are possibly created in the *infrared* regime at finite fermion chemical potential, are then indicated by a dominance in the corresponding "four-difermion" channel. As mentioned above, this is then accompanied with a spontaneous breakdown of the $U(1)_V$ symmetry. We use the following ansatz for the effective action:

$$
\begin{aligned}
\Gamma_{\mathrm{LO}}^{(\mathrm{D})}[\bar{\psi}, \psi] \;=\; & \int_0^{\beta} \mathrm{d}\tau \int \mathrm{d}^3 x \left\{ \bar{\psi}(Z^{\parallel}\mathrm{i}\gamma_0\partial_0 + Z^{\perp}\mathrm{i}\gamma_i\partial_i - Z_\mu\mathrm{i}\mu\gamma_0)\psi + \frac{1}{2}\bar{\lambda}_{\mathrm{D},\sigma}\,(S - P) \right. \\
& \left. -\frac{1}{2}\bar{\lambda}_{\mathrm{DSP}}\,(S\mathcal{C} - P\mathcal{C}) - \frac{1}{2}\bar{\lambda}_{\mathrm{D0}}\left(A_{\parallel}\mathcal{C}\right) \right\},
\end{aligned}
\tag{3.24}
$$

where we defined the following abbreviations for the difermion-type four-fermion interaction channels:

$$
\begin{aligned}
(S\mathcal{C} - P\mathcal{C}) &\equiv (\bar{\psi}\mathcal{C}\bar{\psi}^T)(\psi^T\mathcal{C}\psi) - (\bar{\psi}\gamma_5\mathcal{C}\bar{\psi}^T)(\psi^T\mathcal{C}\gamma_5\psi)\,, \\
(A_\parallel\mathcal{C}) &\equiv (\bar{\psi}\gamma_0\gamma_5\mathcal{C}\bar{\psi}^T)(\psi^T\mathcal{C}\gamma_0\gamma_5\psi)\,.
\end{aligned}
\tag{3.25}
$$

The difermion channels above can be computed from the conventional four-fermion channels by employing a particular type of *Fierz* transformation, see Eq. (B.20). Using this, we can map the effective action (3.24) onto our previously studied effective action (3.6), i.e., the difermion-type interaction channels can be assembled from a combination of conventional four-fermion channels. We then find:

$$
\begin{aligned}
\Gamma_{\mathrm{LO}}^{(\mathrm{D})} = \int_0^\beta \mathrm{d}\tau \int \mathrm{d}^3x \Big\{ &\bar{\psi}(Z^\parallel \mathrm{i}\gamma_0\partial_0 + Z^\perp \mathrm{i}\gamma_i\partial_i - Z_\mu \mathrm{i}\mu\gamma_0)\psi \\
&+ \frac{1}{2}\big(\bar{\lambda}_{\mathrm{D},\sigma} + \bar{\lambda}_{\mathrm{DSP}} + \frac{1}{2}\bar{\lambda}_{\mathrm{D0}}\big)(S - P) \\
&- \frac{1}{2}\big(-\bar{\lambda}_{\mathrm{DSP}} - \frac{3}{2}\bar{\lambda}_{\mathrm{D0}}\big)(V_\parallel) \\
&- \frac{1}{2}\big(-\bar{\lambda}_{\mathrm{DSP}} + \frac{1}{2}\bar{\lambda}_{\mathrm{D0}}\big)(V_\perp) \Big\}\,.
\end{aligned}
\tag{3.26}
$$

From this, we read off the transformation rules mapping the new four-fermion couplings to the old ones. This can be written conveniently in a compact matrix notation:

$$
\begin{pmatrix} \bar{\lambda}_\sigma \\ \bar{\lambda}_V^\parallel \\ \bar{\lambda}_V^\perp \end{pmatrix} = \begin{pmatrix} 1 & 1 & \frac{1}{2} \\ 0 & -1 & -\frac{3}{2} \\ 0 & -1 & \frac{1}{2} \end{pmatrix} \begin{pmatrix} \bar{\lambda}_{\mathrm{D},\sigma} \\ \bar{\lambda}_{\mathrm{DSP}} \\ \bar{\lambda}_{\mathrm{D0}} \end{pmatrix}\,.
\tag{3.27}
$$

The matrix above has full rank. The latter is of great importance as it is not necessarily true for *Fierz*-incomplete basis types. In the next step, we invert the matrix and use it to find the new beta functions associated with our difermion-type four-fermion basis:

$$
\begin{pmatrix} \beta_{\lambda_{\mathrm{D},\sigma}} \\ \beta_{\lambda_{\mathrm{DSP}}} \\ \beta_{\lambda_{\mathrm{D0}}} \end{pmatrix} = \begin{pmatrix} 1 & \frac{1}{2} & \frac{1}{2} \\ 0 & -\frac{1}{4} & -\frac{3}{4} \\ 0 & -\frac{1}{2} & \frac{1}{2} \end{pmatrix} \begin{pmatrix} \beta_{\lambda_\sigma} \\ \beta_{\lambda_V^\parallel} \\ \beta_{\lambda_V^\perp} \end{pmatrix}\,.
\tag{3.28}
$$

Using the new parameterization for our *Fierz*-complete four-fermion basis in our ansatz, we may now check more directly for possible difermion condensates indicating a BCS-type ground state by studying the fate of the $U(1)_V$ symmetry in the *infrared* regime. For example, a dominance in the $(A_\parallel\mathcal{C})$ may now indicate the formation of a condensate $\langle\psi^T\mathcal{C}\gamma_0\gamma_5\psi\rangle$ with positive parity breaking $U(1)_V$ but leaving $U(1)_A$ intact. Moreover, the channel also breaks the *Poincaré* symmetry explicitly. Further, the condensate $\langle\psi^T\mathcal{C}\gamma_5\psi\rangle$ corresponding to the $(S\mathcal{C} - P\mathcal{C})$ channel would be a $J^P = 0^+$ state breaking both, the $U(1)_V$ as well as the chiral $U(1)_A$ symmetry. We stress that the ansatz (3.24) is not more general as it is related to ansatz (3.6) by means of *Fierz* transformations. Our present considerations do only make obvious that a spontaneous breaking of the $U(1)_V$ symmetry could be less visible in the ansatz (3.6) as it would be indicated by a simultaneous dominance in more than one channel, namely in $(V_\parallel)$ and $(V_\perp)$ according to Eq. (3.27).

Let us now discuss the different symmetry breaking patterns by employing the new difermion-type ansatz (3.24) and study the phase boundaries as obtained from a one-channel, two-channel and *Fierz*-complete approximation, see Fig. 3.5. In analogy to our previous study, we deduce the one- and two-channel beta functions by setting all other four-fermion couplings to zero by hand (see our discussion Sec. 3.1.1). Again, we begin with the one-channel ap-
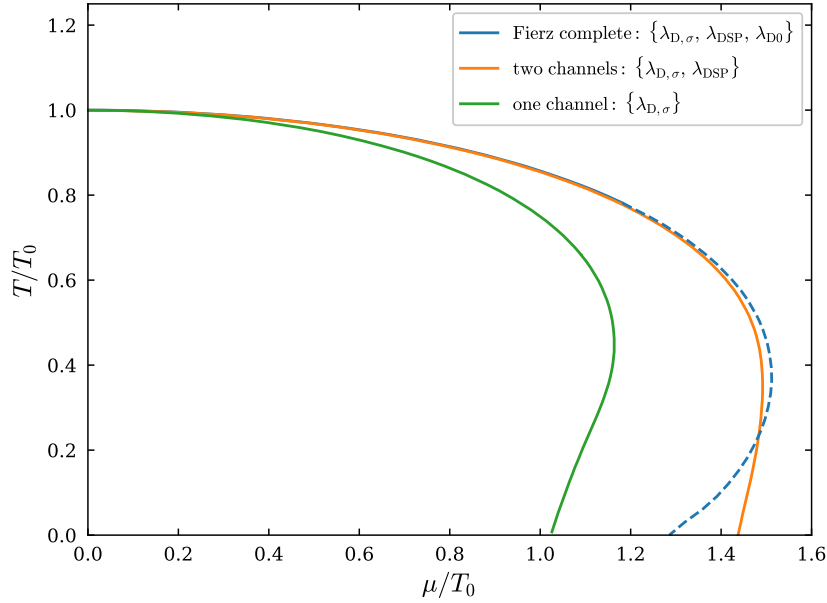
Figure 3.5: We show the phase boundary of the NJL model in the (T, μ) plane using a difermion-type parameterization (3.24). We compare the critical temperatures as it is found from a one-channel (green), a two-channel (orange) and a *Fierz*-complete ansatz. Note that the phase boundary of the *Fierz*-complete study is identical to the one presented in Fig. 3.4 as it should be.

proximation. Here, the phase diagram does not change at all as it can be readily seen from the first row in Eq. (3.27). For our two-channel ansatz, however, we find a qualitative change of the phase boundary. For two channels, we now locate the critical chemical potential above which no spontaneous symmetry breaking of any kind occurs beyond the critical chemical potential associated with the *Fierz*-complete truncation. For the previously used two-channel approximation, this was not the case. Of great importance is the observation that the phase boundary associated with the difermion-type *Fierz*-complete basis is identical to the phase boundary as obtained from our previously employed *Fierz*-complete ansatz Eq. (3.6). This underscores the essential property of *Fierz*-complete basis sets for which physical observables such as the critical temperature $T_{\mathrm{cr}}(\mu)$ are unique and independent of the individual basis choice. For instance, that this is not true for a *Fierz*-incomplete ansatz, can be readily seen for the two-channel truncations. Both, the shape of the phase boundary and the dominance pattern are altered considerably.

A more detailed analysis of the dominance pattern underlying our two-channel and three-channel difermion-type ansätze reveals several differences compared to our previous study, at least for large chemical potential. By considering only two channels, we find that close to the phase boundary, the entire phase diagram is dominated by the $(S - P)$ channel associated with the breakdown of the chiral $U(1)_A$ symmetry. For our *Fierz*-complete three-channel ansatz, we find again more than a single dominance. In the temperature range $1 \gtrsim T/T_0 \gtrsim 0.8$, we observe a dominance of the chiral $(S - P)$ channel in accordance to our findings from our previously discussed *Fierz*-complete ansatz (3.6). On the other hand, in the temperature region $0.8 \gtrsim T/T_0$, we find that the $(A_{\parallel} \mathcal{C})$ channel becomes dominant. The formation of a ground state associated with the $(A_{\parallel} \mathcal{C})$ channel would then break the $U(1)_V$ symmetry spontaneously. Therefore, from the dominance patter of the difermion-type basis choice Eq. (3.24), we indeed find some indications for the formation of *Cooper*-type pairs at large fermion chemical potentials $\mu/T_0 \gtrsim 1.2$.

Let us briefly summarize our observations as obtained from both approaches, see Eqs. (3.6) and (3.24). We begin with the general comment that both basis sets are complete with respect to *Fierz* transformations. A very impressive confirmation of this statement is that both phase boundaries obtained from the different approaches are in perfect

agreement. Using the pointlike limit, we may not be entirely sure about the type of forming condensates in the *infrared*. Nevertheless, as we independently observe a dominance in the $(S - P)$ channel for a temperature range of $1 \gtrsim T/T_0 \gtrsim 0.8$ and chemical potentials $\mu/T_0 \lesssim 1.2$ in both parametrizations, we may carefully conclude that the low-energy physics is dominated by chiral degrees of freedom. For both *Fierz*-complete ansätze, we moreover find a transition of the dominance pattern from a domain presumably governed by spontaneous chiral symmetry breaking, to a region $T/T_0 \lesssim 0.8$ which is potentially dominated by other types of symmetry breaking mechanisms. The observed dominance of the $(A_\parallel \mathcal{C})$-type four-fermion channel suggests that this regime in the (T, μ) plane could be rather governed by difermion-type degrees of freedom. The corresponding condensate would then spontaneously break the *Poincaré* as well as the $U(1)_V$ symmetry of our theory. Note that this should also leaves its imprint in a BCS-type scaling behavior [32] of the critical scale k_{cr} as a function of the fermion chemical potential, see our discussion in Ref. [116]. In this case, we would expect at zero temperature that the phase boundary would extend to arbitrary large values of the chemical potential which we do not observe in our study. Therefore, a final answer to that question lies beyond the scope of the present work and shall be postponed to future studies.

Finally, let us discuss the impact of the threshold functions Eqs. (C.18)-(C.21) computed within our four-dimensional regularization scheme on the underlying fixed-point structure. The threshold functions can be related to one-loop diagrams and depend on the temperature and the fermion chemical potential. Qualitatively, their role can be understood best, by considering a simple one-channel beta function. For this, we investigate the underlying fixed-point dynamics and examine the influence of the threshold function on the expected shape of the phase diagram. In the following, we shall distinguish threshold functions of the $l_+^{(\mathrm{F})}$ (Eqs. (C.18) and (C.19)) from those of the $l_\pm^{(\mathrm{F})}$ (Eqs. (C.20) and (C.21)) type. For the former type of threshold function, the fermion chemical potential appears with a positive sign $+\mathrm{i}\mu$ in each denominator of the propagator structures. For threshold functions of the $l_\pm^{(\mathrm{F})}$ type, however, the chemical potential appears in one denominator of the propagator with a positive $+\mathrm{i}\mu$ and in the other one with a negative $-\mathrm{i}\mu$ sign. In fact, under a variation of the fermionic chemical potential, we find that threshold functions of the $l_+^{(\mathrm{F})}$ type behave very differently compared to those of the $l_\pm^{(\mathrm{F})}$ type as we shall demonstrate below.

Let us now assume that only a $l_+^{(\mathrm{F})}$-type threshold function is present in the one-channel beta function. In this case, we find

$$\partial_t \lambda = 2\lambda - c_+ l_+^{(\mathrm{F})} \lambda^2 \, . \tag{3.29}$$

Here, we assume, without loss of generality, that $c_+ > 0$. We can now draw the corresponding parabola of the beta function (3.29), see the solid black curve on the left-hand-side in Fig. 3.6. As we have already discussed before, we find a *Gaussian* fixed point (black dot) and a non-trivial non-*Gaussian* fixed point λ^* (blue dot). At finite temperature or fermion chemical potential, the vacuum fixed points then turn into pseudo fixed points. For instance, at finite temperature, one can show that

$$l_+^{(\mathrm{F})} \to 0 \quad \text{for} \quad \frac{T}{k} \gg 1 \, . \tag{3.30}$$

This is a consequence of a screening effect due to the finite thermal *Matsubara* mass $\sim T$. For temperatures larger than the RG scale k, the thermal mass suppresses all types of quantum fluctuations, i.e., loop contributions like $\propto \lambda^2$ vanish for $T \gg k$, see Eq. (3.29). This situation is shown on the left-hand side of Fig. 3.6 (red curve) where we show that the pseudo fixed point (blue) drifts towards infinity $\lambda^* \to \infty$ for $T/k \to \infty$. From this, it follows that if one has chosen a starting value for the coupling λ larger than the fixed point $\lambda^{(\mathrm{UV})} > \lambda^*(T = 0)$ so that the system is governed by spontaneous symmetry breaking at zero temperature, then, by increasing the temperature, there exists a value so that the pseudo fixed point becomes larger than the UV initial value $\lambda^{(\mathrm{UV})} \lesssim \lambda^*(T = T_{\mathrm{cr}})$. Eventually, the system is again dominated by the *Gaussian* fixed point and remains in the symmetric phase. Indeed, we also
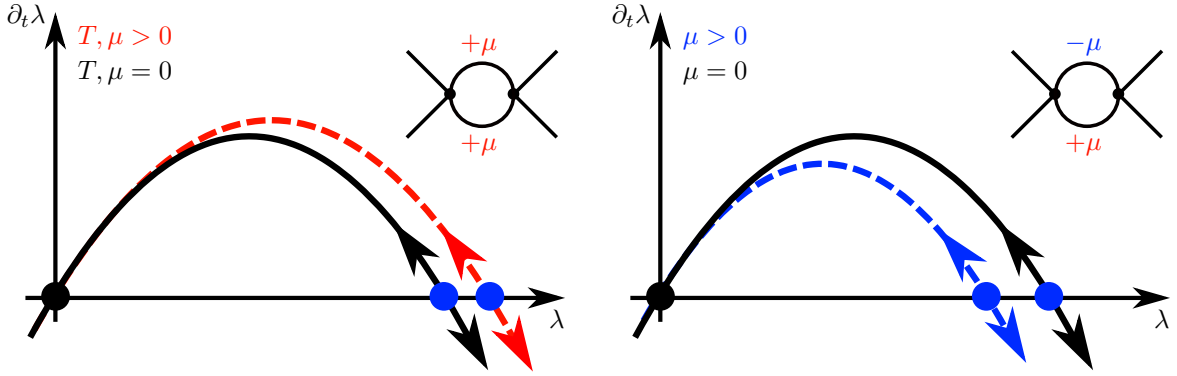
Figure 3.6: Illustration of a one-channel beta function for the special case that it is only governed by $l_+^{(F)}$-type (left) or $l_\pm^{(F)}$-type threshold functions (right). For threshold functions of the $l_+^{(F)}$ type, we find that the non-*Gaussian* fixed point is shifted towards infinity $\lambda^* \to \infty$, by independently increasing the temperature or the fermion chemical potential. In case the one-channel beta function is governed by $l_\pm^{(F)}$-type diagrams, at vanishing temperature, the non-*Gaussian* fixed point drifts towards the *Gaussian* fixed point and merges with the latter in the limit $\mu/k \to \infty$, see main text for details. In this case, any finite value for $\lambda^{(UV)} \gtrsim 0$ suffices to drive the system towards criticality.

find a similar screening behavior for the fermion chemical potential:

$$l_+^{(F)} \to 0 \quad \text{for} \quad \frac{\mu}{k} \gg 1 \,. \tag{3.31}$$

Alone from these considerations, we can conclude that the phase diagram of a four-fermion theory only dominated by diagrams of the $l_+^{(F)}$ type have both, a critical temperature $T_{cr}(\mu)$ and a critical fermion chemical potential at zero temperature μ_{cr} above which no spontaneous symmetry breaking occurs.

We now discuss our second type of diagrams. Again, we assume that only $l_\pm^{(F)}$-type diagrams enter a one-channel beta function of the form

$$\partial_t \lambda = 2\lambda - c_\pm l_\pm^{(F)} \lambda^2 \,, \tag{3.32}$$

with the positive constant $c_\pm$. We begin again with the behavior of the fixed points under a variation of the temperature. As it was the case for the $l_+^{(F)}$-type threshold functions, we observe a thermal screening behavior in the limit of temperatures larger than the RG scale:

$$l_\pm^{(F)} \to 0 \quad \text{for} \quad \frac{T}{k} \gg 1 \,. \tag{3.33}$$

This is not too surprising since the *Matsubara* modes in the propagator structures of $l_\pm^{(F)}$-type threshold functions appear in a similar way as it is the case for threshold functions of the $l_+^{(F)}$ types, see Eqs. (C.18)-(C.21). The more interesting observation can be made at zero temperature and finite fermion chemical potential. Here, we find

$$l_\pm^{(F)} \sim \left(\frac{\mu}{k}\right)^2 \quad \text{for} \quad \frac{\mu}{k} \gg 1 \,. \tag{3.34}$$

On the right-hand side of Fig. 3.6, we show the behavior of the parabola at zero temperature and finite chemical potential (dashed blue curve) compared to the vacuum case (solid black curve). By increasing the fermion chemical potential, the pseudo fixed point "moves" towards the *Gaussian* fixed point and merges with the latter for $\mu/k \to \infty$. At the same time, we find $l_\pm^{(F)} \sim (\mu/k)^2$. We now observe at finite chemical potential and zero temperature that the fermion loops are antiscreened so that the quadratic part $\propto \lambda^2$ of Eq. 3.32 dominates the beta function. For a theory only governed by $l_\pm^{(F)}$-type diagrams, a critical chemical potential at zero temperature μ_{cr} does not exist.

The fact that the *Gaussian* and the non-*Gaussian* fixed point merge in case $\mu/k \to \infty$, can be related to the famous *Cooper* instability [1]: For all $\lambda^{(\mathrm{UV})} > 0$, we have $\lambda^{(\mathrm{UV})} > \lambda^*(\mu \to \infty)$. We then find a diverging four-fermion coupling λ at a critical scale k_{cr} for any $\lambda^{(\mathrm{UV})} > 0$. The latter observation perfectly fits in the picture of BCS theory. Here, it is favorable for weakly-interacting fermions "sitting" on the *Fermi* surface to form *Cooper* pairs. In this case, the *Fermi* surface becomes unstable, which leads to a gapped energy spectrum [2, 3]. We add that the formation of a BCS-type gap also leaves its imprint in the scaling behavior of physical observables such as the critical scale, see Ref. [116, 228] for a detailed discussion.

Due to the thermal *Matsubara* mass for high temperatures $T \gg k$, we found that both, the $l_{\pm}^{(\mathrm{F})}$-type as well as the $l_{+}^{(\mathrm{F})}$-type threshold functions show a screening effect so that loop contributions are suppressed. From this, we conclude that we can always find a critical temperature T_{cr}, above which no spontaneous symmetry breaking is observed. Nevertheless, the RG flow is, in general, governed by a competition between all four-fermion couplings where all kinds of threshold functions are involved simultaneously. It is, therefore, by no means clear that the phase diagram exhibits a critical chemical potential at zero temperature μ_{cr} as we found it in our study, see, e.g., Fig. 3.4. Indeed, we shall see in the second NJL model study in Sec. 3.2 that a μ_{cr} is not observed.

3.1.3   Spatial Regularization

We end the present NJL model study, by discussing to what extent the particular choice of the regularization scheme can change our findings. For this, we employ in the present subsection a so-called spatial regulator for the NJL model, see Eqs. (C.25)-(C.28) for the so-derived threshold functions.

Let us start with the discussion in the limit of vanishing temperature and fermion chemical potential. For consistency, a proper regularization scheme should recover the correct vacuum limit of a given theory for $T \to 0$ and $\mu \to 0$, see Eq. (3.9) and (3.10). For the four-dimensional regularization scheme, we employ throughout this work, the requirement above can readily be verified for our *Fermi*-surface-adapted regulator Eq. (C.2). In the vacuum limit, the latter then turns into the usual four-dimensional exponential regulator [289, 290]. From this, it is straightforward to show that the beta functions at finite temperature and chemical potential Eqs. (E.1)-(E.3) can be reduced to the vacuum limit. For details on our *Fermi*-surface-adapted regulator, we refer to App. C and Refs. [116, 159].

The spatial regulator (C.6), however, breaks the *Poincaré* symmetry even at $T = \mu = 0$. In particular, we find different beta functions for the couplings $\lambda_V^{\parallel}$ and $\lambda_V^{\perp}$ even at zero temperature and fermion chemical potential. In Fig. 3.7, we show the phase boundaries in the (T, μ) plane for our one-flavor and one-color NJL-type model as obtained by employing a *Fermi*-surface-adapted shape function (C.2) in gray and the spatial regulator (C.6) in blue. Using a non-*covariant* regulator, we notice that the phase boundary changes significantly. For example, in contrast to our study using a *covariant* regularization scheme, we cannot observe a critical chemical potential μ_{cr} at zero temperature. Indeed, the vanishing of μ_{cr} can be traced back to the use of the three-dimensional regulator.

The use of a spatial regulator further alters the observed dominance pattern considerably. By employing the *Fermi*-surface-adapted regularization scheme, we find a dominance of the $(S - P)$ channel for $1 \gtrsim T/T_0 \gtrsim 0.8$, indicating the formation of a finite chiral condensate. In Fig. 3.7, we find for the spatial regulator within the same temperature domain a dominance of the $(V_{\parallel})$ channel. The latter would indicate the onset of the formation of a vector condensate with a density-type order parameter $\langle \bar{\psi} \gamma_0 \psi \rangle$. Even more, we encounter a dominance of the $(V_{\parallel})$ channel already in the limit of vanishing chemical potential $\mu = 0$. Using our *covariant* regularization scheme, however, we observe a clear dominance of the $(S - P)$ channel. This example is of importance as it shows how non-*covariant* regularization schemes can considerably spoil the phenomenological interpretation of results already at vanishing chemical potential. Using the spatial regulator, we find for larger chemical potential $\mu/T_0 \gtrsim 1.5$, a transition from a regime which is dominated by the $(V_{\parallel})$ channel towards a regime dominated by the $(V_{\perp})$ channel. However, we never observe a dominance of the $(S - P)$ channel.

For the threshold functions Eqs. (C.25)-(C.28), we further notice some issues from a mathematical point of view. By considering the zero temperature limit $T \to 0$ of the spatially regularized threshold functions, we observe
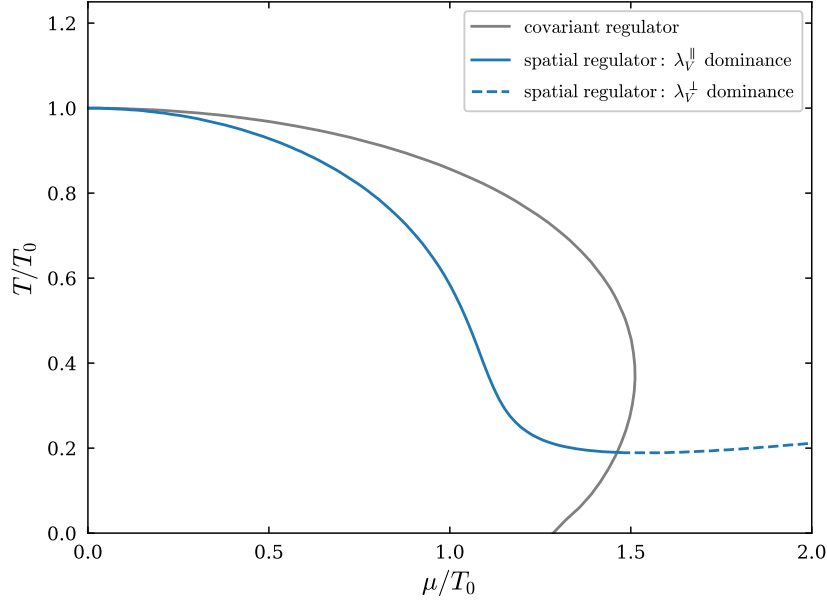
Figure 3.7: Phase boundaries of the *Fierz*-complete NJL model study with one flavor and one color in the (T, μ) plane as it is obtained by using a *covariant Fermi*-surface adapted regulator Eq. (C.2) (gray line) and from a *Fierz*-complete study considering a *Poincaré*-breaking spatial regulator Eq. (C.6) (blue line). A spatial regulator significantly alters the shape and the observed dominances of the phase boundary, see Sec. 3.1.3 for details.

a second-order pole at $\mu/k = 1$. The latter then leads to "spurious" divergences in the integration of the RG flow. As it turns out, the spatially regularized threshold functions do not exhibit a consistent zero temperature limit for any non-zero chemical potential. Only the limit $\mu \to 0$ and $T \to 0$ exists. However, we emphasize that even at $T = \mu = 0$, the vacuum beta functions cannot be reproduced by employing the three-dimensional spatial regulator, see our discussion above.

We emphasize that our *Fermi*-surface-adapted regularization scheme (C.2) is also not free of problems. For instance, our four-dimensional regulator breaks the *Silver-Blaze* symmetry of QFT's at finite chemical potential, see Ref. [285]. Briefly speaking, at zero temperature, the *Silver-Blaze* property requires that for all chemical potentials smaller than the theory's pole mass $\mu < m_f$ all physical observables are invariant under a variation of μ. Note that m_f denotes the dynamically generated fermion mass. To understand this, one may think of the excitation spectrum of our theory. Here, the chemical potential has to exceed a certain critical value (the fermion mass) so that particles can be generated. Only then it is possible that physical observables depend on the chemical potential. We find that our four-dimensional regularization scheme does not fulfill the *Silver-Blaze* property. The reason is that our *Fermi*-surface-adapted regulator introduces artificial poles in the momentum structure of the propagator, spoiling the *Silver-Blaze* symmetry as a consequence. In our case, we therefore find a mild modification for $\mu < m_f$ of, e.g., the critical scale k_{cr}, for any finite value of the chemical potential, see Ref. [116] for a discussion.

We end this subsection with a short summary. We discussed in Sec. 2.2 some convenient requirements a regulator at finite temperature and chemical potential should fulfill, see (iv)-(vii), see p. 23. We notice that the spatial regularization scheme violates the requirement that it should preserve *Poincaré* invariance in the limit of vanishing temperature and fermion chemical potential (v). Further, it also violates requirement (vii) meaning that the temporal direction remains unregularized. Moreover, the considered spatial regulator introduces artificial divergences in the scale integrations. We find that this cumulates in a significantly changed shape of the phase boundary. Furthermore, at vanishing fermion chemical potential the dominance pattern now rather suggests a vector-type than a chiral condensate.

3.2   Nambu–Jona-Lasinio: Two Flavors and Three Colors

Based on our work in Ref. [117], we now study the phase boundary of a two-flavor and N_c-color NJL model at finite temperature and quark chemical potential[11]. The two-flavor NJL model we investigate in the present section shares many properties with two-flavor QCD, e.g., it also obeys a two-flavor $SU(2)_L \times SU(2)_R$ symmetry, which can break spontaneously, see our discussion in Sec. 2.3.2. Therefore, to explore the phase diagram of the NJL model at finite temperature and quark chemical potential, we consider a *Fierz*-complete set of four-fermion interactions which enter our ansatz for the effective averaged action. Working along the lines of our one-flavor and one-color NJL model study from the previous section, we then analyze the fixed-point structure and discuss the symmetry breaking patterns in the (T, μ) plane, see Sec. 2.3.4.

The *Fierz*-complete basis we consider at finite temperature and quark chemical potential obeys a global $SU(N_c) \times SU(2)_L \times SU(2)_R \times U(1)_V$ symmetry and is composed of ten different four-quark interaction channels. At the same time, we observe that a *Fierz*-complete four-quark basis, which is also invariant under $U(1)_A$ transformations, is assembled from eight linearly-independent basis elements. Using this observation, we identify within our ten-channel *Fierz*-complete basis a four-dimensional $U(1)_A$-breaking subspace from which we can deduce two sum rules. We then find that both sum rules are fulfilled exactly if the axial $U(1)_A$ symmetry is preserved. In our study, we further consider a *Fierz*-incomplete one-channel and two-channel approach to study the impact of *Fierz* incompleteness on the phase boundary at finite temperature and quark chemical potential. Furthermore, we analyze the dominance pattern of our running four-quark couplings close to the phase boundary to study the nature of the condensates which are possibly formed in the *infrared* regime.

In a separate study, we further investigate a *Fierz*-incomplete two-channel ansatz which is motivated by the observed dominance patterns at finite temperature and quark chemical potential from the *Fierz*-complete approach. As it turns out, we expect chiral degrees of freedom to be dominant at low quark chemical potential where we expect diquark degrees of freedom to become dominant at large quark chemical potential. For our *Fierz*-incomplete two-channel approach, we then analyze the fixed-point structure and study the pseudo fixed-point dynamics by varying the dimensionless temperature or chemical potential in Sec. 3.2.2. In this context, we deduce from the observed pseudo fixed-point structure a possible mechanism, which allows for a dynamical transition from chiral to diquark degrees of freedom by increasing the chemical potential.

We start with the classical action S underlying our two-flavor and N_c-color NJL model:

$$S[\bar{\psi}, \psi] = \int_0^\beta \mathrm{d}\tau \int \mathrm{d}^3 x \left\{ \bar{\psi} \left(\mathrm{i}\slashed{\partial} - \mathrm{i}\mu\gamma_0 \right) \psi + \frac{1}{2}\bar{\lambda}_{(\sigma\text{-}\pi)} \left[\left(\bar{\psi}\psi \right)^2 - \left(\bar{\psi}\gamma_5\tau_i\psi \right)^2 \right] \right\}, \qquad (3.35)$$

with the inverse temperature $\beta = 1/T$ and the quark chemical potential μ. We note that the model corresponds to the one we have already considered in the vacuum to discuss spontaneous chiral symmetry breaking, see Sec. 2.3.2. The classical action (3.35) obeys a global chiral $SU(2)_L \times SU(2)_R \times U(1)_V$ and a global $SU(N_c)$ color symmetry. We already mentioned that we mostly consider $N_c = 3$ which correspond to QCD. Nevertheless, we shall also discuss some key properties if the large-N_c limit is considered, see our discussion below.

Recall that the scalar-pseudoscalar channel in the classical action serves as an order parameter for spontaneous chiral symmetry breaking. This follows from the fact that the scalar-pseudoscalar channel is related to the bosonic composite fields $\langle \bar{\psi}\psi \rangle \sim \sigma$ and $\langle \bar{\psi}\gamma_5\tau_i\psi \rangle \sim \pi_i$ which can be readily seen by performing a *Hubbard-Stratonovich* transformation, see our discussion in Sec. 2.3.2. For $\langle \bar{\psi}\psi \rangle = 0$, chiral symmetry remains intact where a non-vanishing expectation value $\langle \bar{\psi}\psi \rangle \neq 0$ indicates that the chiral symmetry is spontaneously broken. We know from the criterion defined in Eq. (2.78) that the onset of spontaneous (chiral) symmetry breaking is still indicated by a diverging four-fermion coupling. For details, we refer to Secs. 2.3.2 and 3.1.

Let us now discuss some particular four-quark channels we shall consider in our *Fierz*-complete study below. We begin with the remark that the scalar-pseudoscalar channel in (3.35) breaks the axial $U(1)_A$ symmetry explicitly.

---

[11]We mostly consider $N_c = 3$ as it is the case in QCD. For a detailed large-N_c study, we refer to the original work, see Ref. [117]

Therefore, we note that the influence of the $U(1)_A$ anomaly can be absorbed in the scalar-pseudoscalar channel at the level of the classical action (3.35), see Ref. [27] for a review. However, we can "repair" the axial $U(1)_A$ symmetry by considering the following four-quark channel:

$$\sim \det\left(\bar{\psi}(1+\gamma_5)\psi\right) + \det\left(\bar{\psi}(1-\gamma_5)\psi\right) , \qquad (3.36)$$

where the determinant is defined in flavor space. Four-quark structures like Eq. (3.36) can be deduced from the topologically non-trivial vacuum structure in QCD, which is responsible for the violation of the axial $U(1)_A$ symmetry, see our discussion in Sec. 2.3.2 and Refs. [194, 215, 291–293] for details. In our *Fierz*-complete basis, we also consider a four-quark structure like (3.36) which then serves as a convenient control parameter for the instanton-induced axial $U(1)_A$ breaking. From this, we may also study the influence of a restored $U(1)_A$ symmetry on physical observables like the critical temperature.

From our discussion in Sec. 2.3.4, we shall further include a diquark-type four-quark channel in the *Fierz*-complete basis. Model studies suggest that at large chemical potentials, diquark degrees of freedom may become important. As a consequence, we also include a four-quark channel associated with the formation of a 2SC-type diquark [32, 33, 42, 43] condensate, see Eq. (2.88). A dominance of the associated four-quark channel then suggests the onset of a spontaneous breakdown of the $U(1)_V$ symmetry. Moreover, we further note that the formation of a finite diquark condensate δ^l is also accompanied by a spontaneous breakdown of the (global) color $SU(3)$ symmetry, see Refs. [36–39]. We add that a δ^l-type condensate preserves the chiral $SU(2)_L \times SU(2)_R$ symmetry, see Ref. [277].

In analogy to our study in the previous section, because of the external heat bath and the finite quark chemical potential, the *Poincaré* symmetry and the charge conjugation invariance are broken explicitly, see Sec. 3.1 for a detailed discussion. We consider the following ansatz for the effective average action, which we use to study the two-flavor and N_c-color NJL model at finite temperature and quark chemical potential:

$$\Gamma_{\text{LO}}[\bar{\psi}, \psi] = \int_0^\beta \mathrm{d}\tau \int \mathrm{d}^3x \left\{ \bar{\psi}\left(Z^{\parallel}\mathrm{i}\gamma_0\partial_0 + Z^{\perp}\mathrm{i}\gamma_i\partial_i - Z_\mu\mathrm{i}\mu\gamma_0\right)\psi + \frac{1}{2}\sum_{j\in\mathcal{B}} Z_j\bar{\lambda}_j\,\mathcal{L}_j \right\}, \quad (3.37)$$

where $Z^{\parallel}$ and $Z^{\perp}$ are associated with the temporal and spatial components of the wave-function renormalizations corresponding to the fermion fields. Moreover, the renormalization function Z_μ corresponds to the quark chemical potential μ, see Sec. 3.1 for details. The leading order of the derivative expansion implies again that we treat the four-quark correlation functions in the pointlike limit (2.81). It is then clear from our discussion in the previous section that the wave-function renormalizations $Z^{\parallel} = Z^{\perp} = 1$ remain constant for any value of k.

The *Fierz*-complete basis $\mathcal{B}$ is composed of the four-quark tensor structures denoted by $\mathcal{L}_i$, which are accompanied by a bare coupling $\bar{\lambda}_i$ and a vertex renormalization Z_i. For the renormalization of the four-quark couplings, we refer to Eq. (3.7). The *Fierz*-complete basis associated with a global $SU(N_c) \times SU(2)_L \times SU(2)_R \times U(1)_V$ symmetry has ten basis elements. From these ten channels, we have six which are invariant under global $SU(N_c) \times SU(2)_L \times SU(2)_R \times U(1)_V \times U(1)_A$ transformations:

$$\mathcal{L}_{(V+A)_{\parallel}} = \left(\bar{\psi}\gamma_0\psi\right)^2 + \left(\bar{\psi}\mathrm{i}\gamma_0\gamma_5\psi\right)^2 , \qquad (3.38)$$

$$\mathcal{L}_{(V+A)_{\perp}} = \left(\bar{\psi}\gamma_i\psi\right)^2 + \left(\bar{\psi}\mathrm{i}\gamma_i\gamma_5\psi\right)^2 , \qquad (3.39)$$

$$\mathcal{L}_{(V-A)_{\parallel}} = \left(\bar{\psi}\gamma_0\psi\right)^2 - \left(\bar{\psi}\mathrm{i}\gamma_0\gamma_5\psi\right)^2 , \qquad (3.40)$$

$$\mathcal{L}_{(V-A)_{\perp}} = \left(\bar{\psi}\gamma_i\psi\right)^2 - \left(\bar{\psi}\mathrm{i}\gamma_i\gamma_5\psi\right)^2 , \qquad (3.41)$$

$$\mathcal{L}_{(V+A)_{\parallel}}^{\text{adj}} = \left(\bar{\psi}\gamma_0 T^a\psi\right)^2 + \left(\bar{\psi}\mathrm{i}\gamma_0\gamma_5 T^a\psi\right)^2 , \qquad (3.42)$$

$$\mathcal{L}_{(V-A)_{\perp}}^{\text{adj}} = \left(\bar{\psi}\gamma_i T^a\psi\right)^2 - \left(\bar{\psi}\mathrm{i}\gamma_i\gamma_5 T^a\psi\right)^2 . \qquad (3.43)$$

The remaining four channels are invariant under $SU(N_c) \times SU(2)_L \times SU(2)_R \times U(1)_V$ transformations but break the axial $U(1)_A$ symmetry explicitly to include the effects from the chiral *Adler-Bell-Jackiw*-type anomaly in our ansatz for the effective action:

$$
\mathcal{L}_{(\sigma\text{-}\pi)} = (\bar{\psi}\psi)^2 - (\bar{\psi}\gamma_5\tau_i\psi)^2 , \tag{3.44}
$$

$$
\mathcal{L}_{(S+P)_-} = (\bar{\psi}\psi)^2 - (\bar{\psi}\gamma_5\tau_i\psi)^2 + (\bar{\psi}\gamma_5\psi)^2 - (\bar{\psi}\tau_i\psi)^2 , \tag{3.45}
$$

$$
\mathcal{L}_{\text{csc}} = 4\,(\mathrm{i}\bar{\psi}\gamma_5\tau_2\,T^A\psi^C)\,(\mathrm{i}\bar{\psi}^C\gamma_5\tau_2\,T^A\psi) , \tag{3.46}
$$

$$
\mathcal{L}_{(S+P)_-^{\text{adj}}} = (\bar{\psi}T^a\psi)^2 - (\bar{\psi}\gamma_5\tau_i T^a\psi)^2 + (\bar{\psi}\gamma_5 T^a\psi)^2 - (\bar{\psi}\tau_i T^a\psi)^2 , \tag{3.47}
$$

where, e.g., $(\bar{\psi}\gamma_5\tau_i\psi)^2 \equiv (\bar{\psi}\gamma_5\tau_i\psi)(\bar{\psi}\gamma_5\tau_i\psi)$ and the T^a's denote the generators of $SU(N_c)$. Further, the τ_i are the three *Pauli* matrices which are related to the generators of the $SU(2)$ group. Note also that the group generators with capital index, e.g., the generators T^A, belong to the antisymmetric subspace of the $SU(3)$ *Lie* group in the fundamental representation. The $SU(3)$ generators are represented by the eight *Gell-Mann* matrices, where the three antisymmetric generators are conventionally given by $A \in \{2, 5, 7\}$. We emphasize that the choice of the *Fierz*-complete basis is not unique and motivated by phenomenological considerations. Since we wish to investigate spontaneous chiral symmetry breaking, it is reasonable to include a scalar-pseudoscalar $\mathcal{L}_{(\sigma\text{-}\pi)}$ channel in our approach. As discussed, we also have a determinant-type channel $\mathcal{L}_{(S+P)_-}$ in our ansatz to study the impact of the chiral anomaly on the phase structure. To be further sensitive to the formation of possible diquark condensates at large quark chemical potential, we also consider the channel $\mathcal{L}_{\text{csc}}$.

As mentioned in beginning, the basis Eqs. (3.38)-(3.47) is *Fierz*-complete by assuming that $U(1)_A$ is anomalously broken in the UV. However, the basis is overcomplete if we assume that the $U(1)_A$ symmetry is intact. Then, it turns out that a *Fierz*-complete basis at finite temperature and chemical potential in case of a restored axial symmetry is given by eight linearly-independent channels. In this case, it is clear that the $U(1)_A$-breaking subspace is reducible by means of *Fierz* identities to construct axially symmetric four-quark channels such as

$$
\mathcal{L}_{(S-P)_+} = (\bar{\psi}\psi)^2 - (\bar{\psi}\gamma_5\tau_i\psi)^2 - (\bar{\psi}\gamma_5\psi)^2 + (\bar{\psi}\tau_i\psi)^2 . \tag{3.48}
$$

From the considerations above, we derive two sum rules for the four-quark couplings associated with the four-quark channels in the $U(1)_A$-breaking subspace:

$$
\mathcal{S}_{U(1)_A}^{(1)} = \bar{\lambda}_{\text{csc}} + \bar{\lambda}_{(S+P)_-^{\text{adj}}} = 0 , \tag{3.49}
$$

$$
\mathcal{S}_{U(1)_A}^{(2)} = \bar{\lambda}_{(S+P)_-} - \frac{N_c - 1}{2N_c}\bar{\lambda}_{\text{csc}} + \frac{1}{2}\bar{\lambda}_{(\sigma\text{-}\pi)} = 0 . \tag{3.50}
$$

The sum rules above are only fulfilled if the axial $U(1)_A$ symmetry is respected. Note further that the sum rules are only valid for our particular *Fierz* basis choice which we denote by $\mathcal{B}$. Since all *Fierz*-complete basis sets associated with a specific symmetry group are related to each other by means of *Fierz* transformations, the mapping from one set of couplings to a different one reads

$$
\vec{\lambda}' = M\vec{\lambda}, \tag{3.51}
$$

where M denotes an $n \times n$ matrix with $\det M \neq 0$, see our example in Sec. 3.1.2. Here, $\vec{\lambda}$ is the original coupling set associated with our present *Fierz*-complete basis. The vector $\vec{\lambda}'$ then contains new couplings associated with a new *Fierz* complete basis. Thus, the sum rules (3.49) and (3.50) can be transformed to be used in different *Fierz*-complete parameterizations. Note that there is no necessity to choose four $U(1)_A$-breaking and six $U(1)_A$-invariant channels. For instance, we also found a ten-channel *Fierz*-complete basis with a two-dimensional $U(1)_A$-breaking subspace. The sum rules then become trivial for the following reason: Since an eight-channels basis is already *Fierz*-complete, the remaining two couplings have to be set to zero in order to preserve the axial $U(1)_A$ symmetry.

3.2.1 Fixed-Point and Phase-Structure Analysis

We begin our discussion with a one-channel approach. In complete analogy to our study in Sec. 3.1.1, we only consider the scalar-pseudoscalar channel $\mathcal{L}_{(\sigma\text{-}\pi)}$ and neglect the RG running of all other four-quark channels. Note that we deduce the *Fierz*-incomplete beta functions, i.e., the one-channel and the two-channel approximation, from the *Fierz*-complete RG flow equations (E.4)-(E.13) by setting all other couplings, except the ones we are interested in, to zero. For instance, for the one-channel approximation, we use $\bar{\lambda}_i \to 0$ for all $i \neq (\sigma\text{-}\pi)$. The RG flow equation for the scalar-pseudoscalar coupling then reads

$$\partial_t \lambda_{(\sigma\text{-}\pi)} \quad = \quad 2\lambda_{(\sigma\text{-}\pi)} - 64v_4 \left(2N_{\mathrm{c}} + 1\right)\lambda_{(\sigma\text{-}\pi)}^2 \left(l_{\|+}^{(\mathrm{F})}\left(\tau, 0, -i\tilde{\mu}_\tau\right) + l_{\perp+}^{(\mathrm{F})}\left(\tau, 0, -i\tilde{\mu}_\tau\right)\right), \tag{3.52}$$

with $v_4 = 1/(32\pi^2)$, $\tau = T/k$, and $\tilde{\mu}_\tau = \mu/(2\pi T) = \mu/(2\pi k\tau)$. Let us first discuss the limit of vanishing temperature and quark chemical potential. The vacuum beta function can be extracted from Eq. (3.52) by considering:

$$\lim_{T\to 0} \lim_{\mu\to 0} \left(l_{\|+}^{(\mathrm{F})}\left(\tau, 0, -i\tilde{\mu}_\tau\right) + l_{\perp+}^{(\mathrm{F})}\left(\tau, 0, -i\tilde{\mu}_\tau\right)\right) = \frac{1}{4}. \tag{3.53}$$

The RG flow equation at zero temperature and chemical potential then reads

$$\partial_t \lambda_{(\sigma\text{-}\pi)} \quad = \quad 2\lambda_{(\sigma\text{-}\pi)} - \frac{N_{\mathrm{c}}}{\pi^2}\left(1 + \frac{1}{2N_{\mathrm{c}}}\right)\lambda_{(\sigma\text{-}\pi)}^2. \tag{3.54}$$

Note that we used again the *Fermi*-surface-adapted regulator we already employed in the previous section, see App. C and our discussion in Sec. 3.1.3. For our discussion below, we do not specify the number of color degrees of freedom N_c here.

Let us now discuss the fixed-point structure of the one-channel beta function above. From our previous NJL-type model study, we again expect to find an IR-repulsive non-*Gaussian* as well as an IR-attractive *Gaussian* fixed point. Indeed, for the non-*Gaussian* fixed point we obtain

$$\lambda_{(\sigma\text{-}\pi)}^* = \frac{2\pi^2}{N_{\mathrm{c}} + \frac{1}{2}}. \tag{3.55}$$

Note that the fixed-point value does also depend on the particular regularization scheme and therefore on the regulator shape function r_ψ, see App. C. To trigger spontaneous symmetry breaking in a one-channel approximation, we need to choose $\Delta\lambda_{(\sigma\text{-}\pi)} > 0$, with $\Delta\lambda_{(\sigma\text{-}\pi)} = (\lambda_{(\sigma\text{-}\pi)}^{(\mathrm{UV})} - \lambda_{(\sigma\text{-}\pi)}^*)/\lambda_{(\sigma\text{-}\pi)}^{(\mathrm{UV})}$, see our discussion in Secs. 3.1 and 2.3.2. In this case, the four-quark coupling $\lambda_{(\sigma\text{-}\pi)}$ diverges at a finite critical scale

$$k_{\mathrm{cr}} = \Lambda \left(\Delta\lambda_{(\sigma\text{-}\pi)}\right)^{\frac{1}{2}} \theta(\Delta\lambda_{(\sigma\text{-}\pi)}), \tag{3.56}$$

with the UV cutoff scale Λ. The critical scale then sets the scale of all (chiral) low-energy observables, e.g., the quark mass m_ψ. Note that the equation for the critical scale k_{cr} is identical to the one we found in the previous NJL model study, see also Eq. (3.14).

Interestingly, we observe that the non-*Gaussian* fixed point above is still present by considering a large-N_c expansion of the full *Fierz*-complete set of RG flow equations. Let us, therefore, briefly summarize some key results from the large-N_c study in Ref. [117]. In the large-N_c limit, we observe that the fixed point (3.55) "sits" on the $(\sigma\text{-}\pi)$ axis with one IR-repulsive direction. All other nine directions are IR-attractive. Then, the ten-dimensional *Fierz*-complete theory space is reduced to only one dimension. In this case, the beta function associated with the scalar-pseudoscalar channel decouples from the other nine beta functions so that the RG flow is limited to the direction in theory space which is associated with the $\lambda_{(\sigma\text{-}\pi)}$ coupling. However, the latter is of course only true if we solely tune the $\lambda_{(\sigma\text{-}\pi)}$ coupling in the UV. Since the theory space associated with the *Fierz*-complete ansatz is gov-

erned by $2^{10} = 1024$ fixed points, other choices of initial conditions may then potentially lead to the observation that the RG flow is controlled by a different interacting fixed point, even at small chemical potential.

From the large-N_c observations, we may already suggest that not only the one-channel but also the RG flow associated with the *Fierz*-complete ansatz could be dominated by the non-*Gaussian* fixed point (3.55), at least if we choose our initial conditions sufficiently close to this particular fixed point. In this setting, we expect that the *infrared* physics at small quark chemical potential should be governed again by chiral degrees of freedom and spontaneous chiral symmetry breaking. We stress, however, that beyond the large-N_c limit the non-*Gaussian* fixed point is pushed away from the $\lambda_{(\sigma\text{-}\pi)}$ axis so that all channels are dynamically generated again, even though we only tune the scalar-pseudoscalar coupling in the UV.

Let us now discuss the case of more than one channel where we begin with the scale-fixing procedure in the present NJL-type study at finite temperature and quark chemical potential. In a nutshell, we adopt the scale-fixing prescription as already discussed in Sec. 3.1. Therefore, we only tune the scalar-pseudoscalar coupling in the UV to recover a certain critical temperature at vanishing quark chemical potential. All other couplings are set to zero. Note again that such a scale-fixing procedure can be motivated from QCD studies (cf. Ref. [23]) which expect the scalar-pseudoscalar channel at $T = \mu = 0$ to be of most relevance in the *infrared* regime. The critical temperature we adjust at zero quark chemical potential reads $T_0/\Lambda = T_{\mathrm{cr}}(\mu = 0)/\Lambda = 0.132$ with $\Lambda = 1\,\mathrm{GeV}$ and stems again from a recent lattice QCD study, see Ref. [9]. Note that the critical temperature is still the largest value for the temperature we can compute so that all couplings remain finite for all k, see our definition Eq. (3.20). Below this critical value for the temperature, we find a critical scale k_{cr} and the onset of spontaneous symmetry breaking is signaled by divergences of the four-quark couplings, see also our discussion in Sec. 3.1.1. As we perform the same scale-fixing procedure like in Sec. 3.1, we may compare the results as obtained from our one-flavor and one-color NJL-type model with the results from our present two-flavor and three-color study. In both *Fierz*-complete model calculations, we can then investigate the influence of flavor and color degrees of freedom on the shape and extent of the phase boundary.

We add that the actual scale-fixing procedure differs from the one we employed in the original publication, see Ref. [117]. There, we fixed the scale of our theory at $T = \mu = 0$. By considering the partially bosonized one-channel NJL model within a *mean-field* approach, we derived the relation between the constituent quark mass $m_\psi \sim \langle \bar{\psi}\psi \rangle$ and the critical scale k_{cr}, see our discussion in Sec. 2.3.2. We adjusted the critical scale k_{cr} so that we found a constituent quark mass of $m_\psi/\Lambda = 0.3$ with $\Lambda = 1\,\mathrm{GeV}$ as it is expected in QCD. We then switched to the multi-channel approximation and tuned the UV value of the scalar-pseudoscalar coupling in a way that we obtained the same value for the critical scale k_{cr} as it was found in the *mean-field* approach. The UV values of all other nine couplings were set to zero.

We now discuss the phase diagram for $N_c = 3$ in the (T, μ) plane. For this, we consider three different types of truncations. Besides the one-channel and the *Fierz*-complete approximation, we further use a two-channel ansatz where we choose the scalar-pseudoscalar and the diquark channel. The latter choice can be motivated from our discussion in Sec. 2.3.4 where we mentioned that model studies expect the formation of a diquark condensate at large quark chemical potential. Therefore, to make contact to phenomenology and to study the impact of *Fierz*-incomplete approximations using more than one channel, we also study the phase structure as obtained from a two-channel ansatz below. Our results are shown in Fig. 3.8. We begin with the discussion of the general shape of the phase diagram. Here, we find that for $\mu/T_0 \lesssim 2$ all three phase boundaries lie on top of each other. The latter observation underscores our conjecture that the non-*Gaussian* fixed point (3.55) governs the RG flow at least at low quark chemical potential. Recall that the non-*Gaussian* fixed-point is located on the $(\sigma\text{-}\pi)$ axis of the *Fierz*-complete ansatz for $N_c \to \infty$, see Ref. [117]. Since we only tune the $(\sigma\text{-}\pi)$ channel in the UV, it seems conclusive to find for $N_c = 3$ that the RG flow of the *Fierz*-complete approach is also governed by the fixed point $\lambda^*_{(\sigma\text{-}\pi)}$ at least at low quark chemical potential. For larger quark chemical potential $\mu/T_0 \gtrsim 2$, however, we find that the *Fierz*-complete ansatz differs from the other approximations qualitatively. For the one-channel ansatz, for example,
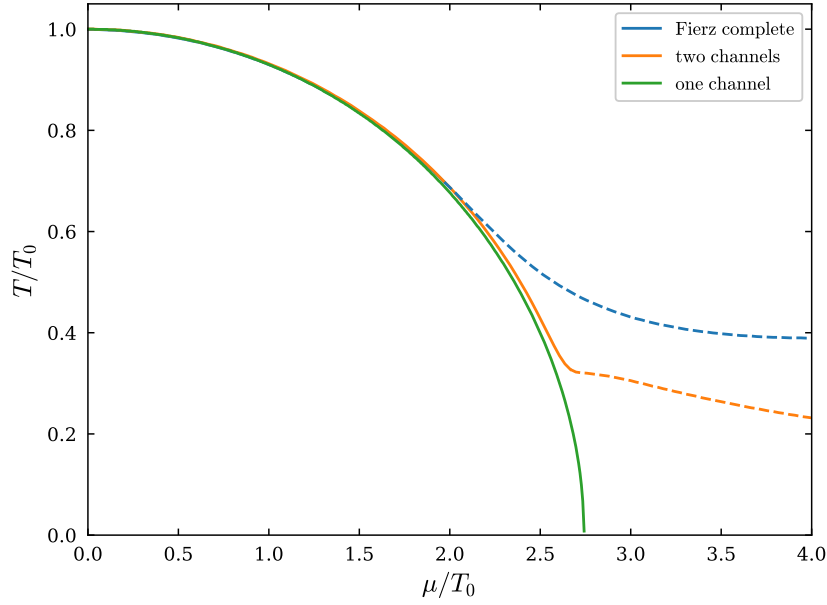
Figure 3.8: Phase diagram of the two-flavor and three-color NJL model in the (T, μ) plane as obtained from a one-channel, two-channel, and *Fierz*-complete calculation. For $\mu/T_0 < 2$, we observe that the scalar-pseudoscalar coupling appears to be most dominant. For larger quark chemical potential, we find a dominance of the csc-channel suggesting the formation of a $J^P = 0^+$-type diquark condensate.

we find a critical chemical potential at $\mu/T_0 \approx 2.75$ above which no spontaneous symmetry breaking of any kind is observed. By studying the one-channel beta function Eq. (3.52), this behavior might have been already expected. From the fact that only l_+-type threshold functions enter the one-channel beta function (3.52), we conclude from our our discussion in the previous section that loop contributions are screened for large quark chemical potential $\mu/k \to \infty$.

Let us now discuss the two-channel and the *Fierz*-complete approach in more detail. We begin with the observation that neither for the two-channel nor for the *Fierz*-complete approach a critical chemical potential μ_{cr} is observed for the studied values of the quark chemical potential in Fig. 3.8. We further observe that the phase boundary associated with the *Fierz*-complete ansatz lies significantly higher (up to 70% for $\mu/T_0 \simeq 4.0$) compared to the one we obtain from the two-channel approach. Let us also compare the phase boundaries we found in the previous section, see Fig. 3.4, with the phase boundaries from the present study where we also consider flavor and color degrees of freedom. We observe that all types of ansätze we have employed in the previous NJL model study exhibit a μ_{cr} at zero temperature. At least for the *Fierz*-complete and the two-channel approach a critical chemical potential is not observed. Even though the one-channel approximations in both model studies exhibit a μ_{cr}, the value of the latter in our present NJL model study is nearly twice as large compared the one we found in the one-flavor and one-color case. Thus, we find that the phase boundary associated with an NJL-type model seems to get "stretched" towards larger quark chemical potential by also including internal color and flavor degrees of freedom.

In Fig. 3.8, we distinguish the most dominant four-quark channels using different line styles. By construction, the one-channel approximation is only governed by the scalar-pseudoscalar channel. For the two-channel and the *Fierz*-complete ansatz, we find that for $\mu/T_0 \lesssim 2$, the scalar-pseudoscalar coupling associated with spontaneous chiral symmetry breaking (solid lines) appears to be the most dominant channel close to the phase boundary. For larger quark chemical potential $\mu/T_0 \gtrsim 2$, however, we find for the two-channel and the *Fierz*-complete approach a regime where the csc-channel becomes dominant (dashed lines). A dominance in the csc-channel then indicates the onset of the spontaneous breakdown of the vector $U(1)_V$ and the (global) color $SU(3)$ symmetry. The latter would
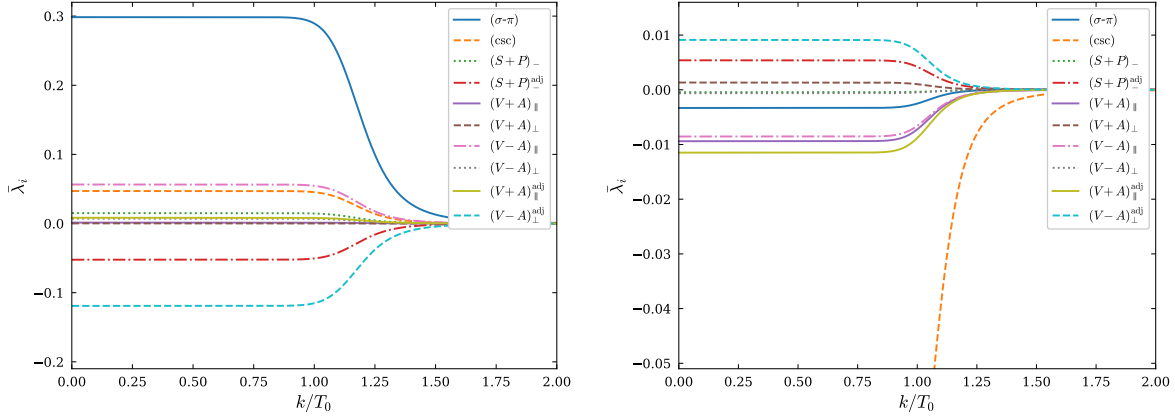
Figure 3.9: Scale dependence of the ten dimensionful four-quark couplings of the *Fierz*-complete basis as a function of the scale parameter k as obtained from two different values of the quark chemical potential at temperatures close to the phase boundary. Left panel: For $\mu/T_0 = 0$ and $T/T_0 \gtrsim 1$, we observe a dominance of the scalar-pseudoscalar channel. Right panel: For $\mu/T_0 = 4$ and $T/T_0 \gtrsim 0.39$, the diquark channel dominates significantly where other channels with a non-trivial color structure like the $(V + A)_{\parallel}^{\mathrm{adj}}$ channel appear to be subleadingly dominant.

imply the formation of a diquark condensate which is associated with a finite diquark gap in the energy excitation spectrum. We emphasize that we did not tune the strength of the diquark channel by hand. As discussed above, we only tuned the UV value associated with the scalar-pseudoscalar coupling. The emergence of a dominance in the diquark channel is therefore a result of non-trivial dynamics in our coupled system of beta functions. Since we observe a change in the dominance pattern already on the level of the rather simple two-channel ansatz, we shall study the latter in more detail in the next subsection. There, we shall investigate the underlying pseudo-fixed-point dynamics at finite temperature and quark chemical potential giving rise to a mechanism which possibly explains the transitions from chiral to diquark degrees of freedom at large μ.

In Fig. 3.9 we present the scale dependence of the various dimensionful four-quark couplings entering our *Fierz*-complete ansatz for two exemplary values of the quark chemical potential slightly above the critical temperature. The left panel shows the competing four-quark channels at $\mu = 0$. Here, we find that the scalar-pseudoscalar coupling appears to be most dominant suggesting the onset of spontaneous chiral symmetry breaking below a critical temperature of $T/T_0 \simeq 1$. Furthermore, we find that the channels $(V - A)_{\perp}^{\mathrm{adj}}$ and $(V - A)_{\parallel}$ are subdominant. The right panel shows the running couplings for $\mu/T_0 = 4$ and $T/T_0 \gtrsim 0.39$ where we now find a dominance of the diquark-type four-quark channel. In the latter case, we would expect that the low-energy regime is governed by a $J^P = 0^+$ diquark state with positive parity. Interestingly, we observe that the channels $(V + A)_{\parallel}^{\mathrm{adj}}$ and $(V - A)_{\perp}^{\mathrm{adj}}$ which do also carry a non-trivial color structure are subdominant.

Even though the phase boundaries differ from each other considerably, it is remarkable that the dominance patterns of our previous NJL model study with $N_f = N_c = 1$ and our present one show similar features. At low fermion/quark chemical potential, physics seems to be governed by a finite chiral condensate, where for large chemical potential difermion-type condensation seems to be favored. For the one-flavor and one-color model, we have already discussed that a dominance in the $(A_{\parallel}\mathcal{C})$ channel may be associated with the breakdown of the global $U(1)_V$. The latter is then accompanied with the formation of *Cooper*-type pairs and the generation of a finite *Meissner* mass. This picture may be adopted for the present theory with QCD-like degrees of freedom where we may also expect from our dominance arguments a breakdown of the vector $U(1)_V$ symmetry. Moreover, in a color superconducting 2SC phase [40], it is expected that the color $SU(3)$ symmetry breaks down to an $SU(2)$. In QCD, the latter would imply that five of the eight gluons acquire a finite *Meissner* mass, see also our discussion in Sec. 2.3.4. Still, we may argue that our specific choice of initial conditions may introduce a bias in our computations leading to a "spurious" dominance of, e.g., the scalar-pseudoscalar channel. However, we shall see that our QCD study from
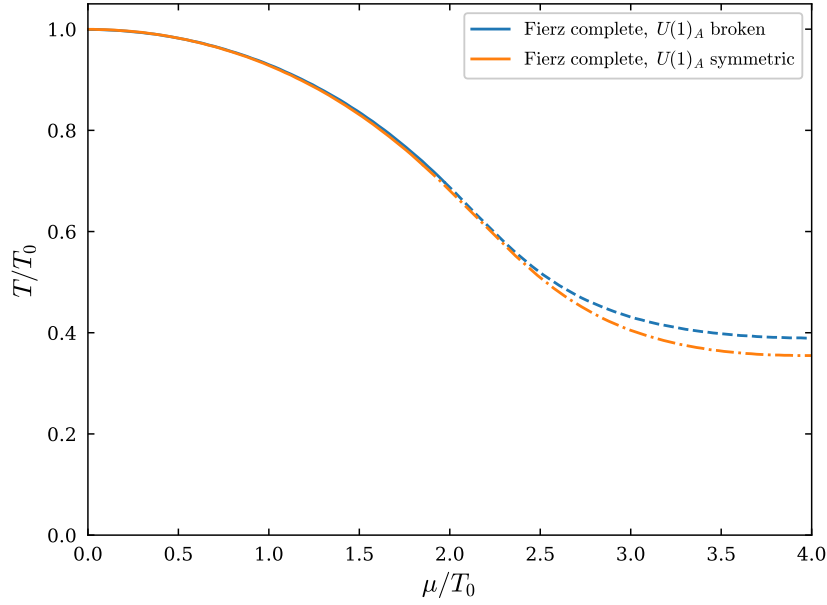
Figure 3.10: Phase boundaries as obtained from our *Fierz*-complete ansatz for $U(1)_A$-breaking (blue curve) and $U(1)_A$-conserving (orange curve) initial conditions. The solid lines denote a dominance of the $(\sigma\text{-}\pi)$ channel where the dashed lines indicate a dominance of the csc-channel. The dashed-dotted part of the orange curve shall indicate a dominance of the $(V + A)_\parallel^{\mathrm{adj}}$ channel.

first-principle confirms our results of the present NJL-type model, see Sec. 3.3.

The UV initial conditions we considered so far break the axial $U(1)_A$ symmetry. One may ask to what extent the phase diagram is modified if $U(1)_A$ is conserved in the RG flow. For this, we need to consider $U(1)_A$-symmetric initial conditions for our *Fierz*-complete four-quark ansatz. To this end, we use the sum rules Eqs. (3.49) and (3.50), which provide us with a class of initial conditions satisfying the requirement to start the RG flow at a $U(1)_A$-symmetric point in theory space. For example, we can require that $\lambda_i^{(\mathrm{UV})} = 0$ for all $i \in \mathcal{B}\backslash\{(\sigma\text{-}\pi),\ (S + P)_-\}$ and choose $\lambda_{(\sigma\text{-}\pi)}^{(\mathrm{UV})} = -2\lambda_{(S+P)_-}^{(\mathrm{UV})}$ so that $U(1)_A$ is conserved. Indeed, we then find that both sum rules are satisfied exactly for all $k > k_{\mathrm{cr}}$. At the critical scale $k = k_{\mathrm{cr}}$, given that the RG flow is rather dominated by the IR-repulsive part of the non-*Gaussian* fixed point, all four-quark couplings diverge and indicate the breakdown of at least one of the continuous symmetries. Since a breakdown of the $SU(2)_L \times SU(2)_R$ symmetry is accompanied by a simultaneous breakdown of the axial $U(1)_A$, the sum rules shall diverge, too.

In Fig. 3.10, we show the phase diagram of our two-flavor and three-color NJL model as obtained from a *Fierz*-complete ansatz using $U(1)_A$-symmetric initial conditions (orange line). Moreover, we compare the phase boundary from the $U(1)_A$-symmetric study with our previous *Fierz*-complete ansatz using $U(1)_A$-violating initial conditions (blue line), see Fig. 3.8. The scale-fixing procedure employed in the symmetric case is chosen in analogy to the $U(1)_A$-violating case: we only tune the UV values of $\lambda_{(\sigma\text{-}\pi)}^{(\mathrm{UV})}$ and $\lambda_{(S+P)_-}^{(\mathrm{UV})}$ according to Eq. (3.50) so that we recover again a critical temperature of $T_0/\Lambda = 0.132$ with $\Lambda = 1\,\mathrm{GeV}$ at zero chemical potential. On a qualitative level, we note that for the two types of initial conditions, the shapes of both phase boundaries appear to be rather similar, see Fig. 3.10. Only for $\mu/T_0 \gtrsim 2.0$, the phase boundaries start to deviate. In particular, at $\mu/T_0 \approx 4.0$ we find that the critical temperature associated with $U(1)_A$-breaking initial conditions lies about 10% higher than the one which was computed from axially symmetric starting values. Leaving the deviation at large quark chemical potential aside, we can conclude that the use of $U(1)_A$-conserving initial conditions has a subleading effect on the the critical temperature for the studied values of the quark chemical potential.

The dominance pattern, however, is modified for large quark chemical potentials. While we still find a domi-

nance of the scalar-pseudoscalar channel for small values of the quark chemical potential, we now observe for $\mu/T_0 \gtrsim$ 1.8 a dominance of the $(V + A)_{\|}^{\mathrm{adj}}$ channel by employing $U(1)_A$-symmetric initial conditions. Interestingly, the condensate associated with the $(V + A)_{\|}^{\mathrm{adj}}$ channel breaks the global color $SU(3)$ symmetry which is compatible with our findings using $U(1)_A$-violating initial conditions. A possible condensate associated with the $(V + A)_{\|}^{\mathrm{adj}}$ channel could be identified, e.g., with a vector-like spin-1 ground state, see Ref. [28] for a review. Nevertheless, we observe for $\mu/T_0 \gtrsim 1.8$ that all channels which carry a non-trivial color structure, i.e., the csc, $(S + P)_{-}^{\mathrm{adj}}$, $(V - A)_{\perp}^{\mathrm{adj}}$ channel, are still subleadingly dominant.

Let us briefly summarize our findings. First, compared to our previous NJL-mode study, we do not observe a critical chemical potential μ_{cr} at zero temperature by employing *Fierz*-complete approaches. We further note that the specific shape of the phase boundary from our *Fierz*-complete ansatz remains almost unchanged if we consider axially symmetric initial conditions. Nevertheless, the influence of the axial $U(1)_A$ anomaly on the phase structure seems to be stronger if we consider larger quark chemical potentials. Second, at least for our actual choice of initial conditions, the dominance pattern we observe close to the phase boundary appears very robust. In particular, we find that at large quark chemical potential $\mu/T_0 \gg 2.0$ diquark-type condensates, which carry a non-trivial color structure, are favored. At small quark chemical potential, however, we always find that the scalar-pseudoscalar channel becomes dominant which is then associated with the spontaneous breakdown of chiral symmetry.

3.2.2 Symmetry-Breaking Mechanism

In the previous subsection we have seen that we find indications for a color-superconducting condensate already on the level of the two-channel approximation. Remarkably, the change from a regime rather dominated by diquark than by chiral degrees of freedom occurs naturally at a large quark chemical potential, i.e., there is no need to tune the diquark channel "by hand" in the UV in order to observe a dominance in the csc-channel. To better understand the physics underlying this mechanism, let us now analyze the fixed-point structure of the *Fierz*-incomplete two-channel ansatz. The beta functions for the $\lambda_{(\sigma\text{-}\pi)}$ and λ_{csc} couplings then read

$$
\begin{aligned}
\partial_t \lambda_{(\sigma\text{-}\pi)} &= 2\lambda_{(\sigma\text{-}\pi)} + 64 v_4 \left(-(2N_\mathrm{c} + 1)\lambda_{(\sigma\text{-}\pi)}^2 + (N_\mathrm{c} + 1)\lambda_{(\sigma\text{-}\pi)}\lambda_{\mathrm{csc}} \right) l_{\|+}^{(\mathrm{F})}(\tau, 0, -i\mu_\tau) \\
&\quad + 64 v_4 \Big(-(2N_\mathrm{c} + 1)\lambda_{(\sigma\text{-}\pi)}^2 + \frac{1}{3}(3N_\mathrm{c} - 1)\lambda_{(\sigma\text{-}\pi)}\lambda_{\mathrm{csc}} \\
&\quad - \frac{1}{3}(N_\mathrm{c} - 2)\lambda_{\mathrm{csc}}^2 \Big) l_{\perp+}^{(\mathrm{F})}(\tau, 0, -i\mu_\tau) \,,
\end{aligned}
\tag{3.57}
$$

$$
\begin{aligned}
\partial_t \lambda_{\mathrm{csc}} &= 2\lambda_{\mathrm{csc}} + 64 v_4 \left(-\lambda_{(\sigma\text{-}\pi)}^2 + (N_\mathrm{c} - 2)\lambda_{\mathrm{csc}}^2 \right) l_{\|+}^{(\mathrm{F})}(\tau, 0, -i\mu_\tau) \\
&\quad + 64 v_4 \left(-\lambda_{(\sigma\text{-}\pi)}^2 - 2\lambda_{(\sigma\text{-}\pi)}\lambda_{\mathrm{csc}} + 4\lambda_{\mathrm{csc}}^2 \right) l_{\|\pm}^{(\mathrm{F})}(\tau, 0, -i\mu_\tau) \\
&\quad + 64 \lambda_{(\sigma\text{-}\pi)}^2 v_4 l_{\perp+}^{(\mathrm{F})}(\tau, 0, -i\mu_\tau) \\
&\quad + 64 v_4 \left(\lambda_{(\sigma\text{-}\pi)}^2 - 2\lambda_{(\sigma\text{-}\pi)}\lambda_{\mathrm{csc}} + 4\lambda_{\mathrm{csc}}^2 \right) l_{\perp\pm}^{(\mathrm{F})}(\tau, 0, -i\mu_\tau) \,,
\end{aligned}
\tag{3.58}
$$

where we have set again all other couplings and their flow equations in our *Fierz*-complete ansatz to zero and considered $N_c = 3$. Interestingly, we do not find any $l_{\pm}^{(\mathrm{F})}$-type threshold functions entering the beta function associated with scalar-pseudoscalar channel. Indeed, this can be compared to the one-channel approximation we discussed in Sec. 3.2.2 where we already observed that only threshold functions of the $l_{+}^{(\mathrm{F})}$ type appeared. From our analysis in the previous section, we know that at zero temperature $l_{+}^{(\mathrm{F})}$ functions show a screening effect for $\mu/k \gg 1$. On the other hand, for a large quark chemical potential, the $l_{\pm}^{(\mathrm{F})}$ threshold functions have an antiscreening effect for sufficiently small temperatures. In our last NJL model study, we then related the $l_{\pm}^{(\mathrm{F})}$-type function to BCS theory in the following sense; we found in a one-channel approach that the non-*Gaussian* pseudo-fixed point moved for $\mu/k \gg 1$ towards the *Gaussian* fixed point and merged with the latter for $\mu/k \to \infty$. Any finite UV value of the four-fermion coupling would be then sufficient to drive the system towards criticality, see our discussion in the
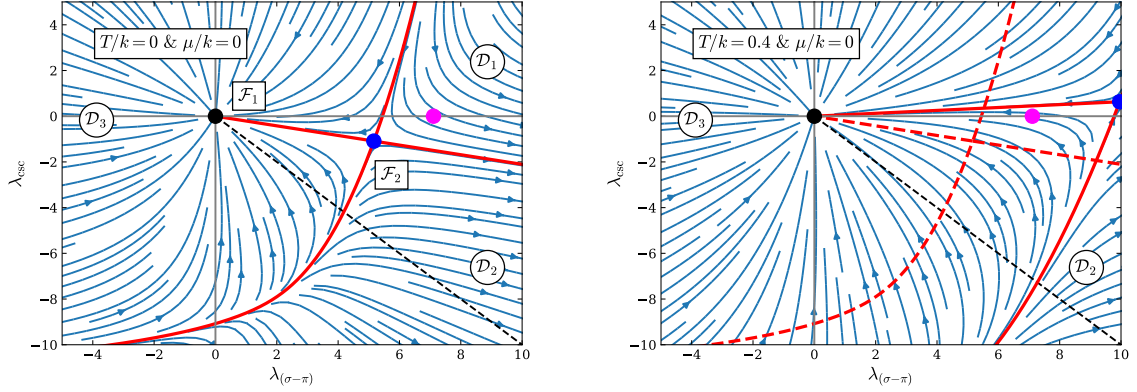
Figure 3.11: RG flow of the beta functions (3.57) and (3.57) at zero temperature and quark chemical potential (left panel) and for non-zero temperature and zero quark chemical potential (right panel), arrows point towards the *infrared*. The pink dot represents our choice of initial condition in the UV. For increasing temperature, the non-*Gaussian* fixed point (blue) is shifted away from the *Gaussian* fixed point (black), increasing the domain $\mathcal{D}_3$. For a critical temperature value, the pink dot lies within the area of influence of the *Gaussian* fixed point. For high temperatures, the theory remains in the symmetric regime as the RG flow is governed by the *Gaussian* fixed point in this case.

previous section. Therefore, it seems reasonable to assume that any kind of BCS-type behavior, has its origin in flow equation associated with λ_{csc}. However, this is of course only true if we employ the simplified two-channel ansatz.

Let us now discuss the vacuum fixed-point structure. For $T = \mu = 0$ and $N_c = 3$, we find four fixed points $\mathcal{F}_j = (\lambda^*_{(\sigma\text{-}\pi),j}, \lambda^*_{\mathrm{csc},j})$:

$$\mathcal{F}_1\big|_{N_c=3} = (0,0)\,, \tag{3.59}$$

$$\mathcal{F}_2\big|_{N_c=3} \approx (5.165, -1.088)\,, \tag{3.60}$$

$$\mathcal{F}_3\big|_{N_c=3} \approx (1.262 - \mathrm{i}1.567, -8.728 - \mathrm{i}0.841)\,, \tag{3.61}$$

$$\mathcal{F}_4\big|_{N_c=3} \approx (1.262 + \mathrm{i}1.567, -8.728 + \mathrm{i}0.841)\,. \tag{3.62}$$

Obviously, only two of the four fixed points are real-valued which shall be important in our study below. Moreover, we already know the non-*Gaussian* fixed point $\mathcal{F}_2$ from the one-channel discussion in the previous section. Considering a large-N_c expansion up to the order $\mathcal{O}(1/N_c^2)$, we find for $\mathcal{F}_2$:

$$\mathcal{F}_2(N_c) = \left(\frac{2\pi^2}{N_c} - \frac{3\pi^2}{2N_c^2}, -\frac{\pi^2}{N_c^2}\right)\,. \tag{3.63}$$

We find that the large-N_c expansion also corresponds to our findings in the one-channel approach (3.55). In leading order and for our present choice of initial conditions, i.e., we only tune $\lambda^{(\mathrm{UV})}_{(\sigma\text{-}\pi)}$ and set $\lambda^{(\mathrm{UV})}_{\mathrm{csc}}$ to zero, the fixed point $\mathcal{F}_2$ controls again the *infrared* behavior of our truncated two-channel approach, see Ref. [117].

Let us now analyze the fixed-point structure of the coupled set of beta functions (3.57) and (3.57), by studying the corresponding RG flow. The left panel of Fig. 3.11 shows the RG flow at $T = \mu = 0$, where the arrows shall indicate the direction of the flow towards the *infrared* regime. We depict the *Gaussian* fixed point in black and the real-valued non-*Gaussian* fixed point $\mathcal{F}_2(N_c = 3)$ in blue. Moreover, we find that the theory space is sliced by separatrices (red lines) into three different domains $\mathcal{D}_i$. The pink dot shall denote an exemplary choice of UV initial conditions where we use $\lambda^{(\mathrm{UV})}_{(\sigma\text{-}\pi)} > 0$ and $\lambda^{(\mathrm{UV})}_{\mathrm{csc}} = 0$ as discussed above. We find that for all UV values which lie in domain $\mathcal{D}_1$ or $\mathcal{D}_2$, the *infrared* regime is governed by a non-trivial vacuum ground state accompanied by a spontaneously broken symmetry. Moreover, for all initial conditions in $\mathcal{D}_1$, we shall observe a dominance of the

scalar-pseudoscalar channel since all trajectories approach the red separatrix pointing in the direction of the $\lambda_{(\sigma\text{-}\pi)}$ coupling. One may now speculate whether it is possible to trigger a dominance in the csc channel by using different initial conditions, e.g., we use a sufficiently large value for $\lambda_{\text{csc}}^{(\text{UV})}$. However, since all trajectories approach the red separatrix in the UV, it appears to be rather difficult to find a set of initial conditions so that a dominance in the csc channel is observed. For initial values in $\mathcal{D}_3$, however, the theory remains ungapped and the RG flow approaches the *Gaussian* fixed point in the deep *infrared*. In this case, all symmetries remain intact in the low-energy regime.

Let us now turn on the dimensionless temperature T/k and discuss how the RG flow changes, see the right panel of Fig. 3.11. The dashed red line shows the separatrices at $T = \mu = 0$ where the solid red lines are the separatrices at $T/k = 0.4$. We find that the domain $\mathcal{D}_3$ is significantly increased. Moreover, The (pseudo) fixed point $\mathcal{F}_2$ is moved towards larger values of $\lambda_{(\sigma\text{-}\pi)}$ so that the separatrices are shifted accordingly. For the presented panel on the right-hand side of Fig. 3.11, the dimensionless temperature $\tau = 0.4$ is chosen sufficiently large so that the pink dot (UV initial value) is now located in $\mathcal{D}_3$ and not in $\mathcal{D}_2$ anymore. This implies that the theory is now dominated by the *Gaussian* fixed point (black). For the *infrared* regime it follows that the ground state becomes trivial and the system remains ungapped. In fact, we have already seen a similar behavior for the parabola associated with the beta function of the one-channel approach we considered in our one-flavor and one-color NJL model study, see Fig. 3.6. Here, the non-*Gaussian*-pseudo-fixed point moved also towards larger values when increasing the dimensionless temperature. In both cases, there exists a critical value for T/k, above which no spontaneous symmetry breaking can occur. This critical temperature then corresponds to the finite-temperature phase boundary $T_{\text{cr}}(\mu)$, separating the broken from the unbroken regime. In the previous section, we already indicated that this behavior can be traced back to the *Matsubara* screening mass $\sim T$ in our propagator structures, see Eq. (C.9).

In the next step, we study the RG flow at zero temperature $T = 0$ and finite quark chemical potential, see Fig. 3.12. The top left panel shows again the RG flow at $T = \mu = 0$, see our discussion above. We now increase the dimensionless quark chemical potential up to a certain critical value $\mu/k = (\mu/k)_0$, where we observe that the formally imaginary fixed points $\mathcal{F}_3$ and $\mathcal{F}_4$ turn into real-valued non-*Gaussian* (pseudo) fixed points, see the two new blue dots "sitting" almost on top of each other in the top right panel of Fig. 3.12. Note that for $0 < \mu/k < (\mu/k)_0 \approx 0.298$ the RG flow should not change at all as a result of the *Silver-Blaze* property, see Refs. [116, 285]. However, we already discussed in Sec. 3.1.3 that our presently used *Fermi*-surface-adapted cutoff scheme (mildly) violates the *Silver-Blaze* symmetry of our theory. As a consequence, we observe a modification of the RG flow for (dimensionless) quark chemical potentials below $(\mu/k)_0$.

The newly emerged real-valued non-*Gaussian* fixed points drastically alter the underlying theory space as they introduce new separatrices creating the domains $\mathcal{D}_4$ and $\mathcal{D}_5$, see the bottom right panel of Fig. 3.12. By further increasing the quark chemical potential, we observe that one of the new non-*Gaussian* fixed points moves towards the former real-valued vacuum fixed point $\mathcal{F}_2$, see the bottom left panel. We further notice that this new non-*Gaussian* fixed point does only have IR repulsive directions, i.e., it defines an unstable point in theory space. Nevertheless, we find that by starting with our choice of UV initial condition (pink dot), the system is still driven in the direction defined by the $\lambda_{(\sigma\text{-}\pi)}$ coupling. By increasing the dimensionless quark chemical potential even further, we observe an annihilation of the old non-*Gaussian* fixed point $\mathcal{F}_2$ and the newly created *non-Gaussian* fixed point, i.e., both fixed points are now located in the complex plane. Again, the structure of the theory space changes. The latter is now divided into three different domains $\mathcal{D}_1$, $\mathcal{D}_3$ and $\mathcal{D}_5$ due to the disappearance of the separatrix which pointed in the direction of the scalar-pseudoscalar channel, see bottom right panel. We stress that this separatrix was responsible for the observed dominance pattern which suggested the onset of spontaneous chiral symmetry breaking at low quark chemical potential. For larger μ/k, the remaining non-*Gaussian* fixed point approaches the *Gaussian* one. It is further important that the remaining fixed point now "sits" almost on the λ_{csc} axis. For $\mu/k \to \infty$ the *Gaussian* and non-*Gaussian* fixed point merge so that a small finite value in the *ultraviolet* suffices to render the system critical. Thus, we find again the famous *Cooper* instability. Moreover, the RG flow is now tilted pointing in the direction associated with the λ_{csc} coupling, see the bottom right panel. This observation is key to understand the change of the dominance pattern we have observed in our phase diagram, see Fig. 3.8. From our starting point
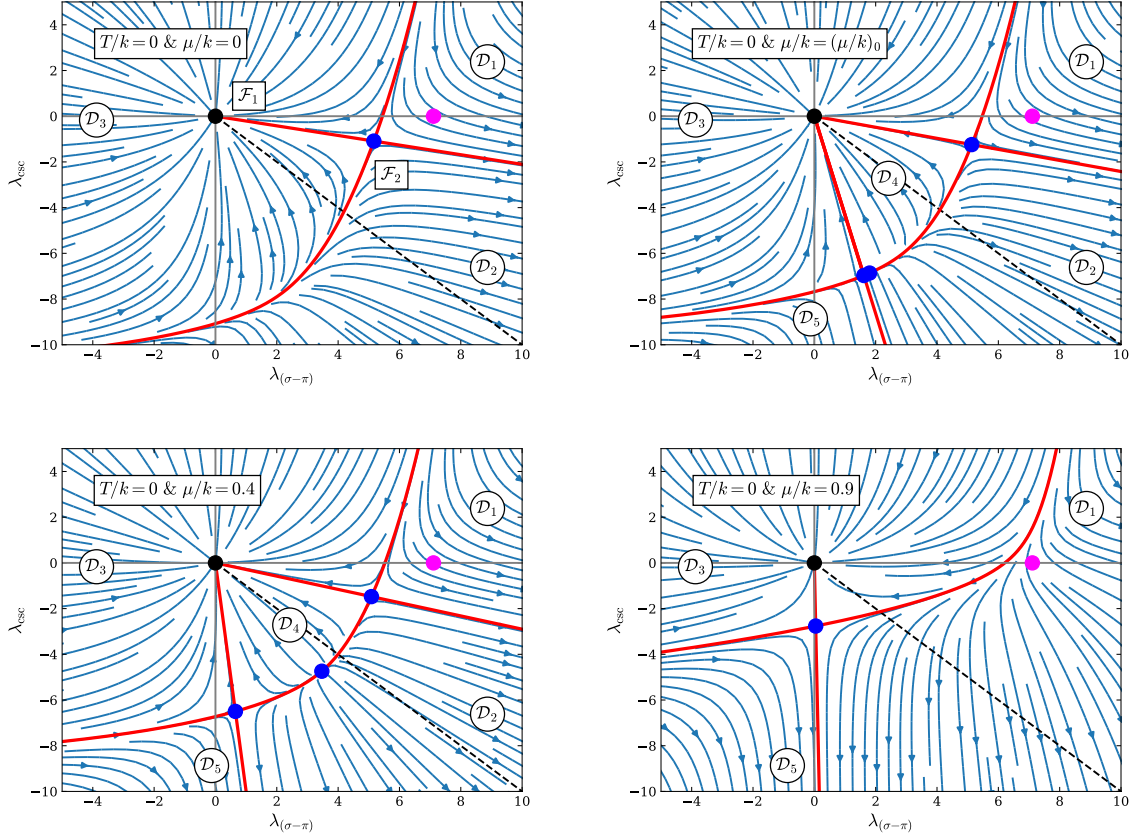
Figure 3.12: RG flow at zero temperature and finite chemical potential as obtained from the beta functions Eqs. (3.57) and (3.58) which we show in the $\lambda_{(\sigma\text{-}\pi)}$-$\lambda_{\text{csc}}$ plane. Top left panel: For $T = \mu = 0$, two of the four fixed points are real-valued, see the *Gaussian* fixed point (black) and the non-*Gaussian* fixed point (blue). For initial conditions of the RG flow starting in $\mathcal{D}_1$, we observe a dominance of the $\lambda_{(\sigma\text{-}\pi)}$ channel, see the red separatrix pointing in the $\lambda_{(\sigma\text{-}\pi)}$ direction. Top right panel: For $\mu/k = (\mu/k)_0 \approx 0.298$, all four (pseudo) fixed points are real valued. Bottom left panel: By further increasing μ/k, one of the newly appeared non-*Gaussian* fixed points drifts towards the λ_{csc} axis. The other one moves towards the old non-*Gaussian* fixed point ($\mathcal{F}_2$). Bottom right panel: The old and the new non-*Gaussian* fixed point annihilate and become imaginary. The RG flow is then tilted and dominated by the remaining non-*Gaussian* fixed point. The corresponding separatrix now points in the λ_{csc} direction which can give rise to a dominance in the diquark channel.

(pink dot), the RG flow is now driven towards the λ_{csc} direction implying a dominance of the diquark channel and the possible emergence of a finite diquark gap.

Even though an analysis of the fixed-point structure of the *Fierz*-complete ansatz seems rather infeasible, the mechanism we observe for two channels can already provide us with valuable insights in the dynamics underlying our *Fierz*-complete phase diagram. For a two-channel approach, we have seen how a dominance in the diquark channel can be induced by fluctuation effects, even though we start the RG flow with $\lambda_{\text{csc}}^{(\text{UV})} = 0$. We further recovered a typical fixed-point behavior as it is expected for BCS-type pairing, i.e., we observed within our two-channel approximation that the non-*Gaussian* fixed point and the *Gaussian* fixed point merge for $\mu/k \to \infty$. We conclude that our two-flavor and three-color NJL-type study suggests that physics at low chemical potential is dominated by a spontaneous breakdown of the chiral $SU(2)_L \times SU(2)_R$ symmetry and the formation of a chiral condensate $\langle \bar{\psi}\psi \rangle \neq 0$. For larger chemical potentials, the breakdown of the vector $U(1)_V$ and the color $SU(3)$ symmetry seems favorable. The low-energy physics would be then dominated by the formation of a diquark condensate $\langle i\bar{\psi}^C \gamma_5 \epsilon_f \varepsilon_c^l \psi \rangle \neq 0$.

3.3   Hot and Dense Two-Flavor QCD

In the present section of the first part, we shall now study two-flavor[12] QCD in the chiral limit, see Ref. [118] for the original publication. To this end, we also take gluon self-interactions from the *Yang-Mills* sector into account by using results for the RG running of the scale-dependent strong gauge coupling from previous works [18–20] computed in the *background-field* formalism. The latter then enters our theory as an external input function as we shall discuss below. Because of two-gluon exchange diagrams, the four-quark interaction channels we discussed in the previous section, are then generated solely from gluon dynamics. From Fig. 2.3, we already know that we need to consider three different types of four-quark diagrams. Each of them then appears in four different versions due to the presence of an external heat bath and finite quark chemical potential.[13]

The structure of the present section is as follows: We begin with an introduction of the ansatz we use for the effective average action. We then analyze the different approximations and truncations we perform and discuss possible improvements for future works. In the next subsection, we examine the general form of our four-quark beta functions and review the mechanism of spontaneous chiral symmetry breaking in QCD at finite temperature. Simultaneously, we analyze the finite-temperature behavior of our strong coupling and discuss our scale-fixing procedure. In the last subsection, we then compare the phase boundaries of two-flavor QCD at finite temperature and quark chemical potential where we use the running strong coupling as obtained from *Yang-Mills* theory ($N_f = 0$) and QCD ($N_f = 2$). In analogy to our previous studies, we also discuss the RG running of the four-quark couplings from which we deduce the symmetry breaking patterns underlying our phase diagram.

For two-flavor QCD with massless quarks, the so-called classical action in the chiral limit reads

$$S_{\mathrm{QCD}}^{(N_f=2)} = \int_0^\beta \mathrm{d}\tau \int \mathrm{d}^3x \ \left\{ \bar{\psi}(\mathrm{i}\gamma_\mu D_\mu + \mathrm{i}\gamma_0\mu)\psi + \frac{1}{4}F_{\mu\nu}^a F_{\mu\nu}^a \right\} , \qquad (3.64)$$

with the *covariant* derivative $D_\mu = \partial_\mu - \mathrm{i}\bar{g}A_\mu^a T^a$ and the quark chemical potential μ. Note that a summation over color and flavor degrees of freedom is implicitly assumed. We know from the quantization of *Yang-Mills* theory in Sec. 2.3.1 that we still need to fix the gauge. Employing the *Faddeev-Popov* method, the resulting *Faddeev-Popov* ghost fields enter our theory as additional degrees of freedom, see our discussion in Sec. 2.3.1.

As an ansatz for the coarse-grained average effective action, we need to anticipate again all possible operators which are compatible with the symmetries and generated in the *Wetterich* equation as a result of quantum fluctuations, e.g., we also need to take arbitrarily high powers of the *Yang-Mills* field strength tensor $F_{\mu\nu}^a F_{\mu\nu}^a$ into account. For the matter sector, we assume that the most important correlation functions to study the onset of spontaneous symmetry breaking are four-quark vertices as discussed in the previous NJL studies. In the present case, however, the four-quark vertices are solely generated from gluodynamics. As a *Fierz*-complete basis, we adopt the four-quark channels which we found in our two-flavor and three-color NJL-type model. An ansatz for the effective action at finite temperature and quark chemical potential is then given by

$$\begin{aligned}\Gamma_{\mathrm{LO}}[A, \bar{\psi}, \psi] \ &= \ \int_0^\beta \mathrm{d}\tau \int \mathrm{d}^3x \ \left\{ \bar{\psi}\left(Z_\psi^{\parallel}\mathrm{i}\gamma_0\partial_0 + Z_\psi^{\perp}\mathrm{i}\gamma_i\partial_i - Z_\mu\mathrm{i}\mu\gamma_0 \right)\psi + Z_g\bar{g}\left(\bar{\psi}\gamma_\mu A_\mu^a T^a \psi\right) \right\} \\ &\quad + \Gamma_{(\bar{\psi}\psi)^2}[\bar{\psi}, \psi] + \Gamma_{\mathrm{YM}}[A] + \Gamma_{\mathrm{gf}}[A] , \end{aligned} \qquad (3.65)$$

---

[12]One may ask what might change if more than two flavors were present. For instance, if we consider a *Fierz*-complete basis for QCD with two massless quark flavors and one massive strange quark. At zero temperature and quark chemical potential, a complete basis would be given by 25 different four-quark channels.

[13]We already observed such a splitting on the level of the purely fermionic threshold functions at finite temperature and quark chemical potential, see, e.g., Eqs. (C.18)-(C.21).

where the abbreviations read

$$\Gamma_{(\bar{\psi}\psi)^2}[\bar{\psi}, \psi] = \frac{1}{2} \int_0^\beta d\tau \int d^3x \sum_{j \in \mathcal{B}} Z_j \bar{\lambda}_j \mathcal{L}_j \,, \tag{3.66}$$

$$\Gamma_{\mathrm{YM}}[A] = \frac{1}{4} \int_0^\beta d\tau \int d^3x \, F_{\mu\nu}^a F_{\mu\nu}^a \,, \tag{3.67}$$

$$\Gamma_{\mathrm{gf}}[A] = \frac{1}{2\xi} \int_0^\beta d\tau \int d^3x \, (\partial_\mu A_\mu^a)^2 \,. \tag{3.68}$$

In Eq. (3.65), the temporal and spatial fermionic wave-function renormalizations are $Z_\psi^\perp$ and $Z_\psi^\parallel$, the renormalization function for the quark chemical potential is Z_μ, and the quark-gluon vertex renormalization is denoted by Z_g. The wave-function renormalization Z_A of the gluon field is encoded in the field strength tensor $F_{\mu\nu}^a$ which reads

$$F_{\mu\nu}^a = Z_A^{1/2} \left(\partial_\mu A_\nu^a - \partial_\nu A_\mu^a + Z_A^{1/2} Z_g \bar{g} f^{abc} A_\mu^b A_\nu^c \right) \,. \tag{3.69}$$

Note that the *Yang-Mills* part Γ_{YM} also contains three-gluon $\sim A^3$ and four-gluon $\sim A^4$ interactions which we shall neglect on the level of the ansatz (3.65). On the level of the running coupling, however, we emphasize that non-trivial gluon self-interactions are included, see Refs. [18–20]. In principle, due to the heat bath, the gluon fields would also require a separate renormalization of the magnetic Z_A^M and the electric Z_A^E field components, see, e.g., Refs. [237, 294]. We further note that same is also true for the quark-gluon vertex renormalization Z_g which then splits into a contribution parallel $Z_g^\parallel$ and perpendicular $Z_g^\perp$ to the heat bath. For simplicity, however, we shall neglect such a rather involved truncation in the present work. For completeness, at least the electric and magnetic wave-function renormalizations appear in our definition of the renormalized gluon propagator, see Eq. (C.16).

Note that we work again in the pointlike limit of the four-quark correlation functions as well as for the quark-gluon three-point vertex. In analogy to our previous studies, we shall further neglect the RG running of the fermionic wave-function renormalizations $\partial_t Z_\psi^\perp = \partial_t Z_\psi^\parallel = \partial_t Z_\mu = 0$ and set $Z_\psi = Z_\psi^\perp = Z_\psi^\parallel = Z_\mu^{-1} \equiv 1$ for all k. Note that the latter assumption was exact in leading order of the derivative expansion when we studied purely fermionic NJL-type models. Including gauge degrees of freedom, however, there exists a non-zero one-gluon exchange diagram contributing to the running of Z_ψ. At least at large momentum scales, however, QCD studies suggest that the running of the latter can be assumed to be subleading, see, e.g., Refs. [23, 240]. Therefore, in our present work, we also neglect the running of the fermionic wave-function renormalization and defer a detailed study to future works.

The term $\Gamma_{(\bar{\psi}\psi)^2}$ in Eq. (3.66) entering our ansatz for the effective action represents the two-flavor and three-color *Fierz*-complete four-quark basis we discussed in Sec. 3.2. Here, the Z_j are associated with the four-quark vertex renormalizations, the $\bar{\lambda}_i$ are the bare four-quark couplings and the $\mathcal{L}_i$ denote our four-quark operators obeying a global $SU(2)_L \times SU(2)_R \times U(1)_V$ symmetry, see also Eqs. (3.38)-(3.47). For the renormalization of the four-quark couplings $\bar{\lambda}_i$, see Eq. (3.7).

In the next step, let us renormalize the quark-gluon vertex in our ansatz. To this end, we use the field redefinitions for the fermionic field, see Eq. (3.8), and for the gluonic fields $A_\mu^a \to A_\mu^a Z_A^{-1/2}$. From this, we find

$$g_k^2 = \frac{Z_g^2 \bar{g}^2}{(Z_\psi^\perp)^2 Z_A} \,, \tag{3.70}$$

with $g_k = \sqrt{4\pi\alpha_{s,k}}$ in $D = 4$. As a consequence of the *modified Ward-Takahashi* identity (mWTI), which arises due to the presence of a regulator function in our functional RG framework, see, e.g., Refs. [159, 295–300], one observes that the beta function of the quark-gluon vertex is also modified by the running four-quark couplings. In this case, diagrams of the type depicted in Fig. 3.13 do also contribute to the beta function of the quark-gluon
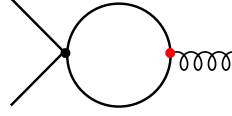
Figure 3.13: 1PI diagram contributing to the beta function of the quark-gluon vertex.

vertex, see Ref. [301] for a detailed discussion. The general form of the relation between the quark-gluon vertex renormalization Z_g and the fermionic wave-function renormalization $Z_\psi^\perp$ can be written as

$$\frac{Z_g}{Z_\psi^\perp} = 1 + \sum_{i \in \mathcal{B}} a_i^{(\mathrm{F})}(T, \mu)\, \lambda_i \,, \tag{3.71}$$

where $\mathcal{B}$ denotes the set of *Fierz*-complete basis elements Eqs. (3.38)-(3.47) and the coefficients $a_i^{(\mathrm{F})}$ are associated with one-loop diagrams and need to be determined in an additional calculation. For convenience, we shall neglect any correction terms imposed by the mWTI in our present work and set $Z_g/Z_\psi^\perp = 1$. Nevertheless, a more careful investigation of the mWTI and their influence on observables is reasonable and should be done in future studies.

A further crucial approximation stems from the way the gauge coupling from the background-field study [18–20] enters our ansatz (3.65). We emphasize that already at zero temperature and quark chemical potential, there are in general three different types of gauge couplings associated with, e.g., four-gluon, three-gluon and quark-gluon vertices which require, in principle, separate vertex renormalizations, see, e.g., Ref. [240]. As it turns out, for sufficiently large momentum scales $k \gg 1\,\mathrm{GeV}$, one observes that all gauge couplings coincide perfectly and follow the perturbative result at one-loop order. In the *infrared* regime, however, the RG flow of the three different gauge couplings usually deviate considerably so that a separate renormalization would be necessary. For our study below, we now identify the running gauge coupling computed in Refs. [18–20] with the quark-gluon vertex defined in Eq. (3.70). This essential approximation is valid at large momentum scales but no longer correct in the non-perturbative *infrared* regime. Nevertheless, from our studies in Secs. 3.1, 3.2, and from Ref. [22], we may expect that the influence of the gauge coupling in the *infrared* regime on the RG flow of the four-quark couplings could be rather weak. The reason for the latter conjecture relies on our findings that the low-energy regime is governed by the non-*Gaussian* fixed points of the purely fermionic low-energy theory dominating the RG flow of the four-quark vertices. Therefore, we expect that once the gauge degrees of freedom rendered the four-quark couplings sufficiently large, the dynamics should mostly be governed by the underlying fixed-point structure of an emerging "NJL-type" model.

The main ingredient from the background-field study [18–20] which we use to compute the running of the quark-gluon vertex is the anomalous dimension

$$\eta_A = -\frac{\partial_t Z_A}{Z_A} \,, \tag{3.72}$$

in $D = 4$. Note that the latter contains non-trivial information from the gauge sector and is a function of the scale-dependent coupling g_k^2, the dimensionless temperature T/k and the number of flavors N_f so that we may write $\eta_A \equiv \eta_A(g^2, T, N_f)$.

We further ignore any dependence of the gauge coupling on the quark chemical potential. The latter would naturally enter the beta function of the strong gauge coupling at one-loop order by virtue of the following vacuum polarization diagram

$$\partial_t Z_A \sim g_k^2\, a^{(\mathrm{F})}(T, \mu) \sim \text{}. \tag{3.73}$$

In our present study, however, we shall adopt the strong coupling as computed from Refs. [18–20] and postpone further improvements on the RG running of g_k^2 to future works.

Eventually, let us now briefly discuss the gauge-fixing condition we employ. For this, we included Γ_{gf} in our ansatz where ξ denotes the gauge-fixing parameter for linear *covariant* gauges. In general, the parameter ξ is also scale dependent $\xi = \xi_k$. From this, it follows that a properly gauge-fixed theory at some initial scale $k = \Lambda$ in the *ultraviolet* flows towards a different gauge in the *infrared* where usually $\xi_{k=0} \neq \xi_{k=\Lambda}$. As it turns out, *Landau* gauge $\xi = 0$ is an attractive *infrared* fixed point in theory space [302] and might therefore be a reasonable choice. For our study at finite temperature and chemical potential, however, we shall work in the *Feynman-'t Hooft* gauge $\xi = 1$ for technical reasons. Due to the broken *Poincaré* symmetry, we find that the use of *Landau* gauge yields an additional mixing of momentum structures in the threshold functions. By considering *Feynman-'t Hooft* gauge $\xi = 1$, a mixing can be avoided as the *Lorentz* structure of the gluon propagator becomes proportional to the identity operator $\mathcal{P}_{AA}^{-1} \sim \delta_{\mu\nu}$, see Eq. (C.16). For convenience, we shall therefore employ *Feynman-'t Hooft* gauge and set $\xi = 1$.

3.3.1 Running Gauge Coupling at Finite Temperature and Scale-Fixing Procedure

Let us now discuss the structure of the four-quark beta functions in our study. Again, we employ software packages [166, 167] to compute the beta functions of our renormalized four-quark couplings. The general workflow is given in App. D. In contrast to our previous NJL studies, we shall not provide a detailed analytical form of the beta functions associated with the four-quark couplings since the corresponding expressions appear to be rather lengthy and even exceed the one we found in case of the purely fermionic two-flavor and three-color NJL model, see App. E. A typical four-quark beta function in our QCD study is assembled from quadratic fermion loops $\sim \lambda_n \lambda_m$, triangle-type diagrams $\sim \lambda_n g_k^2$, and box-type diagrams $\sim g_k^4$. For instance, the beta function associated with a coupling λ_i being part of our ten-channel *Fierz*-complete basis (3.38)-(3.47) can be written in $D = 4$ as:

$$\partial_t \lambda_i = 2\lambda_i + \sum_{n,m \in \mathcal{B}} A_{nm}^{(i)}(T, \mu)\, \lambda_n \lambda_m + \sum_{n \in \mathcal{B}} B_n^{(i)}(T, \mu)\, \lambda_n\, g_k^2(T) + C^{(i)}(T, \mu)\, g_k^4(T)\,, \tag{3.74}$$

where $A_{nm}^{(i)}$, $B^{(i)}$ and $C_n^{(i)}$ can be interpreted as generalized "threshold functions" related to the fermionic-, and mixed-type one-loop diagrams, respectively.

For our semi-analytical derivation, we further made some consistency checks, e.g., we have tested that in the limit $g_k \to 0$, we recover the beta functions corresponding to the purely fermionic NJL-type model Eqs. (E.4)-(E.13). Moreover, for vanishing temperature and quark chemical potential, our system of beta functions is in agreement with *Fierz*-complete vacuum studies from previous works, see, e.g., Ref. [301], at least if we consider a *covariant* four-dimensional regularization scheme.

We briefly review the mechanism of spontaneous symmetry breaking in chiral QCD at finite temperature. In that sense, the present discussion is a sequel of Sec. 2.3.2. At vanishing temperature, we already discussed that for $g_k > 0$ the parabola associated with a one-channel four-quark beta function is shifted downwards, see Fig. 2.5. The *Gaussian* and non-*Gaussian* fixed point then merge at some $g_{\mathrm{cr}} = g_{k=k_{\mathrm{cr}}}$ at a critical scale k_{cr}. In this setting, the RG flow is for $g_k > g_{\mathrm{cr}}$ not controlled by any real-valued fixed point anymore so that spontaneous symmetry breaking can occur. This is the basic mechanism in the vacuum for only one four-quark channel, see Fig. 2.5. We now discuss the modifications when a thermal heat bath is present. At finite temperature, loop contributions are screened due to a thermal *Matsubara* mass, see also our discussion in Sec. 3.1.2. Therefore, one usually observes a complicated interplay between gauge and thermal degrees of freedom. While gauge degrees of freedom "push" the parabola downwards so that the real-valued fixed points disappear, see solid black curve in Fig. 3.14, thermal degrees of freedom suppress loop contributions and can recreate the theory's fixed points in the *infrared* (dashed red curve). In the deep *infrared* $k \to 0$, only the linear part $\sim \lambda_i$ of the beta function is present in Eq. (3.74) as the
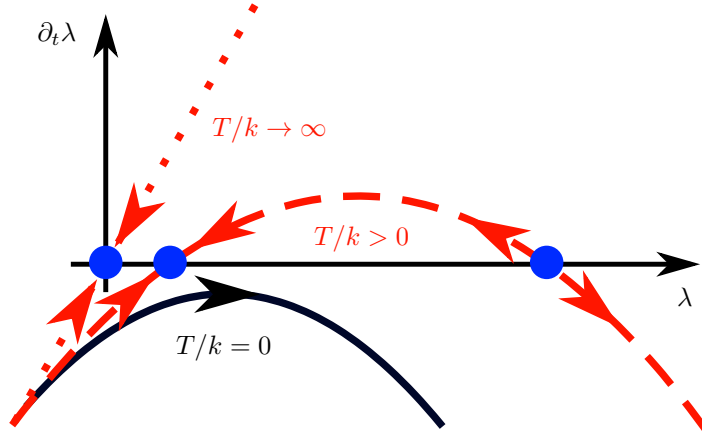
Figure 3.14: Illustration of a typical four-quark beta function at finite temperature. Thermal degrees of freedom broaden and heighten the parabola associated with the four-quark beta function. Even though the parabola is not controlled by real-valued fixed points (solid black curve), spontaneous symmetry breaking can be delayed or even prevented at finite temperature as the fixed points can be recreated in the *infrared* (dashed red curved). In the deep *infrared*, the non-*Gaussian* fixed point is pushed towards infinity so that the *Gaussian* fixed point dominates the RG flow. For details, see main text.

non-*Gaussian* fixed point is moved towards infinity. Therefore, to trigger spontaneous symmetry breaking at finite temperature, the gluon degrees of freedom have to move the parabola downwards "sufficiently" fast as a function of the RG time so that symmetry breaking can occur.

Let us now discuss the scale-fixing procedure of our QCD-type study. To make contact to the NJL-type studies from the previous sections, we adjust the UV value of the strong gauge coupling $g_{k=\Lambda}^2$ at the UV scale $\Lambda = 10\,\text{GeV}$ so that we recover the critical temperature $T_{\text{cr}}(\mu = 0) = T_0 = 0.0132\,\Lambda$ computed in a recent lattice QCD study [9]. Again, the critical temperature T_0 is defined as the value of T below which all four-quark couplings diverge. We stress that we now set the UV values of the four-quark couplings to zero $\lambda_i^{(\text{UV})} = 0$ for all $i \in \mathcal{B}$. The four-quark interactions are then solely generated by strong gauge dynamics. Therefore, for QCD with massless quark flavors the remaining parameter is the strong gauge coupling.

We estimate the influence of the neglected vacuum polarization Eq. (3.73) by comparing the critical temperature in the (T, μ) plane as obtained from two different choices for N_f. On the one hand side, we consider $\alpha_{\text{YM}} = g_k^2(T, N_f = 0)/(4\pi)$ which corresponds to a pure *Yang-Mills* (YM) RG running of the strong gauge coupling. In this case, no fermionic vacuum polarizations are present. On the other hand, we study $\alpha_{\text{QCD}} = g_k^2(T, N_f = 2)/(4\pi)$ associated with the RG running of two-flavor QCD where diagrams like Eq. (3.73) are included, but do not depend on the quark chemical potential. Since α_{YM} does not include any matter contributions whereas the latter are present for all μ in case of α_{QCD}, we expect that the "true" μ-dependent running strong coupling of two-flavor QCD should be located between α_{YM} and α_{QCD}, see Ref. [303]. Note that we use for both types of α_k the same scale-fixing procedure as described above. Naturally, we then have $T_{0,\text{YM}} = T_{0,\text{QCD}}$ by construction. Fixing the critical temperature at zero chemical potential, we obtain the following UV initial values for the strong gauge coupling: $\alpha_{\text{QCD}}^{(\text{UV})} \equiv \alpha_{k=\Lambda}(T/\Lambda = 0.0132, N_f = 2) \simeq 0.212$ (QCD) and $\alpha_{\text{YM}}^{(\text{UV})} \equiv \alpha_{k=\Lambda}(T/\Lambda = 0.0132, N_f = 0) \simeq 0.186$ (YM). The reason why $\alpha_{\text{QCD}}^{(\text{UV})} > \alpha_{\text{YM}}^{(\text{UV})}$ relies on matter screening effects which are present for $N_f > 0$. This can be readily verified by considering the one-loop beta function of the strong gauge coupling:

$$\partial_t g_k^2 = -\left(\frac{22}{3}\,N_c - \frac{4}{3}\,N_f\right)\frac{g_k^4}{(4\pi)^2} + \mathcal{O}(g_k^6).\tag{3.75}$$
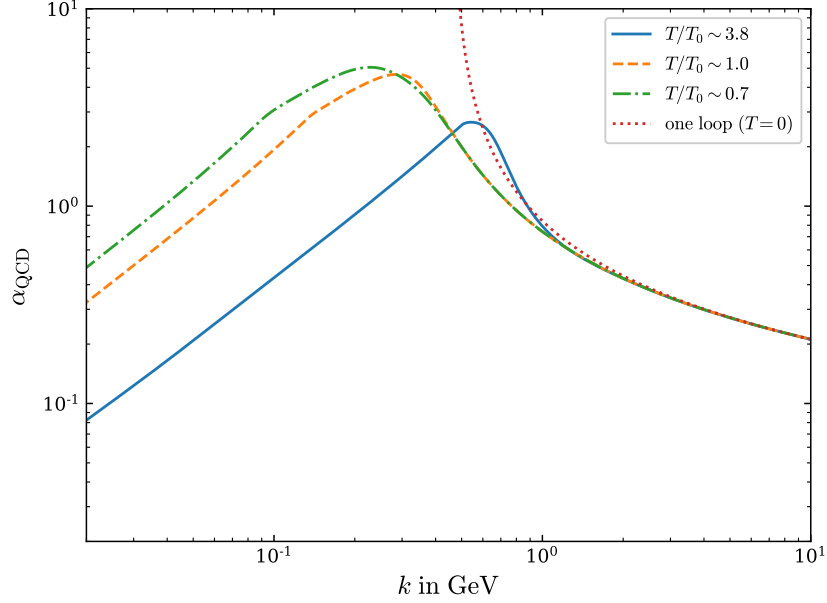
Figure 3.15: Running strong gauge coupling $\alpha_{\mathrm{QCD}} \equiv \alpha_k(T, N_f = 2)$ as a function of the dimensionful scale k as obtained from Refs. [18–20] for three different temperature values as well as from a one-loop study at vanishing temperature. The scale is fixed at $\Lambda = 10\,\mathrm{GeV}$ so that we find a critical temperature $T_0/\Lambda = T_{\mathrm{cr}}(\mu = 0)/\Lambda = 0.0132$, see main text for details.

Here, the matter contribution $\sim N_f$ appears with an opposite sign relative to the *Yang-Mills* term $\sim N_c$. Thus, for increasing N_f, the matter screening effects become larger. As a consequence, $\alpha_{\mathrm{QCD}}^{(\mathrm{UV})}$ has to be greater than $\alpha_{\mathrm{YM}}^{(\mathrm{UV})}$ so that the same critical temperature at zero chemical potential can be adjusted.

Let us further analyze the general behavior of the running strong coupling. In Fig. 3.15, we therefore show the α_{QCD} from [18–20] for three temperature values as a function of the RG scale k. As a comparison, we also present the running of α_k as obtained from a one-loop calculation at zero temperature (dotted red line). The latter exhibits a *Landau*-pole, as soon as the theory becomes strongly coupled by approaching the *infrared* for $k \to 0$. We further note that for large k, all gauge couplings become asymptotically free. Furthermore, we observe for $k \gg T$ that the finite-temperature RG running of the strong gauge couplings from fRG calculations coincide perfectly with the universal vacuum one-loop running from perturbation theory. At $k \sim T$, we can moreover see that the gauge couplings assume a global maximum. Here, we find that the absolute height of this maximum increases for a decreasing temperature and vice versa. This behavior is essential as it controls at which temperature spontaneous symmetry breaking is induced in the four-quark sector. In particular, we observe for $T/T_0 > 1.0$ and $k \to 0$ that the strong gauge coupling α_{QCD} remains below a scale- and temperature-dependent critical value $\alpha_{\mathrm{cr},k}(T)$ rendering all four-quark couplings finite so that no spontaneous symmetry breaking is triggered, see Refs. [18–20] for details. As an example for the latter case, we show α_{QCD} at $T/T_0 \sim 3.8$, see solid blue curve in Fig. 3.15. To trigger spontaneous symmetry breaking, it is necessary that α_{QCD} exceeds $\alpha_{\mathrm{cr},k}(T)$ by approaching the *infrared*. For this, we exemplary show in Fig. 3.15 the strong gauge coupling at $T/T_0 \sim 0.7$ (dashed-dotted green curve) for which we observe that the four-quark couplings diverge at a finite critical scale. Moreover, for momenta $k \ll T$ and $k \to 0$, we observe that the temperature-dependent strong gauge coupling decreases obeying a power-law scaling. The reason for this behavior is based on an effective dimensional reduction of QCD. Since low-lying momentum modes with large wave lengths exceed the finite extent of the temporal box size in *Euclidean* spacetime, the theory becomes effectively three dimensional. The system is then attracted by a non-*Gaussian* IR fixed point of three-dimensional QCD being associated with a power-law scaling behavior for $k \to 0$, see Ref. [18] for details.
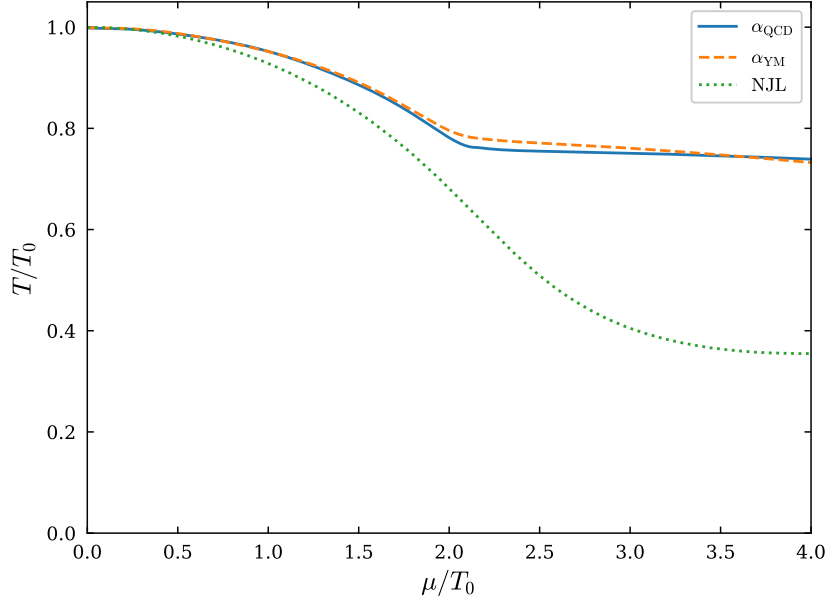
Figure 3.16: Phase boundary of chiral two-flavor QCD in the (T, μ) plane. We compare the critical temperatures as obtained from α_{QCD} with two quark flavors (solid blue line), from pure *Yang-Mills* theory α_{YM} (dashed orange line), and our NJL model study with two flavors and three colors from Sec. 3.2 (dotted green line). See main text for details.

3.3.2   Phase Boundary of Chiral Two-Flavor QCD

Let us eventually discuss the phase structure of two-flavor QCD as it is found by considering the ansatz (3.65) for the effective action. For this, we show in Fig. 3.16 the finite-temperature phase boundary in the (T, μ) plane as it is obtained from α_{YM} ($N_f = 0$, dashed orange line) and from α_{QCD} ($N_f = 2$, solid blue line), see also our discussion in the previous section. We stress again that we only assume a finite UV value for the strong gauge coupling whereas we set $\lambda_i^{(\mathrm{UV})} = 0$ for all $i \in \mathcal{B}$. Note that this choice of UV initial conditions respects the axial $U(1)_A$ symmetry which is then preserved throughout the RG flow. Moreover, we compare the QCD results with the phase boundary we have originally found in the purely fermionic two-flavor and three-color *Fierz*-complete NJL model study using $U(1)_A$-symmetric initial conditions (dotted green line), see also Sec. 3.2.

First, we notice that we cannot find any indications for a critical chemical potential μ_{cr} at zero temperature as it was found, e.g., in our NJL model study with one flavor and one color (Sec. 3.1.2) or for the one-channel approximation in our two-flavor and three-color NJL model (Sec. 3.2.1). Further, we observe that the phase boundaries as obtained from a *Yang-Mills* and QCD running gauge coupling agree well over a wide range of quark chemical potential. Remarkably, we find that both phase boundaries exhibit small "kinks" at a quark chemical potential $\mu/T_0 \sim 2.0$ where the slopes change notably, see also our discussion at the end of this section. By comparing the phase boundaries as obtained from α_{QCD} and α_{YM} with the one originally found in the NJL model study from Sec. 3.2, we observe that the overall shapes of all three phase boundaries qualitatively agree at least for $\mu/T_0 < 2.0$. For larger quark chemical potential, however, this appears not to be the case. In particular, the critical temperature at $\mu/T_0 \sim 4.0$ associated with two-flavor QCD is approximately 100% greater than the one we find in the purely fermionic NJL model. Apparently, from our observations we deduce that gauge degrees of freedom seem to have a significant impact and increase the critical temperature at large quark chemical potential considerably.

Let us now discuss the symmetry breaking patterns in our two-flavor QCD study. In the upper panel of Fig. 3.17, we show the phase boundary in the (T, μ) plane as computed from the running gauge coupling with $N_f = 2$. In this figure, the dominant four-quark couplings close to the phase boundary are highlighted by using two different line colors. In particular, at low quark chemical potential $\mu/T_0 \leq 2.0$, we observe a dominance of the scalar-pseudoscalar channel indicating the spontaneous breakdown of chiral symmetry and the formation of a non-zero chiral condensate (solid blue line). Exemplary, we therefore show the corresponding RG flow of the various dimensionful four-quark couplings $\bar{\lambda}_i$ at $\mu/T_0 \simeq 1.0$ close to the critical temperature $T_{\mathrm{cr}}(\mu/T_0 = 1.0)/T_0 \gtrsim 0.95$ as a function of the RG scale k, see the central panel in Fig. 3.17. By comparing the relative strengths of the ten four-quark channels, we can readily verify that the $(\sigma\text{-}\pi)$ channel appears to be the utmost dominant channel at low quark chemical potential. Note, even though we found in our previous NJL model study (see Fig. 3.10) for $\mu/T_0 \lesssim 1.8$ a dominance of the scalar-pseudoscalar channel, we could not be sure whether the emerging dominance pattern was probably just an "artifact" of the choice of our boundary conditions for the RG flow, i.e., we assumed a non-zero UV value of the scalar-pseudoscalar channel in our study. In the light of our two-flavor QCD study, however, we find that a dominance of the scalar-pseudoscalar channel originates solely from dynamics in the strong gauge sector. In that sense, our previous choice of UV initial conditions for the low-energy model can indeed be justified by the present QCD study.

At large quark chemical potential, we previously found indications for the formation of a diquark condensate implying a (BCS-type) color superconducting ground state. As we shall discuss now, our QCD study confirms these observations. Above, we already mentioned that the slopes of the phase boundaries (cf. Fig. 3.16) change significantly at $\mu/T_0 \sim 2.0$. Interestingly, we observe that the latter quark chemical potential coincides with the one above which the dominance pattern changes. For $\mu/T_0 \gtrsim 2.0$, we then find that the $(S + P)^{\mathrm{adj}}_-$ as well as the csc channel become dominant simultaneously, see dashed orange line. From the sum rule (3.49), this behavior is expected as we start the RG flow with $\lambda_i^{(\mathrm{UV})} = 0$ implying that the axial $U(1)_A$ symmetry is conserved. In the lower panel of Fig. 3.17 we illustrate the RG flow of the ten dimensionful four-quark couplings at $\mu/T_0 \simeq 4.0$ close to the critical temperature $T_{\mathrm{cr}}(\mu/T_0 = 4.0)/T_0 \gtrsim 0.74$. By construction, the RG flows associated with the $(S + P)^{\mathrm{adj}}_-$ and the csc channel fulfill $\bar{\lambda}_{\mathrm{csc}} = -\bar{\lambda}_{(S+P)^{\mathrm{adj}}_-}$. It is remarkable, however, that we observe a dominance of these two channels even though we start with $U(1)_A$-conserving initial conditions. Recall that we found in the NJL-model study the $(V + A)^{\mathrm{adj}}_\parallel$ channel to be dominant for large quark chemical potential in the $U(1)_A$-symmetric case. A dominance of the latter channel would be then associated with the formation of a finite spin-1 condensate. However, our QCD study rather suggests the emergence of a spin-0 condensate which would break the axial $U(1)_A$ symmetry. In principle, we can also "implement" the anomalous breaking of the $U(1)_A$ symmetry on the level of the initial conditions by choosing $\lambda_{(S+P)_-}^{(\mathrm{UV})} > 0$ mimicking the effect of instanton-induced vacuum transitions in the UV. We qualitatively tested such modifications for $0 < \lambda_{(S+P)_-}^{(\mathrm{UV})} \lesssim 1$ and found that the position of the phase boundaries as well as the dominance pattern remain almost unchanged. For a quantitative study it would be necessary to compute the instanton density from which it would be possible to estimate the corresponding value of the $(S + P)_-$ channel at a given RG initial scale, see, e.g., Refs. [193, 194, 293]. In any case, this would go beyond the scope of the present discussion.
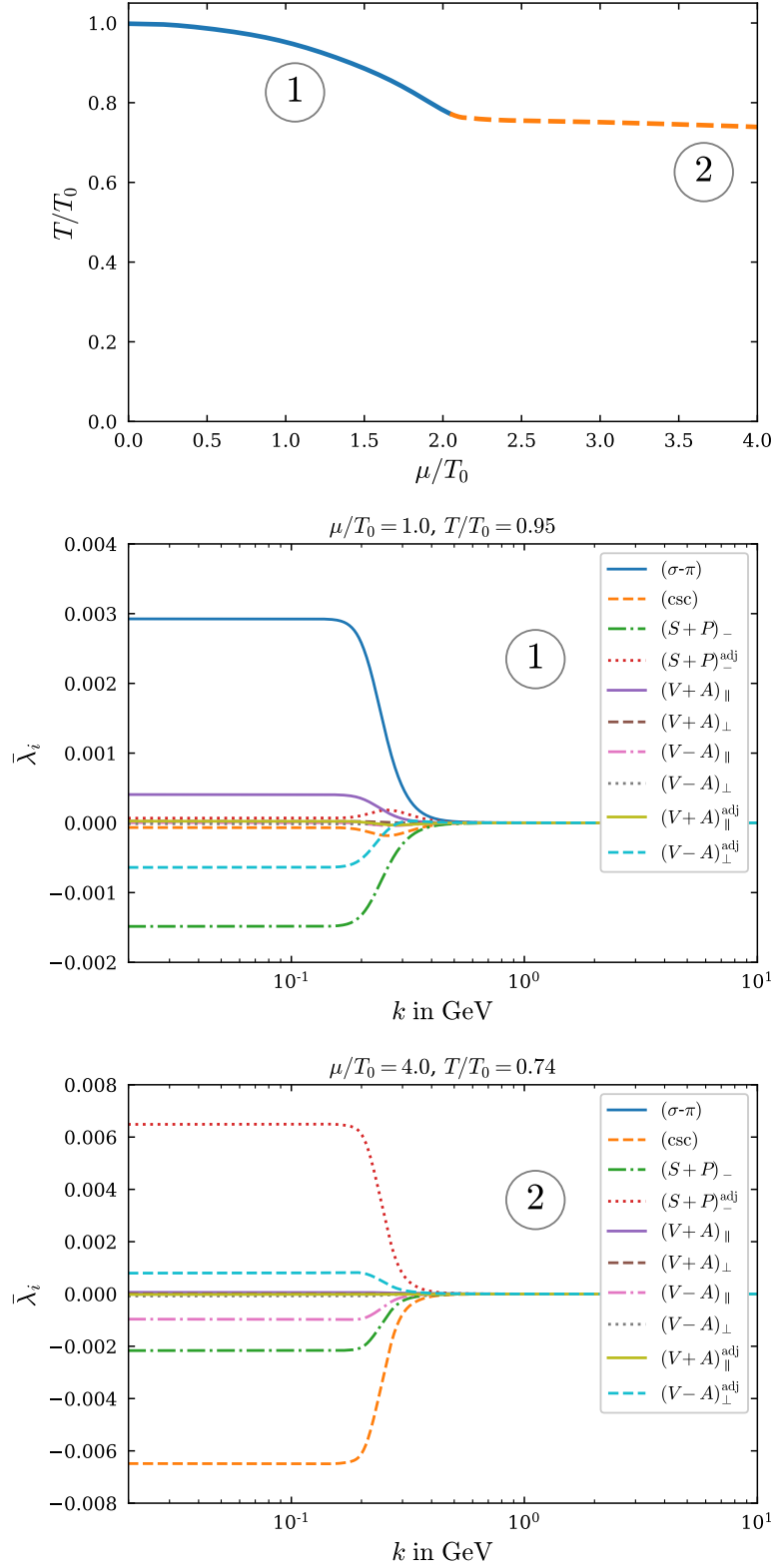
Figure 3.17: Phase structure of two-flavor QCD from the running gauge coupling α_{QCD} (upper panel) in the (T, μ) plane. Central and lower panel: RG running of the dimensionful four-quark couplings for two values of the quark chemical potential close to the phase boundary $T \gtrsim T_{\mathrm{cr}}(\mu)$. For $\mu/T_0 \lesssim 2.0$, the scalar-pseudoscalar channel appears to be dominant (solid blue line) where for $\mu/T_0 \gtrsim 2.0$ the observed dominance pattern suggests a ground state rather dominated by diquarks (dashed orange line), see main text for a discussion.

3.4   Discussion and Outlook

Let us summarize our results from the first part of this thesis and give an outlook to ongoing studies based on the present work. We began in Sec. 3.1 with a *Fierz*-complete NJL-type model with one flavor and one color. First, we studied the RG flow of the four-fermion couplings in the vacuum and analyzed the fixed-point structure of the underlying theory space. At finite temperature T and quark chemical μ, we explored the phase boundary as it was found from a one-channel, two-channel and a *Fierz*-complete three-channel ansatz. We further analyzed how *Fierz*-incomplete truncations affect the predictive power of model studies where we showed that the shapes of the phase boundaries associated with *Fierz*-incomplete approaches are considerably altered. The dominance pattern of the four-fermion channels close to the phase boundary provided us with some indications about the nature of the condensate forming in the low-energy regime. We used two different *Fierz*-complete parametrizations for the four-fermion sector and found that the dynamics close to the phase boundary is governed over a wide range of the quark chemical potential by the scalar-pseudoscalar channel suggesting the onset of spontaneous chiral symmetry breaking. At large quark chemical potential, we found in both *Fierz*-complete parametrizations dominances in channels which are associated with the spontaneous breakdown of the *Poincaré* symmetry.

In Sec. 3.2, we discussed a *Fierz*-complete NJL model with two flavors and N_c colors at finite temperature and quark chemical potential. The *Fierz*-complete basis we found in this case is composed of ten four-quark channels which are invariant under global $SU(N_c) \times SU(2)_L \times SU(2)_R \times U(1)_V$ transformations. We studied the phase structure in the (T, μ) plane and examined the underlying dominance patterns. For $U(1)_A$-breaking initial conditions, we found for our *Fierz*-complete parameterization that the dynamics close to the phase boundary is expected to be dominated by chiral degrees of freedom at small quark chemical potential where a dominance of the diquark channel indicated that a color superconducting ground state is favored at large quark chemical potential. Inspired by the observed dominance pattern of the *Fierz*-complete approach, we studied a *Fierz*-incomplete two-channel ansatz and analyzed the pseudo fixed-point structure which then gave rise to a possible mechanism allowing for a dynamical change in the observed dominance pattern from the scalar-pseudoscalar to the diquark channel by varying the quark chemical potential.

Eventually, we studied the phase boundary and symmetry breaking patterns of two-flavor QCD in the chiral limit, see Sec. 3.3. We employed the ten-channel *Fierz*-complete four-quark basis from Sec. 3.2 and included the quark-gluon vertex in our ansatz. In the *background-field* formalism, we identified the coupling associated with the quark-gluon vertex with the scale-dependent gauge coupling from QCD adopting the one from Refs. [18–20]. Since QCD induces fermion self-interactions at one-loop order by means of two-gluon exchange, the four-quark couplings are now generated dynamically in the RG flow. We studied the phase structure in the (T, μ) plane where we compared the QCD phase boundary with the one we have found in our NJL model study. We observed that gluon degrees of freedom are expected to become particularly important in the regime at large quark chemical potential where we found that the critical temperature in QCD appears to be significantly larger than in the NJL model case. From our *Fierz*-complete analysis of the dominance patterns, we moreover concluded that the regime at low quark chemical potential is expected to be dominated by spontaneous chiral symmetry breaking where at large quark chemical potential the onset of diquark condensation becomes favorable.

A long-term goal of our studies is to provide a fully *ab initio* description of dense strong-interaction matter and a systematic computation of the corresponding equation of state. Clearly, the present study represents only a first step towards future efforts. Nevertheless, as we shall discuss below, the results from the present work can be already helpful to constrain the equation of state at least in the isospin-symmetric case at zero temperature. To compute the equation of state, e.g., the pressure as a function of the chemical potential $P(\mu)$, it is necessary to compute the full quantum effective action since

$$P = -\frac{1}{V_4} \lim_{T \to 0} T\,\Gamma[\Phi_{\mathrm{gs}}]\,, \tag{3.76}$$

where V_4 is the four-dimensional spacetime volume and Φ_{gs} denotes the ground state of the theory under consideration, see, e.g., Ref. [276]. Throughout our *Fierz*-complete four-fermion studies, we employed the derivative expansion in leading order implying the so-called pointlike limit for the four-quark vertex. We further discussed that the pointlike limit neglects relevant information, i.e., it only allows us to detect the onset of spontaneous symmetry breaking but does not allow us to study the system within the broken regime. Therefore, our present truncation is only suited for the symmetric regime and low-energy observables remain inaccessible. In this approximation, the equation of state in the symmetric regime at zero temperature and finite quark chemical potential then corresponds to the *Stefan-Boltzmann* pressure P_{SB} of an ideal gas of non-interacting quarks at zero temperature

$$P_{\mathrm{SB}} = N_c N_f \frac{\mu^4}{12\pi^2} \, . \tag{3.77}$$

From our QCD study with two flavors, we would expect that the low-energy physics is mostly governed by chiral degrees of freedom at low and by diquark degrees of freedom at large quark chemical potential. This observation can be used to construct an effective low-energy model and combine it with the results from our QCD study in order to gain access to low-energy observables and the equation of state, respectively. For this, let us briefly outline the overall strategy:

Our dominance pattern suggests to use a so-called quark-meson-diquark (QMD) model for the low-energy sector which take mesonic, the σ meson and pions, as well as diquark degrees of freedom into account, see Refs. [28, 35, 54, 276, 277, 304, 305]. Together with our *Fierz*-complete QCD study, we can constrain the input parameters of the QMD model by using our findings from the high-energy sector. To this end, we extract at zero temperature the coupling values associated with the $(\sigma$-$\pi)$ and the csc-channel from the *Fierz*-complete QCD RG flow of four-quark couplings at different "transition" scales $\Lambda_0 > k_{\mathrm{cr}}(T = 0, \mu)$ and for different quark chemical potentials μ. In a next step, we can then use the "measured" ratio of the scalar-pseudoscalar and the diquark coupling at the scale Λ_0 as a boundary condition for the parameters entering the QMD model. To analyze the dependence of our predictions for low-energy observables on the "transition" scale, we vary Λ_0. For more details about the boundary conditions and our scale-fixing procedure, we refer to Ref. [54].

Our first very recent study [54] in this direction indicates that the so-derived equation of state of isospin-symmetric nuclear matter already provides reasonable results for the intermediate density regime $20 \lesssim n/n_0 \lesssim 300$, where n_0 denotes the nuclear saturation density. By studying the speed of sound c_s^2 as a function of the nuclear density, one recognizes that at large densities $n/n_0 > 100$, the value of the speed of sound approaches the *Stefan-Boltzmann* limit of an ideal fermion gas $c_s^2 = 1/3$, see, e.g., Refs. [59, 60]. Nevertheless, recent constraints on the speed of sound from mass-radius observations of neutron stars [306] suggest that c_s should exceed this limit at intermediate densities. By also taking diquark degrees of freedom into account, a local maximum of the speed of sound can indeed be observed [54]. Here, the estimated peak height is rather insensitive to a variation of the read-out scale, where we find $c_s^2 \approx 0.42$ for $\Lambda_0 = 450\,\mathrm{MeV}$. The position of the peak, however, is sensitive to the latter and varies between $n/n_0 \approx 10 \ldots 20$ for $\Lambda_0 = 450 \ldots 600\,\mathrm{MeV}$. Moreover, our current research suggests that the consideration of diquark degrees of freedom is crucial for the existence of such a local maximum at intermediate densities. For further details, see Ref. [54].

To study the low-energy regime of QCD in future works, one may further introduce a k-dependent classical field Φ_k allowing for a continuous "transition" from high-energy to low-energy degrees of freedom. Such an ansatz has various advantages, e.g., low-energy observables can be accessed by also taking fluctuations beyond *mean-field* approximation into account, see Refs. [22, 23, 159, 161–164, 235, 240–242, 307]. A next step towards a full *ab initio* description of dense quark matter would be therefore to employ dynamical bosonization techniques. In particular, in a first study it might be sufficient to keep track of all ten four-quark channels and dynamically bosonize only the scalar-pseudoscalar and the diquark channel which we expect to become resonant in the *infrared*. In this case, the order-parameter potential as well as the equation of state can then be computed without any use of a "transition" scale. In fact, since the scale Λ_0 emerges naturally in the dynamical hadronization process, any dependence of the low-energy observables on Λ_0 disappears.

Part II

Non-Relativistic Cold and Dilute Matter

Chapter 4

Renormalization Group and Density Functional Theory

In the second part of the present thesis, we shall now study non-relativistic one-dimensional fermion matter at zero temperature by employing a Renormalization Group inspired approach to Density Functional Theory (DFT-RG). For this, we begin in Sec. 4.1 with a short overview of the main statements of the famous *Hohenberg-Kohn* (HK) theorem as it represents the foundation of conventional Density Functional Theory (DFT).

Starting from a global ansatz for the HK energy density functional, we outline the derivation of the famous *Kohn-Sham* (KS) equations in Sec. 4.2.1. Solving the latter self-consistently then correspond to a minimization of the HK energy density functional. To include *exchange-correlation* effects in conventional DFT studies, we briefly discuss two so-called *coupling-constant* integration techniques and introduce the *Local-Density Approximation* (LDA).

In Sec. 4.3, we introduce a Renormalization Group approach to DFT, which relies on the relation between the HK energy density functional and the two-particle-point-irreducible (2PPI) effective action. For this, we discuss some field-theoretical technicalities of the DFT-RG framework before we present a one-dimensional nuclear model of few fermions which interact via a short-range repulsive and long-range attractive two-body interaction. We show results for the ground-state energy per particle as a function of the confining box size and give an estimate for the few-body ground-state energy in the continuum limit. In the end of Sec. 4.3, we present an improvement for the truncated DFT-RG flow equations by using a KS system as a starting point.

Section 4.4 then deals with a system of quasi-one-dimensional dipolar fermions which are confined in an external harmonic potential. We briefly introduce the setting of our model and compute for different truncated DFT-RG flows the ground-state energy per particle as a function of the dipolar coupling strength where we compare our results with those from exact diagonalization.

4.1   The Hohenberg-Kohn Theorem

DFT is originally based on a very famous theorem by *Hohenberg* and *Kohn* in 1964. The essential statement of the *Hohenberg-Kohn* (HK) theorem [103, 104] is the observation that there exists a one-to-one correspondence between the external potential v_{ext}, the ground-state wave function $|\psi_0\rangle$, and the ground-state density n_{gs} of a many-body quantum system. From this, it can be followed that there exists a universal functional $F[n]$ which is independent on the particular choice of the external potential $v_{\text{ext}}(x)$, see our discussion below. More generally, the HK theorem implies that all ground-state observables can be expressed as functionals of the density which can be advantageous in many-body calculations. For instance, an N-body system is naturally described by at least $3N$ (spatial) coordinates. However, since only three spatial coordinates specify the density, DFT allows for a reduction of the required coordinate space from $3N$ to three. Potentially, it therefore allows for an effective description of
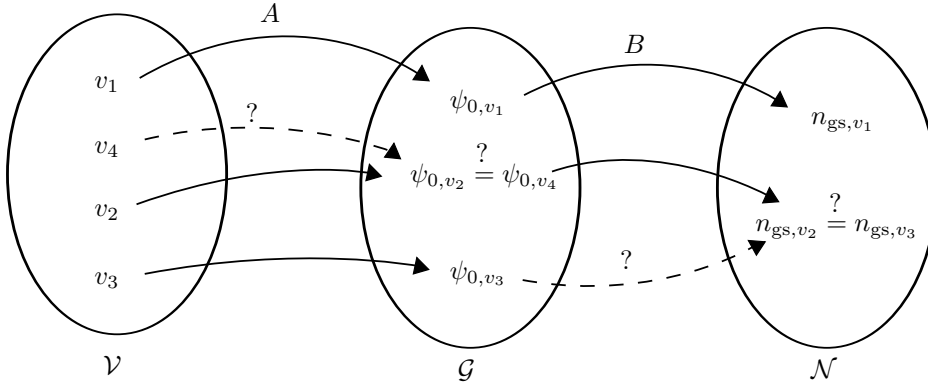
Figure 4.1: The graphic illustrates the main statement of the HK theorem. The latter ensures, e.g., that there is no ground-state wave function which simultaneously belongs to two different external potentials. (figure adopted from Ref. [308]).

many-body systems

Let us now briefly discuss some key aspects of the HK theorem. For this, we adopt the discussion from Ref. [308]. Note that in the following we shall assume that the ground state of a given many-body problem is non-degenerate. We begin with the definition of three sets. The first one contains external potentials v_{ext} which differ by more than a constant:

$$\mathcal{V} \quad = \quad \{v_{\text{ext}} \,|\, v_{\text{ext}} \text{ is multiplicative, corresponding non-degenerate ground state } |\psi_0\rangle \text{ exists,}$$
$$\text{potentials differ by more than a constant } v'_{\text{ext}} \neq v_{\text{ext}} + \text{const.}\} \,. \tag{4.1}$$

We further define a set of distinct ground-state wave functions belonging to the external potentials in $\mathcal{V}$:

$$\mathcal{G} \quad = \quad \{|\psi_0\rangle \,|\, |\psi_0\rangle \text{ is ground state corresponding to one element in } \mathcal{V},$$
$$\text{ground states differ by more than a phase factor } |\psi'\rangle \neq e^{\mathrm{i}\phi} |\psi\rangle\} \,. \tag{4.2}$$

The final set contains ground-state densities which are computed from the ground-state wave functions above:

$$\mathcal{N} = \{n_{\text{gs}} \,|\, n_{\text{gs}} = \langle\psi_0| \, n \, |\psi_0\rangle \text{ is a ground-state density associated with } |\psi_0\rangle \in \mathcal{G}\} \,. \tag{4.3}$$

We may now define two maps $A : \mathcal{V} \to \mathcal{G}$ and $B : \mathcal{G} \to \mathcal{N}$ for the three sets given above. On the one hand, one can now ask whether there is a ground-state wave function in $\mathcal{G}$ which stems simultaneously from two different potentials in $\mathcal{V}$. On the other hand, one may ask whether there exists a ground-state density in $\mathcal{N}$ which originates from two distinct ground-state wave functions in $\mathcal{G}$, see also Fig. 4.1. The important statement of the HK is that this can not be the case. Therefore, the maps A and B are unique. For a proof of the HK theorem, see Ref. [103]. From the uniqueness of A and B we deduce the existence of an inverse map B^{-1} which then defines a unique functional of the density $|\psi[n]\rangle$. The latter maps the ground-state density n_{gs} onto the corresponding ground-state wave function $|\psi_0\rangle$. The so-defined functional is universal and identical for all systems with similar interaction. Moreover, it does not depend on the external potential v_{ext}. Note, however, that the information on v_{ext} is still encoded in the structure of the ground-state density n_{gs} as a consequence of the HK theorem. From the latter, we can now express any observable as a functional of the density

$$O[n] \quad \equiv \quad \langle\psi[n]| \, O \, |\psi[n]\rangle \,. \tag{4.4}$$

In particular, we can define the following universal functional $F[n]$ which is given by

$$F[n] \equiv \langle \psi[n] | \, T + W \, | \psi[n] \rangle \,, \tag{4.5}$$

with a many-body kinetic energy operator T and an interaction W. From this, we can write down the famous energy density functional via

$$E[n] \equiv F[n] + \int_x v_{\text{ext}}(x) n(x) \,. \tag{4.6}$$

From the *Rayleigh-Ritz* variational principle [309], one can further show that the correct ground-state energy of the many-body problem is given by minimizing the energy density functional:

$$E_{\text{gs}} = \inf_n E[n] \,. \tag{4.7}$$

The many-body problem can therefore be reformulated in the following sense. In order to compute the ground-state energy of a quantum system under consideration, it suffices to minimize the energy density functional $E[n]$, instead of diagonalizing the many-body Hamilton operator.

In Eq. (4.7) we defined the ground-state energy as the infimum of the energy density functional $E[n]$. The latter could indicate the existence of a variational principle to compute the ground-state density of a many-body system via

$$\frac{\delta}{\delta n(x)} \left\{ E[n] - \mu \left(\int_x n(x) - N \right) \right\} \bigg|_{n(x)=n_{\text{gs}}(x)} = 0 \,, \tag{4.8}$$

with a chemical potential μ and the particle number N. However, from a mathematical point of view, the existence of the expression (4.8) is not guaranteed as it requires that $E[n]$ is at least defined on a sufficiently dense set of densities n. As one can show, this relates to the problem whether there exists an external potential v_{ext} for all possible normalized densities n, which simultaneously correspond to the ground state of v_{ext}. The question is whether all densities n are *v-representable*. Indeed, one can find counterexamples where even positive-semidefinite and continuous densities do not fulfill this requirement implying that these densities are not *v-representable*, see, e.g., Ref. [310]. For certain systems and external potentials, there exists a solution based on the *Lieb* functional [310–312] representing an extension of the *Hohenberg-Kohn* density functional in a sense that the functional derivative (4.8) exists. However, such a discussion exceeds the scope of the present work. For details, we refer to classical textbooks on this topic, e.g., see Ref. [308].

So far, we did not discuss how the functional $F[n]$ can be derived. Unfortunately, the HK theorem only guarantees the existence of $F[n]$ but does not provide a "recipe" for the computation of the exact energy density functional. Presumably, the structure of the functional $F[n]$ has to be very complicated as it has to be valid for any particle number and external potential for a given W. In general, it is therefore not possible to write down the exact energy density functional. Instead, it is necessary to find reliable expansion and approximation schemes. In Sec. 4.2, we shall discuss this issue in more detail.

In atomic physics, quantum systems like molecules can often be described by employing a *Born-Oppenheimer* approximation [313]. In this case, the electrons seem to be confined within a "static" external potential v_{ext} generated by the surrounding atomic nuclei. For selfbound many-body quantum systems like nuclei, however, no such potential exists. Moreover, in nuclear DFT the construction of the energy density functional does often rely on making a global ansatz for $F[n]$ so that parameters entering such a study originate from fits of external experimental data. In any case, nuclear DFT appears to be the only feasible many-body technique to study nuclei in the heavy mass region. In the past years, the applicability of nuclear DFT in this region has been impressively demonstrated by various work, e.g., by the UNEDF/NUCLEI SciDAC collaboration, see Refs. [99–102] and also Ref. [105]. There-

fore, it is of great importance to further develop new theoretical tools for nuclear DFT to construct both systematic and microscopic nuclear energy density functionals.

4.2   The Kohn-Sham Approach to DFT

In this section, we introduce the KS equations and outline the main steps for their derivation. For this, the HK energy density functional is usually decomposed into different contributions which we shall discuss in detail separately. A minimization of the ansatz then provides us with the self-consistent KS equations which are usually solved by making an initial guess for the density. We further point out the obstacles of conventional DFT when one tries to take *exchange* and *correlation* effects into account. Therefore, we discuss in the second subsection techniques like *coupling constant* integration which allow in principle to include non-trivial *exchange-correlation* contributions in a rather systematic way. Briefly, we also present the *Local-Density Approximation* (LDA) which appears to be a very frequently employed truncation in various DFT calculations.

4.2.1   The Kohn-Sham Equations

The famous KS equations [104] were published one year after the proof of the HK theorem. In their work, *Kohn* and *Sham* used the one-to-one correspondence between the ground-state density n_{gs}, the external potential v_{ext}, and the ground-state wave function $|\psi_0\rangle$ to map the density of an interacting many-body problem onto a problem of non-interacting fermions confined in a suitably chosen external potential v_{KS}. The latter then mimics the complicated many-body *exchange-correlation* contributions which are present in a many-body quantum system. To compute the KS equations (see Ref. [308] for a pedagogical introduction), one starts by considering the following general ansatz for the HK energy density functional:

$$E[n] = T_{\mathrm{s}}[n] + E_{\mathrm{ext}}[n] + E_{\mathrm{H}}[n] + E_{\mathrm{xc}}[n]\,. \tag{4.9}$$

To better understand the idea behind the decomposition (4.9), let us now discuss the different contributions in more detail. The first part $T_{\mathrm{s}}[n]$ denotes the kinetic energy functional of N non-interacting fermions[14] and is defined by

$$\langle\Phi[n]|\,T_{\mathrm{s}}\,|\Phi[n]\rangle = T_{\mathrm{s}}[n] = \sum_i \theta(-\bar{\varepsilon}_i) \int_{x_1} \phi_i^*[n](x_1) \left(-\frac{\partial_{x_1}^2}{2}\right) \phi_i[n](x_1)\,, \tag{4.10}$$

where we use the following convention for the *Heaviside* function:

$$\theta(\pm\bar{\varepsilon}_i) = \begin{cases} 1 & \text{for} \quad \pm\bar{\varepsilon}_i \mp \eta > 0\,, \\ 0 & \text{otherwise}\,, \end{cases} \tag{4.11}$$

with $\bar{\varepsilon}_i = \varepsilon_i - \varepsilon_{\mathrm{F}}$ where we tacitly assume $\eta \to 0^+$. Moreover, $|\Phi[n]\rangle$ shall denote the N-particle *Slater* determinant consisting of an antisymmetrized product of N single-particle states[15]. One may wonder why the single-particle states $\phi[n](x)$ are functionals of the density as well. This observation follows directly from the HK theorem by considering that a variational change in the density, e.g., by a variation of the external potential of the system, leads to a simultaneous response of the orbitals as well.

The second term in Eq. (4.9) contains the external potential and reads

$$E_{\mathrm{ext}}[n] = \int_{x_1} v_{\mathrm{ext}}(x_1)\,n(x_1)\,. \tag{4.12}$$

---

[14]For convenience, we focus in this work on one-dimensional and non-degenerate quantum systems.

[15]Note that we assume for simplicity that the non-interacting ground state is non-degenerate, see, e.g., Ref. [308] for a discussion of generalizations.

Density

$n_{\mathrm{gs}}(x)$

Potential   KS orbitals

$v_{\mathrm{KS}}[n](x)$ $\phi_i[n](x)$
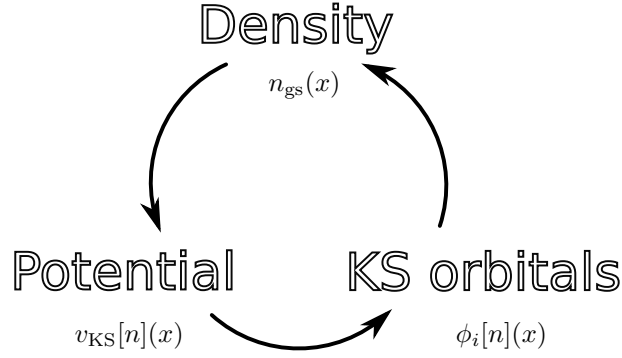
Figure 4.2: Self-consistent *Kohn-Sham* iteration procedure. One usually starts with a trial density n_0 or a trial KS potential $v_{\mathrm{KS},0}$. The KS equations (4.14) are then solved repeatedly until some convergence criterion is achieved, e.g., the difference between ground-state energies of two adjacent iteration steps is smaller than a predefined uncertainty.

Here, we assume that the external potential $v_{\mathrm{ext}}(x)$ is "static" and does not depend on the density. Further, the third term in Eq. (4.9) is known as the so-called *Hartree* contribution which reads

$$E_{\mathrm{H}}[n] = \frac{1}{2} \int_{x_1} \int_{x_2} n(x_1) \, U(x_1, x_2) \, n(x_2) \,. \tag{4.13}$$

Note that the *Hartree* term contains no particle-exchange-type $E_{\mathrm{x}}[n]$ or particle-correlation-type $E_{\mathrm{c}}[n]$ energy contributions. For the latter, we have the fourth term in Eq. (4.9) which is called the *exchange-correlation* energy functional $E_{\mathrm{xc}}[n]$ including all complicated non-trivial particle *exchange* and *correlation* energy contribution which are present in an interacting many-body system. From this, it is clear that this part requires the most attention in a KS study. In general, different approaches are possible. In the next subsection, we shall therefore give a quick overview about possible types of approximations for the *exchange-correlation* energy functional.

   Let us now discuss the *Kohn-Sham* equations. In principle, the derivation of the latter can be done straightforwardly by taking the functional derivative of the functional (4.9) with respect to the density. Eventually, we obtain the famous *Kohn-Sham* equations [104] which read

$$\left(-\frac{\partial_x^2}{2} + v_{\mathrm{KS}}[n](x) \right) \phi_i[n](x) = \varepsilon_i \phi_i[n](x) \,, \tag{4.14}$$

with the KS single-particle orbital $\phi_i[n](x)$, the corresponding KS single-particle energy ε_i and the external KS potential

$$v_{\mathrm{KS}}[n](x) = v_{\mathrm{ext}}(x) + v_{\mathrm{H}}[n](x) + v_{\mathrm{xc}}[n](x) \,. \tag{4.15}$$

Here, $v_{\mathrm{ext}}(x)$ denotes the usual external potential and $v_{\mathrm{H}}[n](x)$ the *Hartree* potential. The latter can be written as

$$v_{\mathrm{H}}[n](x) = \int_{x_1} n(x_1) \, U(x_1, x) \,. \tag{4.16}$$

The last term in Eq. (4.15) denotes the *exchange-correlation* potential which can be formally written as

$$v_{\mathrm{xc}}[n](x) = \frac{\delta E_{\mathrm{xc}}[n]}{\delta n(x)} \,. \tag{4.17}$$

Apparently, the *exchange-correlation* potential is not given in a closed form.

Since we compute Eq. (4.14) from a minimization of the functional Eq. (4.9), the ground-state density associated with the HK energy functional is equivalent to the one we find when we solve the *Kohn-Sham* equations. Then, the ground-state density for a non-degenerate quantum system is given by

$$n_{\mathrm{gs}}(x) = \sum_i \theta(-\bar{\varepsilon}_i) \left| \phi_i[n_{\mathrm{gs}}](x) \right|^2 . \tag{4.18}$$

For the degenerate case, we refer again to textbooks, see, e.g., Ref. [308].

As already indicated, the *Kohn-Sham* equations are solved iteratively, see Fig. 4.2. One usually starts the KS cycle with a trial density $n_{\mathrm{gs},0}$ or a trial potential $v_{\mathrm{KS},0}$. In the next step, the single-particle Schrödinger equation (4.14) is (numerically) solved. After the first iteration step, one usually computes from the KS orbitals the new ground-state density $n_{\mathrm{gs},1}$ which is then used to derive the new KS potential $v_{\mathrm{KS},1}$. The procedure is repeated until some predefined convergence criterion is achieved. For example, one can compute the KS ground-state energy

$$E_{\mathrm{gs}}^{\mathrm{KS}}[n = n_{\mathrm{gs}}] = \sum_i \theta(-\bar{\varepsilon}_i)\, \varepsilon_i - \int_x n_{\mathrm{gs}}(x)\, v_{\mathrm{xc}}[n_{\mathrm{gs}}](x) - E_{\mathrm{H}}[n_{\mathrm{gs}}] + E_{\mathrm{xc}}[n_{\mathrm{gs}}] \,, \tag{4.19}$$

and require that $|E_{\mathrm{gs}}^{\mathrm{KS}}[n_{\mathrm{gs},i+1}] - E_{\mathrm{gs}}^{\mathrm{KS}}[n_{\mathrm{gs},i}]| < \delta$, for a predefined $\delta > 0$. The reason why the KS procedure should converge relies on the fact that it corresponds to a minimization of the HK energy functional. Nevertheless, it is also clear that there can be various local minima lying "close" to the real ground state. In such cases, loosely speaking, the convergence of the self-consistent KS procedure can be even "arbitrarily slow" [314].

Let us add some words of caution concerning the interpretation of the KS single-particle states. The latter shall by no means be confused with real excitation energies of the complicated N-body problem. Even though there are possible physical interpretations of the KS orbitals [315], they should rather be seen as a convenient basis choice to describe the ground-state density. In our Renormalization Group approach to DFT, this property is essential as it allows us to construct an improved starting point for the RG flow from the KS single-particle states, see Sec. 4.3.

4.2.2   Approximations for the Exchange-Correlation Energy Functional

Before we shed some light on different approximation schemes for the *exchange-correlation* functional $E_{\mathrm{xc}}[n]$, we emphasize that the following discussion does not claim to be comprehensive in any sense. Since the development of DFT, there have been many efforts to find good expansion and approximations which systematically describe the complicated many-particle correlations. In principle, there are at least two exact representations of $E_{\mathrm{xc}}[n]$ relying both on the so-called *coupling-constant* integration method, see Ref. [308] for an overview. Therefore, at least in principle, it is possible to give a systematic prescription to include non-trivial particle *exchange-correlations* in DFT.

In the following, we shall discuss two approaches aiming at an exact representation of the *exchange-correlation* functional $E_{\mathrm{xc}}[n]$; the *Kohn-Sham perturbation theory* [316, 317] and the so-called *adiabatic connection* [318, 319]. In both cases, one introduces an auxiliary coupling constant λ ranging between $\lambda \in [0, 1]$. For $\lambda = 0$, one ensures that the system consists of N non-interacting fermions confined in a *Kohn-Sham*-type external potential $v_{\mathrm{KS}}(x)$. The latter is then described by the Hamiltonian

$$H_{\mathrm{KS}} = T + \int_x v_{\mathrm{KS}}(x) n(x) \,. \tag{4.20}$$

For $\lambda = 1$, however, the particle-particle interaction encoded in the two-body operator U is switched on and the KS-type external potential is deformed in a way such that only the external potential remains. For instance, for the so-called *adiabatic connection*, the λ-dependent Hamiltonian reads

$$H_\lambda = T + \int_x v_\lambda^{\mathrm{ac}}(x) n(x) + \lambda\, U \,, \tag{4.21}$$

where one requires for the λ-dependent potential

$$
v_\lambda^{\mathrm{ac}}(x) = \begin{cases} v_{\mathrm{KS}}(x) & \text{for} \quad \lambda = 0\,, \\ \text{unknown} & \text{for} \quad 0 < \lambda < 1\,, \\ v_{\mathrm{ext}}(x) & \text{for} \quad \lambda = 1\,. \end{cases} \tag{4.22}
$$

The Hamiltonian which is associated with *Kohn-Sham perturbation theory* (KSPT) can also be deduced from Eq. (4.21). One only has to replace the λ-dependent potential $v_\lambda(x)$ with

$$
v_\lambda^{\mathrm{KSPT}}(x) \equiv v_{\mathrm{ext}} + (1 - \lambda)(v_{\mathrm{H}} + v_{\mathrm{xc}})\,. \tag{4.23}
$$

Note that the crucial difference between *Kohn-Sham perturbation theory* and the *adiabatic connection* is that in the latter case the density has to fulfill the following boundary condition:

$$
n_{\mathrm{gs},\lambda}(x) = \langle \Psi_{\mathrm{gs}}(\lambda) | \, n(x) \, | \Psi_{\mathrm{gs}}(\lambda) \rangle = n_{\mathrm{gs},\lambda=0}(x)\,. \tag{4.24}
$$

The important assumption in case of the *adiabatic connection* is that the ground-state density $n_{\mathrm{gs}}(x)$ has to be v-*representable* for any unknown potential v_λ^{ac} along its path for $0 < \lambda < 1$. In other words, one tries to find an external potential v_λ^{ac} for $0 < \lambda < 1$ so that the ground-state density remains constant for any value of λ throughout the RG flow. This requirement is, in general, not fulfilled by the potential $v_\lambda^{\mathrm{KSPT}}(x)$, see Eq. (4.23), i.e., for KS *perturbation theory*. In the latter case, the ground-state density depends on the coupling constant λ as well.

For *Kohn-Sham perturbation theory* and for the *adiabatic connection*, one can now construct a differential equation for the λ-dependent ground-state energy:

$$
\partial_\lambda E_{\mathrm{gs},\lambda} = \partial_\lambda \langle \Psi_{\mathrm{gs}}(\lambda) | \, H_\lambda \, | \Psi_{\mathrm{gs}}(\lambda) \rangle\,. \tag{4.25}
$$

This is the starting point for the derivation of an exact expression for the interacting ground-state energy from which one can extract the correct form of the *exchange-correlation* functional E_{xc}, see Ref. [308] for details on the calculation. Note that the so-defined *coupling-constant* integration methods share some aspects with our RG approach to DFT which we shall introduce in the next section. There, we also insert an auxiliary coupling constant λ into the path integral which allows us to turn on the interaction strength gradually. From this, we then derive an exact functional RG equation for the energy density functional, see Sec. 4.3.

The *coupling-constant* integration methods discussed above can, in principle, be used to construct rather systematic approximations for E_{xc}. In practice, however, results from, e.g., the *adiabatic connection*, are often of limited use as the corresponding density functional of the ground-state wave function $|\Psi_{\mathrm{gs}}(\lambda)[n]\rangle$ is unknown. Below, we therefore discuss a different approximation which is employed frequently in DFT studies.

Let us now briefly discuss the *Local-Density Approximation* (LDA) for the *exchange-correlation* energy functional. The method relies on the idea of mapping the *exchange-correlation* energy E_{xc} of the inhomogeneous fermion system onto a corresponding problem in the thermodynamic limit. Here, the particle number N and the volume L are assumed to be infinite where the density N/L is kept constant. Note that the LDA implies that the system cannot depend on any external potential v_{ext} anymore. Therefore, the *homogeneous fermion gas* (HFG) is mostly governed by the kinetic energy T and *exchange-correlation* effects. The HFG has many further advantages, e.g., as a result of homogeneity, the rather complicated density functionals become simple functions of the homogeneous density. Moreover, in most homogeneous systems, plane waves are a natural choice so that computations are simplified considerably. To make the transition from the homogeneous system back to the inhomogeneous, we have to replace the homogeneous density of the HFG by a corresponding local density:

$$
E_{\mathrm{xc}}^{\mathrm{LDA}}[n] = \int_x n(x)\, \epsilon_{\mathrm{HFG}}\left(n_{\mathrm{hom}}\right)\Big|_{n_{\mathrm{hom}} \to n(x)}\,, \tag{4.26}
$$

with the energy density of the homogeneous *Fermi* gas ϵ_{HFG}. In comparison to other approximations for $E_{\mathrm{xc}}[n]$, the LDA has the advantage that it is free of any parameters. Note also that the LDA represents the leading-order term of a *gradient expansion* of the energy density functional. From Eq. (4.26), we can now compute the *exchange-correlation* contribution for the KS potential v_{KS} in LDA. For this, we have to compute the functional derivative of Eq. (4.26) which yields

$$v_{\mathrm{xc}}^{\mathrm{LDA}}[n](x) = \epsilon_{\mathrm{HFG}}\left(n(x)\right) + n(x)\,\frac{\partial \epsilon_{\mathrm{HFG}}\left(n(x)\right)}{\partial n(x)}\,. \tag{4.27}$$

The latter then enters the self-consistent KS equations (4.14). In this section, we only presented a tiny part of all truncation schemes which are employed in DFT these days. For more details on the *gradient expansion* and a general overview of other approximation schemes in DFT, we refer to Ref. [320].

4.3   A Renormalization Group Approach to DFT

The present section deals with an RG approach to DFT applied to one-dimensional fermions at zero temperature. For this, we begin in Sec. 4.3.1 with the derivation of the DFT-RG flow equation by starting from the microscopic (classical) action. We show the relation between the 2PPI effective action and the HK energy density functional and discuss how correlation functions can be computed within the DFT-RG framework.

In Sec. 4.3.2, we discuss a one-dimensional nuclear toy model with a long-range attractive and short-range repulsive two-body interaction based on our work from Ref. [110]. We show some key results where we focus on the calculation of few-body ground-state energies in a finite volume. Therefore, by confining the fermions in an external box, we compute ground-state energies for different box sizes and give an estimate for the continuum limit.

In Sec. 4.3.3, we discuss an improvement scheme for the DFT-RG method based on the self-consistent KS equations. There, we outline the basic idea of a KS-optimized starting point for the truncated DFT-RG flow and give a "recipe" for its computation. Moreover, we further discuss to what extent such an improvement is systematic and can be amended.

4.3.1   Derivation of the DFT-RG Flow Equation

Let us now briefly review the derivation of the DFT-RG equation and its basic properties. Note that the following introduction is mostly based on Ref. [110]. For more details, we refer to the original publication. We begin our discussion with the so-called classical action S in the imaginary time formalism. In the present work, the latter describes a system of one-dimensional identical fermions confined in an (optional) external potential $V_\lambda(x)$ which interact via a two-body potential $U_{2b}(\tau, x, \tau', x')$:

$$
\begin{aligned}
S_\lambda[\psi^*, \psi] \;=\; & \int_\tau \int_x \psi^*(\tau, x)\left(\partial_\tau - \frac{1}{2}\partial_x^2 + V_\lambda(x)\right)\psi(\tau, x) \\
& + \frac{1}{2}\int_\tau\int_x\int_{\tau'}\int_{x'} \psi^*(\tau, x)\psi^*(\tau', x')U_{2b}(\tau, x, \tau', x')\mathcal{R}_\lambda(\tau, x, \tau', x')\psi(\tau', x')\psi(\tau, x)\,, \tag{4.28}
\end{aligned}
$$

The integral abbreviations $\int_{x,\tau}$ depend on the problem's geometry under consideration, e.g., for a box of size L with (anti)periodic boundary conditions, the coordinates x_i are defined for $V_\lambda = 0$ within the interval $x \in [-L/2, L/2)$. For a harmonic trap we use in general $x \in \mathbb{R}$, see App. A. The two-body interaction is assumed to be local in time and does only depend on the relative distance of the particles $U_{2b}(\tau, x, \tau', x') = \delta(\tau - \tau')U(x - x')$. Moreover, we include a regulator-type function $\mathcal{R}_\lambda$ which has to fulfill the properties

$$\lim_{\lambda \to 0}\mathcal{R}_\lambda(\tau, x, \tau', x') = 0\,, \qquad \text{and} \qquad \lim_{\lambda \to 1}\mathcal{R}_\lambda(\tau, x, \tau', x') = 1\,, \tag{4.29}$$

where the flow parameter is defined on the finite interval $\lambda \in [0, 1]$. Note that the external potential does also depend on the regulator choice $\mathcal{R}_\lambda$. Moreover, the boundary conditions for V_λ correspond to the particular system under consideration and shall be discussed below for the different examples separately.

The regulator function $\mathcal{R}_\lambda$ shall gradually turn on the interaction and modify the shape of the external potential in a predefined fashion. For instance, in case of $\lambda = 0$, the system does only consist of non-interacting fermions confined in, e.g., a box with (anti)periodic boundary conditions or in a harmonic trap, respectively. By increasing the auxiliary coupling constant λ from zero to one, the fermions begin to interact via the two-body potential U_{2b}. At $\lambda = 1$ the interaction is fully turned on and the shape of the confining potential V is modified according to the choice of boundary conditions. For example, the confining potential V can be switched off to study selfbound systems. Note that we use throughout this thesis $\mathcal{R}_\lambda \equiv \lambda$. However, in future studies one may also consider different types of regulator functions. As we know from relativistic studies, the choice of the regulator function encodes the specific form of the momentum (shell) integrations in a given theory. Depending on the system under consideration, it could be helpful to adapt the regulator function according to the specific problem of interest to increase, e.g., the speed of convergence, see Ref. [110] for a discussion.

In the previous section, we briefly discussed the basic ideas of *coupling-constant* integration. If we now compare how the parameter λ enters the classical action S_λ, we observe similarities. For example, the coupling constant in S_λ shall also turn on the two-body interaction gradually which is also the case in *coupling-constant* integration techniques. As we shall see below, however, our field-theoretical approach directly provides us with information on the ground-state energy, density and higher correlation functions. Furthermore, *exchange-correlation* effects are systematically included. The latter are encoded in the n-density correlation functions of our theory. Again, the RG flow of the external potential depends on the particular system under consideration. For instance, it is also possible that the external potential remains constant and independent on the flow parameter λ. For example, this is the case in our study of one-dimensional fermions in a periodic box in the next subsection. We also add that the action S_λ, we consider in the present study, contains only a two-body potential U_{2b}. However, it is possible to include higher N-body interactions as it would be necessary if we, e.g., study nuclei with chiral three-nucleon forces, see Ref. [70] for a review.

Let us now turn to the derivation of the DFT-RG flow equations. In analogy to the derivation of the *Wetterich* equation, we begin with the partition function

$$\mathcal{Z}_\lambda[J] \sim \int \mathcal{D}\psi^* \mathcal{D}\psi \, \mathrm{e}^{-S_\lambda[\psi^*, \psi] + \int_\tau \int_x J(\tau, x)(\psi^*(\tau, x)\psi(\tau, x))} \equiv \mathrm{e}^{W_\lambda[J]} , \qquad (4.30)$$

where we coupled a space- and time-dependent source $J(\tau, x)$ to the density-type field $\rho \sim \psi^* \psi$. Moreover, instead of introducing a finite chemical potential, we fix the particle number N by employing appropriate boundary conditions for the initial conditions of the density correlation functions, see Ref. [321]. Note further that the particle number N is conserved by the RG flow, see Ref. [110]. We also stress that the external background potential $V(x)$ in the effective action S_λ can be absorbed completely by the source term J with the shift $J \to J + V$. From a DFT point of view, this is nothing but the *universality* of the energy density functional as stated by *Hohenberg* and *Kohn* [65].

From the generating functional

$$W_\lambda[J] = \ln \mathcal{Z}_\lambda[J] , \qquad (4.31)$$

we can compute *connected* density correlation functions by means of functional derivatives. Further, we may expand the functional $W_\lambda[J]$ in the spirit of a vertex expansion in terms of correlation functions:

$$W_\lambda[J] = G_\lambda^{(0)} + \int_\tau \int_x G_\lambda^{(1)}(\tau, x) J(\tau, x) + \frac{1}{2} \int_{\tau_1} \int_{x_1} \int_{\tau_2} \int_{x_2} G_\lambda^{(2)}(\tau_1, x_1, \tau_2, x_2) J(\tau_1, x_1) J(\tau_2, x_2) + \dots \,. (4.32)$$

Here, we obtain the density correlation function $G_\lambda^{(n)}$ by performing n functional derivatives with respect to the source and set the latter to zero. For example, we compute the time-dependent ground-state density via

$$\rho_{\mathrm{gs},\lambda}(\tau,x) := G_\lambda^{(1)}(\tau,x) = \left.\frac{\delta W_\lambda[J]}{\delta J(\tau,x)}\right|_{J=0}. \tag{4.33}$$

The time-dependent n-density correlation function can then be computed via

$$G_\lambda^{(n)}(\tau_1,x_1,\ldots,\tau_n,x_n) = \left.\frac{\delta^n W_\lambda[J]}{\delta J(\tau_1,x_1)\cdots\delta J(\tau_n,x_n)}\right|_{J=0}. \tag{4.34}$$

We stress that we require an infinite number of correlation functions even for the description of a non-interacting system. Note further that we define the time-independent ground-state density in the following way

$$n_{\mathrm{gs},\lambda}(x) := \lim_{\beta\to\infty}\frac{1}{\beta}\int_{-\beta/2}^{\beta/2}\mathrm{d}\tau\,\rho_{\mathrm{gs},\lambda}(\tau,x)\,, \tag{4.35}$$

where β defines the extent of the imaginary time interval with $\tau \in [-\beta/2,\beta/2)$ and is, moreover, associated with the inverse temperature $\beta = 1/T$. Note that we consider throughout the present work $\beta \to \infty$. In the next step, we define the 2PPI effective action using the functional analogue of a *Legendre* transformation:

$$\Gamma_\lambda[\rho] = \sup_J\left\{-W_\lambda[J] + \int_\tau\int_x J(\tau,x)\rho(\tau,x)\right\}, \tag{4.36}$$

where the supremum ensures the convexity of the density functional $\Gamma_\lambda[\rho]$, see Ref. [110]. Moreover, the 2PPI classical field can be computed from

$$\rho(\tau,x) = \frac{\delta W_\lambda[J]}{\delta J(\tau,x)}. \tag{4.37}$$

Note that this is again in correspondence to the 1PI classical field entering the *Wetterich* equation. As indicated above, the 2PPI effective action $\Gamma_\lambda[\rho]$ is related to the *Hohenberg-Kohn* energy density functional. In contrast to conventional DFT, we use time-dependent source terms $J \equiv J(\tau,x)$ implying time-dependent correlation functions, see Eq. (4.34). For field-theoretical approaches using time-independent sources, see, e.g., Refs. [66, 110, 321–325]. The energy density functional can then be computed from

$$E_\lambda[\rho] = \lim_{\beta\to\infty}\frac{1}{\beta}\Gamma_\lambda[\rho]\,, \tag{4.38}$$

where the ground-state energy can be extracted from the ground-state density:

$$E_{\mathrm{gs},\lambda} = \lim_{\beta\to\infty}\frac{1}{\beta}\Gamma_\lambda[\rho_{\mathrm{gs},\lambda}] = -\lim_{\beta\to\infty}\frac{1}{\beta}W_\lambda[0]\,. \tag{4.39}$$

The expression above can be verified from the spectral decomposition of the partition function $Z_\lambda \sim \sum_n \mathrm{e}^{-\beta E_{n,\lambda}}$ where we assume $E_{n,\lambda} < E_{n+1,\lambda}$ with $n \geq 0$. It can further be shown that the functional $\Gamma_\lambda[\rho]$ does not depend on the source J, as it should be:

$$\left.\frac{\delta\Gamma_\lambda[\rho]}{\delta J}\right|_\rho = 0\,, \tag{4.40}$$

for fixed ρ. Moreover, it is straightforward to show that

$$\frac{\delta\Gamma_\lambda[\rho]}{\delta\rho(x)} = J(x)\,, \tag{4.41}$$

which is the 2PPI version of the *Hohenberg-Kohn* variational principle from which we deduce for $J \to 0$ the ground-state density $\rho_{\mathrm{gs},\lambda}$. The latter is required to compute the λ-dependent ground-state energy $E_{\mathrm{gs},\lambda}$ in our formulation. Further, one can show that two-density correlation functions associated with the functional $W[J]$ and the two-point function associated with $\Gamma[\rho]$ are related in the following sense:

$$\frac{\delta^2 W[J]}{\delta J \,\delta J} = \left(\frac{\delta^2\Gamma[\rho]}{\delta\rho\,\delta\rho}\right)^{-1}\,. \tag{4.42}$$

Higher-order 2PPI correlation functions can then be computed from the connected ones accordingly, see Ref. [110].

Let us now discuss the construction of the n-density correlation functions. For this, we note that the density correlation functions can be constructed from one-particle propagators. In our present work, we shall use this property to derive the two-density and three-density correlation function. In particular, we find for the one-particle propagator:

$$\begin{aligned}
\Delta_0(\tau_1, x_1, \tau_2, x_2) &= -\langle \mathcal{T}\psi(\tau_1, x_1)\psi^*(\tau_2, x_2)\rangle \\
&= -\langle\psi(\tau_1, x_1)\psi^*(\tau_2, x_2)\rangle\,\theta_\sigma(\tau_1 - \tau_2) + \langle\psi^*(\tau_2, x_2)\psi(\tau_1, x_1)\rangle\,\theta_\sigma(\tau_2 - \tau_1)\,, \tag{4.43}
\end{aligned}$$

where $\mathcal{T}$ denotes the time-ordering operator and

$$\theta_\sigma(\tau) = \begin{cases} 1 & \text{for} \quad \tau > 0 \quad \text{and} \quad \tau \to 0^+\,, \\ 0 & \text{otherwise}\,. \end{cases} \tag{4.44}$$

The time-dependent ground-state density of the non-interacting theory can be extracted from the one-particle propagator which we have defined above:

$$\rho_{\mathrm{gs},\lambda=0}(\tau_1, x_1) = \lim_{\tau_2 \to \tau_1^+} \Delta_0(\tau_1, x_1, \tau_2, x_1)\,. \tag{4.45}$$

Note further that the most general n-density correlation function can be derived from one-particle propagators via

$$G^{(n)}_{\lambda=0}(\chi_1, \ldots, \chi_n) = \frac{(-1)^{n+1}}{n} \sum_{(i_1,\ldots,i_n)\in S_n} \Delta_0(\chi_{i_1}, \chi_{i_2})\Delta_0(\chi_{i_2}, \chi_{i_3})\cdots\Delta_0(\chi_{i_{n-1}}, \chi_{i_n})\,, \tag{4.46}$$

with $\chi = (\tau, x)$. Moreover, S_n describes all possible permutations of the indices $i_1, \ldots, i_n$. For example, the (non-interacting) two- and three-density correlation functions read

$$G^{(2)}_{\lambda=0}(\chi_1, \chi_2) = -\Delta_0(\chi_2, \chi_1)\Delta_0(\chi_1, \chi_2)\,, \tag{4.47}$$

and

$$G^{(3)}_{\lambda=0}(\chi_1, \chi_2, \chi_3) = \Delta_0(\chi_1, \chi_2)\Delta_0(\chi_2, \chi_3)\Delta_0(\chi_3, \chi_1) + \Delta_0(\chi_2, \chi_1)\Delta_0(\chi_1, \chi_3)\Delta_0(\chi_3, \chi_2)\,. \tag{4.48}$$

Both identities play a crucial role in our *Kohn-Sham*-improved DFT-RG approach in which we automatically construct the two- and three-density correlation functions from one-particle propagators within our numerical set-up, see Sec. 4.3.3.

Let us now discuss the functional RG equation for the generating functional $W_\lambda[J]$. The latter can be derived

straightforwardly from Eq.(4.31) by taking the derivative with respect to the flow parameter λ. From this, we find

$$
\partial_\lambda W_\lambda[J] = -\int_{\chi_1} (\partial_\lambda V_\lambda(\chi_1)) \frac{\delta W_\lambda[J]}{\delta J(\chi_1)} - \frac{1}{2} \int_{\chi_1} \int_{\chi_2} \frac{\delta W_\lambda[J]}{\delta J(\chi_1)} U_{2b}(\chi_1, \chi_2) (\partial_\lambda \mathcal{R}_\lambda(\chi_1, \chi_2)) \frac{\delta W_\lambda[J]}{\delta J(\chi_2)}
$$
$$
- \frac{1}{2} \int_{\chi_1} \int_{\chi_2} U_{2b}(\chi_1, \chi_2) (\partial_\lambda \mathcal{R}_\lambda(\chi_1, \chi_2)) \left(\frac{\delta^2 W_\lambda[J]}{\delta J(\chi_2) \delta J(\chi_1)} - \frac{\delta W_\lambda[J]}{\delta J(\chi_2)} \delta(\chi_2 - \chi_1) \right) , \quad (4.49)
$$

where we use the shorthand notations $\int_\chi = \int_x \int_\tau$ and $\delta(\chi_1 - \chi_2) = \delta(x_1 - x_2)\,\delta(\tau_1 - \tau_2)$. We add that the DFT-RG flow equation (4.49) can be generalized to higher dimensions. Furthermore, fermions with internal degrees of freedom can be considered as well, see, e.g., Ref. [108] for a study of ultracold spin-1/2 fermions in a box with periodic boundary conditions.

The flow equation above describes the change of the generating functional under a gradual variation of the flow parameter λ: One starts the RG flow at $\lambda = 0$ where the theory is free and the interaction is switched off. At this point, the theory is well understood and the n-density correlation functions we gave in Eq. (4.46) can be computed straightforwardly. However, we emphasize that an exact description of the non-interacting theory still requires an infinite number of n-density correlation functions. The DFT-RG flow equation (4.49) then interpolates between the non-interacting system at $\lambda = 0$ and the interacting many-body problem at $\lambda = 1$ where the interaction is fully switched on. We stress that this is done in a non-perturbative fashion as we automatically include arbitrarily high orders of the interaction U_{2b} by solving the evolution equation (4.49).

We further observe that by considering an expansion scheme like Eq. (4.32), we receive an infinite tower of coupled differential equations for the different n-density correlation functions. For instance, we find that the m-density correlation function $G_\lambda^{(m)}$ depends, in general, on all density correlation functions with order $1 \leq m \leq (n + 2)$ as it can be verified from the structure of the DFT-RG flow equation (4.49). In practice, we therefore need to truncate the tower of flow equations at a given order. For this, it can be shown that results are improved significantly by considering truncations which entail $G_{\lambda=0}^{(n+1)}$ and $G_{\lambda=0}^{(n+2)}$ within the flow equation for $G_\lambda^{(n)}$, even if we set $\partial_\lambda G_\lambda^{(m)} = 0$ for $m \geq (n + 1)$. The reason for this observation relies on the structure of the coupled set of DFT-RG flow equations which can also be related to many-body perturbation theory. Using truncations for the tower of RG flow equations as described above, we could notably reduce certain truncation artifacts, for example, spurious fermion self-interactions, see Ref. [110] for details.

We already mentioned that the functionals $W_\lambda[J]$ and $\Gamma_\lambda[\rho]$ are related and can be transformed into each other. In fact, it is straightforward to compute a functional Renormalization Group equation for the density functional $\Gamma_\lambda[\rho]$. For the latter, we find

$$
\partial_\lambda \Gamma_\lambda[\rho] = \int_{\chi_1} (\partial_\lambda V_\lambda(\chi_1)) \rho(\chi_1) + \frac{1}{2} \int_{\chi_1} \int_{\chi_2} \rho(\chi_1) U_{2b}(\chi_1, \chi_2) (\partial_\lambda \mathcal{R}_\lambda(\chi_1, \chi_2)) \rho(\chi_2)
$$
$$
+ \frac{1}{2} \int_{\chi_1} \int_{\chi_2} U_{2b}(\chi_1, \chi_2) (\partial_\lambda \mathcal{R}_\lambda(\chi_1, \chi_2)) \left(\left(\frac{\delta^2 \Gamma_\lambda[\rho]}{\delta\rho\,\delta\rho} \right)^{-1}(\chi_2, \chi_1) - \rho(\chi_2)\delta(\chi_2 - \chi_1) \right) . \quad (4.50)
$$

Interestingly, the DFT-RG equation for the functional $W_\lambda[J]$ as well as the flow equation for the density functional $\Gamma_\lambda[\rho]$ look very similar. Nevertheless, we emphasize that the correlation functions which enter our flow equations are not identical, see Ref. [110]. The functional $W_\lambda[J]$ relies on connected density correlation functions $W_\lambda^{(n)}$ entering our computations, whereas 2PPI correlation functions underlie the DFT-RG flow of the density functional $\Gamma_\lambda[\rho]$. We further stress that the computation of initial conditions for the 2PPI flow equation (4.50) requires an inversion of the two-density correlation function $G_\lambda^{(2)}$. The latter can be computed from the one-particle propagator given in Eq. (4.43). However, while an inversion of $G_\lambda^{(2)}$ can be simple for theories obeying a translation symmetry in space and time, it can be involved as soon as translation invariance is broken because of, e.g., an external potential. Therefore, throughout the present thesis, we use Eq. (4.49) and consider connected n-density correlation functions as the building blocks in our coupled set of DFT-RG flow equations.

We observe that the structures of the flow equations (4.49) and (4.50) are related to the one we found for the *Wetterich* equation (1PI) (2.23) as they all exhibit a simple one-loop structure. As already indicated, however, this does by no means imply that only one-loop contributions in the sense of perturbation theory are present. Of course, there are also several differences on a technical level. For example, the regulator entering the *Wetterich* equation is inserted in the kinetic part of the classical action which is not the case in our DFT-RG framework. Here, we find that the latter is inserted alongside the two-body interaction of the classical action.

Moreover, we note that the *Callan-Symanzik* equation [133, 134] and the DFT-RG flow equations above are also related. Originally, the *Callan-Symanzik* equation was derived to investigate the scaling behavior of the correlation functions under a variation of the renormalized mass parameter. In our case, we study the scaling relations of the density correlation functions under a variation of the scale parameter λ, see Ref. [110] for a detailed discussion.

Let us further analyze the DFT-RG equations (4.49) and (4.50). The part $\sim \int_{\chi_1, \chi_2} \rho(\chi_1) U(\chi_1, \chi_2) \rho(\chi_2)$ appearing in both DFT-RG equations is often referred to as the *Hartree* term. We already encountered such a contribution in our discussion of conventional DFT, see Eq. (4.16). There, we stated that the latter does not include *exchange-correlation* effects as they are included in *Fock*-type contributions. For this, we find in our present DFT-RG approach the term $\sim \int_{\chi_1, \chi_2} U(\chi_1, \chi_2) W^{(2)}(\chi_2, \chi_1)$ encoding all *exchange* and *correlation* contributions of the many-body problem under consideration. Moreover, we also find a term $\sim \int_{\chi_1, \chi_2} \rho(\chi_2) \delta(\chi_2 - \chi_1)$ present in our evolution equation. The latter is important as it implements the *Pauli* exclusion principle for identical fermions, see our discussion in Ref. [110].

4.3.2 An Introductory Example: A One-Dimensional Nuclear Model

In the present subsection, we review some results of our work in Ref. [110] where we studied a one-dimensional nuclear toy model employing the DFT-RG framework. In particular, we shall focus on the few-body case where we investigate bound-state properties of N identical one-dimensional toy nucleons which are confined within a finite box and interact via a two-body interaction potential. The latter is given by two *Gaussians* with a long-range attractive tail and short-range repulsive "core":

$$U(x_1 - x_2) = \frac{g}{\sigma_1 \sqrt{\pi}} \, \mathrm{e}^{-\frac{(x_1-x_2)^2}{\sigma_1^2}} - \frac{g}{\sigma_2 \sqrt{\pi}} \, \mathrm{e}^{-\frac{(x_1-x_2)^2}{\sigma_2^2}} \, , \tag{4.51}$$

adopting the parameters g, σ_1 and σ_2 from Ref. [326] which read

$$\bar{g} \equiv g L_0 = 2.4 \quad \text{and} \quad \bar{\sigma}_2 \equiv \sigma_2 L_0^{-1} = 4.0 \, . \tag{4.52}$$

Here, the length scale $L_0 \equiv \sigma_1 = 0.2$ defines the extent of our toy model nucleons and serves as a normalization length scale in our study below. Note that the values of these parameters were in Ref. [326] fitted such that the model mimics saturation properties of realistic nuclei.

Let us now discuss the overall set-up we use to compute the ground-state energies of the corresponding few-body systems. First of all, we shall consider periodic boundary conditions for odd particle numbers and antiperiodic boundary conditions for even particle numbers. Note that the latter choice ensures that the non-interacting system of N particles in a box is non-degenerate. Furthermore, we assume that the confining box of length L remains unchanged for any value of λ. Thus, we have $\partial_\lambda V_\lambda(x) = 0$ in our present study. In addition, because of the presence of the box, translation invariance is broken explicitly in our system. Therefore, we use a periodic extension of the interaction potential so that translation invariance is enforced. This can be done by dropping off-diagonal elements of the interaction matrix $\mathfrak{U}_{m,n}$ which is defined by the following *Fourier* decomposition:

$$\mathfrak{U}(x_1 - x_2) = \sum_{m,n} \mathfrak{U}_{m,n} \, (\phi_m^{(P)}(x_1))^* \phi_n^{(P)}(x_2) \, , \tag{4.53}$$

with $U(x_1 - x_2) = g\,\mathfrak{U}(x_1 - x_2)$ and the (anti)periodic plane wave basis functions

$$\phi_n^{(I)}(x) = \frac{1}{\sqrt{L}}\,\mathrm{e}^{-\mathrm{i}p_n^{(I)}x} \quad \text{with} \quad \int_x (\phi_m^{(I)}(x))^* \phi_n^{(I)}(x) = \delta_{m,n}\,. \tag{4.54}$$

Moreover, we have

$$\sum_n (\phi_n^{(I)}(x_1))^* \phi_n^{(I)}(x_2) = \sum_n \delta(x_1 - x_2 + nL)\,, \tag{4.55}$$

where the discretized momenta $p_n^{(I)}$ correspond to antiperiodic or periodic boundary conditions, respectively:

$$p_n^{(A)} = \frac{(2n+1)\pi}{L}\,, \quad \text{and} \quad p_n^{(P)} = \frac{2n\pi}{L}\,, \tag{4.56}$$

with $n, m \in \mathbb{Z}$. The single-particle states $\phi_n^{(I)}(x)$ enter the definition of the one-particle propagator Δ_0. As already discussed, the latter can be considered as the building block for all connected density correlation functions of the non-interacting fermion gas, e.g., see Eqs. (4.47)-(4.48). Using the single-particle states above, we find for the one-particle propagator:

$$\Delta_{\lambda=0}^{(I)}(\tau_1, x_1, \tau_2, x_2) = -\sum_n \int_{-\infty}^{\infty} \frac{\mathrm{d}\omega}{2\pi} \frac{\mathrm{e}^{-\mathrm{i}\omega(\tau_1 - \tau_2)}}{-\mathrm{i}\omega + \bar{\varepsilon}_n^{(I)}} (\phi_n^{(I)}(x_1))^* \phi_n^{(I)}(x_2)$$

$$= -\sum_n \left\{ \theta(\bar{\varepsilon}_n^{(I)})\theta_\sigma(\tau_1 - \tau_2) - \theta(-\bar{\varepsilon}_n^{(I)})\theta_\sigma(\tau_2 - \tau_1) \right\} (\phi_n^{(I)}(x_1))^* \phi_n^{(I)}(x_2)\,\mathrm{e}^{-|\bar{\varepsilon}_n^{(I)}||\tau_1 - \tau_2|}\,, \tag{4.57}$$

where the single-particle energy states are $\varepsilon_n^{(I)} = (p_n^{(I)})^2/2$. Here, we employ a plane-wave basis representation for the one-particle propagator associated with a non-interacting few-fermion system in an (anti)periodic box. Naturally, the basis choice reflects the properties of the quantum system under consideration. For example, in case of non-interacting fermions within an (anti)periodic box, a plane-wave basis is reasonable as the corresponding propagator becomes diagonal. Nevertheless, this basis choice could be inefficient at $\lambda = 1$ where the interaction is fully turned on. Therefore, to anticipate certain properties of the interacting system, a variation of the starting point at $\lambda = 0$ could be worthwhile. In the next section, we shall discuss this in more detail.

Using Eq. (4.57), we can compute the initial conditions for the density correlation functions $G_{\lambda=0}^{(n)}$ which enter our DFT-RG flow equations. For this, we consider density correlation functions up to $G_\lambda^{(4)}$. Because of translation invariance, however, the density correlation function $G_{\lambda=0}^{(3)}$ vanishes identically. Furthermore, the density becomes constant and homogeneous so that $\rho_{\mathrm{gs},\lambda=0} = N/L$. Since translation symmetry is conserved for every RG step, it can be shown that the flow equation for the density vanishes identically $\partial_\lambda \rho_{\mathrm{gs},\lambda} = 0$. As a consequence, the density remains homogeneous for all values of λ, in particular, at $\lambda = 1$. Note that this does not imply that the intrinsic density of the quantum system, the many-body wave function, is also constant. In fact, the latter can be computed from the two-density correlation function and appears to be inhomogeneous, see Ref. [110] for details. Therefore, the remaining density correlation functions which we need to compute at $\lambda = 0$ using the present truncation are $G_{\lambda=0}^{(2)}$ and $G_{\lambda=0}^{(4)}$.

Let us now discuss the overall structure of the RG flow equations for the ground-state energy $E_{\mathrm{gs},\lambda}$ and the two-density correlation function $G_\lambda^{(2)}$. As indicated above, we obtain the flow equations for the different density correlation functions by using the expansion (4.32) of the functional $W[J]$ and plug the latter into Eq. (4.32) where we compare the left- and right-hand side in powers of the source. From this, we find the following DFT-RG flow equations:

$$\partial_\lambda E_{\mathrm{gs},\lambda} = \frac{N^2}{2L^2} \int_{x_1} \int_{x_2} U(x_1 - x_2) + \frac{1}{2} \int_{x_1} \int_{x_2} G_\lambda^{(2)}(0, x_1, 0, x_2)U(x_2 - x_1) - \frac{N}{2}\,U(0)\,, \tag{4.58}$$

$$
\begin{aligned}
\partial_\lambda G_\lambda^{(2)}(\tau_1, x_1, \tau_2, x_2) \quad = \quad & -\int_{\tau_3} \int_{x_3} \int_{x_4} G_\lambda^{(2)}(\tau_1, x_1, \tau_3, x_3) U(x_3 - x_4) G_\lambda^{(2)}(\tau_3, x_4, \tau_2, x_2) \\
& -\frac{1}{2} \int_{\tau_3} \int_{x_3} \int_{x_4} U(x_3 - x_4) G_\lambda^{(4)}(\tau_3, x_4, \tau_3, x_3, \tau_1, x_1, \tau_2, x_2), \quad (4.59)
\end{aligned}
$$

where we have set the flows of all higher correlation functions to zero $\partial_\lambda G_\lambda^{(n)} = 0$ with $n > 2$. For the functional form of the initial conditions for $G_{\lambda=0}^{(2)}$ and $G_{\lambda=0}^{(4)}$ as well as for some further technical details, we refer the reader to Refs. [108, 110].

Neglecting the flow of the two-density correlation function $\partial_\lambda G_\lambda^{(2)} \equiv 0$, we find the simplest truncation possible where we only consider the running of the ground-state energy. In our study, we shall denote this as the leading order (LO) approximation, where only the ground-state energy itself depends on the flow parameter λ. The density as well as the two-density correlation function remain at their initial values throughout the RG flow. Moreover, we denote a truncation, which also includes the running of the two-density correlation function as the next-to-leading order (NLO), as it is the natural extension since the flow equation associated with the ground-state density vanishes. As we have already stressed, we can also expand Eq. (4.32) to even higher density correlation functions to deduce the corresponding RG flow equations, e.g., for $G_\lambda^{(4)}$. From the structure of the DFT-RG equation (4.49), it follows that the latter does also depend on $G_\lambda^{(5)}$ and $G_\lambda^{(6)}$, see our discussion above.

Even though an extension to higher correlation functions is straightforward from a theoretical point of view, it can be rather tedious in practical computations. Therefore, let us briefly discuss the numerical implementation of our DFT-RG flow equation and estimate the required computational resources. For instance, the four-density correlation function $G_\lambda^{(4)}$ depends on four space and time coordinates. If one takes into account that the density correlation functions do only depend on the relative time and space coordinates[16], we still have $(N_L)^3 (N_\beta)^3$ different numerical values which need to be computed and stored in case of $G_\lambda^{(4)}$ in $(1+1)$ dimensions. Here, N_L and N_β denote the number of lattice sites of space and time coordinates, respectively. This example shows that, depending on the number of lattice sites, we expect that the memory demand approximately increases at least exponentially with n being the n-th density correlation function. The rough consideration shows that it is not reasonable at some point to improve a given truncation solely by including higher-order correlation functions. Therefore, further expansion schemes for the functionals $W[J]$ and $\Gamma[\rho]$ are discussed in Ref. [110], which do not rely on an expansion in terms of density correlation functions but rather, e.g., on a derivative-type expansion for the time-dependent density field as it is usually done in relativistic theories, see also Sec. 2.2.2 in the first part of this thesis.

Let us now discuss the results for two particles confined in an antiperiodic box which interact via the two-body potential Eq. (4.51). Again, we use an antiperiodic box to ensure that the ground-state energy of the non-interacting fermion system is not degenerate. In the left panel of Fig. 4.3, we show the ground-state energy per particle as a function of the inverse density as it is obtained in leading order (green) and next-to-leading order (blue) from the truncated DFT-RG flow equations. As a benchmark, we also present the results from an exact diagonalization of the two-body Hamiltonian (black) where the dotted line represents the corresponding continuum limit. We also show the ground-state energy for free fermions in an antiperiodic box (red) as an additional comparison.

We observe that the exact ground-state energy decreases for $1/n_{\mathrm{gs}} \lesssim 7 \, L_0$ starting from a positive value. Intersecting the line of zero energy at $1/n_{\mathrm{gs}} \simeq 5$, the ground-state energy per particle further decreases reaching a local minimum at $1/n_{\mathrm{gs}} \approx 7 \, L_0$. The ground-state energy then slightly increases for larger inverse densities and reaches a local maximum at $1/n_{\mathrm{gs}} \approx 17.5 \, L_0$. For larger inverse densities, the ground-state energy decreases again and approaches slowly the continuum value $E/N|_{\mathrm{cont.}} \approx -0.0094 \, (1/L_0^2)$ from above. Note that the exact value for the two-body ground-state energy in a finite box still differs from the exact continuum value by 10% at $1/n_{\mathrm{gs}} \approx 80 \, L_0$, underscoring the rather slow convergence of the finite-size results towards the continuum. Moreover, the specific shape of the ground-state energy in a finite volume reflects the shape of the corresponding two-body interaction potential, which has a repulsive core at small distances and becomes attractive in the long-range limit.

---

[16]This is only true if translation invariance is intact and not broken due to, e.g., an external potential.
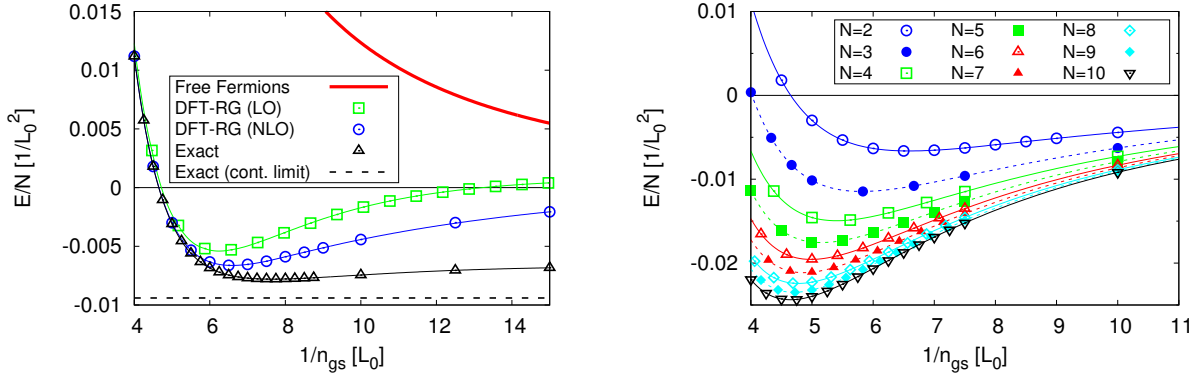
Figure 4.3: Left panel: Energy per particle E_{gs}/N as a function of the inverse ground-state density $1/n_{\mathrm{gs}}$ for two particles. We show the exact two-body results in black where the dotted line represents the continuum value. Leading- and next-to-leading order DFT-RG results are shown in green and blue, respectively, see also Refs. [108, 110] for details. Right panel: Energy per particles over the inverse density for up to $N = 10$ particles. All data points were computed in NLO, see main text for details.

The LO and NLO results from the DFT-RG study are for $1/n_{\mathrm{gs}} \lesssim 5\,L_0$ in agreement with the exact solution. Moreover, they assume for $5 L_0 \leq 1/n_{\mathrm{gs}} \leq 8 L_0$ a local minimum in correspondence with the exact results. Here, we observe for the DFT-RG study at NLO that it provides even better results than the corresponding study at LO. For very large inverse densities $1/n_{\mathrm{gs}} \to \infty$, however, the LO and NLO DFT-RG results approach the zero-energy axis implying that the presently used truncations are not capable to reproduce the correct long-range behavior of the quantum system because of missing higher-order correlation functions. From a simple dimensional analysis, we find that the (dimensionful) ground-state energy needs to fulfill the scaling behavior $E_{\mathrm{gs}}(L) \sim L^{-2}$ in order to remain finite in the limit of low densities. Nevertheless, we observe a significant improvement by going from the LO to the NLO, i.e, by also considering the flow equation associated with the two-density correlation function. In fact, we find that by including higher density correlation functions, the results from the DFT-RG study are improved and approach the exact result from above. The latter observation underscores our claim that the expansion in n-density correlation functions is systematic.

In the right panel of Fig. 4.3, we show the ground-state energy per particle for up to $N = 10$ particles as it is found in NLO of our DFT-RG framework. First of all, we recognize that the overall shape of the curves associated with different N-particle ground-state energies as a function of the inverse density looks quite similar on a qualitative level. For all computed particle numbers the ground-state energies start at large densities, decrease, assume a local minimum and then tend to zero in the low-density regime in correspondence to the two-body case. Note that the location of the local minimum is shifted towards higher densities by increasing the particle number N.

Even though the present truncation is incapable to reproduce the ground-state energy in the long-range limit, we can still estimate the ground-state energy in the continuum. To this end, we use the observation that the results from our DFT-RG study approach the exact two-body solution from above. Assuming that this is true for $N > 2$, we can estimate the continuum ground-state energy with

$$E_\infty = \inf_L E(L)\,. \tag{4.60}$$

In Fig. 4.4, we show the continuum results for the ground-state energy per particle computed by using the estimate Eq. (4.60) for different particle numbers within the NLO of the DFT-RG method. As a comparison, we also show the exact two-body result (black triangle) as well as results for four and eight particles from a *Monte-Carlo* (MC) study (red diamonds), see Ref. [326]. Note that the error bars associated with the MC study results are smaller than the red symbols according to Ref. [326]. We find that our DFT-RG approach is in qualitative agreement with both the exact and the MC results. However, our NLO study still underestimates the exact two-body ground-state energy
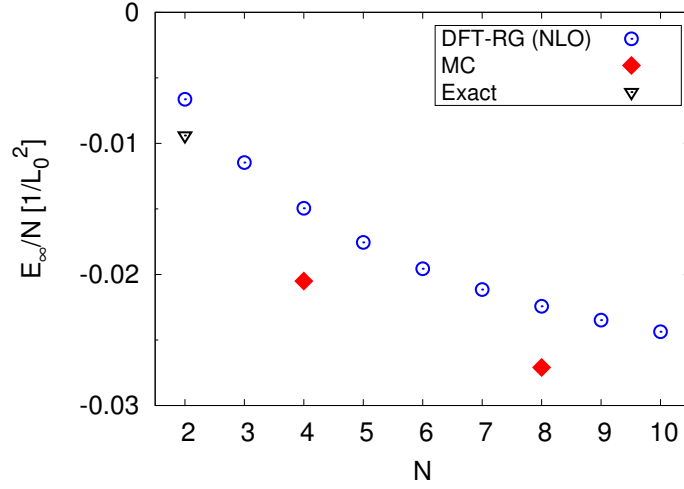
Figure 4.4: Estimated binding energy E/N as a function of the particle number for $N = 2, \ldots, 10$. We also show the exact result for two particles (black triangle) and *Monte-Carlo* results (red diamonds) from Ref. [326].

by $\sim 30\%$. By comparing our DFT-RG results in NLO with those from the MC study, we find that the ground-state energies are found to be consistently greater but the relative difference decreases with N. Moreover, this is also compatible with our observation in the thermodynamic limit ($N/L = \mathrm{const.}$ and $L \to \infty$), where we perfectly recover the *Hartree-Fock* (HF) approximation, see Ref. [110] for details.

In our brief review of aspects of Ref. [110], we focused on the ground-state energies of few-body systems confined in a finite box with (anti)periodic boundary conditions. As we have seen above, the DFT-RG approach provides a systematic framework to use DFT for *ab initio* studies. Nevertheless, we also indicated that the memory demand of higher density correlation functions increases exponentially making an improvement of a given truncation rather infeasible at some point. Therefore, it would be desirable to find an improvement for a given truncation at some order by keeping the number of correlation functions fixed.

4.3.3 A Kohn-Sham Improvement for DFT-RG

The basic idea to improve our DFT-RG framework relies on a *Kohn-Sham*-optimized starting point. We use that the solution of the self-consistent KS equations already provides us with a KS single-particle basis which can be seen as "optimized" to represent the interacting many-body ground-state density. The KS ground-state density $n_{\mathrm{gs}}(x)$, which is constructed from the KS single-particle orbitals $\phi_i[n_{\mathrm{gs}}](x)$, then minimizes a given ansatz for the energy density functional (4.9) and corresponds to a KS system of N non-interacting fermions. Therefore, we use the non-interacting KS system as a starting point for the truncated DFT-RG flow and expect that we include sufficient information on the interacting many-body ground state already at the beginning of the DFT-RG flow to improve our results. To establish such a method, however, we need to consider a KS-improved external potential $v_{\mathrm{KS}}(x)$ in our set of DFT-RG flow equations breaking translation invariance explicitly. For our present proof-of-concept study, let us therefore concentrate on a scenario where the fermions are confined in a λ-dependent external potential in which case the density is inhomogeneous for any value of λ.

The KS single-particle orbitals $\phi_i[n_{\mathrm{gs}}](x)$, which correspond to the KS system, then enter our RG study at the level of the one-particle propagator Δ_0. The latter then becomes a density functional itself:

$$\phi_i(x) \to \phi_i[n_{\mathrm{gs}}](x) , \quad \text{and therefore:} \quad \Delta_0(\tau_1, x_1, \tau_2, x_2) \to \Delta_0[n_{\mathrm{gs}}](\tau_1, x_1, \tau_2, x_2) . \tag{4.61}$$

One may argue that one still has the issue to compute *exchange* and *correlation* contributions which remain unknown in a conventional KS ansatz, e.g., in $v_{\mathrm{xc}}(x)$. However, we emphasize that we only use the KS system as a starting

point for the RG flow. In principle, it should not be necessary to include *exchange-correlation* effects in our KS ansatz at all as they are generated dynamically by solving the DFT-RG flow equations.

Let us summarize the individual steps for our KS-improved DFT-RG framework:

(i) Make an initial guess for the KS potential v_{KS} and solve the KS equations self-consistently. From this, one finds the KS single-particle states and single-particle energies. We stress that the ansatz for $v_{\mathrm{KS}}(x)$ does not need to be very sophisticated, e.g., we may drop all *exchange-correlation*-type effects. This potential now determines the non-interacting starting point of our RG flow.

(ii) Compute the n-density correlation functions $G^{(n)}_{\lambda=0}$ from the single-particle orbitals $\phi_i[n_{\mathrm{gs}}]$ which enter the density correlation function through the one-particle propagator $\Delta_0[n_{\mathrm{gs}}]$.

(iii) Solve the DFT-RG flow equations for the KS-improved n-density correlation functions within a given truncation. Here, one may choose different boundary conditions for the external KS trap, e.g., one can switch it off in the RG flow $V_{\lambda=1}(x) = 0$ or use $V_{\lambda=1}(x) = v_{\mathrm{ext}}(x)$, depending on the physical system under consideration.

We emphasize that the KS step (i) is mainly included to generate a better suited basis set. Note further that the initial condition for the RG flow equation associated with the ground-state energy $E_{\mathrm{gs},\lambda=0}$ is not identical to the KS ground-state energy (4.19). The latter is associated with the ground-state energy of the interacting many-body system described by the HK energy functional (4.9) and evaluated at the ground-state density $n_{\mathrm{gs}}(x)$. The starting point of our DFT-RG flow, however, corresponds to a system of non-interacting fermions which are trapped in an external KS potential. In this case, the initial condition for the ground-state energy is the sum over the KS single-particle energy states:

$$E_{\mathrm{gs},\lambda=0} = \sum_i \theta(-\bar{\varepsilon}_i)\,\varepsilon_i\,. \tag{4.62}$$

In general, it is by no means ensured that the so-defined KS-improved DFT-RG framework performs even better than the usual DFT-RG flow equations without an optimized starting point. However, the KS improvement we discussed above can be implemented in an existing DFT-RG code rather easily and "adds" a secondary control parameter to improve results as obtained from the DFT-RG method. For example, the so-defined KS-improvement scheme enables us to possibly amend a specific truncation in n-density correlation functions even further by also considering, e.g., LDA-type *exchange-correlation* contributions in the KS potential $v_{\mathrm{KS}}(x)$. Nevertheless, such a further improvement lies beyond the scope of the present thesis. In our study below, we shall only consider a *Hartree*-type contribution as an ansatz for the KS potential $v_{\mathrm{KS}}(x)$ neglecting all *exchange-correlation* effects. The latter are then included by solving the corresponding DFT-RG flow equations.

4.4   Quasi-One-Dimensional Fermions in a Harmonic Trap

In the present section, we now discuss a proof-of-concept study where we apply our KS-improved DFT-RG approach for a system of quasi-one-dimensional fermions which mimics the situation in dipolar *Fermi* gases [327–331]. We assume that the fermions are confined within a one-dimensional trap even in case the interaction is fully turned on. In particular, we require at the starting point of the RG flow $V_{\lambda=0}(x) = v_{\mathrm{KS}}(x)$, with the KS potential $v_{\mathrm{KS}}(x)$ computed from a self-consistent KS procedure in a *Hartree* approximation. At the end point of the RG flow, we have $V_{\lambda=1}(x) = v_{\mathrm{ext}}(x)$ so that the auxiliary KS potential present at $\lambda = 0$ is switched off leaving us solely with a harmonic potential describing the experimental situation.

We begin this section with a brief introduction to our model and introduce the two-body dipolar interaction potential we shall consider throughout this study. In the second subsection, we then present the DFT-RG flow equations underlying our computations. Afterwards, we present the ground-state energy per particle as a function of the dipolar coupling strength, where we employ different truncation types using the DFT-RG framework. In
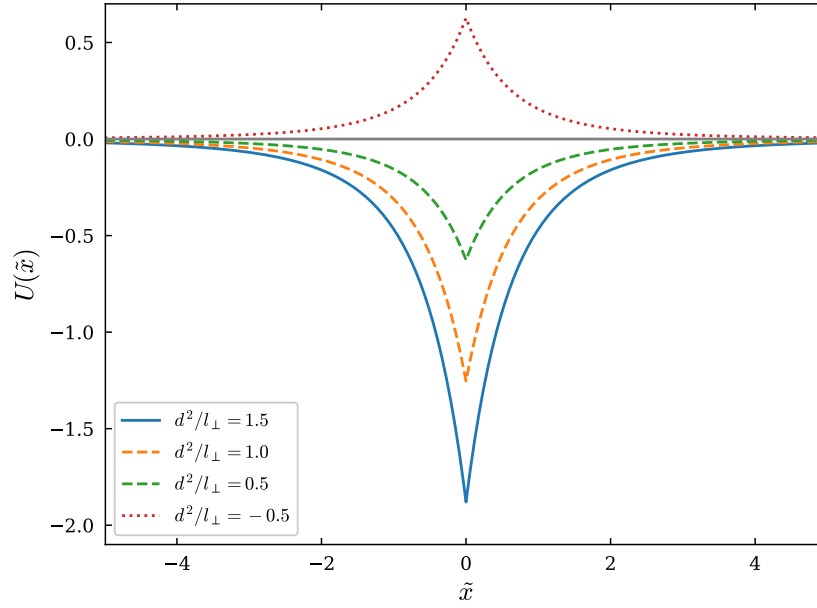
Figure 4.5: Quasi-one-dimensional dipolar interaction $U(\tilde{x})$ adopted from Refs. [327–329]. We show the two-body potential for attractive $d^2 > 0$ values as well as for one repulsive $d^2 < 0$ value of the dipole interaction strength d^2, see main text for details.

particular, we consider the DFT-RG flow equations associated with the ground-state energy $\partial_\lambda E_{\text{gs},\lambda}$ as well as the ground-state density $\partial_\lambda n_{\text{gs},\lambda}$ and discuss our results as obtained from a KS-improved starting point for the DFT-RG flow. As a benchmark, we consider exact diagonalization to compute the ground-state energies per particle up to $N = 5$.

4.4.1 Dipolar Interaction

Let us begin our discussion with an introduction to the model for which we employ the DFT-RG approach. In our study, we shall investigate a single-component one-dimensional system of few fermions confined within a harmonic potential v_{ext} at zero temperature. We further assume that the identical fermions interact via a tunable dipolar two-body interaction which we shall introduce below.

Before we discuss the details of the interaction potential, we emphasize that ultracold[17] one-dimensional few-body systems are also of great interest from an experimental point of view and have become a frequently studied subject in recent years, see, e.g., Refs. [335–339] and Refs. [334, 340] for reviews. To this end, one considers so-called cigar-shaped quasi-one-dimensional microtraps [341] which basically consist of three-dimensional optical traps with frequencies $\omega_\parallel$ for the y-z plane and $\omega_\perp$ along the x-direction. Given that $\omega_\perp \gg \omega_\parallel$, the fermions with mass m are effectively confined within an effective harmonic potential $v_{\text{ext}}(x) = (1/2)m\omega_\parallel^2 x^2$ along the x-direction.

Let us now discuss the two-body interaction we assume for our system throughout our studies. The effective dipole-dipole[18] interaction which we use is adopted from Refs. [327–329] and reads

$$U(\tilde{x}) = -\frac{d^2}{2l_\perp^3}\left[\sqrt{2\pi}\,\mathrm{e}^{\tilde{x}^2/2}\left(1 + \tilde{x}^2\right)\left(1 - \mathrm{erf}\left(\frac{\tilde{x}}{\sqrt{2}}\right)\right) - 2\tilde{x}\right], \tag{4.63}$$

---

[17]Note that at sufficiently low temperatures, single-component *Fermi* gases are dominated by the p-wave channel since the s-wave channel is forbidden as a consequence of the *Pauli* exclusion principle, e.g., see Refs. [332–334].

[18]The nature of the dipoles can be magnetic or electric, depending on the actual system under consideration.

with the error function $\text{erf}(x)$ and the reduced relative coordinate $\tilde{x} = |x_1 - x_2|/l_\perp$. Here, the length scales read $l_{\parallel/\perp} = \sqrt{1/(m\omega_{\parallel/\perp})}$, where $\omega_{\parallel/\perp}$ defines the longitudinal or transverse trap frequencies of a fictitious experimental set-up, respectively. Initially, this effective dipole-dipole interaction potential was constructed from the usual dipole interaction $\propto 1/|\vec{r}|^3$ in a so-called single-mode approximation where the dipole interaction was averaged over the ground state of the purely transverse motion, see, e.g., Ref. [327] for details.

In our study, we fix the trap frequencies as well as the fermion masses such that $m = \omega_\perp = \omega_\parallel = 1$ which means that we measure all relevant dimensionful quantities, e.g., the ground-state energy or the dipole interaction strength d^2, in natural units of one. Clearly, from an experimental point of view the assumption of equal transverse and longitudinal trap frequencies is not compatible with the construction of a cigar-shaped potential within an experimental set-up. However, in the present study we rather concentrate on the KS improvement of our theoretical DFT-RG framework. For simplicity, we therefore make the approximation $\omega_\parallel = \omega_\perp$.

The dipole-type interaction potential Eq. (4.63) is presented in Fig. 4.5 for different values of the dipole strength d^2, playing the role of a tunable coupling constant in our study. We shall investigate both, the repulsive $d^2 < 0$ as well as the attractive $d^2 > 0$ regime by varying the interaction strength d^2, see our study below. Note, for large spatial distances $\tilde{x} \gg 1$, the interaction potential Eq. (4.63) tends to zero such as $U(x) \simeq -2d^2/|x|^3$ which corresponds to the usual limiting behavior of a classical dipole-dipole interaction, see Ref. [330]. Nevertheless, for $\tilde{x} \to 0$ the interaction remains finite where its amplitude is controlled by the dipole coupling constant d^2. The effective dipole-dipole interaction potential can therefore be understood as a mixture between a local and a non-local two-body interaction.

4.4.2   DFT-RG Approach to Quasi-One-Dimensional Fermions

Let us now study quasi-one-dimensional fermions with an effective dipole-dipole interaction using our DFT-RG framework. In principle, the rather general classical action Eq. (4.28) we have considered in our introductory example in Sec. 4.3.2 can be reused for the system of fermions trapped in an external potential. In the previous model, we have set the flow of the external potential $\partial_\lambda V_\lambda(x)$ to zero as the (anti)periodic box remained to be unchanged for any value of the flow parameter λ. We now start the DFT-RG flow with a KS-improved trap at $\lambda = 0$ fully switching off the auxiliary KS potential at $\lambda = 1$. To this end, we define a λ-dependent external potential:

$$V_\lambda(x) = \lambda\, v_\text{ext}(x) + (1 - \lambda)\, v_\text{KS}[n](x)\,. \tag{4.64}$$

For the KS potential $v_\text{KS}[n](x)$, which enters the self-consistent KS equations (4.14), we use

$$v_\text{KS}[n](x) = v_\text{ext}(x) + v_\text{H}[n](x)\,, \tag{4.65}$$

neglecting all types of *exchange-correlation* terms $v_\text{xc}[n]$ for convenience in the present feasibility study which then only enter within our DFT-RG framework. From the definition of our λ-dependent external potential $V_\lambda(x)$, we can now compute the derivative with respect to the RG flow parameter $\partial_\lambda V_\lambda(x)$, see Eq. (4.49). We have

$$\delta V(x) = \partial_\lambda V_\lambda(x) = -v_\text{H}[n](x)\,, \tag{4.66}$$

where we find that the only term from the KS procedure, which enters the DFT-RG flow equations, stems from the *Hartree* contribution of the KS potential.

Let us now discuss the DFT-RG flow equations in leading and next-to-leading order for the few-body quantum system under consideration. In principle, since the derivation of the DFT-RG flow equations for the different n-density correlation functions is similar to the example in Sec. 4.3.2, we refer to Refs. [108, 110] for details on the computation. The main difference in our present study is that we now consider a λ-dependent external trap. We use the external potential given in (4.66) as well as the DFT-RG flow equation (4.49) where we find for the flow equation

of the ground-state energy

$$
\begin{aligned}
\partial_\lambda E_{\mathrm{gs},\lambda} &= \int_{x_1} \delta V(x_1)\, n_\lambda(x_1) + \frac{1}{2} \int_{x_1} \int_{x_2} n_\lambda(x_1)\, U(x_1 - x_2)\, n_\lambda(x_2) \\
&\quad + \frac{1}{2} \int_{x_1} \int_{x_2} U(x_2 - x_1)\, G^{(2)}_{\lambda=0}(0, x_1, 0, x_2) - \frac{N}{2}\, U(0)\,,
\end{aligned}
\tag{4.67}
$$

and for the flow equation of the ground-state density

$$
\begin{aligned}
\partial_\lambda n_\lambda(x) &= -\int_{\tau_1} \int_{x_1} \delta V(x_1)\, G^{(2)}_{\lambda=0}(\tau_1, x_1, 0, x) - \int_{\tau_1} \int_{x_1} \int_{x_2} n_\lambda(x_1)\, U(x_1 - x_2)\, G^{(2)}_{\lambda=0}(\tau_1, x_2, 0, x) \\
&\quad - \frac{1}{2} \int_{\tau_1} \int_{x_1} \int_{x_2} U(x_2 - x_1)\, G^{(3)}_{\lambda=0}(\tau_1, x_1, \tau_1, x_2, 0, x) \\
&\quad + \frac{1}{2} \int_{\tau_1} \int_{x_1} G^{(2)}_{\lambda=0}(\tau_1, x_1, 0, x)\, U(0)\,.
\end{aligned}
\tag{4.68}
$$

We already indicated that, because of the presence of a finite external potential, translation invariance is explicitly broken. Thus, in contrast to our study in Sec. 4.3.2, the flow equation associated with the ground-state density does not vanish identically. Note that the same is true for the initial condition of the three-density correlation function $G^{(3)}_{\lambda=0}$ which now enters the RG flow equation of the ground-state density. According to our previous definition, we entitle the truncation which only considers the RG flow equation of the ground-state energy as the leading order (LO) where the truncation which also takes the RG flow of the ground-state density into account as the next-to-leading order (NLO). Thus, in our present study, the two-density correlation function $G^{(2)}_{\lambda=0}$ and the three-density correlation function $G^{(3)}_{\lambda=0}$ are independent of the flow parameter λ and stay at their initial value throughout the DFT-RG flow.

Let us briefly discuss the numerical set-up of our DFT-RG approach. We derive the initial conditions for the n-density correlation functions by using the one-particle propagator (4.57) computed on a spatial lattice of size L with N_L grid points and a temporal lattice of size β with N_β grid points. In particular, we use $x_l = -L/2 + l\,(L/N_L)$ with $l \in [0, N_L - 1]$ for the spatial and $\tau_m = -\beta/2 + m\,(\beta/N_\beta)$ with $m \in [0, N_\beta - 1]$ for the temporal lattice. Note that we consider periodic boundary conditions for all lattice types. Moreover, we only use even values for N_β in order to guarantee that the limit $\tau \to 0$ is included. We moreover implement the single-particle orbitals from the KS system into our DFT-RG framework by making the following substitutions in Eq. (4.57):

$$
\phi_n^{(I)}(x) \to \phi_n^{(\mathrm{KS})}(x) \qquad \text{and} \qquad \bar{\varepsilon}_n^{(I)} \to \bar{\varepsilon}_n^{(\mathrm{KS})}\,,
\tag{4.69}
$$

where $\phi_n^{(\mathrm{KS})}(x)$ and $\bar{\varepsilon}_n^{(\mathrm{KS})}$ are the KS single-particle orbitals and energies of the KS system, we discussed above. Further, for the *Fermi* energy we use $\varepsilon_{N-1}^{(\mathrm{KS})} = \varepsilon_{\mathrm{F}}^{(\mathrm{KS})}$ in our non-degenerate system. Note that the sum over the single-particle states in Eq. (4.57) is now bounded by a cutoff mode $n_{\max}$. The latter corresponds to the maximum number of spatial grid points of the model space which is used to solve the KS equations (4.14) iteratively.

For the numerical implementation of the one-particle propagator, it is crucial that the time ordering, which is encoded in the *Heaviside* function $\theta_\sigma(\tau)$, is properly implemented. For example, it is important to guarantee that $\lim_{\tau \to 0^-} \Delta_0(\tau, x, 0, x) = n_{\mathrm{gs}}(x)$. We moreover checked that the flow equation for the ground-state density vanishes if translation-invariant boundary conditions are used, i.e., we could reproduce the leading-order result from our one-dimensional nuclear model in Sec. 4.3.2. Instead computing the time-independent ground-state density via Eq. (4.35), we further assume $\rho_{\mathrm{gs}}(0, x) \simeq n_{\mathrm{gs}}(x)$ within our numerical implementation of Eqs. (4.67) and (4.68). The latter appears to be a good approximation given that the temporal box β is chosen suitably large. At least in our present study, we observe that this approximation has a rather small impact on the ground-state energy.

Let us also discuss some details on the used lattice sizes in our study. We consider different grid sizes and numbers of grid points for the spatial and temporal coordinates where we keep $N_L/L = 4\,, 6\,, 8$ fixed. We observe that
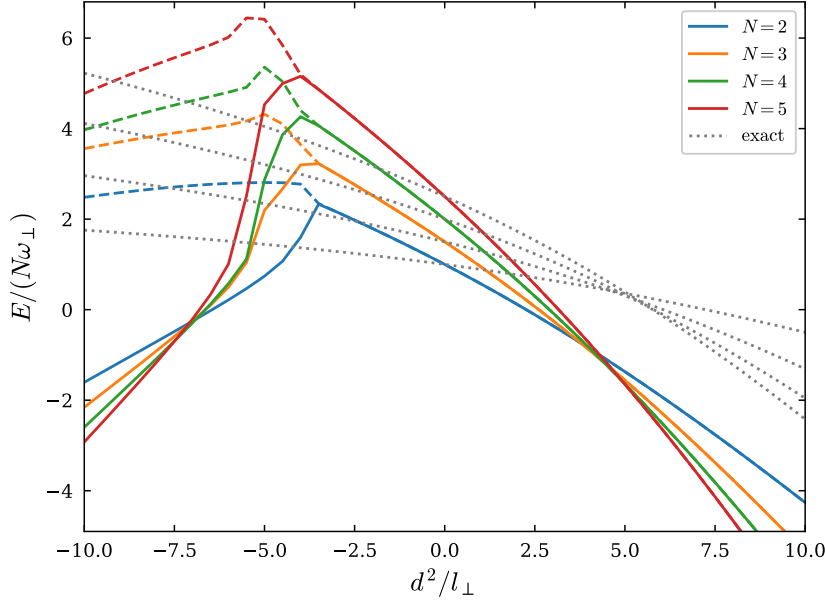
Figure 4.6: Ground-state energy per particle as a function of the dipole interaction strength $d^2/l_\perp$ for $N = 2, \ldots, 5$ fermions as obtained from a self-consistent KS approach using a *Hartree* approximation (solid colored lines). We compare the KS ground-state energy after $i = 30$ (solid) and $i = 31$ (dashed) iteration steps, see main text for details. The KS ground-state energy is further compared to results as obtained from exact diagonalization (dotted gray lines).

a spatial grid size of $L = 10$ appears to be sufficient for the presently investigated particle numbers and interaction strengths. In our study, we compute the ground-state energy as a function of N_L/L and use an extrapolation to the limit $N_L/L \to \infty$. In case of the temporal lattice, we find $\beta = 20$ with $N_\beta/\beta = 4, 6, 8$ to be sufficient for our few-body system under consideration. In analogy to the treatment of the spatial grid, we also perform $N_\beta/\beta \to \infty$ for the ground-state energy as obtained from our DFT-RG study below. In order to have a benchmark, we further use exact diagonalization to compute the ground-state energy for $N = 2, \ldots, 5$ particles. In this case, we employ *Slater* determinants as a many-body basis using harmonic oscillator single-particle states. For this, we use up to $N_{HO} \leq 9$ basis functions and extrapolate the ground-state energy to $N_{HO} \to \infty$.

Before we discuss the full KS-optimized DFT-RG computation, let us begin with the results from the self-consistent KS procedure. As an initial guess for the ground-state density n_{gs}, we choose the one corresponding to a system of N non-interacting identical fermions in a harmonic trap. During the KS iteration, we compute the KS ground-state energy per particle (4.19) of two successive iteration steps and stop the self-consistent procedure as soon as some predefined convergence criterion is achieved. The results of the KS ground-state energy (see Eq. (4.19)) as a function of the dipole interaction strength $d^2/l_\perp$ using a *Hartree* approximation (HKS) is presented in Fig. 4.6. In particular, we show the ground-state energy as obtained after $i = 30$ (solid lines) and $i = 31$ (dashed lines) iterations. For comparison, we also show results from an exact diagonalization of this problem (dotted gray lines), see our discussion above. For coupling values $d^2/l_\perp \gtrsim -3.0$, we observe that both ground-state energies coincide perfectly. For instance, at $d^2/l_\perp \simeq 10.0$ the relative deviation between the two ground-state energies is negligible $|(E_{\mathrm{gs},i=30}^{\mathrm{HKS}} - E_{\mathrm{gs},i=31}^{\mathrm{HKS}})/E_{\mathrm{gs},i=30}^{\mathrm{HKS}}| \ll 10^{-10}$. From this, we can follow that the self-consistent KS procedure is converged for $i \gtrsim 30$ at least for $d^2/l_\perp \gtrsim -3.0$.

On the other hand, we find that for dipolar coupling strengths $d^2/l_\perp \lesssim -3.0$, the ground-state energies from two successive iteration steps significantly deviate. A more careful analysis reveals that the HKS ground-state energy "jumps" for two consecutive iteration steps between the depicted ground-state energies shown for $d^2/l_\perp \lesssim -3.0$
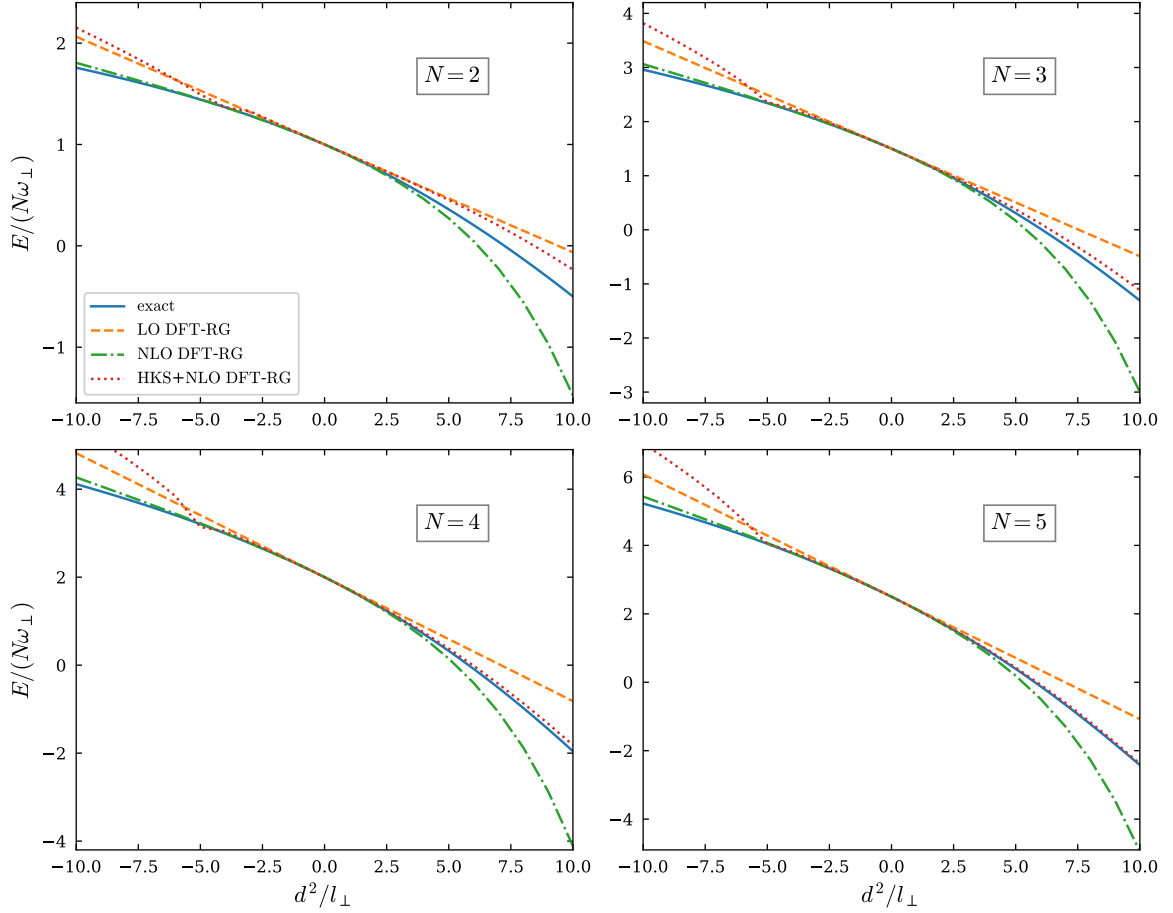
Figure 4.7: Ground-state energy per particle as a function of the dipole coupling $d^2/l_\perp$ for up to $N = 5$ particles and for different truncation types for our DFT-RG framework. At LO (dashed orange lines) and NLO (dashed-dotted green lines), we show "unimproved" results for the ground-state energy using our DFT-RG approach and compare them with a KS-improved NLO DFT-RG calculation (dotted red lines) starting the RG flow from a KS system in a *Hartree* approximation. As a benchmark, we show ground-state energies from exact diagonalization (solid blue lines).

in Fig. 4.6. The fact that we do not find a self-consistent solution for the KS equations for $d^2/l_\perp \lesssim -3.0$ also leaves its imprint in the KS-improved version of the DFT-RG approach as we shall discuss below. Nevertheless, we stress that there is, in principle, no need for the DFT-RG method to start the RG flow at a point which is associated with a self-consistent KS solution. However, since we perform the KS procedure in order to shift the starting point of the DFT-RG flow "closer" to the actual interacting many-body ground state, the use of non-self-consistent KS solutions appears at least debatable.

By comparing the ground-state energies from the HKS framework with those from exact diagonalization, we find that the HKS results reproduce the exact results only on a qualitative level at best, see Fig.. 4.6. This observation is expected since we neglect any *exchange-correlation* effects on the level of the KS potential v_{KS}. We further observe in Fig. 4.6 that all ground-state energies per particle from the exact computations seem to intersect at $d^2/l_\perp \approx 5.0$. Note that the same behavior is also observed for the ground-state energies from the HKS approach, where the intersection point is shifted towards smaller values of $d^2/l_\perp$ compared to the exact results.

Finally, let us discuss the results from our KS-improved DFT-RG framework. In Fig. 4.7, we present the (dimensionless) ground-state energy per particle $E_{\text{gs}}/(N\omega_\perp)$ as a function of the dipole interaction strength $d^2/l_\perp$. We

show the LO (dashed orange lines) and NLO (dashed-dotted green lines) results from an "unimproved" DFT-RG study starting the DFT-RG flow from a system of non-interacting fermions in a harmonic trap. Moreover, we also show our results from exact diagonalization (solid blue lines) representing our benchmark for the ground-state energy. Further, we present a KS-improved DFT-RG approach in a *Hartree* approximation (dotted red line). Note that we use the NLO truncation of the DFT-RG flow equations for our HKS-improved DFT-RG study (HKS+NLO).

We start with the discussion of the LO results computed within our DFT-RG framework. Here, we find that for all considered particle numbers, the DFT-RG computation in LO agrees well for very small coupling constants $|d^2|/l_\perp \lesssim 1$ but fails to describe the ground-state energy behavior for strong attractive or repulsive couplings. Taking also the running of the ground-state density into account, our findings in NLO are improved significantly at least in the repulsive regime, i.e., at $d^2/l_\perp \simeq -10.0$, the relative deviation from the exact results is reduced from $\Delta E_{\text{gs}}^{\text{LO}}/E_{\text{gs}}^{\text{exact}} \simeq 16\%$ in LO to $\Delta E_{\text{gs}}^{\text{NLO}}/E_{\text{gs}}^{\text{exact}} \simeq 3\%$ in NLO. Note that this observation appears to be rather independent of the particle number. For attractive dipolar coupling constants, however, we find that the NLO results from our DFT-RG study overestimate the exact ground-state energies for stronger attractive interactions considerably. For small (positive) couplings $0 \lesssim d^2/l_\perp \lesssim 2.5$, the NLO results still agree reasonably well with those from exact diagonalization. Nevertheless, for higher attractive interactions $d^2/l_\perp > 2.5$, our results from NLO do reproduce the exact ground-state energies only qualitatively.

Let us now turn to the KS-improved DFT-RG study in next-to-leading order (HKS+NLO) where we start the RG flow at $\lambda = 0$ with a KS system using a *Hartree* approximation for the KS potential. Throughout this study, we use the KS single-particle states as obtained after $i = 30$ KS iterations. In the repulsive regime, we observe for $-3.0 \lesssim d^2/l_\perp \lesssim 0$ that the HKS+NLO results are in good agreement with those from the NLO study where both are already capable to reproduce the exact ground-state energy reasonably well. For stronger repulsive interactions, however, we observe that the HKS+NLO approximation fails and performs even worse than the usual DFT-RG approach in LO. From our discussion of the pure KS system, see Fig. 4.6, we observe that within our presently used *Hartree* approximation for the KS potential, the point where the HKS+NLO truncation breaks down, coincides with the dipole interaction strength $d^2/l_\perp \simeq -3.0$ below which the KS procedure does not converge anymore. Note, we also tested to start the RG flow using the KS single-particle orbitals and energies from the KS system after $i = 31$ KS iterations. However, we observed that the issues persisted. From this, we deduce that the KS-improved DFT-RG method within the used HKS+NLO approximation appears to be not well-suited to describe the repulsive regime of the few-body system under consideration. For repulsive couplings, it turns out that the system of non-interacting fermions confined in a harmonic trap already represents a reasonable starting point for the DFT-RG flow.

Let us now discuss the attractive regime. Here, we find that the HKS+NLO truncation performs significantly better than the NLO approach, improving our findings for the ground-state energy as a function of the coupling strength considerably. For strong attractive interactions $d^2/l_\perp \simeq 10.0$, we find that the HKS+NLO approximation underestimates the exact ground-state energy for two particles (see upper left panel of Fig. 4.7) still by $\Delta E_{\text{gs}}^{\text{HKS+NLO}}/E_{\text{gs}}^{\text{exact}} \simeq 50\%$, where the usual NLO approach overestimates the exact ground-state energy by nearly $\Delta E_{\text{gs}}^{\text{NLO}}/E_{\text{gs}}^{\text{exact}} \simeq 200\%$. We further observe that the HKS+NLO approach provides better results in case of larger particle numbers. For example, in case of $N = 5$ particles, the NLO approach misses the correct ground-state energy by $\Delta E_{\text{gs}}^{\text{NLO}}/E_{\text{gs}}^{\text{exact}} \simeq 100\%$ whereas the HKS+NLO study predicts the exact value of the five-body ground-state energy better than $\Delta E_{\text{gs}}^{\text{HKS+NLO}}/E_{\text{gs}}^{\text{exact}} \simeq 2\%$ for the depicted coupling range, see the bottom-right panel of Fig. 4.7.

Our study indicates that the HKS-improved DFT-RG approach provides reasonably well results within the attractive regime of our dipolar two-body interaction. Moreover, the KS-improved DFT-RG framework works particularly well for large particle numbers. For instance, the HKS+NLO ground-state energy for $N = 5$ particles is in good agreement with the results from our exact study. Note, we already observed that the DFT-RG method provides better results for increasing particle numbers in our nuclear toy-model study [110] using an "unimproved" starting point for the RG flow. In our present study, we emphasize that we have chosen the most simple KS potential possible. On the level of the self-consistent KS procedure, we completely neglected all *exchange-correlation* effects, which

only entered our approach through the DFT-RG flow equations for the ground-state energy and density. Indeed, the fact that the strongly-interacting five-body system in the attractive regime can be well-described by employing our comparably simple truncations is promising for future studies.

Furthermore, by using the DFT-RG flow equations (4.67) and (4.68), it would be interesting to study if more sophisticated approximations for the KS potential $v_{\text{KS}}(x)$ are capable to improve our results from the HKS+NLO truncation even further. For example, we may also consider an *exchange-correlation* term in the KS potential using, e.g., an LDA-type approximation. In this context, it would also be interesting to study if a so-improved KS potential could be better suited to provide a description for the repulsive regime.

Chapter 5

Conclusion

The first part of this thesis was dedicated to the study of the phase structure of relativistic hot and dense strong-interaction matter working in the framework of the functional Renormalization Group. Studying *Fierz*-complete NJL models and two-flavor QCD, we analyzed the fixed-point structure and symmetry breaking patterns at finite temperature and quark chemical potential where we examined the impact of *Fierz* incompleteness on physical observables.

In the second part, we employed a Renormalization Group inspired approach to Density Functional Theory studying bound-state properties of non-relativistic one-dimensional fermions at zero temperature where we aimed to improve the truncated DFT-RG flow equations based on an optimization of the starting point. To this end, we solved the KS equations self-consistently and initialized the RG flow from the non-interacting KS system.

We began our discussion in Sec. 3.1 with a one-flavor and one-color NJL-type model at finite temperature and fermion chemical potential, considering a classical action being invariant under global $U(1)_A \times U(1)_V$ symmetry transformations. As an ansatz for the effective action at leading order of the derivative expansion, we then found six four-fermion channels obeying the underlying symmetries. Moreover, by means of *Fierz* transformations the six channels could be reduced to a three-channel *Fierz*-complete basis. We showed that we recover the vacuum results from previous NJL model studies given that we use a *covariant* four-dimensional regularization scheme. By analyzing the underlying fixed-point structure in theory space, we then found two real-valued non-*Gaussian* fixed points controlling the RG flow in theory space.

At finite temperature and fermion chemical potential, we then studied the phase boundary separating the gapped from the ungapped regime by using a one-channel, two-channel, and a three-channel *Fierz*-complete set of four-fermion channels as a basis in theory space. To fix the scale, we tuned the UV value associated with the scalar-pseudoscalar coupling to recover a certain critical temperature at zero quark chemical potential. In our study, we observed that the use of *Fierz*-incomplete approaches could have a significant impact on the shape of the phase boundary. For instance, we found that the critical chemical potential μ_{cr} above which no spontaneous symmetry breaking of any kind is observed, is about 20% greater in a *Fierz*-complete approach than in a one-channel study, see Fig. 3.4. We further considered a *Fierz*-complete difermion-type parameterization as a basis, where we observed that the phase boundaries of the corresponding *Fierz*-complete studies are identical as it should be. We also showed that this is not the case for *Fierz*-incomplete approaches. For example, the critical chemical potentials as obtained from different two-channel parametrizations differ significantly, see Figs. 3.4 and 3.5. We conclude that *Fierz*-incomplete approximations can either overestimate or underestimate the extent of the phase boundary which is associated with spontaneous symmetry breaking. We found that the error depends strongly on the type and number of considered four-fermion channels in a *Fierz*-incomplete basis. Since we worked in the pointlike limit of the four-fermion correlation functions, a detailed study of the theory's ground state in the regime which is governed by a spontaneously broken symmetry is not possible. To still get some insights in the structure of the ground state in the *infrared*, we an-

alyzed the dominance pattern of the scale-dependent four-fermion couplings close to the phase boundary. For this, we "monitored" their relative strength and argued that a dominance in a particular channel can be considered as an indication for the onset of the corresponding condensate. This is also supported by recent condensed-matter studies [342]. We observed that for a wide range of fermion chemical potential, the utmost dominant channel in both *Fierz*-complete parameterizations is the scalar-pseudoscalar channel associated with spontaneous chiral symmetry breaking. The dominance pattern in the regime of large fermion chemical potential, however, is inconclusive. We found that channels which explicitly break the *Poincaré* symmetry appear to be dominant in both *Fierz*-complete studies.

To gain further insights from the theory's ground state, we analyzed the scaling relations of the one-loop diagrams which enter our four-fermion study using a simple one-channel truncation, see Fig. 3.6. In particular, we discussed the fixed-point behavior under a variation of the temperature and fermion chemical potential where we could distinguish two types of loop diagrams exhibiting different kinds of scaling behavior: One class of diagrams generates a BCS-type scaling behavior of physical observables and is found to dominate the regime at large quark chemical potential, whereas a second class of diagrams suppresses this scaling behavior in the latter regime.

We further discussed the impact of a non-*covariant* regularization scheme on the phase boundary at finite temperature and fermion chemical potential. We observed that both the dominance pattern and the shape of the phase diagram are changed significantly. Even at $\mu = 0$ where the study using a *covariant* regulator indicated the formation of a chiral condensate, we found a vector-type condensate to be favored by employing a non-*covariant* regulator type. Moreover, our study at low temperature using a non-*covariant* regulator suggested that the theory's ground state is governed by spontaneous symmetry breaking for all investigated values of the chemical potential, see Fig. 3.7.

In Sec. 3.2, we studied the phase structure of a *Fierz*-complete NJL model with two flavors and N_c colors at leading order of the derivative expansion. We found that a *Fierz*-complete four-quark basis is given by ten channels obeying a global $SU(N_c) \times SU(2)_L \times SU(2)_R \times U(1)_V$ symmetry. In particular, the *Fierz*-complete basis is composed of six channels which are invariant under global $SU(N_c) \times SU(2)_L \times SU(2)_R \times U(1)_V \times U(1)_A$ transformations and four channels which break the axial $U(1)_A$ symmetry explicitly. In our *Fierz*-complete basis, we included a scalar-pseudoscalar channel since its corresponding condensate serves as an order parameter for spontaneous chiral symmetry breaking and a diquark channel associated with BCS-type pairing. Moreover, from the $U(1)_A$-breaking subspace of our *Fierz*-complete four-quark basis, we deduced sum rules which are exactly fulfilled given that the axial symmetry is intact. The sum rules then imply that a *Fierz*-complete basis which respects the $U(1)_A$ symmetry has eight independent channels. The latter then implies that the ten-dimensional theory space can be reduced to eight dimensions.

In our RG study of this model, we began with a discussion of a one-channel approximation where we only considered the scalar-pseudoscalar channel. In the vacuum limit, we then studied the fixed-point structure where we found a real-valued non-*Gaussian* fixed point dominating the RG flow towards the *infrared* regime. We found that a corresponding fixed point also exists in case of the full *Fierz*-complete study. In particular, by considering a large-N_c expansion at leading order of the full *Fierz*-complete set of four-quark interactions, we observed that the specific non-*Gaussian* fixed point is located precisely on the axis associated with the scalar-pseudoscalar coupling. A stability analysis moreover revealed that this fixed point has only one repulsive IR direction which points into the direction of the scalar-pseudoscalar axis. All other nine directions were found to be IR attractive. We followed that, if the RG flow is initiated sufficiently "close" to the fixed point, the latter should dominate the low-energy regime at low quark chemical potential.

Furthermore, we studied the phase structure in the (T, μ) plane using the one-channel ansatz from the vacuum study, a two-channel approximation composed of a scalar-pseudoscalar and a diquark channel, and the full ten-channel *Fierz*-complete approach, see Fig. 3.8. To fix the scale, we tuned again only the scalar-pseudoscalar coupling in the UV to recover $T_0 \simeq 132\,\mathrm{MeV}$ which corresponds to the chiral phase transition temperature recently found in lattice QCD studies [9]. We observed that the regime at small chemical potential $\mu \lesssim 260\,\mathrm{MeV}$ appears to

be mostly governed by the aforementioned non-*Gaussian* fixed point which leaves its imprint in the observation that the phase boundaries from all three truncations coincide. At large quark chemical potential, however, we observed again how *Fierz*-incomplete truncations can affect important key properties. In particular, we found that the phase boundary associated with the one-channel approximation exhibits a critical chemical potential $\mu_{\mathrm{cr}} \simeq 360 \, \mathrm{MeV}$ whereas a non-trivial ground state governs the phase diagrams associated with the two-channel and *Fierz*-complete approximation for all studied values of μ. We further found that the phase boundary of the *Fierz*-complete approach is about 70% greater at $\mu \simeq 530 \, \mathrm{MeV}$, than the corresponding phase boundary of the two-channel ansatz. At small quark chemical potential $\mu \lesssim 260 \, \mathrm{MeV}$, we then detected a dominance of the scalar-pseudoscalar channel in all truncations. For larger quark chemical potential, we deduced from the dominance pattern of the *Fierz*-complete ansatz that the formation of a non-zero diquark condensate is favored. We further observed that four-quark channels, other than the diquark channel, which correspond to a ground state with a non-trivial color structure are subdominant, e.g., $(V + A)_{\parallel}^{\mathrm{adj}}$- and $(V - A)_{\parallel}^{\mathrm{adj}}$-type channels.

We further studied the impact of $U(1)_A$-symmetric initial conditions on the phase structure of the NJL model where we found that the overall shape of the phase boundary remains mostly unaffected, see Fig. 3.10. At small quark chemical potential, we still observed a dominance of the scalar-pseudoscalar channel in agreement with our study using a set of $U(1)_A$-breaking initial conditions. At large quark chemical potential, we recognized a change of the dominance pattern and found indications for a diquark condensate associated with the $(V + A)_{\parallel}^{\mathrm{adj}}$ channel.

Since the scalar-pseudoscalar and the diquark channel were found to be most dominant over a wide range of the phase diagram, we studied the pseudo fixed-point structure of the corresponding *Fierz*-incomplete two-channel ansatz in more detail, see Fig. 3.12. To this end, we investigated the behavior of the pseudo fixed points under a variation of the dimensionless quark chemical potential. Our studies reveal an intriguing mechanism of fixed-point creation and annihilation which can lead to a change in the dominance pattern, and explains the appearance of diquark dominance at large chemical potential.

In the final study of the first part, we explored the phase structure of QCD with two massless quark flavors at finite temperature and quark chemical potential, see Sec. 3.3. To this end, we considered the *Fierz*-complete four-quark basis from Sec. 3.2 and included the quark-gluon vertex in our ansatz. We identified the coupling associated with the quark-gluon vertex with the scale-dependent strong gauge coupling g_k from a *background-field* study, see Refs. [18–20]. Moreover, to estimate the effects of matter contributions to the running of the strong coupling, we considered two different types of scale-dependent strong couplings, namely α_{QCD} $(N_f = 2)$ and α_{YM} $(N_f = 0)$. To fix the scale in our QCD study, we tuned the strong gauge couplings in the UV so that we found $T_0 \simeq 132 \, \mathrm{MeV}$ at $\mu = 0$ corresponding to the value of the transition temperature in the aforementioned lattice QCD studies [9]. In the four-quark sector, we set the initial conditions of all four-quark couplings to zero to ensure that they are generated dynamically in the RG flow.

With this set-up at hand, we studied the phase structure in the (T, μ) plane as obtained from α_{QCD} and α_{YM} using the *Fierz*-complete four-quark basis from Sec. 3.2. Here, we found that both phase boundaries agree well over a wide range of the quark chemical potential. We further compared the results from QCD with those from our NJL model study in Sec. 3.2. We observed at $\mu \simeq 530 \, \mathrm{MeV}$ that the critical transition temperature is about 100% greater than the one we found in the NJL model case. The latter implies that gauge degrees of freedom are expected to become essential at large quark chemical potential and have a crucial impact on the phase structure. We further studied the dominance pattern of QCD where we found the scalar-pseudoscalar channel to be dominant at small chemical potential $\mu \lesssim 260 \, \mathrm{MeV}$. At larger chemical potential, we found a simultaneous dominance of the diquark and the $(S + P)_-^{\mathrm{adj}}$ channel. Since we used $U(1)_A$-conserving initial conditions $(\lambda_i^{(\mathrm{UV})} = 0)$, this observation is a direct consequence of the sum rules for the four-quark interactions, see (3.49).

Even though our study cannot provide a final answer concerning the condensate forming in the low-energy regime, the fixed-point structure found in our large-N_c analysis and the dominance pattern provide several indications that the gapped phase is governed by chiral degrees of freedom at low, and by diquark degrees of freedom at large chemical potential. Still, the specific type of the diquark condensate remains to be unknown. From our

present work, however, a chirally symmetric $J^P = 0^+$ diquark condensate appears to be favored.

Let us now give a brief outlook to future studies of hot and dense strong-interaction matter using the functional Renormalization Group. In Sec. 3.4, we already discussed that we have the long-term goal to compute the equation of state from first principles. To this end, it is required to better understand the true nature of the ground state of high-density QCD in the regime, which is governed by spontaneous symmetry breaking. Therefore, a meaningful step towards the description of isospin-symmetric nuclear matter would be to employ dynamical bosonization techniques [22, 23, 159, 161–164, 235, 240–242, 307] in order to study bound-state properties of diquarks and mesons, see our discussion in Sec. 2.3.3. However, a description of, e.g., dense neutron-rich matter, which is expected to exist within the core of neutron stars, would further require to introduce an isospin asymmetry in our ansatz for the effective action. In this case, the *Fierz*-complete four-quark basis has to be reconsidered as well. Since it is more-over expected [130, 343–345] that fluctuations in the strange sector could have a sizable effect on thermodynamic quantities, it might be worthwhile to also consider strange quark degrees of freedom in future works. As we foresee that such a study might be rather involved, it could be then also necessary to further develop existing numerical and analytical tools [166, 167, 346] in order to gain access to the equation of state of QCD at large density.

In the second part of the present thesis, we began with a short introduction to DFT based on the famous *Hohenberg-Kohn* theorem and discussed a conventional approach to DFT by employing the self-consistent *Kohn-Sham* equations, see Chap. 4. There, we also gave a brief overview of how *exchange-correlation* effects can be included in DFT calculations before we presented an RG approach to DFT based on a microscopic formulation for the HK energy density functional. We showed that the latter is related to the 2PPI effective action for which we presented an RG flow equation in the spirit of the *Wetterich* equation.

As a preliminary example, we showed some key results from a nuclear toy model study [110] where we considered one-dimensional identical fermions which interact via a long-range attractive and short-range repulsive two-body interaction, see Sec. 4.3.2. We confined the fermions in a box with (anti)periodic boundary conditions and considered a periodic extension of the two-body interaction rendering the latter translation invariant. In this case, we showed that the DFT-RG flow preserves translation invariance as it should be. Using the DFT-RG framework, we derived flow equations for the ground-state energy (LO) and the two-density correlation function (NLO). In LO and NLO of the DFT-RG flow equations, we then computed the ground-state energy for two particles as a function of the inverse homogeneous density from the DFT-RG approach and used results from an exact diagonalization method to benchmark our findings, see Fig. 4.3. We found that the DFT-RG method is systematic as results from the DFT-RG framework are improved by taking the flow of higher-order correlation functions into account. Using our present truncations, we found that for small box sizes our results agree with the exact ones. In the large-volume limit, however, our results as obtained from our DFT-RG approach in LO and NLO did not converge to the known exact values for the ground-state energy. Furthermore, we also showed ground-state energy results as a function of the inverse density for up to ten particles. To estimate the few-body ground-state energy in the continuum limit, we utilized the observation that the results in LO and NLO of the DFT-RG framework approach the exact two-body ground-state energy from above. Using this approximation, we compared the few-body ground-state energy in the continuum limit as found from the DFT-RG approach in NLO with MC results from Ref. [326]. We observed that the ground-state energies from our DFT-RG flow equations in NLO are in a qualitative agreement with the MC findings where we found that our present truncation still overestimates the exact two-body ground-state energy by $\sim 30\%$. For increasing particle number, the relative difference continuously decreases. For $N = 8$, for example, the difference is smaller than $\sim 20\%$.

In Sec. 4.3.3, we introduced a possible improvement scheme for our DFT-RG framework. In particular, we discussed the idea that we initialize the DFT-RG flow at a KS system assuming that the KS single-particle orbitals already represent an "optimized" basis for the ground-state density. The single-particle states enter the definition of the one-particle propagator which represents the building block of all higher density correlation functions. Further-more, we gave a "recipe" how such a KS improvement scheme can be implemented in a given DFT-RG framework.

As a proof-of-concept study, we considered quasi-one-dimensional identical fermions at zero temperature which

interact via a dipolar two-body potential in a harmonic trap, see Sec. 4.4. We derived the DFT-RG flow equations for the ground-state energy (LO) and density (NLO) where we computed initial conditions for density correlation functions up to $G_{\lambda=0}^{(n)}$ with $n \leq 3$. For the KS potential, we used a *Hartree* truncation dropping all types of *exchange-correlation* effects. In our first study, we computed the few-body ground-state energy for up to five particles for attractive and repulsive dipolar interaction strengths as it is obtained from the self-consistent KS procedure. To benchmark our findings, we used an exact diagonalization of the corresponding Hamiltonian. We observed that the KS ground-state energy can reproduce our exact results only on a qualitative level. We further found that the KS procedure converges for attractive dipolar interaction strengths. However, for sufficiently large repulsive dipolar couplings, we found that KS procedure is non-convergent. In particular, we observed that the ground-state energy "jumped" between two values for consecutive iteration steps.

For up to five particles, we then studied the ground-state energies for various coupling strengths in LO and NLO of the DFT-RG flow equations. We used a "conventional" approach where the starting point of the RG flow corresponds to a non-interacting fermion system in an external harmonic trap (NLO). As an alternative starting point, we considered a system of non-interacting fermions in a KS potential (HKS+NLO) where we gradually switched off the KS contributions at $\lambda = 1$ while solving the RG equations. For small repulsive interactions, the conventional NLO and the improved HKS+NLO approximations perform both reasonably well compared to exact results. For large repulsive interaction strengths, however, we found that the conventional NLO approach performs in the present truncation scheme better than the HKS+NLO approximation. We backtraced this behavior to the KS procedure which did not converge for sufficiently large repulsive interaction strengths. For attractive interaction strengths, we observed that the HKS+NLO DFT-RG approximation performs better than the conventional LO and NLO approximations. For instance, for the two-body problem, we found a deviation relative to the exact results of about $\sim 200\%$ for the strongest considered couplings in the conventional NLO approximation, compared to $\sim 50\%$ using the HKS+NLO truncation. For five particles, we observed for the same coupling strength a relative deviation of $\sim 100\%$ in the conventional NLO approximation whereas the HKS+NLO approach predicts the ground-state energy better than $\sim 2\%$.

Let us discuss possible amendments to the DFT-RG framework. A first reasonable step towards a better understanding of the KS-improved DFT-RG flow would be to study whether a KS potential which also includes *exchange-correlation* effects could systematically improve our results for the ground-state energy. A possible choice would be to consider an LDA term $v_{\mathrm{xc}}^{\mathrm{LDA}}(x)$ in our ansatz for the KS potential $v^{\mathrm{KS}}(x)$ which might be seen as a "natural" extension beyond the presently employed *Hartree* approximation. A further crucial step would also be to consider the flow equation associated with the density correlation function $G_{\lambda}^{(2)}$ which would require $G_{\lambda=0}^{(4)}$ entering as an initial condition. In order to study systems like nuclei, an extension of the DFT-RG flow equation towards higher dimensions is worthwhile.

The present thesis represents a step forward to better understand critical phenomena in strong-interaction matter at large densities, and to the development of efficient theoretical techniques to study bound-state properties of few- and many-fermion systems from first principles. Therefore, our work may be helpful to guide the construction of improved hadronic equations of state from *ab initio* calculations for astrophysical applications in the future.

Appendices

Appendix A

Notations and Conventions

In this appendix, we shall give some frequently used notations and conventions appearing within the two parts of the work.

A.1   Relativistic Conventions

Throughout the thesis, we consider natural units where we set $\hbar = c = k_\mathrm{B} = 1$. Note that we use the same convention in the non-relativistic part of this work. As a consequence, we can express all dimensionful physical quantities in terms of energy or length scales, respectively:

$$[\text{length}]^{-1} = [\text{momentum}] = [\text{energy}] = [\text{temperature}]\,. \tag{A.1}$$

Using the definitions above, the (quantum) fields in position space entering our studies have the following mass dimension:

$$[\psi] = [\bar\psi] \quad = \quad \frac{D-1}{2} \times [\text{momentum}]\,, \tag{A.2}$$

$$[A_\mu] = [\phi] \quad = \quad \frac{D-2}{2} \times [\text{momentum}]\,, \tag{A.3}$$

where $D = d + 1$ is the number of spacetime dimensions. Here, ψ and $\bar\psi$ shall denote fermionic spinor fields, e.g., quarks, where ϕ and A_μ shall denote bosonic fields, e.g., mesons and gluons. Note that both field types fulfill distinct commutation relations. For instance, bosonic fields commute whereas fermionic fields are *Grassmann*-valued and anticommute, see, e.g., Ref. [125], which is reflected by the underlying field-space metric, see Ref. [159]. If not mentioned otherwise, we do not resolve internal *Dirac*, color and flavor indices of spinor fields. Further, we usually assume a summation over indices in contracted tensor structures. We further introduce the super field Φ and the super source J in position space:

$$\Phi = \begin{pmatrix} \psi \\ \bar\psi^T \\ A_\mu^a \\ \phi \end{pmatrix}\,, \quad \Phi^T = \begin{pmatrix} \psi^T & \bar\psi & A_\mu^a & \phi \end{pmatrix}\,, \quad J = \begin{pmatrix} -\bar J_\psi^T \\ J_{\bar\psi} \\ J_{A,\mu}^a \\ J_\phi \end{pmatrix}\,, \quad J^T = \begin{pmatrix} \bar J_\psi & -J_{\bar\psi}^T & J_{A,\mu}^a & J_\phi \end{pmatrix}\,. \tag{A.4}$$

Note that functional derivatives with respect to the super field/source are defined in field space as followed: derivatives acting from the left are represented by column vectors whereas derivatives acting from the right are represented by row vectors. The latter definition is a consequence of the non-trivial metric the field-space obeys. For conve-

nience, we further define

$$J^T \cdot \Phi = \int_{V_D} \left(\bar{J}_\psi \psi + \bar{\psi} J_{\bar{\psi}} + J^a_{A,\mu} A^a_\mu + J_\phi \phi \right), \tag{A.5}$$

where V_D is the D-dimensional spacetime volume. Because of the aforementioned non-trivial field-space metric, the regulator matrix R_k has a non-diagonal structure. For the latter, we therefore use the following matrix representation:

$$R_k = \begin{pmatrix} 0 & -R^T_{\psi,k} & 0 & 0 \\ R_{\psi,k} & 0 & 0 & 0 \\ 0 & 0 & R^{ab,\mu\nu}_{A,k} & 0 \\ 0 & 0 & 0 & R_{\phi,k} \end{pmatrix}. \tag{A.6}$$

Note that the definition of the regulator matrix in field space above also corresponds to our present definition of the super field Φ.

At finite temperature, the temporal direction in *Euclidean* spacetime is distinguished explicitly. Moreover, the latter direction is compactified so that we have for the imaginary time $\tau \in (0, \beta]$ with the inverse temperature $\beta = 1/T$. Therefore, the integration over the D-dimensional spacetime volume is modified as follows:

$$\int \mathrm{d}^D x \quad \rightarrow \quad \int_0^\beta \mathrm{d}\tau \int \mathrm{d}^d x, \tag{A.7}$$

$$\int \frac{\mathrm{d}^D p}{(2\pi)^D} \quad \rightarrow \quad T \sum_{n=-\infty}^{\infty} \int \frac{\mathrm{d}^d p}{(2\pi)^d}, \tag{A.8}$$

with $d = D - 1$. Moreover, our *Fourier* conventions for the fermionic spinor fields ψ, $\bar{\psi}$ and the boson field ϕ at non-zero temperature read:

$$
\begin{aligned}
\psi(\tau, \vec{x}) &= T \sum_{n=-\infty}^{\infty} \int \frac{\mathrm{d}^d p}{(2\pi)^d} \, \psi(\nu_n, \vec{p}) \, \mathrm{e}^{\mathrm{i} p_\mu x^\mu}, \\
\bar{\psi}(\tau, \vec{x}) &= T \sum_{n=-\infty}^{\infty} \int \frac{\mathrm{d}^d p}{(2\pi)^d} \, \bar{\psi}(\nu_n, \vec{p}) \, \mathrm{e}^{-\mathrm{i} p_\mu x^\mu}, \\
\phi(\tau, \vec{x}) &= T \sum_{n=-\infty}^{\infty} \int \frac{\mathrm{d}^d p}{(2\pi)^d} \, \phi(\omega_n, \vec{p}) \, \mathrm{e}^{\mathrm{i} p_\mu x^\mu},
\end{aligned}
\tag{A.9}
$$

where we use the shorthand notation $p_\mu x^\mu \equiv p_0 \tau + \vec{p} \cdot \vec{x}$ and $p_0 \in \{\omega_n, \nu_n\}$. Here, we have introduced the *Matsubara* frequencies associated with bosonic $\omega_n = 2n\pi T$ and fermionic $\nu_n = (2n + 1)\pi T$ modes, respectively.

A.2 Non-Relativistic Conventions

In this subsection, we give a few abbreviations we use in the second part of this thesis at hand.

A.2.1 One-dimensional Fermions in a Box

In our brief review of Ref. [110], we use antiperiodic boundary conditions $p_n^{(A)} = (2n+1)/L$ for even particle numbers and periodic boundary conditions $p_n^{(P)} = 2n\pi/L$ for odd particle numbers ensuring that the non-interacting

ground state is non-degenerate. In a finite box of size L, we use the following abbreviations

$$
\int_\tau \equiv \int_{-\infty}^{\infty} \mathrm{d}\tau\,, \qquad\qquad \int_\omega \equiv \int_{-\infty}^{\infty} \frac{\mathrm{d}\omega}{2\pi}\,,
$$

$$
\int_x \equiv \int_{-\frac{L}{2}}^{\frac{L}{2}} \mathrm{d}x\,, \qquad\qquad \sum_n \equiv \sum_{n=-\infty}^{\infty}\,. \tag{A.10}
$$

A.2.2 One-dimensional Fermions in a Harmonic Trap

In our feasibility study of one-dimensional fermions confined within a harmonic trap, we use

$$
\int_\tau \equiv \int_{-\infty}^{\infty} \mathrm{d}\tau\,, \qquad\qquad \int_\omega \equiv \int_{-\infty}^{\infty} \frac{\mathrm{d}\omega}{2\pi}\,,
$$

$$
\int_x \equiv \int_{-\infty}^{\infty} \mathrm{d}x\,, \qquad\qquad \sum_n \equiv \sum_{n\geq 0}\,. \tag{A.11}
$$

Appendix B

Identities and Fierz Transformations

In this appendix, we give some identities at hand which can be helpful in relativistic calculations. Moreover, we give our definitions for the *Clifford* and the $SU(N)$ algebra. Furthermore, we shall discuss the *Fierz* transformations in more detail and introduce some *Fierz* identities we use in this work.

B.1 Euclidean Clifford-Algebra in $D = 3 + 1$

We define the *Clifford* algebra in $D = 3 + 1$ *Euclidean* spacetime dimensions via:

$$\left\{\gamma^\mu, \gamma^\nu\right\} = \gamma^\mu \gamma^\nu + \gamma^\nu \gamma^\mu = 2\delta^{\mu\nu}\, \mathbb{1}_D \,, \tag{B.1}$$

$$\left(\gamma^\mu\right)^\dagger = \gamma^\mu \,, \tag{B.2}$$

$$\gamma_5 \equiv \gamma_1 \gamma_2 \gamma_3 \gamma_0 \,, \tag{B.3}$$

$$\sigma_{\mu\nu} \equiv \frac{\mathrm{i}}{2}\left[\gamma^\mu, \gamma^\nu\right] = \frac{\mathrm{i}}{2}\left(\gamma^\mu \gamma^\nu - \gamma^\nu \gamma^\mu\right). \tag{B.4}$$

Further, we provide the following useful relations for various combinations and traces of *Dirac* matrices:

$$\left\{\gamma^\mu, \gamma_5\right\} = 0 \,, \tag{B.5}$$

$$\left(\gamma_5\right)^\dagger = \gamma_5 \,, \tag{B.6}$$

$$\left(\gamma^\mu\right)^2 = \left(\gamma_5\right)^2 = \mathbb{1}_D \,, \tag{B.7}$$

$$\gamma^\mu \gamma^\nu = \mathbb{1}_D\, \delta^{\mu\nu} - \mathrm{i}\sigma^{\mu\nu} \,, \tag{B.8}$$

$$\gamma^\mu \gamma^\nu \gamma^\lambda = \delta^{\mu\nu} \gamma^\lambda - \delta^{\mu\lambda} \gamma^\nu + \delta^{\nu\lambda} \gamma^\mu + \varepsilon_{\mu\nu\lambda\rho} \gamma^\rho \gamma_5 \,, \tag{B.9}$$

$$\frac{1}{4}\mathrm{Tr}\left(\gamma^\mu \gamma^\nu \gamma^\lambda \gamma^\rho\right) = \delta^{\mu\nu}\delta^{\lambda\rho} - \delta^{\mu\lambda}\delta^{\nu\rho} + \delta^{\mu\rho}\delta^{\nu\lambda} \,, \tag{B.10}$$

$$\frac{1}{4}\mathrm{Tr}\left(\gamma^\mu \gamma^\nu \gamma^\lambda \gamma^\rho \gamma_5\right) = \mathrm{i}\varepsilon_{\mu\nu\lambda\rho} \,, \tag{B.11}$$

where $\mathbb{1}_D$ denotes the four-dimensional identity matrix in *Dirac* space and $\varepsilon_{\mu\nu\lambda\rho}$ the four-dimensional *Levi-Civita* symbol.

B.2 $SU(N)$ Algebra

The commutation relation for the $N^2 - 1$ generators T^a of the $SU(N)$ *Lie* group reads

$$[T^a, T^b] = \mathrm{i} f^{abc} T^c \,, \tag{B.12}$$

with the antisymmetric structure constant f^{abc}. We further define

$$T^a = \frac{1}{2} \tau^a \,, \tag{B.13}$$

where τ^a are, e.g., the *Pauli* matrices in case of $SU(2)$ or *Gell-Mann* matrices in case of $SU(3)$, see also App. B.3. The generators T^a are ortho-normalized and fulfill

$$\mathrm{Tr}(T^a T^b) = \frac{1}{2} \delta^{ab} \,. \tag{B.14}$$

The *Fierz* identities of $SU(N)$ generators are discussed in the section below.

B.3   Fierz Transformations

Non-trivial *Fierz* identities can be derived for practically all n-point functions given that at least four *Grassmann*-valued fields are involved. From a reordering of the latter, one can deduce relations between different interaction channels. In the present thesis, we focus on four-quark interactions which appear to be most relevant to study spontaneous symmetry breaking in QCD. For this, we shall discuss in this appendix two types of field reorderings in more detail. First, we note that the 16 *Dirac* matrices

$$\Gamma^A = \left\{ \mathbb{1}, \gamma_5, \gamma_\mu, \mathrm{i}\gamma_\mu\gamma_5, \sigma_{\mu\nu} \right\} \,, \tag{B.15}$$

with $\mu > \nu$, form a basis in the space of complex 4×4 matrices. Furthermore, this basis is ortho-normalized and fulfills

$$\mathrm{Tr}\left(\Gamma^A \Gamma^B \right) = 4\delta^{AB} \,. \tag{B.16}$$

Let us now consider a fermionic four-point function with the four anticommuting fermion fields $\bar{\psi}, \psi$. From a reordering of the latter, we can now deduce non-trivial relations between the tensor structures. For this, we write

$$\Gamma^A_{ij} \Gamma^A_{kl} \, \bar{\psi}_i \psi_j \bar{\psi}_k \psi_l = \sum_B c^{AB} \, \Gamma^B_{il} \Gamma^B_{kj} \, \bar{\psi}_i \psi_j \bar{\psi}_k \psi_l = -\sum_B c^{AB} \, \Gamma^B_{il} \Gamma^B_{kj} \, \bar{\psi}_i \psi_l \bar{\psi}_k \psi_j \,. \tag{B.17}$$

For this type of field reordering, we derive the following *Fierz* transformations:

$$
\begin{pmatrix}
(\mathbb{1})_{ij} \otimes (\mathbb{1})_{kl} \\
(\gamma_5)_{ij} \otimes (\gamma_5)_{kl} \\
(\gamma_\mu)_{ij} \otimes (\gamma_\mu)_{kl} \\
(\mathrm{i}\gamma_\mu\gamma_5)_{ij} \otimes (\mathrm{i}\gamma_\mu\gamma_5)_{kl} \\
(\sigma_{\mu\nu})_{ij} \otimes (\sigma_{\mu\nu})_{kl}
\end{pmatrix}
=
\begin{pmatrix}
\frac{1}{4} & \frac{1}{4} & \frac{1}{4} & \frac{1}{4} & \frac{1}{8} \\
\frac{1}{4} & \frac{1}{4} & -\frac{1}{4} & -\frac{1}{4} & \frac{1}{8} \\
1 & -1 & -\frac{1}{2} & \frac{1}{2} & 0 \\
1 & -1 & \frac{1}{2} & -\frac{1}{2} & 0 \\
3 & 3 & 0 & 0 & -\frac{1}{2}
\end{pmatrix}
\begin{pmatrix}
(\mathbb{1})_{il} \otimes (\mathbb{1})_{kj} \\
(\gamma_5)_{il} \otimes (\gamma_5)_{kj} \\
(\gamma_\mu)_{il} \otimes (\gamma_\mu)_{kj} \\
(\mathrm{i}\gamma_\mu\gamma_5)_{il} \otimes (\mathrm{i}\gamma_\mu\gamma_5)_{kj} \\
(\sigma_{\mu\nu})_{il} \otimes (\sigma_{\mu\nu})_{kj}
\end{pmatrix} \,. \tag{B.18}
$$

Similar to the reordering given above, there exists a second type of non-trivial *Fierz* identities. The latter can be derived by considering:

$$\Gamma^A_{ij}\Gamma^A_{kl}\,\bar\psi_i\psi_j\bar\psi_k\psi_l = \sum_B c^{AB}\,(\Gamma^B\mathcal{C})_{ik}(\mathcal{C}\Gamma^B)_{lj}\,\bar\psi_i\bar\psi_k\psi_l\psi_j\,, \tag{B.19}$$

with $\mathcal{C} = \mathrm{i}\gamma_2\gamma_0$. Note, the minus sign is missing since we performed an even number of permutations of *Grassman*-valued fields. The *Fierz* transformations now read:

$$\begin{pmatrix} (\mathbb{1})_{ij}\otimes(\mathbb{1})_{kl} \\ (\gamma_5)_{ij}\otimes(\gamma_5)_{kl} \\ (\gamma_\mu)_{ij}\otimes(\gamma_\mu)_{kl} \\ (\mathrm{i}\gamma_\mu\gamma_5)_{ij}\otimes(\mathrm{i}\gamma_\mu\gamma_5)_{kl} \\ (\sigma_{\mu\nu})_{ij}\otimes(\sigma_{\mu\nu})_{kl} \end{pmatrix} = \begin{pmatrix} \frac14 & \frac14 & \frac14 & \frac14 & \frac18 \\ \frac14 & \frac14 & -\frac14 & \frac14 & \frac18 \\ -1 & 1 & \frac12 & -\frac12 & 0 \\ 1 & -1 & \frac12 & -\frac12 & 0 \\ -3 & -3 & 0 & 0 & \frac12 \end{pmatrix} \begin{pmatrix} (\mathcal{C})_{ik}\otimes(\mathcal{C})_{lj} \\ (\gamma_5\mathcal{C})_{ik}\otimes(\mathcal{C}\gamma_5)_{lj} \\ (\gamma_\mu\mathcal{C})_{ik}\otimes(\mathcal{C}\gamma_\mu)_{lj} \\ (\mathrm{i}\gamma_\mu\gamma_5\mathcal{C})_{ik}\otimes(\mathrm{i}\mathcal{C}\gamma_\mu\gamma_5)_{lj} \\ (\sigma_{\mu\nu}\mathcal{C})_{ik}\otimes(\mathcal{C}\sigma_{\mu\nu})_{lj} \end{pmatrix}. \tag{B.20}$$

In principle, there are other reorderings of our fermion fields possible. As it turns out, however, in case of four-fermion interactions, all reorderings other than described above lead to rather trivial identities, see Ref. [238] for a detailed discussion about *Fierz* identities in four-fermion theories.

We do also find *Fierz* transformations for the generators of the $SU(N)$ *Lie* group associated with, e.g., the color space (*Gell-Mann* matrices) or the flavor space (*Pauli* matrices). For this, we find

$$\begin{pmatrix} (\mathbb{1})_{ij}\otimes(\mathbb{1})_{kl} \\ (\tau^a)_{ij}\otimes(\tau^a)_{kl} \end{pmatrix} \begin{pmatrix} \frac1N & \frac12 \\ \frac{2N^2-2}{N^2} & -\frac1N \end{pmatrix} \begin{pmatrix} (\mathbb{1})_{il}\otimes(\mathbb{1})_{kj} \\ (\tau^a)_{il}\otimes(\tau^a)_{kj}\,. \end{pmatrix} \tag{B.21}$$

For the second type of field reordering Eq. (B.19), we find

$$\begin{pmatrix} (\mathbb{1})_{ij}\otimes(\mathbb{1})_{kl} \\ (\tau^a)_{ij}\otimes(\tau^a)_{kl} \end{pmatrix} \begin{pmatrix} \frac12 & \frac12 \\ \frac{N-1}{N} & -\frac{N+1}{N} \end{pmatrix} \begin{pmatrix} (\tau^S)_{ik}\otimes(\tau^S)_{lj} \\ (\tau^A)_{ik}\otimes(\tau^A)_{lj}\,, \end{pmatrix} \tag{B.22}$$

where $\mathrm{Tr}(\tau^a\tau^b) = 2\delta^{ab}$. Here, the matrices τ^S (τ^A) belong to the symmetric (antisymmetric) subspace of the corresponding $SU(N)$ group. Note that the symmetric subspace does also contain the normalized identity matrix $\tau^S_0 = \sqrt{2/N}\,\mathbb{1}$.

B.3.1 Fierz Identities: NJL Model with One Flavor and One Color

In this subsection, we show the *Fierz* identities we derive from the four-fermion channels in the one-flavor and one-color NJL model at finite temperature and fermion chemical potential, see Sec. 3.1. Recall that this model obeys a global $U(1)_V \times U(1)_A$ symmetry. We begin with the *Fierz* identities of the "fermion-antifermion" type where we find:

$$(A_\parallel) = \frac12(S-P) - \frac12\left(V_\parallel\right) + \frac12\left(V_\perp\right)\,, \tag{B.23}$$

$$(A_\perp) = \frac32(S-P) + \frac32\left(V_\parallel\right) + \frac12\left(V_\perp\right)\,, \tag{B.24}$$

$$(T_\parallel) = 3\left(V_\parallel\right) - \left(V_\perp\right)\,. \tag{B.25}$$

On the other hand, the *Fierz* identities which correspond to the "fermion-difermion" type read:

$$(S\mathcal{C} - P\mathcal{C}) = -(S - P) - (V_\parallel) - (V_\perp) \,, \tag{B.26}$$

$$(A_\parallel \mathcal{C}) = -\frac{1}{2}(S - P) - \frac{3}{2}(V_\parallel) + \frac{1}{2}(V_\perp) \,, \tag{B.27}$$

$$(A_\perp \mathcal{C}) = -\frac{3}{2}(S - P) + \frac{3}{2}(V_\parallel) - \frac{1}{2}(V_\perp) \,, \tag{B.28}$$

where we use the abbreviations

$$(S\mathcal{C} - P\mathcal{C}) = (\bar\psi\mathcal{C}\bar\psi^T)(\psi^T\mathcal{C}\psi) - (\bar\psi\gamma_5\mathcal{C}\bar\psi^T)(\psi^T\mathcal{C}\gamma_5\psi) \,, \tag{B.29}$$

$$(A_\parallel\mathcal{C}) = (\bar\psi\gamma_0\gamma_5\mathcal{C}\bar\psi^T)(\psi^T\mathcal{C}\gamma_0\gamma_5\psi) \,, \tag{B.30}$$

$$(A_\perp\mathcal{C}) = (\bar\psi\gamma_i\gamma_5\mathcal{C}\bar\psi^T)(\psi^T\mathcal{C}\gamma_i\gamma_5\psi) \,. \tag{B.31}$$

Here, the charge conjugation operator is defined as $\mathcal{C} = \mathrm{i}\gamma_2\gamma_0$. Using the identities above, the overcomplete ansatz (3.5) can be reduced from six to three four-fermion channels, see Sec. 3.1 for details.

B.3.2   Fierz Identities: NJL Model with Two Flavors and N_c Colors

Let us also discuss the derivation of the *Fierz*-complete four-quark basis which we use in our two-flavor and N_c-color NJL-type study, see Sec. 3.2. In principle, we need to consider the most general ansatz invariant under global $SU(N_c) \times SU(2)_L \times SU(2)_R \times U(1)_V$ transformations. We find 10 color-singlet channels:

$$\mathcal{L}_{(S-P)_+} = (\bar\psi\psi)^2 - (\bar\psi\gamma_5\tau^a\psi)^2 - (\bar\psi\gamma_5\psi)^2 + (\bar\psi\tau^a\psi)^2 \,, \tag{B.32}$$

$$\mathcal{L}_{(S+P)_-} = (\bar\psi\psi)^2 - (\bar\psi\gamma_5\tau^a\psi)^2 + (\bar\psi\gamma_5\psi)^2 - (\bar\psi\tau^a\psi)^2 \,, \tag{B.33}$$

$$\mathcal{L}_{(V)_\parallel} = (\bar\psi\gamma_0\psi)^2 \,, \tag{B.34}$$

$$\mathcal{L}_{(V)_\perp} = (\bar\psi\gamma_i\psi)^2 \,, \tag{B.35}$$

$$\mathcal{L}_{(A)_\parallel} = (\bar\psi\mathrm{i}\gamma_0\gamma_5\psi)^2 \,, \tag{B.36}$$

$$\mathcal{L}_{(A)_\perp} = (\bar\psi\mathrm{i}\gamma_i\gamma_5\psi)^2 \,, \tag{B.37}$$

$$\mathcal{L}_{(V-A)_\parallel^f} = (\bar\psi\gamma_0\tau^a\psi)^2 - (\bar\psi\mathrm{i}\gamma_0\gamma_5\tau^a\psi)^2 \,, \tag{B.38}$$

$$\mathcal{L}_{(V-A)_\perp^f} = (\bar\psi\gamma_i\tau^a\psi)^2 - (\bar\psi\mathrm{i}\gamma_i\gamma_5\tau^a\psi)^2 \,, \tag{B.39}$$

$$\mathcal{L}_{(T)_0} = (\bar\psi\sigma_{0i}\psi)^2 - (\bar\psi\sigma_{0i}\gamma_5\tau^a\psi)^2 \,, \tag{B.40}$$

$$\mathcal{L}_{(T)_0^f} = (\bar\psi\sigma_{0i}\tau^a\psi)^2 - (\bar\psi\sigma_{0i}\gamma_5\psi)^2 \,, \tag{B.41}$$

with the *Pauli* matrices τ^a. The four-quark channels given above can also appear as color multiplets:

$$\mathcal{L}_{(S-P)_+^{\mathrm{adj}}} = (\bar\psi T^a\psi)^2 - (\bar\psi\gamma_5\tau^b T^a\psi)^2 - (\bar\psi\gamma_5 T^a\psi)^2 + (\bar\psi\tau^b T^a\psi)^2 \,, \tag{B.42}$$

$$\mathcal{L}_{(S+P)_-^{\mathrm{adj}}} = (\bar\psi T^a\psi)^2 - (\bar\psi\gamma_5\tau^b T^a\psi)^2 + (\bar\psi\gamma_5 T^a\psi)^2 - (\bar\psi\tau^b T^a\psi)^2 \,, \tag{B.43}$$

$$\mathcal{L}_{(V)_\parallel^{\mathrm{adj}}} = (\bar\psi\gamma_0 T^a\psi)^2 \,, \tag{B.44}$$

$$\mathcal{L}_{(V)_\perp^{\mathrm{adj}}} = (\bar\psi\gamma_i T^a\psi)^2 \,, \tag{B.45}$$

$$\mathcal{L}_{(A)_\parallel^{\mathrm{adj}}} = (\bar\psi\mathrm{i}\gamma_0\gamma_5 T^a\psi)^2 \,, \tag{B.46}$$

$$\mathcal{L}_{(A)_\perp^{\mathrm{adj}}} = (\bar\psi\mathrm{i}\gamma_i\gamma_5 T^a\psi)^2 \,, \tag{B.47}$$

$$\mathcal{L}_{(V-A)_\parallel^{f,\mathrm{adj}}} = \left(\bar{\psi}\gamma_0\tau^b T^a\psi\right)^2 - \left(\bar{\psi}\mathrm{i}\gamma_0\gamma_5\tau^b T^a\psi\right)^2 , \tag{B.48}$$

$$\mathcal{L}_{(V-A)_\perp^{f,\mathrm{adj}}} = \left(\bar{\psi}\gamma_i\tau^b T^a\psi\right)^2 - \left(\bar{\psi}\mathrm{i}\gamma_i\gamma_5\tau^b T^a\psi\right)^2 , \tag{B.49}$$

$$\mathcal{L}_{(T)_0^{\mathrm{adj}}} = \left(\bar{\psi}\sigma_{0i} T^a\psi\right)^2 - \left(\bar{\psi}\sigma_{0i}\gamma_5\tau^b T^a\psi\right)^2 , \tag{B.50}$$

$$\mathcal{L}_{(T)_0^{f,\mathrm{adj}}} = \left(\bar{\psi}\sigma_{0i}\tau^b T^a\psi\right)^2 - \left(\bar{\psi}\sigma_{0i}\gamma_5 T^a\psi\right)^2 , \tag{B.51}$$

with the generators in color space T^a. We emphasize that these 20 channels are still not all four-quark channels which may be possible. For instance, we could further construct various linear combinations or consider diquark-type four-quark interactions which respect the underlying symmetries. As it turns out, however, the set of four-quark channels presented above is already overcomplete. Moreover, diquark-type four-quark channels are also encoded indirectly. For example, the csc channel we consider in our two-flavor and N_c-color NJL model study can be completely decomposed into "quark-antiquark-type" four-quark channels using

$$\mathcal{L}_{\mathrm{csc}} = -\frac{1}{3}\mathcal{L}_{(V-A)_\parallel} - \frac{1}{3}\mathcal{L}_{(V-A)_\perp} + \mathcal{L}_{(V-A)_\parallel^{\mathrm{adj}}} + \mathcal{L}_{(V-A)_\perp^{\mathrm{adj}}} - \frac{1}{3}\mathcal{L}_{(S+P)_-} + \mathcal{L}_{(S+P)_-^{\mathrm{adj}}} , \tag{B.52}$$

where we choose $N_c = 3$. Let us now briefly discuss how we extract our *Fierz*-complete four-quark basis from the set of 20 channels. Instead of deriving the various *Fierz* identities analytically like in App. B.3.1, we use an alternative way and employ a numerical approach. For this, it is required that the tensor structures of the four-quark channels are represented as large column vectors. We then compute the rank of the corresponding matrix where we observe that only 10 channels from those given above are linear independent. We therefore deduce that our *Fierz*-complete basis consists of ten four-quark channels, see Eqs. (3.38)-(3.47) for our individual choice.

Appendix C

Regulators, Propagators and Threshold Functions

In this appendix, we introduce the regulators, propagators and the (purely) fermionic threshold functions at finite temperature and quark chemical potential we employ in this thesis.

C.1 Regulators

We shall briefly discuss the regularization schemes we used in our present work. For this, we introduce two different regulators which are representatives of two distinct classes of regularization schemes, namely so-called four-dimensional/*covariant* and three-dimensional/spatial regularization schemes. In Sec. 3.1.3, we discuss the advantages and disadvantages of the two different schemes from a physical point of view. Here, we shall rather focus on the explicit form of the regulators and discuss (some) technicalities.

C.1.1 *Covariant* Regulators

In this subsection, we introduce the four-dimensional regulator functions we use in our studies of hot and dense quark matter. Let us begin with the *Fermi*-surface-adapted regulator we use for fermionic propagators. In the spirit of regulators employed in RG studies of ultracold *Fermi* gases [347] with spin- and mass-imbalance [348, 349], we tailored a *covariant* regularization scheme which ensures that fluctuation effects are integrated out around the *Fermi* surface. Momenta on the *Fermi* surface $|\vec{p}| \simeq \mu$ are then only taken into account for $k \to 0$ where the regulator vanishes. For details on the construction of the *Fermi*-surface-adapted regularization scheme, a general discussion about *covariant* regulators, and remarks to the *Silver-Blaze* symmetry of field theories, we refer to Ref. [116]. Here, we shall only give the explicit form of our four-dimensional regulator we use in this work. Our *Fermi*-surface-adapted regulator reads

$$R_k^{\psi} = -(\not{p} + \mathrm{i}\gamma_0\mu)r_{\psi} \,, \tag{C.1}$$

where r_{ψ} is the so-called regulator shape function, which is assumed to be dimensionless and real-valued, depends on the momenta p_0, $\vec{p}$, the chemical potential μ and the RG scale k. Moreover, the latter has to fulfill some necessary constraints which we shall not discuss here. For details, we refer to Sec. 2.2 and Ref. [63, 116]. In our studies, we

use an exponential regulator shape function[19] which can be written as:

$$r_\psi = \frac{1}{\sqrt{1 - e^{-\bar{\omega}_+ \bar{\omega}_-}}} - 1 \,, \tag{C.2}$$

with the dimensionless quantity $\bar{\omega}_\pm = \omega_\pm / k$, where

$$\omega_\pm^2 \equiv \omega_\pm^2(p_0, \vec{p}) = p_0^2 + (|\vec{p}| \pm \mu)^2 \,. \tag{C.3}$$

Note that $\omega_\pm$ can be related to the quasiparticle dispersion relation of ungapped chiral fermions. In this case, $\omega_-(0, \vec{p})$ can be interpreted as the energy which is necessary to create a particle above the *Fermi* surface with momentum $\vec{p}$. On the other hand, $\omega_+(0, \vec{p})$ corresponds to the energy which is required to create an antiparticle. In the limit of vanishing chemical potential, $\omega_\pm$ reduces to

$$\omega_\pm^2\big|_{\mu=0} = p_0^2 + \vec{p}^2 \,, \tag{C.4}$$

so that r_ψ turns into the conventionally *covariant* chirally symmetric regulator function.

Of course, our choice for the shape function is not unique. For instance, we could also employ, e.g., so-called *Litim*-type regulators [350–352] where we would need to substitute $\omega_+ \omega_-$ for the momentum p^2 in the argument of the corresponding shape function. For more details about the properties a *Fermi*-surface adapted regulator shape function needs to fulfill in general, we refer to Ref. [116].

Let us now give the explicit expression of the four-dimensional regulator shape function we consider for our internal gluonic lines. In our QCD studies, we consider an exponential shape function which reads:

$$r_A^n = \frac{y^{n-1}}{e^{y^n} - 1} \,, \tag{C.5}$$

with $y = p^2/k^2$. Note that we use for our actual computations in this work $n = 1$.

C.1.2 Spatial Regulator

In our one-color and one-flavor NJL-type study, see Sec. 3.1.3, we also investigate the influence of so-called three-dimensional regularization schemes which only act on spatial momenta whereas they leave temporal momenta unregularized, see Refs. [233, 353–355]. As already discussed in Sec. 3.1.3, this class of regulators introduces an artificial breaking of the *Poincaré* symmetry even in case of vanishing temperature and chemical potential, see also Sec. 2.2 for a discussion. The general form of such a spatial regulator reads

$$R_k^\psi(p) = -\slashed{\vec{p}}\, r_\psi\left(\frac{\vec{p}^2}{k^2}\right) \,, \tag{C.6}$$

with the regulator shape function r_ψ. The latter does only act on spatial momenta:

$$r_\psi = \left(\sqrt{\frac{k^2}{\vec{p}^2}} - 1\right) \theta(k^2 - \vec{p}^2) \,. \tag{C.7}$$

We note that in most cases the momentum integrations and the *Matsubara* summations may be performed analytically by employing the regulator shape function above which can be advantageous in certain situations.

---

[19]Throughout this thesis, we do not consider scale-dependent renormalization factors $Z^{\parallel}$, $Z^{\perp}$, and Z_μ. The following replacements might be necessary in the definition of the regulator function R_k^ψ and within the shape function r_ψ if such renormalization factors were included: $p_0 \to Z^{\parallel} p_0$, $p_i \to Z^{\perp} p_i$, and $\mu \to Z_\mu \mu$.

C.2   Propagators

In this section, we introduce the dressed propagators using *covariant* and non-*covariant* regulators we use in Chap. 3. The so-defined dressed propagators (inverse two-point functions) then enter *DoFun* [166, 346] and *FormTracer* [167], which we employ to derive the RG flow equations corresponding to the renormalized four-quark couplings. We start with the fermionic two-point function which reads

$$\Gamma^{(1,1)}_{\bar{\psi}\psi}\Big|_{\Phi=0} = -Z^{\perp}_{\psi}(\gamma_0[\hat{z}_\psi\, p_0 + \hat{z}_\mu\, \mathrm{i}\mu] + \vec{\gamma}\cdot\vec{p})\,\delta_{c_1 c_2}\,\delta_{f_1 f_2}\,, \tag{C.8}$$

with $\hat{z}_\psi = Z^{\parallel}_\psi/Z^{\perp}_\psi$ and $\hat{z}_\mu = Z_\mu/Z^{\perp}_\psi$. Note that indices, which are associated with the fundamental representation of the $SU(3)$ color group, are denoted by $c_1, c_2, \ldots$, where those, which are associated with the fundamental representation of the $SU(2)$ flavor group, are denoted by $f_1, f_2, \ldots$. For the adjoint representation of the $SU(3)$ color group, we choose $a, b, \ldots$. We stress that *Dirac* indices shall not be resolved. Using a *covariant* regularization scheme, we find for the dressed quark propagator

$$\left(\Gamma^{(1,1)}_{\bar{\psi}\psi}\Big|_{\Phi=0} + R_{\psi,k}\right)^{-1} = (\mathcal{P}_{\bar{\psi}\psi})^{-1} = -\frac{\gamma_0[\hat{z}_\psi\, p_0 + \hat{z}_\mu\, \mathrm{i}\mu] + \vec{\gamma}\cdot\vec{p}}{([\hat{z}_\psi\, p_0 + \hat{z}_\mu\, \mathrm{i}\mu]^2 + \vec{p}^2)\,(1 + r_\psi)Z^{\perp}_\psi}\,\delta_{c_1 c_2}\,\delta_{f_1 f_2}\,. \tag{C.9}$$

Using a non-*covariant* regularization scheme, the dressed quark propagator reads

$$\left(\Gamma^{(1,1)}_{\bar{\psi}\psi}\Big|_{\Phi=0} + R_{\psi,k}\right)^{-1} = (\mathcal{P}_{\bar{\psi}\psi})^{-1} = -\frac{\gamma_0[\hat{z}_\psi\, p_0 + \hat{z}_\mu\, \mathrm{i}\mu] + \vec{\gamma}\cdot\vec{p}(1 + r_\psi)}{([\hat{z}_\psi\, p_0 + \hat{z}_\mu\, \mathrm{i}\mu]^2 + \vec{p}^2(1 + r_\psi)^2)\,Z^{\perp}_\psi}\,\delta_{c_1 c_2}\,\delta_{f_1 f_2}\,. \tag{C.10}$$

The corresponding regulator shape functions r_ψ for the three- and four-dimensional regularization schemes we use in our work can be found in App. C.1.

Let us now turn to the gauge sector. We begin again with the bosonic two-point function for the gluons. For this, we write

$$\Gamma^{(1,1)}_{AA}\Big|_{\Phi=0} = \delta^{ab}\, p^2\, Z^M_A\left(\hat{z}^E_A P^E_{\mu\nu} + P^M_{\mu\nu} + \frac{\hat{z}^L_A}{\xi}\,\Pi^L_{\mu\nu}\right)\,, \tag{C.11}$$

with the gauge-fixing parameter ξ, the reduced wave function renormalizations $\hat{z}^E_A = Z^E_A/Z^M_A$, $\hat{z}^L_A = Z^L_A/Z^M_A$, and the four-momentum $p = (p_0, \vec{p})$. For convenience, we introduced magnetic and electric projectors above:

$$P^M_{\mu\nu} = (1 - \delta_{\mu 0})(1 - \delta_{\nu 0})\left(\delta_{\mu\nu} - \frac{p_\mu p_\nu}{\vec{p}^2}\right)\,, \tag{C.12}$$

$$P^E_{\mu\nu} = \Pi^T_{\mu\nu} - P^M_{\mu\nu}\,. \tag{C.13}$$

Here, we further used transversal and longitudinal polarization tensors which read

$$\Pi^T_{\mu\nu} = \left(\delta_{\mu\nu} - \frac{p_\mu p_\nu}{p^2}\right)\,, \tag{C.14}$$

$$\Pi^L_{\mu\nu} = \frac{p^\mu p^\nu}{p^2}\,. \tag{C.15}$$

Note that the projectors $\Pi^{T/L}_{\mu\nu}$, $P^{E/M}_{\mu\nu}$ fulfill the usual projection rules, e.g., $P^E_{\mu\nu}P^M_{\nu\rho} = 0$ and $P^E_{\mu\nu}P^E_{\nu\rho} = P^E_{\mu\rho}$, as one can check straightforwardly. We add that we do not distinguish between color-electrical and color-magnetic components of the gluon propagator in the present work. Nevertheless, for the sake of completeness, we decompose the dressed gluon propagator in *Euclidean* spacetime at finite temperature into magnetic and electric field components

where we obtain:

$$\left(\left.\Gamma_{AA}^{(1,1)}\right|_{\Phi=0} + R_{A,k}\right)^{-1} = (\mathcal{P}_{AA})^{-1} = \frac{\delta^{ab}}{p^2(1+r_A)Z_A^M} \left(\frac{1}{\hat{z}_A^E}P_{\mu\nu}^E + P_{\mu\nu}^M + \frac{\xi}{\hat{z}_L}\Pi_{\mu\nu}^L\right).$$
(C.16)

For details on the workflow using *DoFun* and *FormTracer*, we refer to App. D.

C.3   Threshold Functions

We introduce the threshold functions we use in our thesis. Recall that the threshold functions can be related to one-loop diagrams, see also Fig. 2.3. We add that, in this appendix, we focus on the purely fermionic threshold functions which play a major role in our NJL model studies in Secs. 3.1 and 3.2. Note that the so-defined threshold functions appear in all our studies within Chap. 3.

C.3.1   *Covariant* Regularization

For convenience, we define a shorthand notation for the dimensionless (regularized) fermion propagator:

$$\tilde{G}_\psi(y_0, y, \omega) = \frac{1}{(y_0 + y)(1 + r_\psi)^2 + \omega}.$$
(C.17)

Using a four-dimensional regularization scheme, e.g., the *Fermi*-surface-adapted shape function (C.2), the threshold functions associated with purely fermionic one-loop diagrams can be written as:

$$l_{\|+}^{(\mathrm{F})}(\tau, \omega, \tilde{\mu}_\tau) = -\frac{\tau}{2}\sum_{n=-\infty}^{+\infty}\int_0^\infty \mathrm{d}y\, y^{\frac{1}{2}} \tilde{\partial}_t \left[(\tilde{\nu}_n + 2\pi\tau\tilde{\mu}_\tau)^2 (1 + r_\psi)^2 \right.$$
$$\left. \times \left(\tilde{G}_\psi((\tilde{\nu}_n + 2\pi\tau\tilde{\mu}_\tau)^2, y, \omega)\right)^2\right],$$
(C.18)

$$l_{\perp+}^{(\mathrm{F})}(\tau, \omega, \tilde{\mu}_\tau) = -\frac{\tau}{2}\sum_{n=-\infty}^{+\infty}\int_0^\infty \mathrm{d}y\, y^{\frac{1}{2}} \tilde{\partial}_t \left[(y(1 + r_\psi)^2 + \omega) \left(\tilde{G}_\psi((\tilde{\nu}_n + 2\pi\tau\tilde{\mu}_\tau)^2, y, \omega)\right)^2\right],$$
(C.19)

$$l_{\|\pm}^{(\mathrm{F})}(\tau, \omega, \tilde{\mu}_\tau) = -\frac{\tau}{2}\sum_{n=-\infty}^{+\infty}\int_0^\infty \mathrm{d}y\, y^{\frac{1}{2}} \tilde{\partial}_t \left[(\tilde{\nu}_n + 2\pi\tau\tilde{\mu}_\tau)(\tilde{\nu}_n - 2\pi\tau\tilde{\mu}_\tau)(1 + r_\psi)^2 \right.$$
$$\left. \times \tilde{G}_\psi((\tilde{\nu}_n + 2\pi\tau\tilde{\mu}_\tau)^2, y, \omega)\tilde{G}_\psi((\tilde{\nu}_n - 2\pi\tau\tilde{\mu}_\tau)^2, y, \omega)\right],$$
(C.20)

$$l_{\perp\pm}^{(\mathrm{F})}(\tau, \omega, \tilde{\mu}_\tau) = -\frac{\tau}{2}\sum_{n=-\infty}^{+\infty}\int_0^\infty \mathrm{d}y\, y^{\frac{1}{2}} \tilde{\partial}_t \left[(y(1+r_\psi)^2 + \omega) \right.$$
$$\left. \times \tilde{G}_\psi((\tilde{\nu}_n + 2\pi\tau\tilde{\mu}_\tau)^2, y, \omega)\tilde{G}_\psi((\tilde{\nu}_n - 2\pi\tau\tilde{\mu}_\tau)^2, y, \omega)\right],$$
(C.21)

with $y = p^2/k^2$ where the scale derivative $\tilde{\partial}_t$ can formally be defined as $\tilde{\partial}_t = (\partial_t r_\psi)\frac{\partial}{\partial r_\psi}$. Above, we further used $\partial_t Z^\perp = \partial_t Z^\| = \partial_t Z_\mu = 0$ as it is the case at leading order of the derivative expansion in our NJL model studies. Note that the latter appears to be an approximation in our QCD study, see our discussion in Sec. 3.3. In case of our four-dimensional *Fermi*-surface-adapted regularization scheme, the scale derivative can be written as:

$$\tilde{\partial}_t = \frac{(y_0 + y)\mathrm{e}^{-(y_0+y)}}{(1 - \mathrm{e}^{-(y_0+y)})^{\frac{3}{2}}} \frac{\partial}{\partial r_\psi}.$$
(C.22)

In the limit of vanishing quark chemical potential, one can moreover show that the four threshold functions (C.18)-(C.21) can be reduced to two threshold functions:

$$l^{(\mathrm{F})}_{\|+}(\tau,\omega,0) = l^{(\mathrm{F})}_{\|\pm}(\tau,\omega,0) \equiv l^{(\mathrm{F})}_{\|}(\tau,\omega,0)\,,$$
$$l^{(\mathrm{F})}_{\perp+}(\tau,\omega,0) = l^{(\mathrm{F})}_{\perp\pm}(\tau,\omega,0) \equiv l^{(\mathrm{F})}_{\perp}(\tau,\omega,0)\,.$$

Further, one can show that

$$l^{(\mathrm{F})}_{\|}(\tau,\omega,0) + l^{(\mathrm{F})}_{\perp}(\tau,\omega,0) = \tau \sum_{n=-\infty}^{+\infty} \int_0^\infty \mathrm{d}y\, y^{\frac{1}{2}} \frac{(\partial_t r_\psi)(1+r_\psi)(\tilde{\nu}_n^2 + y)}{\left[(\tilde{\nu}_n^2 + y)(1+r_\psi)^2 + \omega\right]^2}\,. \tag{C.23}$$

Let us briefly comment on the box-type and triangle-type diagrams, we employ in our study in Sec. 3.3. As already discussed in Sec. 3.3, we shall not give the explicit form of the four-quark beta functions corresponding to our QCD study as they appear to be rather lengthy. Therefore, it would also be less reasonable to give an explicit form of the threshold function associated with box- and triangle-type diagrams at this point. Here, we only note that at finite temperature and quark chemical potential the boson-fermion diagrams in *Feynman* gauge $\xi = 1$ do also appear in four different "versions" in analogy to our purely fermionic diagrams above, i.e., parallel/transversal to the heat bath and the quark chemical potential appears with $+\mathrm{i}\mu/\pm\mathrm{i}\mu$ in the denominators. For further details on the mixed-type threshold functions in the vacuum, e.g., see Ref. [228].

C.3.2   Spatial Regularization

In analogy to Sec. C.3.1, we define a dimensionless propagator where we now use a spatial/three-dimensional regularization scheme:

$$\tilde{G}^{\mathrm{spatial}}_\psi(y_0, y, \omega) = \frac{1}{y_0 + y(1+r_\psi)^2 + \omega}\,. \tag{C.24}$$

For the purely fermionic threshold functions, we then find:

$$l^{(\mathrm{F})}_{\|+,\mathrm{spatial}}(\tau,\omega,\tilde{\mu}_\tau) = -\frac{1}{2}\tau \sum_{n=-\infty}^{+\infty} \int_0^\infty dy\, y^{\frac{1}{2}} \tilde{\partial}_t \Big[(\tilde{\nu}_n + 2\pi\tau\tilde{\mu}_\tau)^2 \times$$
$$\times \left(\tilde{G}^{\mathrm{spatial}}_\psi((\tilde{\nu}_n + 2\pi\tau\tilde{\mu}_\tau)^2, y, \omega)\right)^2 \Big]\,, \tag{C.25}$$

$$l^{(\mathrm{F})}_{\perp+,\mathrm{spatial}}(\tau,\omega,\tilde{\mu}_\tau) = -\frac{1}{2}\tau \sum_{n=-\infty}^{+\infty} \int_0^\infty dy\, y^{\frac{1}{2}} \tilde{\partial}_t \big[(y(1+r_\psi)^2 + \omega) \times$$
$$\times \left(\tilde{G}^{\mathrm{spatial}}_\psi((\tilde{\nu}_n + 2\pi\tau\tilde{\mu}_\tau)^2, y, \omega)\right)^2 \Big]\,, \tag{C.26}$$

$$l^{(\mathrm{F})}_{\|\pm,\mathrm{spatial}}(\tau,\omega,\tilde{\mu}_\tau) = -\frac{1}{2}\tau \sum_{n=-\infty}^{+\infty} \int_0^\infty dy\, y^{\frac{1}{2}} \tilde{\partial}_t \Big[(\tilde{\nu}_n + 2\pi\tau\tilde{\mu}_\tau)(\tilde{\nu}_n - 2\pi\tau\tilde{\mu}_\tau) \times$$
$$\times \tilde{G}^{\mathrm{spatial}}_\psi((\tilde{\nu}_n + 2\pi\tau\tilde{\mu}_\tau)^2, y, \omega)\tilde{G}^{\mathrm{spatial}}_\psi((\tilde{\nu}_n - 2\pi\tau\tilde{\mu}_\tau)^2, y, \omega) \Big]\,, \tag{C.27}$$

$$l^{(\mathrm{F})}_{\perp\pm,\mathrm{spatial}}(\tau,\omega,\tilde{\mu}_\tau) = -\frac{1}{2}\tau \sum_{n=-\infty}^{+\infty} \int_0^\infty dy\, y^{\frac{1}{2}} \tilde{\partial}_t \big[(y(1+r_\psi)^2 + \omega) \times$$
$$\times \tilde{G}^{\mathrm{spatial}}_\psi((\tilde{\nu}_n + 2\pi\tau\tilde{\mu}_\tau)^2, y, \omega)\tilde{G}^{\mathrm{spatial}}_\psi((\tilde{\nu}_n - 2\pi\tau\tilde{\mu}_\tau)^2, y, \omega) \Big]\,, \tag{C.28}$$

where $y = \vec{p}^2/k^2$. Using the shape function Eq. (C.7), we obtain for the scale derivative

$$\tilde{\partial}_t = \frac{1}{y^{\frac{1}{2}}}\theta(1-y)\frac{\partial}{\partial r_\psi}\,, \tag{C.29}$$

where we used $\partial_t Z^\parallel = \partial_t Z^\perp = \partial_t Z_\mu = 0$ again. Employing the shape function Eq. (C.7), the threshold functions can be computed analytically. For instance, we find:

$$l^{(F)}_{\parallel+,\text{spatial}}(\tau,\omega,-\mathrm{i}\tilde{\mu}_\tau) + l^{(F)}_{\perp+,\text{spatial}}(\tau,\omega,-\mathrm{i}\tilde{\mu}_\tau)$$
$$= \frac{1}{6}\frac{\partial}{\partial\omega}\left\{\frac{1}{\sqrt{1+\omega}}\left[\tanh\left(\frac{2\pi\tau\tilde{\mu}_\tau - \sqrt{1+\omega}}{2\tau}\right) - \tanh\left(\frac{2\pi\tau\tilde{\mu}_\tau + \sqrt{1+\omega}}{2\tau}\right)\right]\right\}\,, \tag{C.30}$$

$$l^{(F)}_{\parallel\pm,\text{spatial}}(\tau,\omega,-\mathrm{i}\tilde{\mu}_\tau) + l^{(F)}_{\perp\pm,\text{spatial}}(\tau,\omega,-\mathrm{i}\tilde{\mu}_\tau)$$
$$= -\frac{1}{6}\frac{\partial}{\partial\omega}\left\{\frac{1}{|\sqrt{1+\omega} - 2\pi\tau\tilde{\mu}|}\tanh\left(\frac{|\sqrt{1+\omega} - 2\pi\tau\tilde{\mu}|}{2\tau}\right)\right.$$
$$\left. + \frac{1}{|\sqrt{1+\omega} + 2\pi\tau\tilde{\mu}|}\tanh\left(\frac{|\sqrt{1+\omega} + 2\pi\tau\tilde{\mu}|}{2\tau}\right)\right\}\,. \tag{C.31}$$

In Sec. 3.1.3, we already mentioned that the purely fermionic threshold functions exhibit a second-order pole in the zero-temperature limit given that one uses the three-dimensional regularization scheme Eq. (C.7). We emphasize that this second-order pole emerges at $\mu = \sqrt{k^2 + \omega}$ in Eq. (C.31) not only in the sum $l^{(F)}_{\parallel\pm,\text{spatial}}(\tau,\omega,-\mathrm{i}\tilde{\mu}_\tau)$ and $l^{(F)}_{\perp\pm,\text{spatial}}(\tau,\omega,-\mathrm{i}\tilde{\mu}_\tau)$, but also in the individual threshold functions. We further note that the threshold functions with the spatial regulator (C.7) yield the same result in the limit $\tau \to 0$, $\tilde{\mu}_\tau \to 0$, and $\omega \to 0$:

$$l^{(F)}_{\parallel+,\text{spatial}}(0,0,0) = l^{(F)}_{\perp+,\text{spatial}}(0,0,0) = l^{(F)}_{\parallel\pm,\text{spatial}}(0,0,0) = l^{(F)}_{\perp\pm,\text{spatial}}(0,0,0) = \frac{1}{12}\,. \tag{C.32}$$

Appendix D

Derivation of Flow Equations with *DoFun* and *FormTracer*

We give a basic overview on how we compute the RG flow for the four-fermion couplings using the software packages *DoFun* [166, 346] and *FormTracer*[20] [167]. For this, we give a "cooking recipe" at hand to calculate the beta function associated with the four-fermion channels in this thesis. Note that the general idea of this "recipe" can also be applied to the running of couplings other than four-fermion vertices. Clearly, some steps need to be adapted in this case.

(i) Define the effective action, renormalized propagators, and vertices (App. C) as described in Ref. [166]. Note that vertices like the four-fermion vertex `V[psib[q1,...],psib[q2,...],psi[q3,...], psi[q4,...]]`, and propagators like the fermion propagator `P[psi[q1,...],psib[q2,...]]` often entail internally contracted operators. To ensure that the traces in the next steps are computed correctly, it is highly recommended to collect all internal (dummy) indices and define local variables for them within the `Module` of the corresponding vertex or propagator.

(ii) Compute the right-hand side of the *Wetterich* equation using the *DoFun* function `doRGE`. Note that we use in our present implementation the optional argument `tDerivative->False` as we later compute the threshold functions "by hand". We also stress that the index ordering in the definition of the functions `doRGE` and `getFR` differs. The latter is especially important in case of *Grassmann*-valued fields. For details, we refer to Ref. [166].

(iii) Throughout our work, we usually have more than one four-fermion channel present in our ansatz for the effective action. In order to project the tensor-valued result from `doRGE` onto our original scalar four-fermion couplings in our ansatz, it is necessary to construct suitable projectors. To ensure that the latter set is complete, it appears to be most convenient to construct the set of projectors $P^{(i)}_{(\bar{\psi}\psi)^2}$ from the *Fierz*-complete tensor basis we use for the four-fermion vertex. It is then straightforward for the i-th projector to set $\bar{\lambda}_j \to 0$ where $i \neq j$ in the four-fermion vertex `V` defined in step (i). Note that the so-defined projectors are not yet ortho-normalized.

(iv) With the aid of the function `FormTrace` included in the package *FormTracer*, we compute the traces in, e.g., *Dirac*, flavor and color space. We begin with the left-hand side of the *Wetterich* equation using

$$\text{Tr}\left[P^{(i)}_{(\bar{\psi}\psi)^2} \Gamma^{(2,2)}_{(\bar{\psi}\psi)^2} \right] \,, \tag{D.1}$$

where $\Gamma^{(2,2)}_{(\bar{\psi}\psi)^2}$ is the tensor-valued four-fermion vertex we defined in *DoFun* in step (i), see also Eq. (2.81). The result of (D.1) for a projector $P^{(i)}_{(\bar{\psi}\psi)^2}$ associated with a channel i is a linear combination of the various

---

[20]In this work, we use *DoFun* 2.0.4 and *FormTracer* 2.3.6

four-fermion couplings $\sim a_{ij}\bar{\lambda}_j$. We compute the trace (D.1) for all channels i in our complete basis $\mathcal{B}$. From this, we further identify the coefficients a_{ij} of the matrix A. For instance, in case of our *Fierz*-complete four-quark basis with ten channels, the coefficient matrix A is a ten by ten square matrix with full rank implying that A can be inverted.

(v) Using `FormTrace`, we compute the traces of the projectors from step (iii) together with the algebraic expression of the four-fermion correlation function from `getAE`. For convenience, in our semi-analytical computations we identify the threshold functions already within this step and analyze them separately. We emphasize again that the functions `doRGE` and `getFR` use different index orderings. It is therefore necessary to perform the identification of auxiliary indices used in `doRGE` with "physical" indices in `getAE` with some care to avoid sign issues, see also Ref. [166]. For instance, in case of our four-fermion vertex, we assign in our present implementation the field `psib[q2,...]` to the first auxiliary index `aux1` whereas we assign `psib[q1,...]` to `aux2`.

(vi) Since our projectors are not ortho-normalized, we need to invert the matrix A from step (iv) to derive the RG flow equations associated with the four-fermion couplings. In particular, we need to solve the simple matrix equation

$$a_{ij}\bar{\lambda}_j = b_i \,, \tag{D.2}$$

where the vector b_i entails the projected and traced results from step (v). Inverting the matrix (a_{ij}) yields the set of RG flow equations for our four-fermion couplings $\bar{\lambda}_i$.

Appendix E

Beta Functions

In this appendix, we present the RG flow equations of the one-flavor and one-color (Sec. 3.1) as well as of the two-flavor and N_c-color NJL model (Sec. 3.2). Note that we do not show the RG flow equations associated with the QCD calculations in Sec. 3.3 as they appear to be very lengthy and less instructive. Note also that we derived the RG flow equations using already existing software packages [166, 167, 346]. We also refer to App. D for more details.

E.1 Beta Functions: NJL Model with One Flavor and One Color

We start with the *Fierz*-complete set of RG flow equations of our one-flavor and one-color NJL-type model. For the latter, we find

$$
\begin{aligned}
\partial_t \lambda_\sigma \;=\; & 2\lambda_\sigma - 16 v_4 \left(-\lambda_\sigma^2 + 2\lambda_V^\parallel \lambda_V^\perp + (\lambda_V^\perp)^2 - 2\lambda_\sigma \lambda_V^\perp \right) l_{\perp\pm}^{(\mathrm{F})}(\tau, 0, -\mathrm{i}\tilde\mu_\tau) \\
& -16 v_4 \left(3\lambda_\sigma^2 + 2\lambda_V^\parallel (\lambda_\sigma + \lambda_V^\perp) + (\lambda_V^\perp)^2 + 8\lambda_\sigma \lambda_V^\perp \right) l_{\perp+}^{(\mathrm{F})}(\tau, 0, -\mathrm{i}\tilde\mu_\tau) \\
& -16 v_4 \left(-\lambda_\sigma^2 - 2\lambda_\sigma \lambda_V^\parallel + 3(\lambda_V^\perp)^2 \right) l_{\parallel\pm}^{(\mathrm{F})}(\tau, 0, -\mathrm{i}\tilde\mu_\tau) \\
& -16 v_4 \left(3\lambda_\sigma^2 + 4\lambda_\sigma \lambda_V^\parallel + 3(\lambda_V^\perp)^2 + 6\lambda_\sigma \lambda_V^\perp \right) l_{\parallel+}^{(\mathrm{F})}(\tau, 0, -\mathrm{i}\tilde\mu_\tau) \,,
\end{aligned} \tag{E.1}
$$

$$
\begin{aligned}
\partial_t \lambda_V^\parallel \;=\; & 2\lambda_V^\parallel + 16 v_4 \left(-\lambda_\sigma^2 + 2\lambda_\sigma \lambda_V^\parallel + 4\lambda_V^\parallel \lambda_V^\perp - (\lambda_V^\perp)^2 - 4\lambda_\sigma \lambda_V^\perp \right) l_{\perp\pm}^{(\mathrm{F})}(\tau, 0, -\mathrm{i}\tilde\mu_\tau) \\
& +16 v_4 \left(-\lambda_\sigma^2 - 2(\lambda_V^\parallel)^2 - 2\lambda_\sigma \lambda_V^\parallel - 6\lambda_V^\parallel \lambda_V^\perp - (\lambda_V^\perp)^2 - 4\lambda_\sigma \lambda_V^\perp \right) l_{\perp+}^{(\mathrm{F})}(\tau, 0, -\mathrm{i}\tilde\mu_\tau) \\
& +16 v_4 \left(3\lambda_\sigma^2 + (\lambda_V^\parallel)^2 + 6(\lambda_V^\perp)^2 + 6\lambda_\sigma \lambda_V^\perp \right) l_{\parallel\pm}^{(\mathrm{F})}(\tau, 0, -\mathrm{i}\tilde\mu_\tau) \\
& +16 v_4 \left(-\lambda_\sigma^2 + (\lambda_V^\parallel)^2 + 4\lambda_\sigma \lambda_V^\parallel + 6\lambda_V^\parallel \lambda_V^\perp + 6\lambda_\sigma \lambda_V^\perp \right) l_{\parallel+}^{(\mathrm{F})}(\tau, 0, -\mathrm{i}\tilde\mu_\tau) \,,
\end{aligned} \tag{E.2}
$$

$$
\begin{aligned}
\partial_t \lambda_V^\perp \;=\; & 2\lambda_V^\perp + \frac{16}{3} v_4 \left(-\lambda_\sigma^2 - (\lambda_V^\parallel)^2 - 2\lambda_V^\parallel (\lambda_V^\perp - \lambda_\sigma) - 10(\lambda_V^\perp)^2 - 4\lambda_\sigma \lambda_V^\perp \right) l_{\perp\pm}^{(\mathrm{F})}(\tau, 0, -\mathrm{i}\tilde\mu_\tau) \\
& -\frac{16}{3} v_4 \left(3\lambda_\sigma^2 + (\lambda_V^\parallel)^2 + 2\lambda_\sigma \lambda_V^\parallel + 10(\lambda_V^\perp)^2 \right) l_{\perp+}^{(\mathrm{F})}(\tau, 0, -\mathrm{i}\tilde\mu_\tau) \\
& -16 v_4 \left(\lambda_\sigma^2 - 2\lambda_V^\parallel \lambda_V^\perp - (\lambda_V^\perp)^2 + 2\lambda_\sigma \lambda_V^\perp \right) l_{\parallel\pm}^{(\mathrm{F})}(\tau, 0, -\mathrm{i}\tilde\mu_\tau) \\
& -16 v_4 \left(\lambda_\sigma^2 + 4\lambda_V^\parallel \lambda_V^\perp + 5(\lambda_V^\perp)^2 + 6\lambda_\sigma \lambda_V^\perp \right) l_{\parallel+}^{(\mathrm{F})}(\tau, 0, -\mathrm{i}\tilde\mu_\tau) \,,
\end{aligned} \tag{E.3}
$$

with $v_4 = 1/(32\pi^2)$. For the threshold functions, we refer to App. C. Note that the presently used parameterization $(\lambda_\sigma, \lambda_V^\parallel, \lambda_V^\perp)$ for the RG flow equations is not unique. In general, considering suitable *Fierz* transformations, we may transform the current four-fermion basis into a different one. For instance, we also use a difermion-type

parameterization for the beta functions which we discuss in detail in Sec. 3.1.2. The explicit transformation rules are given in Eq. (3.28).

E.2 Beta Functions: NJL Model with Two Flavors and N_c Colors

In this subsection, we show the beta functions of our *Fierz*-complete NJL model study with two flavors and N_c colors. Note that the parameterization we use as a *Fierz*-complete four-quark basis is based on phenomenological considerations, see our discussion in Sec. 3.2. For our ten channels, we obtain:

$$
\begin{aligned}
\partial_t \lambda_{(\sigma\text{-}\pi)} =\ & 2\lambda_{(\sigma\text{-}\pi)} + 64 v_4 \Big(-\lambda_{(\sigma\text{-}\pi)}^2 - 4\lambda_{(\sigma\text{-}\pi)}\lambda_{(S+P)_-} - 4\lambda_{(S+P)_-}^2 + \lambda_{(\sigma\text{-}\pi)}\lambda_{(V+A)_\parallel} + \lambda_{(\sigma\text{-}\pi)}\lambda_{(V-A)_\parallel} \\
& + 3\lambda_{(\sigma\text{-}\pi)}\lambda_{(V+A)_\perp} - \lambda_{(V+A)_\parallel}^{\mathrm{adj}}\lambda_{(V+A)_\perp} + \lambda_{(\sigma\text{-}\pi)}\lambda_{(V-A)_\perp} + 2\lambda_{(\sigma\text{-}\pi)}\lambda_{(V-A)_\perp^{\mathrm{adj}}} - \frac{1}{N_c^2}\lambda_{(S+P)_-^{\mathrm{adj}}}^2 \\
& + \frac{2}{N_c}\lambda_{(\sigma\text{-}\pi)}\lambda_{(S+P)_-^{\mathrm{adj}}} + \frac{4}{N_c}\lambda_{(S+P)_-}\lambda_{(S+P)_-^{\mathrm{adj}}} + \frac{1}{N_c}\lambda_{(S+P)_-^{\mathrm{adj}}}^2 - \frac{1}{2N_c}\lambda_{(\sigma\text{-}\pi)}\lambda_{(V+A)_\parallel^{\mathrm{adj}}} \\
& - \frac{1}{2N_c}\lambda_{(\sigma\text{-}\pi)}\lambda_{(V-A)_\perp^{\mathrm{adj}}} - 2N_c\lambda_{(\sigma\text{-}\pi)}^2 - 4N_c\lambda_{(\sigma\text{-}\pi)}\lambda_{(S+P)_-} - 4N_c\lambda_{(S+P)_-}^2 - N_c\lambda_{(\sigma\text{-}\pi)}\lambda_{(S+P)_-^{\mathrm{adj}}} \\
& - 2N_c\lambda_{(S+P)_-}\lambda_{(S+P)_-^{\mathrm{adj}}} + \frac{N_c}{2}\lambda_{(\sigma\text{-}\pi)}\lambda_{(V+A)_\parallel^{\mathrm{adj}}} + \lambda_{(\sigma\text{-}\pi)}\lambda_{\mathrm{csc}} - \lambda_{(S+P)_-^{\mathrm{adj}}}\lambda_{\mathrm{csc}} + N_c\lambda_{(\sigma\text{-}\pi)}\lambda_{\mathrm{csc}} \\
& + 2N_c\lambda_{(S+P)_-}\lambda_{\mathrm{csc}} + N_c\lambda_{(S+P)_-^{\mathrm{adj}}}\lambda_{\mathrm{csc}} \Big) l_{\parallel+}^{(\mathrm{F})}(\tau, 0, -\mathrm{i}\tilde{\mu}_\tau) \\
& + 64 v_4 \Big(-\lambda_{(\sigma\text{-}\pi)}\lambda_{(V+A)_\parallel} + \lambda_{(\sigma\text{-}\pi)}\lambda_{(V+A)_\perp} + \lambda_{(V+A)_\parallel^{\mathrm{adj}}}\lambda_{(V+A)_\perp} + \frac{1}{2N_c}\lambda_{(\sigma\text{-}\pi)}\lambda_{(V+A)_\parallel^{\mathrm{adj}}} \Big) l_{\parallel\pm}^{(\mathrm{F})}(\tau, 0, -\mathrm{i}\tilde{\mu}_\tau) \\
& + 64 v_4 \Big(-\lambda_{(\sigma\text{-}\pi)}^2 - 4\lambda_{(\sigma\text{-}\pi)}\lambda_{(S+P)_-} - 4\lambda_{(S+P)_-}^2 - \frac{2}{3}\lambda_{(\sigma\text{-}\pi)}\lambda_{(S+P)_-^{\mathrm{adj}}} - \frac{4}{3}\lambda_{(S+P)_-}\lambda_{(S+P)_-^{\mathrm{adj}}} \\
& + \lambda_{(\sigma\text{-}\pi)}\lambda_{(V+A)_\parallel} + \frac{1}{3}\lambda_{(\sigma\text{-}\pi)}\lambda_{(V-A)_\parallel} - \frac{1}{3}\lambda_{(V+A)_\parallel}\lambda_{(V+A)_\parallel^{\mathrm{adj}}} + 3\lambda_{(\sigma\text{-}\pi)}\lambda_{(V+A)_\perp} - \frac{2}{3}\lambda_{(V+A)_\parallel^{\mathrm{adj}}}\lambda_{(V+A)_\perp} \\
& + \frac{1}{3}\lambda_{(\sigma\text{-}\pi)}\lambda_{(V-A)_\perp} + \frac{2}{3}\lambda_{(\sigma\text{-}\pi)}\lambda_{(V-A)_\perp^{\mathrm{adj}}} - \frac{1}{N_c^2}\lambda_{(S+P)_-^{\mathrm{adj}}}^2 + \frac{2}{N_c}\lambda_{(\sigma\text{-}\pi)}\lambda_{(S+P)_-^{\mathrm{adj}}} + \frac{4}{N_c}\lambda_{(S+P)_-}\lambda_{(S+P)_-^{\mathrm{adj}}} \\
& + \frac{5}{3N_c}\lambda_{(S+P)_-^{\mathrm{adj}}}^2 - \frac{1}{2N_c}\lambda_{(\sigma\text{-}\pi)}\lambda_{(V+A)_\parallel^{\mathrm{adj}}} + \frac{1}{6N_c}\lambda_{(V+A)_\parallel^{\mathrm{adj}}}^2 - \frac{1}{6N_c}\lambda_{(\sigma\text{-}\pi)}\lambda_{(V-A)_\perp^{\mathrm{adj}}} - 2N_c\lambda_{(\sigma\text{-}\pi)}^2 \\
& - 4N_c\lambda_{(\sigma\text{-}\pi)}\lambda_{(S+P)_-} - 4N_c\lambda_{(S+P)_-}^2 - N_c\lambda_{(\sigma\text{-}\pi)}\lambda_{(S+P)_-^{\mathrm{adj}}} - 2N_c\lambda_{(S+P)_-}\lambda_{(S+P)_-^{\mathrm{adj}}} - \frac{N_c}{3}\lambda_{(S+P)_-^{\mathrm{adj}}}^2 \\
& + \frac{N_c}{2}\lambda_{(\sigma\text{-}\pi)}\lambda_{(V+A)_\parallel^{\mathrm{adj}}} - \frac{N_c}{12}\lambda_{(V+A)_\parallel^{\mathrm{adj}}}^2 - \frac{1}{3}\lambda_{(\sigma\text{-}\pi)}\lambda_{\mathrm{csc}} - \frac{4}{3}\lambda_{(S+P)_-}\lambda_{\mathrm{csc}} - \frac{1}{3}\lambda_{(S+P)_-^{\mathrm{adj}}}\lambda_{\mathrm{csc}} \\
& + \frac{2}{3N_c}\lambda_{(S+P)_-^{\mathrm{adj}}}\lambda_{\mathrm{csc}} + N_c\lambda_{(\sigma\text{-}\pi)}\lambda_{\mathrm{csc}} + 2N_c\lambda_{(S+P)_-}\lambda_{\mathrm{csc}} + \frac{N_c}{3}\lambda_{(S+P)_-^{\mathrm{adj}}}\lambda_{\mathrm{csc}} + \frac{2}{3}\lambda_{\mathrm{csc}}^2 \\
& - \frac{N_c}{3}\lambda_{\mathrm{csc}}^2 \Big) l_{\perp+}^{(\mathrm{F})}(\tau, 0, -\mathrm{i}\tilde{\mu}_\tau) \\
& + 64 v_4 \Big(\frac{1}{3}\lambda_{(\sigma\text{-}\pi)}\lambda_{(V+A)_\parallel} + \frac{1}{3}\lambda_{(V+A)_\parallel}\lambda_{(V+A)_\parallel^{\mathrm{adj}}} - \frac{5}{3}\lambda_{(\sigma\text{-}\pi)}\lambda_{(V+A)_\perp} - \frac{2}{3}\lambda_{(V+A)_\parallel^{\mathrm{adj}}}\lambda_{(V+A)_\perp} \\
& - \frac{1}{6N_c}\lambda_{(\sigma\text{-}\pi)}\lambda_{(V+A)_\parallel^{\mathrm{adj}}} - \frac{1}{6N_c}\lambda_{(V+A)_\parallel^{\mathrm{adj}}}^2 \Big) l_{\perp\pm}^{(\mathrm{F})}(\tau, 0, -\mathrm{i}\tilde{\mu}_\tau) \,,
\end{aligned}
\tag{E.4}
$$

$$
\begin{aligned}
\partial_t \lambda_{\mathrm{csc}} =\ & 2\lambda_{\mathrm{csc}} + 64 v_4 \Big(-\lambda_{(\sigma\text{-}\pi)}^2 + 2\lambda_{(\sigma\text{-}\pi)}\lambda_{(V+A)_\parallel^{\mathrm{adj}}} - \lambda_{(V+A)_\parallel^{\mathrm{adj}}}^2 + 3\lambda_{(V-A)_\perp}\lambda_{(V-A)_\perp^{\mathrm{adj}}} - \frac{3}{2N_c}\lambda_{(V-A)_\perp^{\mathrm{adj}}}^2 \\
& + \frac{3N_c}{4}\lambda_{(V-A)_\perp^{\mathrm{adj}}}^2 + 2\lambda_{(V-A)_\parallel}\lambda_{\mathrm{csc}} - \frac{3}{2}\lambda_{(V-A)_\perp^{\mathrm{adj}}}\lambda_{\mathrm{csc}} + \frac{3N_c}{2}\lambda_{(V-A)_\perp^{\mathrm{adj}}}\lambda_{\mathrm{csc}} - 2\lambda_{\mathrm{csc}}^2 \\
& + N_c\lambda_{\mathrm{csc}}^2 \Big) l_{\parallel+}^{(\mathrm{F})}(\tau, 0, -\mathrm{i}\tilde{\mu}_\tau) \\
& + 64 v_4 \Big(-\lambda_{(\sigma\text{-}\pi)}^2 - 4\lambda_{(\sigma\text{-}\pi)}\lambda_{(S+P)_-} - 4\lambda_{(S+P)_-}^2 - 4\lambda_{(\sigma\text{-}\pi)}\lambda_{(S+P)_-^{\mathrm{adj}}} - 8\lambda_{(S+P)_-}\lambda_{(S+P)_-^{\mathrm{adj}}} - \lambda_{(S+P)_-^{\mathrm{adj}}}^2
\end{aligned}
$$

$$
-3\lambda_{(V-A)_\perp}\lambda_{(V-A)_\perp^{\mathrm{adj}}} - \frac{1}{N_c^2}\lambda_{(S+P)_-^{\mathrm{adj}}}^2 + \frac{2}{N_c}\lambda_{(\sigma\text{-}\pi)}\lambda_{(S+P)_-^{\mathrm{adj}}} + \frac{4}{N_c}\lambda_{(S+P)_-}\lambda_{(S+P)_-^{\mathrm{adj}}} + \frac{4}{N_c}\lambda_{(S+P)_-^{\mathrm{adj}}}^2 +
$$

$$
\frac{3}{2N_c}\lambda_{(V-A)_\perp^{\mathrm{adj}}}^2 - 2\lambda_{(\sigma\text{-}\pi)}\lambda_{\mathrm{csc}} - 4\lambda_{(S+P)_-}\lambda_{\mathrm{csc}} + 2\lambda_{(S+P)_-^{\mathrm{adj}}}\lambda_{\mathrm{csc}} - \lambda_{(V-A)_\parallel}\lambda_{\mathrm{csc}} - 3\lambda_{(V-A)_\perp}\lambda_{\mathrm{csc}}
$$

$$
+\frac{3}{2}\lambda_{(V-A)_\perp^{\mathrm{adj}}}\lambda_{\mathrm{csc}} + \frac{2}{N_c}\lambda_{(S+P)_-^{\mathrm{adj}}}\lambda_{\mathrm{csc}} + \frac{3}{2N_c}\lambda_{(V-A)_\perp^{\mathrm{adj}}}\lambda_{\mathrm{csc}} + 4\lambda_{\mathrm{csc}}^2\Big)l_{\parallel\pm}^{(\mathrm{F})}(\tau,0,-\mathrm{i}\tilde\mu_\tau)
$$

$$
+64v_4\Big(\lambda_{(\sigma\text{-}\pi)}^2 - 2\lambda_{(\sigma\text{-}\pi)}\lambda_{(V+A)_\parallel^{\mathrm{adj}}} + \lambda_{(V+A)_\parallel^{\mathrm{adj}}}^2 + \lambda_{(V-A)_\parallel}\lambda_{(V-A)_\perp^{\mathrm{adj}}} - 2\lambda_{(V-A)_\perp}\lambda_{(V-A)_\perp^{\mathrm{adj}}} + \frac{1}{N_c}\lambda_{(V-A)_\perp^{\mathrm{adj}}}^2
$$

$$
-\frac{N_c}{2}\lambda_{(V-A)_\perp^{\mathrm{adj}}}^2 + 2\lambda_{(V-A)_\perp}\lambda_{\mathrm{csc}} + \frac{1}{2}\lambda_{(V-A)_\perp^{\mathrm{adj}}}\lambda_{\mathrm{csc}} - \frac{1}{N_c}\lambda_{(V-A)_\perp^{\mathrm{adj}}}\lambda_{\mathrm{csc}}
$$

$$
-\frac{N_c}{2}\lambda_{(V-A)_\perp^{\mathrm{adj}}}\lambda_{\mathrm{csc}}\Big)l_{\perp+}^{(\mathrm{F})}(\tau,0,-\mathrm{i}\tilde\mu_\tau)
$$

$$
+64v_4\Big(\lambda_{(\sigma\text{-}\pi)}^2 + 4\lambda_{(\sigma\text{-}\pi)}\lambda_{(S+P)_-} + 4\lambda_{(S+P)_-}^2 + \lambda_{(S+P)_-^{\mathrm{adj}}}^2 - \lambda_{(V-A)_\parallel}\lambda_{(V-A)_\perp^{\mathrm{adj}}} - 2\lambda_{(V-A)_\perp}\lambda_{(V-A)_\perp^{\mathrm{adj}}}
$$

$$
+\frac{1}{N_c^2}\lambda_{(S+P)_-^{\mathrm{adj}}}^2 - \frac{2}{N_c}\lambda_{(\sigma\text{-}\pi)}\lambda_{(S+P)_-^{\mathrm{adj}}} - \frac{4}{N_c}\lambda_{(S+P)_-}\lambda_{(S+P)_-^{\mathrm{adj}}} + \frac{1}{N_c}\lambda_{(V-A)_\perp^{\mathrm{adj}}}^2 - 2\lambda_{(\sigma\text{-}\pi)}\lambda_{\mathrm{csc}}
$$

$$
-4\lambda_{(S+P)_-}\lambda_{\mathrm{csc}} + 2\lambda_{(S+P)_-^{\mathrm{adj}}}\lambda_{\mathrm{csc}} - \lambda_{(V-A)_\parallel}\lambda_{\mathrm{csc}} - 3\lambda_{(V-A)_\perp}\lambda_{\mathrm{csc}} + \frac{3}{2}\lambda_{(V-A)_\perp^{\mathrm{adj}}}\lambda_{\mathrm{csc}}
$$

$$
+\frac{2}{N_c}\lambda_{(S+P)_-^{\mathrm{adj}}}\lambda_{\mathrm{csc}} + \frac{3}{2N_c}\lambda_{(V-A)_\perp^{\mathrm{adj}}}\lambda_{\mathrm{csc}} + 4\lambda_{\mathrm{csc}}^2\Big)l_{\perp\pm}^{(\mathrm{F})}(\tau,0,-\mathrm{i}\tilde\mu_\tau)\,,
\tag{E.5}
$$

$$
\begin{aligned}
\partial_t\lambda_{(S+P)_-^{\mathrm{adj}}} =\;& 2\lambda_{(S+P)_-^{\mathrm{adj}}} + 64v_4\Big(\lambda_{(\sigma\text{-}\pi)}^2 + 2\lambda_{(S+P)_-^{\mathrm{adj}}}\lambda_{(V+A)_\parallel} - \frac{3}{2}\lambda_{(\sigma\text{-}\pi)}\lambda_{(V+A)_\parallel^{\mathrm{adj}}} + \lambda_{(S+P)_-}\lambda_{(V+A)_\parallel^{\mathrm{adj}}} \\
&+\lambda_{(V+A)_\parallel^{\mathrm{adj}}}^2 + 2\lambda_{(\sigma\text{-}\pi)}\lambda_{(V+A)_\perp} + 4\lambda_{(S+P)_-}\lambda_{(V+A)_\perp} + 2\lambda_{(S+P)_-^{\mathrm{adj}}}\lambda_{(V+A)_\perp} - 3\lambda_{(V-A)_\perp}\lambda_{(V-A)_\perp^{\mathrm{adj}}} \\
&-\frac{3}{2N_c}\lambda_{(S+P)_-^{\mathrm{adj}}}\lambda_{(V+A)_\parallel^{\mathrm{adj}}} - \frac{2}{N_c}\lambda_{(S+P)_-^{\mathrm{adj}}}\lambda_{(V+A)_\perp} + \frac{3}{2N_c}\lambda_{(V-A)_\perp^{\mathrm{adj}}}^2 + \frac{N_c}{2}\lambda_{(S+P)_-^{\mathrm{adj}}}\lambda_{(V+A)_\parallel^{\mathrm{adj}}} \\
&-\frac{3N_c}{4}\lambda_{(V-A)_\perp^{\mathrm{adj}}}^2 + 2\lambda_{(V+A)_\parallel}\lambda_{\mathrm{csc}} - 2\lambda_{(V-A)_\parallel}\lambda_{\mathrm{csc}} - \frac{1}{2}\lambda_{(V+A)_\parallel^{\mathrm{adj}}}\lambda_{\mathrm{csc}} + \frac{3}{2}\lambda_{(V-A)_\perp^{\mathrm{adj}}}\lambda_{\mathrm{csc}} \\
&-\frac{1}{N_c}\lambda_{(V+A)_\parallel^{\mathrm{adj}}}\lambda_{\mathrm{csc}} + \frac{N_c}{2}\lambda_{(V+A)_\parallel^{\mathrm{adj}}}\lambda_{\mathrm{csc}} - \frac{3N_c}{2}\lambda_{(V-A)_\perp^{\mathrm{adj}}}\lambda_{\mathrm{csc}} + 2\lambda_{\mathrm{csc}}^2 - N_c\lambda_{\mathrm{csc}}^2\Big)l_{\parallel+}^{(\mathrm{F})}(\tau,0,-\mathrm{i}\tilde\mu_\tau) \\
&+64v_4\Big(\lambda_{(\sigma\text{-}\pi)}^2 + 4\lambda_{(\sigma\text{-}\pi)}\lambda_{(S+P)_-} + 4\lambda_{(S+P)_-}^2 + 4\lambda_{(\sigma\text{-}\pi)}\lambda_{(S+P)_-^{\mathrm{adj}}} + 8\lambda_{(S+P)_-}\lambda_{(S+P)_-^{\mathrm{adj}}} \\
&+\lambda_{(S+P)_-^{\mathrm{adj}}}^2 - \lambda_{(S+P)_-^{\mathrm{adj}}}\lambda_{(V-A)_\parallel} + 2\lambda_{(\sigma\text{-}\pi)}\lambda_{(V-A)_\perp} + 4\lambda_{(S+P)_-}\lambda_{(V-A)_\perp} - \lambda_{(S+P)_-^{\mathrm{adj}}}\lambda_{(V-A)_\perp} \\
&-\frac{1}{2}\lambda_{(\sigma\text{-}\pi)}\lambda_{(V-A)_\perp^{\mathrm{adj}}} - \lambda_{(S+P)_-}\lambda_{(V-A)_\perp^{\mathrm{adj}}} + \lambda_{(S+P)_-^{\mathrm{adj}}}\lambda_{(V-A)_\perp^{\mathrm{adj}}} + 3\lambda_{(V-A)_\perp}\lambda_{(V-A)_\perp^{\mathrm{adj}}} \\
&+\frac{1}{N_c^2}\lambda_{(S+P)_-^{\mathrm{adj}}}^2 + \frac{1}{N_c^2}\lambda_{(S+P)_-^{\mathrm{adj}}}\lambda_{(V-A)_\perp^{\mathrm{adj}}} - \frac{2}{N_c}\lambda_{(\sigma\text{-}\pi)}\lambda_{(S+P)_-^{\mathrm{adj}}} - \frac{4}{N_c}\lambda_{(S+P)_-}\lambda_{(S+P)_-^{\mathrm{adj}}} \\
&-\frac{4}{N_c}\lambda_{(S+P)_-^{\mathrm{adj}}}^2 - \frac{2}{N_c}\lambda_{(S+P)_-^{\mathrm{adj}}}\lambda_{(V-A)_\perp} - \frac{1}{N_c}\lambda_{(\sigma\text{-}\pi)}\lambda_{(V-A)_\perp^{\mathrm{adj}}} - \frac{2}{N_c}\lambda_{(S+P)_-}\lambda_{(V-A)_\perp^{\mathrm{adj}}} \\
&+\frac{1}{N_c}\lambda_{(S+P)_-^{\mathrm{adj}}}\lambda_{(V-A)_\perp^{\mathrm{adj}}} - \frac{3}{2N_c}\lambda_{(V-A)_\perp^{\mathrm{adj}}}^2\Big)l_{\parallel\pm}^{(\mathrm{F})}(\tau,0,-\mathrm{i}\tilde\mu_\tau) \\
&+64v_4\Big(-\lambda_{(\sigma\text{-}\pi)}^2 + \frac{2}{3}\lambda_{(\sigma\text{-}\pi)}\lambda_{(V+A)_\parallel} + \frac{4}{3}\lambda_{(S+P)_-}\lambda_{(V+A)_\parallel} + \frac{2}{3}\lambda_{(S+P)_-^{\mathrm{adj}}}\lambda_{(V+A)_\parallel} + \frac{11}{6}\lambda_{(\sigma\text{-}\pi)}\lambda_{(V+A)_\parallel^{\mathrm{adj}}} \\
&-\frac{1}{3}\lambda_{(S+P)_-}\lambda_{(V+A)_\parallel^{\mathrm{adj}}} - \lambda_{(V+A)_\parallel^{\mathrm{adj}}}^2 + \frac{4}{3}\lambda_{(\sigma\text{-}\pi)}\lambda_{(V+A)_\perp} + \frac{8}{3}\lambda_{(S+P)_-}\lambda_{(V+A)_\perp} \\
&+\frac{10}{3}\lambda_{(S+P)_-^{\mathrm{adj}}}\lambda_{(V+A)_\perp} - \lambda_{(V-A)_\parallel}\lambda_{(V-A)_\perp^{\mathrm{adj}}} + 2\lambda_{(V-A)_\perp}\lambda_{(V-A)_\perp^{\mathrm{adj}}} + \frac{1}{3N_c^2}\lambda_{(S+P)_-^{\mathrm{adj}}}\lambda_{(V+A)_\parallel^{\mathrm{adj}}} \\
&-\frac{2}{3N_c}\lambda_{(S+P)_-^{\mathrm{adj}}}\lambda_{(V+A)_\parallel} - \frac{1}{3N_c}\lambda_{(\sigma\text{-}\pi)}\lambda_{(V+A)_\parallel^{\mathrm{adj}}} - \frac{2}{3N_c}\lambda_{(S+P)_-}\lambda_{(V+A)_\parallel^{\mathrm{adj}}}
\end{aligned}
$$

$$-\frac{1}{6N_c}\lambda_{(S+P)_-^{\mathrm{adj}}}\lambda_{(V+A)_\parallel^{\mathrm{adj}}} - \frac{4}{3N_c}\lambda_{(S+P)_-^{\mathrm{adj}}}\lambda_{(V+A)_\perp} - \frac{1}{N_c}\lambda_{(V-A)_\perp^{\mathrm{adj}}}^2 - \frac{N_c}{6}\lambda_{(S+P)_-^{\mathrm{adj}}}\lambda_{(V+A)_\parallel^{\mathrm{adj}}}$$

$$+\frac{N_c}{2}\lambda_{(V-A)_\perp^{\mathrm{adj}}}^2 + \frac{1}{6}\lambda_{(V+A)_\parallel^{\mathrm{adj}}}\lambda_{\mathrm{csc}} + 2\lambda_{(V+A)_\perp}\lambda_{\mathrm{csc}} - 2\lambda_{(V-A)_\perp}\lambda_{\mathrm{csc}} - \frac{1}{2}\lambda_{(V-A)_\perp^{\mathrm{adj}}}\lambda_{\mathrm{csc}}$$

$$+\frac{1}{N_c}\lambda_{(V-A)_\perp^{\mathrm{adj}}}\lambda_{\mathrm{csc}} - \frac{N_c}{6}\lambda_{(V+A)_\parallel^{\mathrm{adj}}}\lambda_{\mathrm{csc}} + \frac{N_c}{2}\lambda_{(V-A)_\perp^{\mathrm{adj}}}\lambda_{\mathrm{csc}} \Big)l_{\perp+}^{(\mathrm{F})}(\tau,0,-\mathrm{i}\tilde{\mu}_\tau)$$

$$+64v_4\Big(-\lambda_{(\sigma\text{-}\pi)}^2 - 4\lambda_{(\sigma\text{-}\pi)}\lambda_{(S+P)_-} - 4\lambda_{(S+P)_-}^2 - \lambda_{(S+P)_-^{\mathrm{adj}}}^2 + \frac{2}{3}\lambda_{(\sigma\text{-}\pi)}\lambda_{(V-A)_\parallel}$$

$$+\frac{4}{3}\lambda_{(S+P)_-}\lambda_{(V-A)_\parallel} - \frac{1}{3}\lambda_{(S+P)_-^{\mathrm{adj}}}\lambda_{(V-A)_\parallel} + \frac{4}{3}\lambda_{(\sigma\text{-}\pi)}\lambda_{(V-A)_\perp} + \frac{8}{3}\lambda_{(S+P)_-}\lambda_{(V-A)_\perp}$$

$$-\frac{5}{3}\lambda_{(S+P)_-^{\mathrm{adj}}}\lambda_{(V-A)_\perp} - \frac{5}{6}\lambda_{(\sigma\text{-}\pi)}\lambda_{(V-A)_\perp^{\mathrm{adj}}} - \frac{5}{3}\lambda_{(S+P)_-}\lambda_{(V-A)_\perp^{\mathrm{adj}}} + \frac{2}{3}\lambda_{(S+P)_-^{\mathrm{adj}}}\lambda_{(V-A)_\perp^{\mathrm{adj}}}$$

$$+\lambda_{(V-A)_\parallel}\lambda_{(V-A)_\perp^{\mathrm{adj}}} + 2\lambda_{(V-A)_\perp}\lambda_{(V-A)_\perp^{\mathrm{adj}}} - \frac{1}{N_c^2}\lambda_{(S+P)_-^{\mathrm{adj}}}^2 + \frac{2}{3N_c^2}\lambda_{(S+P)_-^{\mathrm{adj}}}\lambda_{(V-A)_\perp^{\mathrm{adj}}}$$

$$+\frac{2}{N_c}\lambda_{(\sigma\text{-}\pi)}\lambda_{(S+P)_-^{\mathrm{adj}}} + \frac{4}{N_c}\lambda_{(S+P)_-}\lambda_{(S+P)_-^{\mathrm{adj}}} - \frac{2}{3N_c}\lambda_{(S+P)_-^{\mathrm{adj}}}\lambda_{(V-A)_\parallel} - \frac{4}{3N_c}\lambda_{(S+P)_-^{\mathrm{adj}}}\lambda_{(V-A)_\perp}$$

$$-\frac{2}{3N_c}\lambda_{(\sigma\text{-}\pi)}\lambda_{(V-A)_\perp^{\mathrm{adj}}} - \frac{4}{3N_c}\lambda_{(S+P)_-}\lambda_{(V-A)_\perp^{\mathrm{adj}}} + \frac{5}{3N_c}\lambda_{(S+P)_-^{\mathrm{adj}}}\lambda_{(V-A)_\perp^{\mathrm{adj}}}$$

$$-\frac{1}{N_c}\lambda_{(V-A)_\perp^{\mathrm{adj}}}^2 \Big)l_{\perp\pm}^{(\mathrm{F})}(\tau,0,-\mathrm{i}\tilde{\mu}_\tau)\,, \tag{E.6}$$

$$\partial_t\lambda_{(S+P)_-} = 2\lambda_{(S+P)_-} + 64v_4\Big(-\frac{1}{2}\lambda_{(\sigma\text{-}\pi)}^2 + \lambda_{(\sigma\text{-}\pi)}\lambda_{(S+P)_-} + 2\lambda_{(S+P)_-}^2 + \frac{1}{2}\lambda_{(\sigma\text{-}\pi)}\lambda_{(V+A)_\parallel}$$

$$+2\lambda_{(S+P)_-}\lambda_{(V+A)_\parallel} - \frac{1}{2}\lambda_{(\sigma\text{-}\pi)}\lambda_{(V-A)_\parallel} + \lambda_{(\sigma\text{-}\pi)}\lambda_{(V+A)_\parallel^{\mathrm{adj}}} + \frac{1}{4}\lambda_{(S+P)_-^{\mathrm{adj}}}\lambda_{(V+A)_\parallel^{\mathrm{adj}}} - \frac{1}{2}\lambda_{(V+A)_\parallel^{\mathrm{adj}}}^2$$

$$-\frac{1}{2}\lambda_{(\sigma\text{-}\pi)}\lambda_{(V+A)_\perp} + 2\lambda_{(S+P)_-}\lambda_{(V+A)_\perp} + \lambda_{(S+P)_-^{\mathrm{adj}}}\lambda_{(V+A)_\perp} + \frac{1}{2}\lambda_{(V+A)_\parallel^{\mathrm{adj}}}\lambda_{(V+A)_\perp}$$

$$-\frac{1}{2}\lambda_{(\sigma\text{-}\pi)}\lambda_{(V-A)_\perp} - \lambda_{(\sigma\text{-}\pi)}\lambda_{(V-A)_\perp^{\mathrm{adj}}} + \frac{3}{2}\lambda_{(V-A)_\perp}\lambda_{(V-A)_\perp^{\mathrm{adj}}} - \frac{3}{8}\lambda_{(V-A)_\perp^{\mathrm{adj}}}^2 + \frac{1}{2N_c^2}\lambda_{(S+P)_-^{\mathrm{adj}}}^2$$

$$-\frac{1}{4N_c^2}\lambda_{(S+P)_-^{\mathrm{adj}}}\lambda_{(V+A)_\parallel^{\mathrm{adj}}} - \frac{1}{N_c^2}\lambda_{(S+P)_-^{\mathrm{adj}}}\lambda_{(V+A)_\perp} + \frac{3}{4N_c^2}\lambda_{(V-A)_\perp^{\mathrm{adj}}}^2$$

$$+\frac{1}{2N_c}\lambda_{(\sigma\text{-}\pi)}^2 - \frac{1}{2N_c}\lambda_{(\sigma\text{-}\pi)}\lambda_{(S+P)_-^{\mathrm{adj}}} - \frac{2}{N_c}\lambda_{(S+P)_-}\lambda_{(S+P)_-^{\mathrm{adj}}} - \frac{1}{2N_c}\lambda_{(S+P)_-^{\mathrm{adj}}}^2 - \frac{1}{N_c}\lambda_{(\sigma\text{-}\pi)}\lambda_{(V+A)_\parallel^{\mathrm{adj}}}$$

$$-\frac{1}{2N_c}\lambda_{(S+P)_-}\lambda_{(V+A)_\parallel^{\mathrm{adj}}} + \frac{1}{2N_c}\lambda_{(V+A)_\parallel^{\mathrm{adj}}}^2 + \frac{1}{N_c}\lambda_{(\sigma\text{-}\pi)}\lambda_{(V+A)_\perp} + \frac{2}{N_c}\lambda_{(S+P)_-}\lambda_{(V+A)_\perp}$$

$$+\frac{1}{4N_c}\lambda_{(\sigma\text{-}\pi)}\lambda_{(V-A)_\perp} - \frac{3}{2N_c}\lambda_{(V-A)_\perp}\lambda_{(V-A)_\perp^{\mathrm{adj}}} - \frac{3}{4N_c}\lambda_{(V-A)_\perp^{\mathrm{adj}}}^2 + 2N_c\lambda_{(S+P)_-}^2$$

$$+N_c\lambda_{(S+P)_-}\lambda_{(S+P)_-^{\mathrm{adj}}} + \frac{N_c}{2}\lambda_{(S+P)_-}\lambda_{(V+A)_\parallel^{\mathrm{adj}}} + \frac{3N_c}{8}\lambda_{(V-A)_\perp^{\mathrm{adj}}}^2 - \lambda_{(\sigma\text{-}\pi)}\lambda_{\mathrm{csc}} + \frac{1}{2}\lambda_{(S+P)_-^{\mathrm{adj}}}\lambda_{\mathrm{csc}}$$

$$-\lambda_{(V+A)_\parallel}\lambda_{\mathrm{csc}} + \lambda_{(V-A)_\parallel}\lambda_{\mathrm{csc}} + \frac{1}{2}\lambda_{(V+A)_\parallel^{\mathrm{adj}}}\lambda_{\mathrm{csc}} - \frac{3}{2}\lambda_{(V-A)_\perp^{\mathrm{adj}}}\lambda_{\mathrm{csc}} - \frac{1}{2N_c^2}\lambda_{(V+A)_\parallel^{\mathrm{adj}}}\lambda_{\mathrm{csc}}$$

$$+\frac{1}{N_c}\lambda_{(V+A)_\parallel}\lambda_{\mathrm{csc}} - \frac{1}{N_c}\lambda_{(V-A)_\parallel}\lambda_{\mathrm{csc}} + \frac{1}{4N_c}\lambda_{(V+A)_\parallel^{\mathrm{adj}}}\lambda_{\mathrm{csc}} + \frac{3}{4N_c}\lambda_{(V-A)_\perp^{\mathrm{adj}}}\lambda_{\mathrm{csc}} - N_c\lambda_{(S+P)_-}\lambda_{\mathrm{csc}}$$

$$-\frac{N_c}{2}\lambda_{(S+P)_-^{\mathrm{adj}}}\lambda_{\mathrm{csc}} - \frac{N_c}{4}\lambda_{(V+A)_\parallel^{\mathrm{adj}}}\lambda_{\mathrm{csc}} + \frac{3N_c}{4}\lambda_{(V-A)_\perp^{\mathrm{adj}}}\lambda_{\mathrm{csc}} - \frac{3}{2}\lambda_{\mathrm{csc}}^2 + \frac{1}{N_c}\lambda_{\mathrm{csc}}^2$$

$$+\frac{N_c}{2}\lambda_{\mathrm{csc}}^2 \Big)l_{\parallel+}^{(\mathrm{F})}(\tau,0,-\mathrm{i}\tilde{\mu}_\tau)$$

$$+64v_4\Big(-\frac{1}{2}\lambda_{(\sigma\text{-}\pi)}^2 - 2\lambda_{(\sigma\text{-}\pi)}\lambda_{(S+P)_-} - 2\lambda_{(S+P)_-}^2 - 2\lambda_{(\sigma\text{-}\pi)}\lambda_{(S+P)_-^{\mathrm{adj}}} - 4\lambda_{(S+P)_-}\lambda_{(S+P)_-^{\mathrm{adj}}}$$

$$-\frac{1}{2}\lambda_{(S+P)_-^{\mathrm{adj}}}^2 + \frac{1}{2}\lambda_{(\sigma\text{-}\pi)}\lambda_{(V+A)_\parallel} - \frac{1}{2}\lambda_{(\sigma\text{-}\pi)}\lambda_{(V-A)_\parallel} - \lambda_{(S+P)_-}\lambda_{(V-A)_\parallel} - \frac{1}{2}\lambda_{(\sigma\text{-}\pi)}\lambda_{(V+A)_\perp}$$

$$-\frac{1}{2}\lambda_{(V+A)_\parallel^{\mathrm{adj}}}\lambda_{(V+A)_\perp} - \frac{1}{2}\lambda_{(\sigma\text{-}\pi)}\lambda_{(V-A)_\perp} - \lambda_{(S+P)_-}\lambda_{(V-A)_\perp} + \lambda_{(S+P)_-^{\mathrm{adj}}}\lambda_{(V-A)_\perp}$$

$$+\frac{1}{2}\lambda_{(\sigma\text{-}\pi)}\lambda_{(V-A)_\perp^{\mathrm{adj}}} + \lambda_{(S+P)_-}\lambda_{(V-A)_\perp^{\mathrm{adj}}} - \frac{1}{4}\lambda_{(S+P)_-^{\mathrm{adj}}}\lambda_{(V-A)_\perp^{\mathrm{adj}}} - \frac{3}{2}\lambda_{(V-A)_\perp}\lambda_{(V-A)_\perp^{\mathrm{adj}}}$$

$$+\frac{1}{2N_c^3}\lambda_{(S+P)_-^{\mathrm{adj}}}^2 + \frac{1}{2N_c^3}\lambda_{(S+P)_-^{\mathrm{adj}}}\lambda_{(V-A)_\perp^{\mathrm{adj}}} - \frac{1}{N_c^2}\lambda_{(\sigma\text{-}\pi)}\lambda_{(S+P)_-^{\mathrm{adj}}} - \frac{2}{N_c^2}\lambda_{(S+P)_-}\lambda_{(S+P)_-^{\mathrm{adj}}}$$

$$-\frac{5}{2N_c^2}\lambda_{(S+P)_-^{\mathrm{adj}}}^2 - \frac{1}{N_c^2}\lambda_{(S+P)_-^{\mathrm{adj}}}\lambda_{(V-A)_\perp} - \frac{1}{2N_c^2}\lambda_{(\sigma\text{-}\pi)}\lambda_{(V-A)_\perp^{\mathrm{adj}}} - \frac{1}{N_c^2}\lambda_{(S+P)_-}\lambda_{(V-A)_\perp^{\mathrm{adj}}}$$

$$+\frac{1}{4N_c^2}\lambda_{(S+P)_-^{\mathrm{adj}}}\lambda_{(V-A)_\perp^{\mathrm{adj}}} - \frac{3}{4N_c^2}\lambda_{(V-A)_\perp^{\mathrm{adj}}}^2 + \frac{1}{2N_c}\lambda_{(\sigma\text{-}\pi)}^2 + \frac{2}{N_c}\lambda_{(\sigma\text{-}\pi)}\lambda_{(S+P)_-} + \frac{2}{N_c}\lambda_{(S+P)_-}^2$$

$$+\frac{3}{N_c}\lambda_{(\sigma\text{-}\pi)}\lambda_{(S+P)_-^{\mathrm{adj}}} + \frac{6}{N_c}\lambda_{(S+P)_-}\lambda_{(S+P)_-^{\mathrm{adj}}} + \frac{5}{2N_c}\lambda_{(S+P)_-^{\mathrm{adj}}}^2 - \frac{1}{4N_c}\lambda_{(\sigma\text{-}\pi)}\lambda_{(V+A)_\parallel^{\mathrm{adj}}}$$

$$+\frac{1}{N_c}\lambda_{(\sigma\text{-}\pi)}\lambda_{(V-A)_\perp} + \frac{2}{N_c}\lambda_{(S+P)_-}\lambda_{(V-A)_\perp} - \frac{1}{2N_c}\lambda_{(S+P)_-^{\mathrm{adj}}}\lambda_{(V-A)_\perp^{\mathrm{adj}}} + \frac{3}{2N_c}\lambda_{(V-A)_\perp}\lambda_{(V-A)_\perp^{\mathrm{adj}}}$$

$$+\frac{3}{4N_c}\lambda_{(V-A)_\perp^{\mathrm{adj}}}^2\Big)l_{\parallel\pm}^{(\mathrm{F})}(\tau,0,-\mathrm{i}\tilde{\mu}_\tau)$$

$$+64v_4\Big(\frac{1}{2}\lambda_{(\sigma\text{-}\pi)}^2 + \lambda_{(\sigma\text{-}\pi)}\lambda_{(S+P)_-} + 2\lambda_{(S+P)_-}^2 + \frac{1}{3}\lambda_{(\sigma\text{-}\pi)}\lambda_{(S+P)_-^{\mathrm{adj}}} + \frac{2}{3}\lambda_{(S+P)_-}\lambda_{(S+P)_-^{\mathrm{adj}}}$$

$$-\frac{1}{6}\lambda_{(\sigma\text{-}\pi)}\lambda_{(V+A)_\parallel} + \frac{2}{3}\lambda_{(S+P)_-}\lambda_{(V+A)_\parallel} + \frac{1}{3}\lambda_{(S+P)_-^{\mathrm{adj}}}\lambda_{(V+A)_\parallel} - \frac{1}{6}\lambda_{(\sigma\text{-}\pi)}\lambda_{(V-A)_\parallel}$$

$$-\frac{5}{6}\lambda_{(\sigma\text{-}\pi)}\lambda_{(V+A)_\parallel^{\mathrm{adj}}} + \frac{1}{3}\lambda_{(S+P)_-}\lambda_{(V+A)_\parallel^{\mathrm{adj}}} - \frac{1}{12}\lambda_{(S+P)_-^{\mathrm{adj}}}\lambda_{(V+A)_\parallel^{\mathrm{adj}}} + \frac{1}{6}\lambda_{(V+A)_\parallel}\lambda_{(V+A)_\parallel^{\mathrm{adj}}}$$

$$+\frac{1}{2}\lambda_{(V+A)_\parallel^{\mathrm{adj}}}^2 + \frac{1}{6}\lambda_{(\sigma\text{-}\pi)}\lambda_{(V+A)_\perp} + \frac{10}{3}\lambda_{(S+P)_-}\lambda_{(V+A)_\perp} + \frac{2}{3}\lambda_{(S+P)_-^{\mathrm{adj}}}\lambda_{(V+A)_\perp}$$

$$+\frac{1}{3}\lambda_{(V+A)_\parallel^{\mathrm{adj}}}\lambda_{(V+A)_\perp} - \frac{1}{6}\lambda_{(\sigma\text{-}\pi)}\lambda_{(V-A)_\perp} - \frac{1}{3}\lambda_{(\sigma\text{-}\pi)}\lambda_{(V-A)_\perp^{\mathrm{adj}}} + \frac{1}{2}\lambda_{(V-A)_\parallel}\lambda_{(V-A)_\perp^{\mathrm{adj}}}$$

$$-\lambda_{(V-A)_\perp}\lambda_{(V-A)_\perp^{\mathrm{adj}}} + \frac{1}{4}\lambda_{(V-A)_\perp^{\mathrm{adj}}}^2 + \frac{1}{6N_c^3}\lambda_{(S+P)_-^{\mathrm{adj}}}\lambda_{(V+A)_\parallel^{\mathrm{adj}}} + \frac{1}{2N_c^2}\lambda_{(S+P)_-^{\mathrm{adj}}}^2$$

$$-\frac{1}{3N_c^2}\lambda_{(S+P)_-^{\mathrm{adj}}}\lambda_{(V+A)_\parallel} - \frac{1}{6N_c^2}\lambda_{(\sigma\text{-}\pi)}\lambda_{(V+A)_\parallel^{\mathrm{adj}}} - \frac{1}{3N_c^2}\lambda_{(S+P)_-}\lambda_{(V+A)_\parallel^{\mathrm{adj}}}$$

$$+\frac{1}{12N_c^2}\lambda_{(S+P)_-^{\mathrm{adj}}}\lambda_{(V+A)_\parallel^{\mathrm{adj}}} - \frac{2}{3N_c^2}\lambda_{(S+P)_-^{\mathrm{adj}}}\lambda_{(V+A)_\perp} - \frac{1}{2N_c^2}\lambda_{(V-A)_\perp^{\mathrm{adj}}}^2 - \frac{1}{2N_c}\lambda_{(\sigma\text{-}\pi)}^2$$

$$-\frac{1}{2N_c}\lambda_{(\sigma\text{-}\pi)}\lambda_{(S+P)_-^{\mathrm{adj}}} - \frac{2}{N_c}\lambda_{(S+P)_-}\lambda_{(S+P)_-^{\mathrm{adj}}} - \frac{5}{6N_c}\lambda_{(S+P)_-^{\mathrm{adj}}}^2 + \frac{1}{3N_c}\lambda_{(\sigma\text{-}\pi)}\lambda_{(V+A)_\parallel}$$

$$+\frac{2}{3N_c}\lambda_{(S+P)_-}\lambda_{(V+A)_\parallel} + \frac{1}{N_c}\lambda_{(\sigma\text{-}\pi)}\lambda_{(V+A)_\parallel^{\mathrm{adj}}} - \frac{1}{2N_c}\lambda_{(S+P)_-}\lambda_{(V+A)_\parallel^{\mathrm{adj}}} - \frac{1}{3N_c}\lambda_{(S+P)_-^{\mathrm{adj}}}\lambda_{(V+A)_\parallel^{\mathrm{adj}}}$$

$$-\frac{7}{12N_c}\lambda_{(V+A)_\parallel^{\mathrm{adj}}}^2 + \frac{2}{3N_c}\lambda_{(\sigma\text{-}\pi)}\lambda_{(V+A)_\perp} + \frac{4}{3N_c}\lambda_{(S+P)_-}\lambda_{(V+A)_\perp} + \frac{1}{12N_c}\lambda_{(\sigma\text{-}\pi)}\lambda_{(V-A)_\perp^{\mathrm{adj}}}$$

$$-\frac{1}{2N_c}\lambda_{(V-A)_\parallel}\lambda_{(V-A)_\perp^{\mathrm{adj}}} + \frac{1}{N_c}\lambda_{(V-A)_\perp}\lambda_{(V-A)_\perp^{\mathrm{adj}}} + \frac{1}{2N_c}\lambda_{(V-A)_\perp^{\mathrm{adj}}}^2 + 2N_c\lambda_{(S+P)_-}^2$$

$$+N_c\lambda_{(S+P)_-}\lambda_{(S+P)_-^{\mathrm{adj}}} + \frac{N_c}{6}\lambda_{(S+P)_-^{\mathrm{adj}}}^2 + \frac{N_c}{2}\lambda_{(S+P)_-}\lambda_{(V+A)_\parallel^{\mathrm{adj}}} + \frac{N_c}{6}\lambda_{(S+P)_-^{\mathrm{adj}}}\lambda_{(V+A)_\parallel^{\mathrm{adj}}}$$

$$+\frac{N_c}{24}\lambda_{(V+A)_\parallel^{\mathrm{adj}}}^2 - \frac{N_c}{4}\lambda_{(V-A)_\perp^{\mathrm{adj}}}^2 - \frac{1}{3}\lambda_{(\sigma\text{-}\pi)}\lambda_{\mathrm{csc}} + \frac{2}{3}\lambda_{(S+P)_-}\lambda_{\mathrm{csc}} + \frac{1}{6}\lambda_{(S+P)_-^{\mathrm{adj}}}\lambda_{\mathrm{csc}} - \lambda_{(V+A)_\perp}\lambda_{\mathrm{csc}}$$

$$+\lambda_{(V-A)_\perp}\lambda_{\mathrm{csc}} + \frac{1}{2}\lambda_{(V-A)_\perp^{\mathrm{adj}}}\lambda_{\mathrm{csc}} + \frac{1}{2N_c^2}\lambda_{(V-A)_\perp^{\mathrm{adj}}}\lambda_{\mathrm{csc}} - \frac{1}{3N_c}\lambda_{(S+P)_-^{\mathrm{adj}}}\lambda_{\mathrm{csc}} + \frac{1}{12N_c}\lambda_{(V+A)_\parallel^{\mathrm{adj}}}\lambda_{\mathrm{csc}}$$

$$+\frac{1}{N_c}\lambda_{(V+A)_\perp}\lambda_{\mathrm{csc}} - \frac{1}{N_c}\lambda_{(V-A)_\perp}\lambda_{\mathrm{csc}} - \frac{3}{4N_c}\lambda_{(V-A)_\perp^{\mathrm{adj}}}\lambda_{\mathrm{csc}} - N_c\lambda_{(S+P)_-}\lambda_{\mathrm{csc}} - \frac{N_c}{6}\lambda_{(S+P)_-^{\mathrm{adj}}}\lambda_{\mathrm{csc}}$$

$$-\frac{N_c}{12}\lambda_{(V+A)_\parallel^{\mathrm{adj}}}\lambda_{\mathrm{csc}} - \frac{N_c}{4}\lambda_{(V-A)_\perp^{\mathrm{adj}}}\lambda_{\mathrm{csc}} - \frac{1}{3}\lambda_{\mathrm{csc}}^2 + \frac{N_c}{6}\lambda_{\mathrm{csc}}^2\Big)l_{\perp+}^{(\mathrm{F})}(\tau,0,-\mathrm{i}\tilde{\mu}_\tau)$$

$$+64v_4\Big(\frac{1}{2}\lambda_{(\sigma\text{-}\pi)}^2 + 2\lambda_{(\sigma\text{-}\pi)}\lambda_{(S+P)_-} + 2\lambda_{(S+P)_-}^2 + \frac{1}{2}\lambda_{(S+P)_-^{\mathrm{adj}}}^2 - \frac{1}{6}\lambda_{(\sigma\text{-}\pi)}\lambda_{(V+A)_\parallel} - \frac{1}{6}\lambda_{(\sigma\text{-}\pi)}\lambda_{(V-A)_\parallel}$$

$$-\frac{1}{3}\lambda_{(S+P)_-}\lambda_{(V-A)_\parallel} + \frac{1}{3}\lambda_{(S+P)_-^{\mathrm{adj}}}\lambda_{(V-A)_\parallel} - \frac{1}{6}\lambda_{(V+A)_\parallel}\lambda_{(V+A)_\parallel^{\mathrm{adj}}} + \frac{5}{6}\lambda_{(\sigma\text{-}\pi)}\lambda_{(V+A)_\perp}$$

$$+\frac{1}{3}\lambda_{(V+A)_\parallel^{\mathrm{adj}}}\lambda_{(V+A)_\perp} - \frac{5}{6}\lambda_{(\sigma\text{-}\pi)}\lambda_{(V-A)_\perp} - \frac{5}{3}\lambda_{(S+P)_-}\lambda_{(V-A)_\perp} + \frac{2}{3}\lambda_{(S+P)_-^{\mathrm{adj}}}\lambda_{(V-A)_\perp}$$

$$+\frac{1}{3}\lambda_{(\sigma\text{-}\pi)}\lambda_{(V-A)_\perp^{\mathrm{adj}}} + \frac{2}{3}\lambda_{(S+P)_-}\lambda_{(V-A)_\perp^{\mathrm{adj}}} - \frac{5}{12}\lambda_{(S+P)_-^{\mathrm{adj}}}\lambda_{(V-A)_\perp^{\mathrm{adj}}} - \frac{1}{2}\lambda_{(V-A)_\parallel}\lambda_{(V-A)_\perp^{\mathrm{adj}}}$$

$$-\lambda_{(V-A)_\perp}\lambda_{(V-A)_\perp^{\mathrm{adj}}} - \frac{1}{2N_c^3}\lambda_{(S+P)_-^{\mathrm{adj}}}^2 + \frac{1}{3N_c^3}\lambda_{(S+P)_-^{\mathrm{adj}}}\lambda_{(V-A)_\perp^{\mathrm{adj}}} + \frac{1}{N_c^2}\lambda_{(\sigma\text{-}\pi)}\lambda_{(S+P)_-^{\mathrm{adj}}}$$

$$+\frac{2}{N_c^2}\lambda_{(S+P)_-}\lambda_{(S+P)_-^{\mathrm{adj}}} + \frac{1}{2N_c^2}\lambda_{(S+P)_-^{\mathrm{adj}}}^2 - \frac{1}{3N_c^2}\lambda_{(S+P)_-^{\mathrm{adj}}}\lambda_{(V-A)_\parallel} - \frac{2}{3N_c^2}\lambda_{(S+P)_-^{\mathrm{adj}}}\lambda_{(V-A)_\perp}$$

$$-\frac{1}{3N_c^2}\lambda_{(\sigma\text{-}\pi)}\lambda_{(V-A)_\perp^{\mathrm{adj}}} - \frac{2}{3N_c^2}\lambda_{(S+P)_-}\lambda_{(V-A)_\perp^{\mathrm{adj}}} + \frac{5}{12N_c^2}\lambda_{(S+P)_-^{\mathrm{adj}}}\lambda_{(V-A)_\perp^{\mathrm{adj}}} - \frac{1}{2N_c^2}\lambda_{(V-A)_\perp^{\mathrm{adj}}}^2$$

$$-\frac{1}{2N_c}\lambda_{(\sigma\text{-}\pi)}^2 - \frac{2}{N_c}\lambda_{(\sigma\text{-}\pi)}\lambda_{(S+P)_-} - \frac{2}{N_c}\lambda_{(S+P)_-}^2 - \frac{1}{N_c}\lambda_{(\sigma\text{-}\pi)}\lambda_{(S+P)_-^{\mathrm{adj}}} - \frac{2}{N_c}\lambda_{(S+P)_-}\lambda_{(S+P)_-^{\mathrm{adj}}}$$

$$-\frac{1}{2N_c}\lambda_{(S+P)_-^{\mathrm{adj}}}^2 + \frac{1}{3N_c}\lambda_{(\sigma\text{-}\pi)}\lambda_{(V-A)_\parallel} + \frac{2}{3N_c}\lambda_{(S+P)_-}\lambda_{(V-A)_\parallel} + \frac{1}{12N_c}\lambda_{(\sigma\text{-}\pi)}\lambda_{(V+A)_\parallel^{\mathrm{adj}}}$$

$$+\frac{1}{12N_c}\lambda_{(V+A)_\parallel^{\mathrm{adj}}}^2 + \frac{2}{3N_c}\lambda_{(\sigma\text{-}\pi)}\lambda_{(V-A)_\perp} + \frac{4}{3N_c}\lambda_{(S+P)_-}\lambda_{(V-A)_\perp} - \frac{1}{3N_c}\lambda_{(S+P)_-^{\mathrm{adj}}}\lambda_{(V-A)_\perp^{\mathrm{adj}}}$$

$$+\frac{1}{2N_c}\lambda_{(V-A)_\parallel}\lambda_{(V-A)_\perp^{\mathrm{adj}}} + \frac{1}{N_c}\lambda_{(V-A)_\perp}\lambda_{(V-A)_\perp^{\mathrm{adj}}} + \frac{1}{2N_c}\lambda_{(V-A)_\perp^{\mathrm{adj}}}^2 \Big) l_{\perp\pm}^{(\mathrm{F})}(\tau, 0, -\mathrm{i}\tilde{\mu}_\tau)\,, \qquad (\mathrm{E.7})$$

$$\partial_t \lambda_{(V+A)_\parallel} = 2\lambda_{(V+A)_\parallel} + 64v_4\Big(\frac{1}{2}\lambda_{(\sigma\text{-}\pi)}^2 + 2\lambda_{(\sigma\text{-}\pi)}\lambda_{(S+P)_-} + 2\lambda_{(S+P)_-}^2 + \frac{1}{2}\lambda_{(\sigma\text{-}\pi)}\lambda_{(S+P)_-^{\mathrm{adj}}}$$

$$+\lambda_{(S+P)_-}\lambda_{(S+P)_-^{\mathrm{adj}}} + \lambda_{(S+P)_-^{\mathrm{adj}}}^2 + \frac{1}{2}\lambda_{(V+A)_\parallel}^2 + 2\lambda_{(\sigma\text{-}\pi)}\lambda_{(V-A)_\parallel} + \lambda_{(V+A)_\parallel}\lambda_{(V-A)_\parallel}$$

$$+\frac{1}{8}\lambda_{(V+A)_\parallel^{\mathrm{adj}}}^2 + \frac{3}{2}\lambda_{(V+A)_\perp}^2 - 3\lambda_{(V+A)_\parallel}\lambda_{(V-A)_\perp} + \frac{3}{4}\lambda_{(\sigma\text{-}\pi)}\lambda_{(V-A)_\perp^{\mathrm{adj}}} - \frac{1}{2N_c^2}\lambda_{(S+P)_-^{\mathrm{adj}}}^2$$

$$-\frac{1}{8N_c^2}\lambda_{(V+A)_\parallel^{\mathrm{adj}}}^2 - \frac{1}{N_c^2}\lambda_{(\sigma\text{-}\pi)}\lambda_{(V-A)_\perp^{\mathrm{adj}}} - \frac{1}{2N_c}\lambda_{(S+P)_-^{\mathrm{adj}}}^2 - \frac{1}{2N_c}\lambda_{(V+A)_\parallel^{\mathrm{adj}}}\lambda_{(V+A)_\perp}$$

$$+\frac{2}{N_c}\lambda_{(\sigma\text{-}\pi)}\lambda_{(V-A)_\perp} + \frac{1}{N_c}\lambda_{(\sigma\text{-}\pi)}\lambda_{(V-A)_\perp^{\mathrm{adj}}} + \frac{3}{2N_c}\lambda_{(V+A)_\parallel}\lambda_{(V-A)_\perp^{\mathrm{adj}}} - 4N_c\lambda_{(V+A)_\parallel}\lambda_{(V-A)_\parallel}$$

$$-\frac{3N_c}{2}\lambda_{(V+A)_\parallel}\lambda_{(V-A)_\perp^{\mathrm{adj}}} - \lambda_{(\sigma\text{-}\pi)}\lambda_{\mathrm{csc}} - \lambda_{(S+P)_-}\lambda_{\mathrm{csc}} + \frac{3}{2}\lambda_{(S+P)_-^{\mathrm{adj}}}\lambda_{\mathrm{csc}} - \lambda_{(V+A)_\parallel}\lambda_{\mathrm{csc}}$$

$$-\frac{1}{N_c^2}\lambda_{(S+P)_-^{\mathrm{adj}}}\lambda_{\mathrm{csc}} + \frac{2}{N_c}\lambda_{(\sigma\text{-}\pi)}\lambda_{\mathrm{csc}} + \frac{2}{N_c}\lambda_{(S+P)_-}\lambda_{\mathrm{csc}} - \frac{1}{2N_c}\lambda_{(S+P)_-^{\mathrm{adj}}}\lambda_{\mathrm{csc}} + N_c\lambda_{(V+A)_\parallel}\lambda_{\mathrm{csc}}$$

$$+\lambda_{\mathrm{csc}}^2 - \frac{1}{N_c}\lambda_{\mathrm{csc}}^2\Big) l_{\parallel+}^{(\mathrm{F})}(\tau, 0, -\mathrm{i}\tilde{\mu}_\tau)$$

$$+64v_4\Big(-\frac{1}{2}\lambda_{(\sigma\text{-}\pi)}^2 - \frac{1}{2}\lambda_{(V+A)_\parallel}^2 + \frac{1}{4}\lambda_{(\sigma\text{-}\pi)}\lambda_{(V+A)_\parallel^{\mathrm{adj}}} - \frac{1}{8}\lambda_{(V+A)_\parallel^{\mathrm{adj}}}^2 - \frac{3}{2}\lambda_{(V+A)_\perp}^2$$

$$+\frac{1}{8N_c^2}\lambda_{(V+A)_\parallel^{\mathrm{adj}}}^2 + \frac{2}{N_c}\lambda_{(\sigma\text{-}\pi)}\lambda_{(V+A)_\perp} + \frac{1}{2N_c}\lambda_{(V+A)_\parallel^{\mathrm{adj}}}\lambda_{(V+A)_\perp}\Big) l_{\parallel\pm}^{(\mathrm{F})}(\tau, 0, -\mathrm{i}\tilde{\mu}_\tau)$$

$$+64v_4\Big(\frac{1}{2}\lambda_{(\sigma\text{-}\pi)}\lambda_{(S+P)_-^{\mathrm{adj}}} + \lambda_{(S+P)_-}\lambda_{(S+P)_-^{\mathrm{adj}}} + \frac{1}{3}\lambda_{(S+P)_-^{\mathrm{adj}}}^2 - 2\lambda_{(\sigma\text{-}\pi)}\lambda_{(V-A)_\parallel} - \lambda_{(V+A)_\parallel}\lambda_{(V-A)_\parallel}$$

$$-\frac{1}{24}\lambda_{(V+A)_\parallel^{\mathrm{adj}}}^2 + \lambda_{(V+A)_\parallel}\lambda_{(V+A)_\perp} + \lambda_{(V+A)_\perp}^2 + 3\lambda_{(V+A)_\parallel}\lambda_{(V-A)_\perp} - \frac{3}{4}\lambda_{(\sigma\text{-}\pi)}\lambda_{(V-A)_\perp^{\mathrm{adj}}}$$

$$+\frac{1}{3N_c^2}\lambda_{(S+P)_-^{\mathrm{adj}}}^2 + \frac{1}{12N_c^2}\lambda_{(V+A)_\parallel^{\mathrm{adj}}}^2 + \frac{2}{3N_c^2}\lambda_{(\sigma\text{-}\pi)}\lambda_{(V-A)_\perp^{\mathrm{adj}}} - \frac{1}{3N_c}\lambda_{(\sigma\text{-}\pi)}\lambda_{(S+P)_-^{\mathrm{adj}}}$$

$$-\frac{2}{3N_c}\lambda_{(S+P)_-}\lambda_{(S+P)_-^{\mathrm{adj}}} - \frac{1}{2N_c}\lambda_{(S+P)_-^{\mathrm{adj}}}^2 + \frac{2}{3N_c}\lambda_{(\sigma\text{-}\pi)}\lambda_{(V-A)_\parallel} - \frac{1}{6N_c}\lambda_{(V+A)_\parallel}\lambda_{(V+A)_\parallel^{\mathrm{adj}}}$$

$$-\frac{1}{3N_c}\lambda_{(V+A)_\parallel^{\mathrm{adj}}}\lambda_{(V+A)_\perp} - \frac{4}{3N_c}\lambda_{(\sigma\text{-}\pi)}\lambda_{(V-A)_\perp} + \frac{1}{3N_c}\lambda_{(\sigma\text{-}\pi)}\lambda_{(V-A)_\perp^{\mathrm{adj}}} - \frac{3}{2N_c}\lambda_{(V+A)_\parallel}\lambda_{(V-A)_\perp^{\mathrm{adj}}}$$

$$+ 4 N_c \lambda_{(V+A)_\parallel} \lambda_{(V-A)_\parallel} + \frac{3 N_c}{2} \lambda_{(V+A)_\parallel} \lambda_{(V-A)_\perp^{\mathrm{adj}}} + \lambda_{(\sigma\text{-}\pi)} \lambda_{\mathrm{csc}} + \lambda_{(S+P)_-} \lambda_{\mathrm{csc}} + \frac{1}{6} \lambda_{(S+P)_-^{\mathrm{adj}}} \lambda_{\mathrm{csc}}$$

$$+ \lambda_{(V+A)_\parallel} \lambda_{\mathrm{csc}} + \frac{1}{3 N_c^2} \lambda_{(S+P)_-^{\mathrm{adj}}} \lambda_{\mathrm{csc}} - \frac{2}{3 N_c} \lambda_{(\sigma\text{-}\pi)} \lambda_{\mathrm{csc}} - \frac{2}{3 N_c} \lambda_{(S+P)_-} \lambda_{\mathrm{csc}} - \frac{1}{6 N_c} \lambda_{(S+P)_-^{\mathrm{adj}}} \lambda_{\mathrm{csc}}$$

$$- N_c \lambda_{(V+A)_\parallel} \lambda_{\mathrm{csc}} - \frac{1}{6} \lambda_{\mathrm{csc}}^2 + \frac{1}{3 N_c} \lambda_{\mathrm{csc}}^2 \Big) l_{\perp+}^{(\mathrm{F})}(\tau, 0, -\mathrm{i}\tilde{\mu}_\tau)$$

$$+ 64 v_4 \Big(\frac{1}{4} \lambda_{(\sigma\text{-}\pi)} \lambda_{(V+A)_\parallel^{\mathrm{adj}}} - \lambda_{(V+A)_\parallel} \lambda_{(V+A)_\perp} + \lambda_{(V+A)_\perp}^2 - \frac{1}{3 N_c^2} \lambda_{(\sigma\text{-}\pi)} \lambda_{(V+A)_\parallel^{\mathrm{adj}}} - \frac{1}{12 N_c^2} \lambda_{(V+A)_\parallel^{\mathrm{adj}}}^2$$

$$+ \frac{2}{3 N_c} \lambda_{(\sigma\text{-}\pi)} \lambda_{(V+A)_\parallel} + \frac{1}{6 N_c} \lambda_{(V+A)_\parallel} \lambda_{(V+A)_\parallel^{\mathrm{adj}}} - \frac{4}{3 N_c} \lambda_{(\sigma\text{-}\pi)} \lambda_{(V+A)_\perp}$$

$$- \frac{1}{3 N_c} \lambda_{(V+A)_\parallel^{\mathrm{adj}}} \lambda_{(V+A)_\perp} \Big) l_{\perp\pm}^{(\mathrm{F})}(\tau, 0, -\mathrm{i}\tilde{\mu}_\tau) \,, \tag{E.8}$$

$$\partial_t \lambda_{(V+A)_\perp} = 2 \lambda_{(V+A)_\perp} + 64 v_4 \Big(-\frac{1}{2 N_c} \lambda_{(S+P)_-^{\mathrm{adj}}}^2 + \frac{1}{2} \lambda_{(S+P)_-^{\mathrm{adj}}}^2 + \frac{1}{2} \lambda_{\mathrm{csc}} \lambda_{(S+P)_-^{\mathrm{adj}}} + \frac{1}{2} \lambda_{(\sigma\text{-}\pi)} \lambda_{(S+P)_-^{\mathrm{adj}}}$$

$$+ \lambda_{(S+P)_-} \lambda_{(S+P)_-^{\mathrm{adj}}} - \frac{1}{2 N_c} \lambda_{\mathrm{csc}} \lambda_{(S+P)_-^{\mathrm{adj}}} + \lambda_{(V+A)_\perp}^2 + \lambda_{\mathrm{csc}} \lambda_{(\sigma\text{-}\pi)} + \lambda_{\mathrm{csc}} \lambda_{(S+P)_-}$$

$$- 2 \lambda_{(\sigma\text{-}\pi)} \lambda_{(V-A)_\perp} - \frac{1}{4} \lambda_{(\sigma\text{-}\pi)} \lambda_{(V-A)_\perp^{\mathrm{adj}}} + \lambda_{\mathrm{csc}} \lambda_{(V+A)_\perp} + \lambda_{(V-A)_\parallel} \lambda_{(V+A)_\perp} + \lambda_{(V-A)_\perp} \lambda_{(V+A)_\perp}$$

$$+ \lambda_{(V+A)_\parallel} \lambda_{(V+A)_\perp} - N_c \lambda_{\mathrm{csc}} \lambda_{(V+A)_\perp} + 4 N_c \lambda_{(V-A)_\perp} \lambda_{(V+A)_\perp} + \frac{N_c}{2} \lambda_{(V-A)_\perp^{\mathrm{adj}}} \lambda_{(V+A)_\perp}$$

$$+ \frac{1}{N_c} \lambda_{(\sigma\text{-}\pi)} \lambda_{(V-A)_\perp^{\mathrm{adj}}} - \frac{1}{2 N_c} \lambda_{(V-A)_\perp^{\mathrm{adj}}} \lambda_{(V+A)_\perp} - \frac{1}{2 N_c} \lambda_{(V+A)_\parallel^{\mathrm{adj}}} \lambda_{(V+A)_\perp} \Big) l_{\parallel+}^{(\mathrm{F})}(\tau, 0, -\mathrm{i}\tilde{\mu}_\tau)$$

$$+ 64 v_4 \Big(\lambda_{(V+A)_\perp}^2 - \lambda_{(V+A)_\parallel} \lambda_{(V+A)_\perp} + \frac{1}{2 N_c} \lambda_{(V+A)_\parallel^{\mathrm{adj}}} \lambda_{(V+A)_\perp} + \frac{1}{4} \lambda_{(\sigma\text{-}\pi)} \lambda_{(V+A)_\parallel^{\mathrm{adj}}} \Big) l_{\parallel\pm}^{(\mathrm{F})}(\tau, 0, -\mathrm{i}\tilde{\mu}_\tau)$$

$$+ 64 v_4 \Big(\frac{1}{6} \lambda_{\mathrm{csc}}^2 + \frac{1}{3} \lambda_{(\sigma\text{-}\pi)} \lambda_{\mathrm{csc}} + \frac{1}{3} \lambda_{(S+P)_-} \lambda_{\mathrm{csc}} + \frac{1}{2} \lambda_{(S+P)_-^{\mathrm{adj}}} \lambda_{\mathrm{csc}} + \frac{1}{3} \lambda_{(V+A)_\perp} \lambda_{\mathrm{csc}}$$

$$- \frac{N_c}{3} \lambda_{(V+A)_\perp} \lambda_{\mathrm{csc}} - \frac{1}{6 N_c} \lambda_{(S+P)_-^{\mathrm{adj}}} \lambda_{\mathrm{csc}} + \frac{1}{6} \lambda_{(\sigma\text{-}\pi)}^2 + \frac{2}{3} \lambda_{(S+P)_-}^2 + \frac{1}{2} \lambda_{(S+P)_-^{\mathrm{adj}}}^2 + \frac{1}{6} \lambda_{(V+A)_\parallel}^2$$

$$+ \frac{7}{6} \lambda_{(V+A)_\perp}^2 + \frac{2}{3} \lambda_{(\sigma\text{-}\pi)} \lambda_{(S+P)_-} + \frac{1}{2} \lambda_{(\sigma\text{-}\pi)} \lambda_{(S+P)_-^{\mathrm{adj}}} + \lambda_{(S+P)_-} \lambda_{(S+P)_-^{\mathrm{adj}}} - \frac{2}{3} \lambda_{(\sigma\text{-}\pi)} \lambda_{(V-A)_\perp}$$

$$- \frac{1}{12} \lambda_{(\sigma\text{-}\pi)} \lambda_{(V-A)_\perp^{\mathrm{adj}}} + \frac{1}{3} \lambda_{(V-A)_\parallel} \lambda_{(V+A)_\perp} + \frac{1}{3} \lambda_{(V-A)_\perp} \lambda_{(V+A)_\perp} + \frac{2}{3} \lambda_{(V+A)_\parallel} \lambda_{(V+A)_\perp}$$

$$+ \frac{4}{3} N_c \lambda_{(V-A)_\perp} \lambda_{(V+A)_\perp} + \frac{N_c}{6} \lambda_{(V-A)_\perp^{\mathrm{adj}}} \lambda_{(V+A)_\perp} - \frac{1}{2 N_c} \lambda_{(S+P)_-^{\mathrm{adj}}}^2 - \frac{1}{3 N_c} \lambda_{(\sigma\text{-}\pi)} \lambda_{(S+P)_-^{\mathrm{adj}}}$$

$$- \frac{2}{3 N_c} \lambda_{(S+P)_-} \lambda_{(S+P)_-^{\mathrm{adj}}} + \frac{1}{3 N_c} \lambda_{(\sigma\text{-}\pi)} \lambda_{(V-A)_\perp^{\mathrm{adj}}} - \frac{1}{6 N_c} \lambda_{(V+A)_\parallel} \lambda_{(V+A)_\parallel^{\mathrm{adj}}}$$

$$- \frac{1}{6 N_c} \lambda_{(V-A)_\perp^{\mathrm{adj}}} \lambda_{(V+A)_\perp} - \frac{1}{3 N_c} \lambda_{(V+A)_\parallel^{\mathrm{adj}}} \lambda_{(V+A)_\perp} + \frac{1}{6 N_c^2} \lambda_{(S+P)_-^{\mathrm{adj}}}^2$$

$$+ \frac{1}{24 N_c^2} \lambda_{(V+A)_\parallel^{\mathrm{adj}}}^2 \Big) l_{\perp+}^{(\mathrm{F})}(\tau, 0, -\mathrm{i}\tilde{\mu}_\tau)$$

$$+ 64 v_4 \Big(-\frac{1}{6} \lambda_{(\sigma\text{-}\pi)}^2 - \frac{1}{12} \lambda_{(V+A)_\parallel^{\mathrm{adj}}} \lambda_{(\sigma\text{-}\pi)} - \frac{1}{6} \lambda_{(V+A)_\parallel}^2 - \frac{1}{24} \lambda_{(V+A)_\parallel^{\mathrm{adj}}}^2 - \frac{7}{6} \lambda_{(V+A)_\perp}^2$$

$$+ \frac{2}{3} \lambda_{(V+A)_\parallel} \lambda_{(V+A)_\perp} + \frac{1}{6 N_c} \lambda_{(V+A)_\parallel} \lambda_{(V+A)_\parallel^{\mathrm{adj}}} - \frac{1}{3 N_c} \lambda_{(V+A)_\parallel^{\mathrm{adj}}} \lambda_{(V+A)_\perp}$$

$$- \frac{1}{24 N_c^2} \lambda_{(V+A)_\parallel^{\mathrm{adj}}}^2 \Big) l_{\perp\pm}^{(\mathrm{F})}(\tau, 0, -\mathrm{i}\tilde{\mu}_\tau) \,, \tag{E.9}$$

$$\partial_t \lambda_{(V-A)_\parallel} = 2 \lambda_{(V-A)_\parallel} + 64 v_4 \Big(\frac{1}{2} N_c \lambda_{\mathrm{csc}}^2 - \frac{1}{2} \lambda_{\mathrm{csc}}^2 - \lambda_{(V-A)_\parallel} \lambda_{\mathrm{csc}} - \frac{3}{2} \lambda_{(V-A)_\perp^{\mathrm{adj}}} \lambda_{\mathrm{csc}} + N_c \lambda_{(V-A)_\parallel} \lambda_{\mathrm{csc}}$$

$$+ \frac{3}{2} N_c \lambda_{(V-A)_\perp^{\mathrm{adj}}} \lambda_{\mathrm{csc}} - \frac{1}{2} \lambda_{(\sigma\text{-}\pi)}^2 + \frac{3}{2} \lambda_{(V-A)_\parallel}^2 + \frac{3}{2} \lambda_{(V-A)_\perp}^2 - \frac{1}{2} \lambda_{(V+A)_\parallel^{\mathrm{adj}}}^2 - 3 \lambda_{(V-A)_\parallel} \lambda_{(V-A)_\perp}$$

$$+ \frac{3}{2} \lambda_{(V-A)_\perp} \lambda_{(V-A)_\perp^{\mathrm{adj}}} + 2 \lambda_{(\sigma\text{-}\pi)} \lambda_{(V+A)_\parallel} + \lambda_{(\sigma\text{-}\pi)} \lambda_{(V+A)_\parallel^{\mathrm{adj}}} - 2 N_c \lambda_{(V-A)_\parallel}^2 + \frac{3}{8} N_c \lambda_{(V-A)_\perp^{\mathrm{adj}}}^2$$

$$- 2 N_c \lambda_{(V+A)_\parallel}^2 - \frac{3}{2} N_c \lambda_{(V-A)_\parallel} \lambda_{(V-A)_\perp^{\mathrm{adj}}} - \frac{3}{4 N_c} \lambda_{(V-A)_\perp^{\mathrm{adj}}}^2 + \frac{1}{2 N_c} \lambda_{(V+A)_\parallel^{\mathrm{adj}}}^2$$

$$+ \frac{3}{2 N_c} \lambda_{(V-A)_\parallel} \lambda_{(V-A)_\perp^{\mathrm{adj}}} - \frac{3}{2 N_c} \lambda_{(V-A)_\perp} \lambda_{(V-A)_\perp^{\mathrm{adj}}} - \frac{1}{N_c} \lambda_{(\sigma\text{-}\pi)} \lambda_{(V+A)_\parallel^{\mathrm{adj}}}$$

$$+ \frac{3}{8 N_c^2} \lambda_{(V-A)_\perp^{\mathrm{adj}}}^2 \Big) l_{\parallel+}^{(\mathrm{F})}(\tau, 0, -\mathrm{i}\tilde{\mu}_\tau)$$

$$+ 64 v_4 \Big(- \frac{3}{2} \lambda_{(\sigma\text{-}\pi)}^2 - 6 \lambda_{(S+P)_-} \lambda_{(\sigma\text{-}\pi)} - 3 \lambda_{(S+P)_-^{\mathrm{adj}}} \lambda_{(\sigma\text{-}\pi)} + \frac{3}{N_c} \lambda_{(S+P)_-^{\mathrm{adj}}} \lambda_{(\sigma\text{-}\pi)} - 6 \lambda_{(S+P)_-}^2$$

$$- \frac{3}{2} \lambda_{(S+P)_-^{\mathrm{adj}}}^2 - \frac{1}{2} \lambda_{(V-A)_\parallel}^2 - \frac{3}{2} \lambda_{(V-A)_\perp}^2 - \frac{3}{8} \lambda_{(V-A)_\perp^{\mathrm{adj}}}^2 - 6 \lambda_{(S+P)_-} \lambda_{(S+P)_-^{\mathrm{adj}}}$$

$$- \frac{3}{2} \lambda_{(V-A)_\perp} \lambda_{(V-A)_\perp^{\mathrm{adj}}} + \frac{3}{N_c} \lambda_{(S+P)_-^{\mathrm{adj}}}^2 + \frac{3}{4 N_c} \lambda_{(V-A)_\perp^{\mathrm{adj}}}^2 + \frac{6}{N_c} \lambda_{(S+P)_-} \lambda_{(S+P)_-^{\mathrm{adj}}}$$

$$+ \frac{3}{2 N_c} \lambda_{(V-A)_\perp} \lambda_{(V-A)_\perp^{\mathrm{adj}}} - \frac{3}{2 N_c^2} \lambda_{(S+P)_-^{\mathrm{adj}}}^2 - \frac{3}{8 N_c^2} \lambda_{(V-A)_\perp^{\mathrm{adj}}}^2 \Big) l_{\parallel\pm}^{(\mathrm{F})}(\tau, 0, -\mathrm{i}\tilde{\mu}_\tau)$$

$$+ 64 v_4 \Big(\frac{1}{2} \lambda_{(\sigma\text{-}\pi)}^2 - 2 \lambda_{(V+A)_\parallel} \lambda_{(\sigma\text{-}\pi)} - \lambda_{(V+A)_\parallel^{\mathrm{adj}}} \lambda_{(\sigma\text{-}\pi)} + \frac{1}{N_c} \lambda_{(V+A)_\parallel^{\mathrm{adj}}} \lambda_{(\sigma\text{-}\pi)} - \lambda_{(V-A)_\parallel}^2 - \lambda_{(V-A)_\perp}^2$$

$$+ \frac{1}{2} \lambda_{(V+A)_\parallel^{\mathrm{adj}}}^2 + \lambda_{\mathrm{csc}} \lambda_{(V-A)_\parallel} + 4 \lambda_{(V-A)_\parallel} \lambda_{(V-A)_\perp} + \lambda_{\mathrm{csc}} \lambda_{(V-A)_\perp^{\mathrm{adj}}} + \frac{1}{2} \lambda_{(V-A)_\parallel} \lambda_{(V-A)_\perp^{\mathrm{adj}}}$$

$$- \lambda_{(V-A)_\perp} \lambda_{(V-A)_\perp^{\mathrm{adj}}} + 2 N_c \lambda_{(V-A)_\parallel}^2 - \frac{N_c}{4} \lambda_{(V-A)_\perp^{\mathrm{adj}}}^2 + 2 N_c \lambda_{(V+A)_\parallel}^2 - N_c \lambda_{\mathrm{csc}} \lambda_{(V-A)_\parallel}$$

$$- N_c \lambda_{\mathrm{csc}} \lambda_{(V-A)_\perp^{\mathrm{adj}}} + \frac{3}{2} N_c \lambda_{(V-A)_\parallel} \lambda_{(V-A)_\perp^{\mathrm{adj}}} + \frac{1}{2 N_c} \lambda_{(V-A)_\perp^{\mathrm{adj}}}^2 - \frac{1}{2 N_c} \lambda_{(V+A)_\parallel^{\mathrm{adj}}}^2$$

$$- \frac{2}{N_c} \lambda_{(V-A)_\parallel} \lambda_{(V-A)_\perp^{\mathrm{adj}}} + \frac{1}{N_c} \lambda_{(V-A)_\perp} \lambda_{(V-A)_\perp^{\mathrm{adj}}} - \frac{1}{4 N_c^2} \lambda_{(V-A)_\perp^{\mathrm{adj}}}^2 \Big) l_{\perp+}^{(\mathrm{F})}(\tau, 0, -\mathrm{i}\tilde{\mu}_\tau)$$

$$+ 64 v_4 \Big(\frac{1}{2} \lambda_{(\sigma\text{-}\pi)}^2 + 2 \lambda_{(S+P)_-} \lambda_{(\sigma\text{-}\pi)} + \lambda_{(S+P)_-^{\mathrm{adj}}} \lambda_{(\sigma\text{-}\pi)} - \frac{1}{N_c} \lambda_{(S+P)_-^{\mathrm{adj}}} \lambda_{(\sigma\text{-}\pi)} + 2 \lambda_{(S+P)_-}^2 + \frac{1}{2} \lambda_{(S+P)_-^{\mathrm{adj}}}^2$$

$$- \lambda_{(V-A)_\perp}^2 - \frac{1}{4} \lambda_{(V-A)_\perp^{\mathrm{adj}}}^2 + 2 \lambda_{(S+P)_-} \lambda_{(S+P)_-^{\mathrm{adj}}} - \lambda_{(V-A)_\parallel} \lambda_{(V-A)_\perp} - \frac{1}{2} \lambda_{(V-A)_\parallel} \lambda_{(V-A)_\perp^{\mathrm{adj}}}$$

$$- \lambda_{(V-A)_\perp} \lambda_{(V-A)_\perp^{\mathrm{adj}}} - \frac{1}{N_c} \lambda_{(S+P)_-^{\mathrm{adj}}}^2 + \frac{1}{2 N_c} \lambda_{(V-A)_\perp^{\mathrm{adj}}}^2 - \frac{2}{N_c} \lambda_{(S+P)_-} \lambda_{(S+P)_-^{\mathrm{adj}}}$$

$$+ \frac{1}{2 N_c} \lambda_{(V-A)_\parallel} \lambda_{(V-A)_\perp^{\mathrm{adj}}} + \frac{1}{N_c} \lambda_{(V-A)_\perp} \lambda_{(V-A)_\perp^{\mathrm{adj}}} + \frac{1}{2 N_c^2} \lambda_{(S+P)_-^{\mathrm{adj}}}^2$$

$$- \frac{1}{4 N_c^2} \lambda_{(V-A)_\perp^{\mathrm{adj}}}^2 \Big) l_{\perp\pm}^{(\mathrm{F})}(\tau, 0, -\mathrm{i}\tilde{\mu}_\tau) \,, \tag{E.10}$$

$$\partial_t \lambda_{(V-A)_\perp} = 2 \lambda_{(V-A)_\perp} + 64 v_4 \Big(\frac{N_c}{2} \lambda_{\mathrm{csc}}^2 + \frac{1}{N_c} \lambda_{\mathrm{csc}}^2 - \frac{3}{2} \lambda_{\mathrm{csc}}^2 + \lambda_{(V-A)_\perp} \lambda_{\mathrm{csc}} - \frac{3}{2} \lambda_{(V-A)_\perp^{\mathrm{adj}}} \lambda_{\mathrm{csc}}$$

$$- N_c \lambda_{(V-A)_\perp} \lambda_{\mathrm{csc}} + \frac{N_c}{2} \lambda_{(V-A)_\perp^{\mathrm{adj}}} \lambda_{\mathrm{csc}} + \frac{1}{N_c} \lambda_{(V-A)_\perp^{\mathrm{adj}}} \lambda_{\mathrm{csc}} - \frac{1}{2} \lambda_{(\sigma\text{-}\pi)}^2 - \frac{5}{8} \lambda_{(V-A)_\perp^{\mathrm{adj}}}^2 - \frac{1}{2} \lambda_{(V+A)_\parallel^{\mathrm{adj}}}^2$$

$$+ 2 \lambda_{(V-A)_\parallel} \lambda_{(V-A)_\perp} + \frac{3}{2} \lambda_{(V-A)_\perp} \lambda_{(V-A)_\perp^{\mathrm{adj}}} + \lambda_{(\sigma\text{-}\pi)} \lambda_{(V+A)_\parallel^{\mathrm{adj}}} - 2 \lambda_{(\sigma\text{-}\pi)} \lambda_{(V+A)_\perp} + 2 N_c \lambda_{(V-A)_\perp}^2$$

$$+ \frac{3}{8} N_c \lambda_{(V-A)_\perp^{\mathrm{adj}}}^2 + 2 N_c \lambda_{(V+A)_\perp}^2 + \frac{N_c}{2} \lambda_{(V-A)_\perp} \lambda_{(V-A)_\perp^{\mathrm{adj}}} + \frac{1}{N_c} \lambda_{(\sigma\text{-}\pi)}^2 - \frac{3}{4 N_c} \lambda_{(V-A)_\perp^{\mathrm{adj}}}^2$$

$$+ \frac{1}{2 N_c} \lambda_{(V+A)_\parallel^{\mathrm{adj}}}^2 - \frac{2}{N_c} \lambda_{(V-A)_\perp} \lambda_{(V-A)_\perp^{\mathrm{adj}}} - \frac{1}{N_c} \lambda_{(\sigma\text{-}\pi)} \lambda_{(V+A)_\parallel^{\mathrm{adj}}} + \frac{1}{N_c^2} \lambda_{(V-A)_\perp^{\mathrm{adj}}}^2 \Big) l_{\parallel+}^{(\mathrm{F})}(\tau, 0, -\mathrm{i}\tilde{\mu}_\tau)$$

$$+ 64 v_4 \Big(\frac{1}{N_c} \lambda_{(\sigma\text{-}\pi)}^2 - \frac{1}{2} \lambda_{(\sigma\text{-}\pi)}^2 - 2 \lambda_{(S+P)_-} \lambda_{(\sigma\text{-}\pi)} - \lambda_{(S+P)_-^{\mathrm{adj}}} \lambda_{(\sigma\text{-}\pi)} + \frac{4}{N_c} \lambda_{(S+P)_-} \lambda_{(\sigma\text{-}\pi)}$$

$$
\begin{aligned}
&+\frac{3}{N_c}\lambda_{(S+P)_-^{\mathrm{adj}}}\lambda_{(\sigma\text{-}\pi)} - \frac{2}{N_c^2}\lambda_{(S+P)_-^{\mathrm{adj}}}\lambda_{(\sigma\text{-}\pi)} - 2\lambda_{(S+P)_-}^2 - \frac{1}{2}\lambda_{(S+P)_-^{\mathrm{adj}}}^2 - \lambda_{(V-A)_\perp}^2 - \frac{1}{4}\lambda_{(V-A)_\perp^{\mathrm{adj}}}^2 \\
&-2\lambda_{(S+P)_-}\lambda_{(S+P)_-^{\mathrm{adj}}} - \lambda_{(V-A)_\parallel}\lambda_{(V-A)_\perp} - \frac{3}{2}\lambda_{(V-A)_\perp}\lambda_{(V-A)_\perp^{\mathrm{adj}}} + \frac{4}{N_c}\lambda_{(S+P)_-}^2 + \frac{2}{N_c}\lambda_{(S+P)_-^{\mathrm{adj}}}^2 \\
&+\frac{3}{4N_c}\lambda_{(V-A)_\perp^{\mathrm{adj}}}^2 + \frac{6}{N_c}\lambda_{(S+P)_-}\lambda_{(S+P)_-^{\mathrm{adj}}} + \frac{3}{2N_c}\lambda_{(V-A)_\perp}\lambda_{(V-A)_\perp^{\mathrm{adj}}} - \frac{5}{2N_c^2}\lambda_{(S+P)_-^{\mathrm{adj}}}^2 \\
&-\frac{1}{2N_c^2}\lambda_{(V-A)_\perp^{\mathrm{adj}}}^2 - \frac{4}{N_c^2}\lambda_{(S+P)_-}\lambda_{(S+P)_-^{\mathrm{adj}}} + \frac{1}{N_c^3}\lambda_{(S+P)_-^{\mathrm{adj}}}^2\Big)l_{\parallel\pm}^{(\mathrm{F})}(\tau,0,-\mathrm{i}\tilde\mu_\tau) \\
&+64v_4\Big(-\frac{1}{3N_c}\lambda_{\mathrm{csc}}^2 + \frac{1}{3}\lambda_{\mathrm{csc}}^2 + \frac{1}{3}\lambda_{(V-A)_\perp}\lambda_{\mathrm{csc}} + \lambda_{(V-A)_\perp^{\mathrm{adj}}}\lambda_{\mathrm{csc}} - \frac{N_c}{3}\lambda_{(V-A)_\perp}\lambda_{\mathrm{csc}} \\
&-\frac{N_c}{3}\lambda_{(V-A)_\perp^{\mathrm{adj}}}\lambda_{\mathrm{csc}} - \frac{2}{3N_c}\lambda_{(V-A)_\perp^{\mathrm{adj}}}\lambda_{\mathrm{csc}} + \frac{1}{2}\lambda_{(\sigma\text{-}\pi)}^2 + \frac{1}{6}\lambda_{(V-A)_\parallel}^2 + \frac{3}{2}\lambda_{(V-A)_\perp}^2 + \frac{13}{24}\lambda_{(V-A)_\perp^{\mathrm{adj}}}^2 \\
&+\frac{1}{2}\lambda_{(V+A)_\parallel^{\mathrm{adj}}}^2 - \frac{1}{3}\lambda_{(V-A)_\parallel}\lambda_{(V-A)_\perp} + \frac{1}{2}\lambda_{(V-A)_\parallel}\lambda_{(V-A)_\perp^{\mathrm{adj}}} - \lambda_{(V-A)_\perp}\lambda_{(V-A)_\perp^{\mathrm{adj}}} - \lambda_{(\sigma\text{-}\pi)}\lambda_{(V+A)_\parallel^{\mathrm{adj}}} \\
&-\frac{2}{3}\lambda_{(\sigma\text{-}\pi)}\lambda_{(V+A)_\perp} + \frac{2}{3}N_c\lambda_{(V-A)_\perp}^2 - \frac{N_c}{4}\lambda_{(V-A)_\perp^{\mathrm{adj}}}^2 + \frac{2}{3}N_c\lambda_{(V+A)_\perp}^2 + \frac{N_c}{6}\lambda_{(V-A)_\perp}\lambda_{(V-A)_\perp^{\mathrm{adj}}} \\
&-\frac{1}{3N_c}\lambda_{(\sigma\text{-}\pi)}^2 + \frac{1}{2N_c}\lambda_{(V-A)_\perp^{\mathrm{adj}}}^2 - \frac{1}{2N_c}\lambda_{(V+A)_\parallel^{\mathrm{adj}}}^2 - \frac{1}{2N_c}\lambda_{(V-A)_\parallel}\lambda_{(V-A)_\perp^{\mathrm{adj}}} \\
&+\frac{5}{6N_c}\lambda_{(V-A)_\perp}\lambda_{(V-A)_\perp^{\mathrm{adj}}} + \frac{1}{N_c}\lambda_{(\sigma\text{-}\pi)}\lambda_{(V+A)_\parallel^{\mathrm{adj}}} - \frac{19}{24N_c^2}\lambda_{(V-A)_\perp^{\mathrm{adj}}}^2\Big)l_{\perp+}^{(\mathrm{F})}(\tau,0,-\mathrm{i}\tilde\mu_\tau) \\
&+64v_4\Big(-\frac{1}{3N_c}\lambda_{(\sigma\text{-}\pi)}^2 + \frac{1}{6}\lambda_{(\sigma\text{-}\pi)}^2 + \frac{2}{3}\lambda_{(S+P)_-}\lambda_{(\sigma\text{-}\pi)} + \frac{1}{3}\lambda_{(S+P)_-^{\mathrm{adj}}}\lambda_{(\sigma\text{-}\pi)} - \frac{4}{3N_c}\lambda_{(S+P)_-}\lambda_{(\sigma\text{-}\pi)} \\
&-\frac{1}{N_c}\lambda_{(S+P)_-^{\mathrm{adj}}}\lambda_{(\sigma\text{-}\pi)} + \frac{2}{3N_c^2}\lambda_{(S+P)_-^{\mathrm{adj}}}\lambda_{(\sigma\text{-}\pi)} + \frac{2}{3}\lambda_{(S+P)_-}^2 + \frac{1}{6}\lambda_{(S+P)_-^{\mathrm{adj}}}^2 - \frac{1}{6}\lambda_{(V-A)_\parallel}^2 - \frac{7}{6}\lambda_{(V-A)_\perp}^2 \\
&-\frac{7}{24}\lambda_{(V-A)_\perp^{\mathrm{adj}}}^2 + \frac{2}{3}\lambda_{(S+P)_-}\lambda_{(S+P)_-^{\mathrm{adj}}} - \frac{2}{3}\lambda_{(V-A)_\parallel}\lambda_{(V-A)_\perp} - \frac{1}{2}\lambda_{(V-A)_\parallel}\lambda_{(V-A)_\perp^{\mathrm{adj}}} \\
&-\lambda_{(V-A)_\perp}\lambda_{(V-A)_\perp^{\mathrm{adj}}} - \frac{4}{3N_c}\lambda_{(S+P)_-}^2 - \frac{2}{3N_c}\lambda_{(S+P)_-^{\mathrm{adj}}}^2 + \frac{1}{2N_c}\lambda_{(V-A)_\perp^{\mathrm{adj}}}^2 - \frac{2}{N_c}\lambda_{(S+P)_-}\lambda_{(S+P)_-^{\mathrm{adj}}} \\
&+\frac{1}{2N_c}\lambda_{(V-A)_\parallel}\lambda_{(V-A)_\perp^{\mathrm{adj}}} + \frac{1}{N_c}\lambda_{(V-A)_\perp}\lambda_{(V-A)_\perp^{\mathrm{adj}}} + \frac{5}{6N_c^2}\lambda_{(S+P)_-^{\mathrm{adj}}}^2 - \frac{5}{24N_c^2}\lambda_{(V-A)_\perp^{\mathrm{adj}}}^2 \\
&+\frac{4}{3N_c^2}\lambda_{(S+P)_-}\lambda_{(S+P)_-^{\mathrm{adj}}} - \frac{1}{3N_c^3}\lambda_{(S+P)_-^{\mathrm{adj}}}^2\Big)l_{\perp\pm}^{(\mathrm{F})}(\tau,0,-\mathrm{i}\tilde\mu_\tau)\,, \tag{E.11}
\end{aligned}
$$

$$
\begin{aligned}
\partial_t\lambda_{(V+A)_\parallel^{\mathrm{adj}}} =\ & 2\lambda_{(V+A)_\parallel^{\mathrm{adj}}} + 64v_4\Big(2N_c\lambda_{\mathrm{csc}}\lambda_{(S+P)_-^{\mathrm{adj}}} - \frac{2}{N_c}\lambda_{\mathrm{csc}}\lambda_{(S+P)_-^{\mathrm{adj}}} + N_c\lambda_{\mathrm{csc}}^2 - \frac{2}{N_c}\lambda_{(\sigma\text{-}\pi)}\lambda_{(V-A)_\perp^{\mathrm{adj}}} \\
&+N_c\lambda_{(S+P)_-^{\mathrm{adj}}}^2 - \frac{2}{N_c}\lambda_{(S+P)_-^{\mathrm{adj}}}^2 + \frac{3}{2N_c}\lambda_{(V-A)_\perp^{\mathrm{adj}}}\lambda_{(V+A)_\parallel^{\mathrm{adj}}} + \frac{N_c}{4}\lambda_{(V+A)_\parallel^{\mathrm{adj}}}^2 - \frac{1}{2N_c}\lambda_{(V+A)_\parallel^{\mathrm{adj}}}^2 \\
&+4\lambda_{\mathrm{csc}}\lambda_{(\sigma\text{-}\pi)} + 4\lambda_{\mathrm{csc}}\lambda_{(S+P)_-} - 2\lambda_{\mathrm{csc}}\lambda_{(S+P)_-^{\mathrm{adj}}} - \lambda_{\mathrm{csc}}\lambda_{(V+A)_\parallel^{\mathrm{adj}}} - 2\lambda_{\mathrm{csc}}^2 + 2\lambda_{(\sigma\text{-}\pi)}\lambda_{(S+P)_-^{\mathrm{adj}}} \\
&+4\lambda_{(\sigma\text{-}\pi)}\lambda_{(V-A)_\perp} + 2\lambda_{(\sigma\text{-}\pi)}\lambda_{(V-A)_\perp^{\mathrm{adj}}} + 4\lambda_{(S+P)_-}\lambda_{(S+P)_-^{\mathrm{adj}}} + \lambda_{(V-A)_\parallel}\lambda_{(V+A)_\parallel^{\mathrm{adj}}} \\
&-3\lambda_{(V-A)_\perp}\lambda_{(V+A)_\parallel^{\mathrm{adj}}} + \lambda_{(V+A)_\parallel}\lambda_{(V+A)_\parallel^{\mathrm{adj}}} - \lambda_{(V+A)_\parallel^{\mathrm{adj}}}\lambda_{(V+A)_\perp}\Big)l_{\parallel+}^{(\mathrm{F})}(\tau,0,-\mathrm{i}\tilde\mu_\tau) \\
&+64v_4\Big(\frac{1}{2N_c}\lambda_{(V+A)_\parallel^{\mathrm{adj}}}^2 + 4\lambda_{(\sigma\text{-}\pi)}\lambda_{(V+A)_\perp} - \lambda_{(V+A)_\parallel}\lambda_{(V+A)_\parallel^{\mathrm{adj}}} + \lambda_{(V+A)_\parallel^{\mathrm{adj}}}\lambda_{(V+A)_\perp}\Big)l_{\parallel\pm}^{(\mathrm{F})}(\tau,0,-\mathrm{i}\tilde\mu_\tau) \\
&+64v_4\Big(-\frac{2}{3}N_c\lambda_{\mathrm{csc}}\lambda_{(S+P)_-^{\mathrm{adj}}} + \frac{2}{3N_c}\lambda_{\mathrm{csc}}\lambda_{(S+P)_-^{\mathrm{adj}}} - \frac{N_c}{3}\lambda_{\mathrm{csc}}^2 + \frac{4}{3N_c}\lambda_{(\sigma\text{-}\pi)}\lambda_{(V-A)_\perp^{\mathrm{adj}}} \\
&-\frac{N_c}{3}\lambda_{(S+P)_-^{\mathrm{adj}}}^2 + \frac{2}{3N_c}\lambda_{(S+P)_-^{\mathrm{adj}}}^2 - \frac{3}{2N_c}\lambda_{(V-A)_\perp^{\mathrm{adj}}}\lambda_{(V+A)_\parallel^{\mathrm{adj}}} - \frac{N_c}{12}\lambda_{(V+A)_\parallel^{\mathrm{adj}}}^2 + \frac{1}{6N_c}\lambda_{(V+A)_\parallel^{\mathrm{adj}}}^2 \\
&-\frac{4}{3}\lambda_{\mathrm{csc}}\lambda_{(\sigma\text{-}\pi)} - \frac{4}{3}\lambda_{\mathrm{csc}}\lambda_{(S+P)_-} + \frac{2}{3}\lambda_{\mathrm{csc}}\lambda_{(S+P)_-^{\mathrm{adj}}} + \lambda_{\mathrm{csc}}\lambda_{(V+A)_\parallel^{\mathrm{adj}}} + \frac{2}{3}\lambda_{\mathrm{csc}}^2 - \frac{2}{3}\lambda_{(\sigma\text{-}\pi)}\lambda_{(S+P)_-^{\mathrm{adj}}}
\end{aligned}
$$

$$
\begin{aligned}
&+ \frac{4}{3}\lambda_{(\sigma\text{-}\pi)}\lambda_{(V-A)_\parallel} - \frac{8}{3}\lambda_{(\sigma\text{-}\pi)}\lambda_{(V-A)_\perp} + \frac{2}{3}\lambda_{(\sigma\text{-}\pi)}\lambda_{(V-A)_\perp^{\mathrm{adj}}} - \frac{4}{3}\lambda_{(S+P)_-}\lambda_{(S+P)_-^{\mathrm{adj}}} - \lambda_{(V-A)_\parallel}\lambda_{(V+A)_\parallel^{\mathrm{adj}}} \\
&+ 3\lambda_{(V-A)_\perp}\lambda_{(V+A)_\parallel^{\mathrm{adj}}} - \frac{1}{3}\lambda_{(V+A)_\parallel}\lambda_{(V+A)_\parallel^{\mathrm{adj}}} + \frac{1}{3}\lambda_{(V+A)_\parallel^{\mathrm{adj}}}\lambda_{(V+A)_\perp}\Big) l_{\perp+}^{(\mathrm{F})}(\tau,0,-\mathrm{i}\tilde\mu_\tau) \\
&+ 64 v_4 \Big(-\frac{2}{3N_c}\lambda_{(\sigma\text{-}\pi)}\lambda_{(V+A)_\parallel^{\mathrm{adj}}} - \frac{1}{6N_c}\lambda_{(V+A)_\parallel^{\mathrm{adj}}}^2 + \frac{4}{3}\lambda_{(\sigma\text{-}\pi)}\lambda_{(V+A)_\parallel} - \frac{8}{3}\lambda_{(\sigma\text{-}\pi)}\lambda_{(V+A)_\perp} \\
&+ \frac{1}{3}\lambda_{(V+A)_\parallel}\lambda_{(V+A)_\parallel^{\mathrm{adj}}} - \frac{5}{3}\lambda_{(V+A)_\parallel^{\mathrm{adj}}}\lambda_{(V+A)_\perp}\Big) l_{\perp\pm}^{(\mathrm{F})}(\tau,0,-\mathrm{i}\tilde\mu_\tau)\,,
\end{aligned}
\tag{E.12}
$$

$$
\begin{aligned}
\partial_t \lambda_{(V-A)_\perp^{\mathrm{adj}}} = \; & 2\lambda_{(V-A)_\perp^{\mathrm{adj}}} + 64 v_4 \Big(-2N_c\lambda_{\mathrm{csc}}\lambda_{(V-A)_\perp^{\mathrm{adj}}} - N_c\lambda_{\mathrm{csc}}^2 - \frac{5}{4}N_c\lambda_{(V-A)_\perp^{\mathrm{adj}}}^2 + \frac{2}{N_c}\lambda_{(V-A)_\perp^{\mathrm{adj}}}^2 \\
& + 3\lambda_{\mathrm{csc}}\lambda_{(V-A)_\perp^{\mathrm{adj}}} + 2\lambda_{\mathrm{csc}}^2 - 2\lambda_{(\sigma\text{-}\pi)}\lambda_{(V+A)_\parallel^{\mathrm{adj}}} + 2\lambda_{(\sigma\text{-}\pi)}^2 + 2\lambda_{(V-A)_\parallel}\lambda_{(V-A)_\perp^{\mathrm{adj}}} \\
& - 4\lambda_{(V-A)_\perp}\lambda_{(V-A)_\perp^{\mathrm{adj}}} + \lambda_{(V-A)_\perp^{\mathrm{adj}}}^2 + \lambda_{(V+A)_\parallel^{\mathrm{adj}}}^2 \Big) l_{\parallel+}^{(\mathrm{F})}(\tau,0,-\mathrm{i}\tilde\mu_\tau) \\
& + 64 v_4 \Big(-\frac{4}{N_c}\lambda_{(\sigma\text{-}\pi)}\lambda_{(S+P)_-^{\mathrm{adj}}} - \frac{8}{N_c}\lambda_{(S+P)_-}\lambda_{(S+P)_-^{\mathrm{adj}}} - \frac{4}{N_c}\lambda_{(S+P)_-^{\mathrm{adj}}}^2 + \frac{2}{N_c^2}\lambda_{(S+P)_-^{\mathrm{adj}}}^2 \\
& - \frac{1}{2N_c}\lambda_{(V-A)_\perp^{\mathrm{adj}}}^2 + 8\lambda_{(\sigma\text{-}\pi)}\lambda_{(S+P)_-} + 4\lambda_{(\sigma\text{-}\pi)}\lambda_{(S+P)_-^{\mathrm{adj}}} + 2\lambda_{(\sigma\text{-}\pi)}^2 + 8\lambda_{(S+P)_-}\lambda_{(S+P)_-^{\mathrm{adj}}} \\
& + 8\lambda_{(S+P)_-}^2 + 2\lambda_{(S+P)_-^{\mathrm{adj}}}^2 - \lambda_{(V-A)_\parallel}\lambda_{(V-A)_\perp^{\mathrm{adj}}} + \lambda_{(V-A)_\perp}\lambda_{(V-A)_\perp^{\mathrm{adj}}}\Big) l_{\parallel\pm}^{(\mathrm{F})}(\tau,0,-\mathrm{i}\tilde\mu_\tau) \\
& + 64 v_4 \Big(\frac{4}{3}N_c\lambda_{\mathrm{csc}}\lambda_{(V-A)_\perp^{\mathrm{adj}}} + \frac{N_c}{3}\lambda_{\mathrm{csc}}^2 + \frac{13}{12}N_c\lambda_{(V-A)_\perp^{\mathrm{adj}}}^2 - \frac{7}{3N_c}\lambda_{(V-A)_\perp^{\mathrm{adj}}}^2 - \lambda_{\mathrm{csc}}\lambda_{(V-A)_\perp^{\mathrm{adj}}} \\
& - \frac{2}{3}\lambda_{\mathrm{csc}}^2 + 2\lambda_{(\sigma\text{-}\pi)}\lambda_{(V+A)_\parallel^{\mathrm{adj}}} - \frac{2}{3}\lambda_{(\sigma\text{-}\pi)}^2 - \frac{4}{3}\lambda_{(V-A)_\parallel}\lambda_{(V-A)_\perp^{\mathrm{adj}}} + \frac{14}{3}\lambda_{(V-A)_\perp}\lambda_{(V-A)_\perp^{\mathrm{adj}}} \\
& + \frac{1}{3}\lambda_{(V-A)_\perp^{\mathrm{adj}}}^2 - \lambda_{(V+A)_\parallel^{\mathrm{adj}}}^2 \Big) l_{\perp+}^{(\mathrm{F})}(\tau,0,-\mathrm{i}\tilde\mu_\tau) \\
& + 64 v_4 \Big(\frac{4}{3N_c}\lambda_{(\sigma\text{-}\pi)}\lambda_{(S+P)_-^{\mathrm{adj}}} + \frac{8}{3N_c}\lambda_{(S+P)_-}\lambda_{(S+P)_-^{\mathrm{adj}}} + \frac{4}{3N_c}\lambda_{(S+P)_-^{\mathrm{adj}}}^2 - \frac{2}{3N_c^2}\lambda_{(S+P)_-^{\mathrm{adj}}}^2 \\
& + \frac{1}{6N_c}\lambda_{(V-A)_\perp^{\mathrm{adj}}}^2 - \frac{8}{3}\lambda_{(\sigma\text{-}\pi)}\lambda_{(S+P)_-} - \frac{4}{3}\lambda_{(\sigma\text{-}\pi)}\lambda_{(S+P)_-^{\mathrm{adj}}} - \frac{2}{3}\lambda_{(\sigma\text{-}\pi)}^2 - \frac{8}{3}\lambda_{(S+P)_-}\lambda_{(S+P)_-^{\mathrm{adj}}} \\
& - \frac{8}{3}\lambda_{(S+P)_-}^2 - \frac{2}{3}\lambda_{(S+P)_-^{\mathrm{adj}}}^2 + \frac{1}{3}\lambda_{(V-A)_\parallel}\lambda_{(V-A)_\perp^{\mathrm{adj}}} \\
& - \frac{1}{3}\lambda_{(V-A)_\perp}\lambda_{(V-A)_\perp^{\mathrm{adj}}}\Big) l_{\perp\pm}^{(\mathrm{F})}(\tau,0,-\mathrm{i}\tilde\mu_\tau)\,.
\end{aligned}
\tag{E.13}
$$

Bibliography

[1] L. N. Cooper. "Bound electron pairs in a degenerate Fermi gas". In: *Phys. Rev.* 104 (1956), pp. 1189–1190.

[2] J. Bardeen, L. N. Cooper, and J. R. Schrieffer. "Theory of superconductivity". In: *Phys. Rev.* 108 (1957), pp. 1175–1204.

[3] J. Bardeen, L. N. Cooper, and J. R. Schrieffer. "Microscopic theory of superconductivity". In: *Phys. Rev.* 106 (1957), p. 162.

[4] H. Fritzsch, M. Gell-Mann, and H. Leutwyler. "Advantages of the color octet gluon picture". In: *Phys. Lett.* B47 (1973), pp. 365–368.

[5] C. N. Yang and R. L. Mills. "Conservation of Isotopic Spin and Isotopic Gauge Invariance". In: *Phys. Rev.* 96 (Oct. 1954), pp. 191–195.

[6] D. J. Gross and F. Wilczek. "Ultraviolet behavior of non-abelian gauge theoriess". In: *Phys. Rev. Lett.* 30 (1973), pp. 1343–1346.

[7] H. D. Politzer. "Reliable perturbative results for strong interactions?" In: *Phys. Rev. Lett.* 30 (1973), pp. 1346–1349.

[8] M. Gell-Mann. "A Schematic Model of Baryons and Mesons". In: *Phys. Lett.* 8 (1964), pp. 214–215.

[9] H. T. Ding et al. "The chiral phase transition temperature in (2+1)-flavor QCD". In: *arXiv e-prints* (2019). arXiv: `1903.04801` [`hep-lat`].

[10] F. Karsch. "Critical behavior and net-charge fluctuations from lattice QCD". In: *arXiv e-prints* (2019). arXiv: `1905.03936` [`hep-lat`].

[11] G. Boyd et al. "Thermodynamics of SU(3) lattice gauge theory". In: *Nuc. Phys* B469.3 (1996), pp. 419–444. arXiv: `hep-lat/9602007` [`hep-lat`].

[12] J. Engels et al. "High Temperature SU(2) Gluon Matter on the Lattice". In: *Phys. Lett.* B101 (1981). [,293(1980)], p. 89.

[13] L. D. McLerran and B. Svetitsky. "Quark liberation at high temperature: A Monte Carlo study of SU(2) gauge theory". In: *Phys. Rev.* D24 (2 1981), pp. 450–460.

[14] R. Hagedorn. "Statistical thermodynamics of strong interactions at high-energies". In: *Nuovo Cim. Suppl.* 3 (1965), pp. 147–186.

[15] D. Boyanovsky, H. J. de Vega, and D. J. Schwarz. "Phase Transitions in the Early and Present Universe". In: *Annu. Rev. Nucl. Part. S.* 56.1 (2006), pp. 441–500. arXiv: `hep-ph/0602002` [`hep-ph`].

[16] K. G. Wilson. "Confinement of quarks". In: *Phys. Rev.* D10 (1974), pp. 2445–2459.

[17] T. Kugo and I. Ojima. "Local covariant operator formalism of nonabelian gauge theories and quark confinement problem". In: *Prog. Theor. Phys. Suppl.* 66 (1979), p. 1.

[18] J. Braun. "Functional renormalization group methods in quantum chromodynamics". PhD thesis. Heidelberg U., 2006.

[19]   J. Braun and H. Gies. "Running coupling at finite temperature and chiral symmetry restoration in QCD". In: *Phys. Lett.* B645 (2007), pp. 53–58. arXiv: `hep-ph/0512085`.

[20]   J. Braun and H. Gies. "Chiral phase boundary of QCD at finite temperature". In: *J. High Energy Phys.* 06 (2006), p. 024. arXiv: `hep-ph/0602226`.

[21]   H. Gies and J. Jaeckel. "Chiral phase structure of QCD with many flavors". In: *Eur. Phys. J.* C46 (2006), pp. 433–438. eprint: `hep-ph/0507171`.

[22]   H. Gies and C. Wetterich. "Renormalization flow of bound states". In: *Phys. Rev.* D65 (2002), p. 065001. eprint: `hep-th/0107221`.

[23]   M. Mitter, J. M. Pawlowski, and N. Strodthoff. "Chiral symmetry breaking in continuum QCD". In: *Phys. Rev.* D91 (2015), p. 054035. arXiv: `1411.7978 [hep-ph]`.

[24]   G. Aarts. "Introductory lectures on lattice QCD at nonzero baryon number". In: *J. Phys. Conf. Ser.* Vol. 706. J. Phys. Conf. Ser. 2016, p. 022004. arXiv: `1512.05145 [hep-lat]`.

[25]   Y. Nambu and G. Jona-Lasinio. "Dynamical model of elementary particles based on an analogy with superconductivity. II". In: *Phys. Rev.* 124 (1961), pp. 246–254.

[26]   Y. Nambu and G. Jona-Lasinio. "Dynamical model of elementary particles based on an analogy with superconductivity. I". In: *Phys. Rev.* 122 (1961), pp. 345–358.

[27]   S. P. Klevansky. "The Nambu-Jona-Lasinio model of quantum chromodynamics". In: *Rev. Mod. Phys.* 64 (1992), pp. 649–708.

[28]   M. Buballa. "NJL model analysis of quark matter at large density". In: *Phys. Rept.* 407 (2005), pp. 205–376. arXiv: `hep-ph/0402234 [hep-ph]`.

[29]   K. Fukushima. "QCD matter in extreme environments". In: *J. Phys.* G39 (2012), p. 013101. arXiv: `1108.2939 [hep-ph]`.

[30]   J. O. Andersen, W. R. Naylor, and A. Tranberg. "Phase diagram of QCD in a magnetic field: A review". In: *Rev. Mod. Phys.* 88 (2016), p. 025001. arXiv: `1411.7176 [hep-ph]`.

[31]   R. Anglani et al. "Crystalline color superconductors". In: *Rev. Mod. Phys.* 86 (2014), pp. 509–561. arXiv: `1302.4264 [hep-ph]`.

[32]   D. Bailin and A. Love. "Superfluidity and Superconductivity in Relativistic Fermion Systems". In: *Phys. Rept.* 107 (1984), p. 325.

[33]   M. G. Alford, K. Rajagopal, and F. Wilczek. "QCD at finite baryon density: Nucleon droplets and color superconductivity". In: *Phys. Lett.* B422 (1998), pp. 247–256. arXiv: `hep-ph/9711395 [hep-ph]`.

[34]   M. Alford, J. A. Bowers, and K. Rajagopal. "Crystalline color superconductivity". In: *Phys. Rev. D* 63 (7 2001), p. 074016.

[35]   M. G. Alford et al. "Color superconductivity in dense quark matter". In: *Rev. Mod. Phys.* 80 (2008), pp. 1455–1515. arXiv: `0709.4635 [hep-ph]`.

[36]   P. W. Anderson. "Plasmons, Gauge Invariance, and Mass". In: *Phys. Rev.* 130 (Apr. 1963), pp. 439–442.

[37]   P. W. Higgs. "Broken Symmetries and the Masses of Gauge Bosons". In: *Phys. Rev. Lett.* 13 (Oct. 1964), pp. 508–509.

[38]   F. Englert and R. Brout. "Broken Symmetry and the Mass of Gauge Vector Mesons". In: *Phys. Rev. Lett.* 13 (Aug. 1964), pp. 321–323.

[39]   G. S. Guralnik, C. R. Hagen, and T. W. Kibble. "Global Conservation Laws and Massless Particles". In: *Phys. Rev. Lett.* 13 (Nov. 1964), pp. 585–587.

[40]   D. H. Rischke. "Debye screening and the Meissner effect in a two-flavor color superconductor". In: *Phys. Rev. D62* (3 2000), p. 034007.

[41]   W. Meissner and R. Ochsenfeld. "Ein neuer Effekt bei Eintritt der Supraleitfähigkeit". In: *Naturwissenschaften* 21 (Nov. 1933), pp. 787–788.

[42]   I. Workshop on Hadronic Matter at Extreme Energy Density (1978 : Erice, N Cabibbo, and. Sertorio Luigi. *Hadronic matter at extreme energy density*. English. Conference Proceedings. "Proceedings of the Workshop on Hadronic Matter at Extreme Energy Density, held at ... Erice, Italy, October 13-21, 1978.". 1980.

[43]   B. C. Barrois. "Superconducting quark matter". In: *Nucl. Phys.* B129.3 (1977), pp. 390 –396. ISSN: 0550-3213.

[44]   G. Baym et al. "From hadrons to quarks in neutron stars: a review". In: *Rep. Prog. Phys.* 81.5, 056902 (2018), p. 056902. arXiv: 1707.04966 [astro-ph.HE].

[45]   J. M. Lattimer and M. Prakash. "The Physics of Neutron Stars". In: *Science* 304.5670 (2004), pp. 536–542. arXiv: astro-ph/0405262 [astro-ph].

[46]   M. McNeil Forbes et al. "Constraining the neutron-matter equation of state with gravitational waves". In: *arXiv e-prints* (2019). arXiv: 1904.04233 [astro-ph.HE].

[47]   T. Hinderer et al. "Tidal deformability of neutron stars with realistic equations of state and their gravitational wave signatures in binary inspiral". In: *Phys. Rev.* D81.12, 123016 (2010), p. 123016. arXiv: 0911.3535 [astro-ph.HE].

[48]   S. De et al. "Tidal Deformabilities and Radii of Neutron Stars from the Observation of GW170817". In: *Phys. Rev. Lett.* 121 (9 2018), p. 091102.

[49]   S. Han and A. W. Steiner. "Tidal deformability with sharp phase transitions in binary neutron stars". In: *Phys. Rev.* D99.8, 083014 (2019), p. 083014. arXiv: 1810.10967 [nucl-th].

[50]   A. L. Watts et al. "Colloquium: Measuring the neutron star equation of state using x-ray timing". In: *Rev. Mod. Phys.* 88 (2 2016), p. 021001.

[51]   K. C. Gendreau et al. *The Neutron star Interior Composition Explorer (NICER): design and development*. 2016.

[52]   M. Coleman Miller and F. K. Lamb. "Observational constraints on neutron star masses and radii". In: *Eur. Phys. J.* A52.3 (2016), p. 63. ISSN: 1434-601X.

[53]   M. C. Miller. "THE CASE FOR PSR J1614−2230 AS ANICERTARGET". In: *Astrophys. J.* 822.1 (2016), p. 27.

[54]   M. Leonhardt et al. "Symmetric nuclear matter from the strong interaction". In: *arXiv e-prints* (2019). arXiv: 1907.05814 [nucl-th].

[55]   C. Drischler, K. Hebeler, and A. Schwenk. "Asymmetric nuclear matter based on chiral two- and three-nucleon interactions". In: *Phys. Rev.* C 93.5, 054314 (2016), p. 054314. arXiv: 1510.06728 [nucl-th].

[56]   C. Drischler, K. Hebeler, and A. Schwenk. "Chiral interactions up to next-to-next-to-next-to-leading order and nuclear saturation". In: *arXiv e-prints* (2017). arXiv: 1710.08220 [nucl-th].

[57]   C. Drischler et al. "Neutron matter from chiral two- and three-nucleon calculations up to N^{3}LO". In: *Phys. Rev.* C94.5, 054307 (2016), p. 054307. arXiv: 1608.05615 [nucl-th].

[58]   K. Hebeler et al. "Equation of State and Neutron Star Properties Constrained by Nuclear Physics and Observation". In: *Astrophys. Jour.* 773.1, 11 (2013), p. 11. arXiv: 1303.4662 [astro-ph.SR].

[59]   A. Kurkela, P. Romatschke, and A. Vuorinen. "Cold quark matter". In: *Phys. Rev.* 81.10, 105021 (2010), p. 105021. arXiv: 0912.1856 [hep-ph].

[60]   T. Gorda et al. "NNNLO pressure of cold quark matter: leading logarithm". In: *arXiv e-prints* (2018). arXiv: 1807.04120 [hep-ph].

[61] I. Ghişoiu et al. "On high-order perturbative calculations at finite density". In: *Nucl. Phys.* B915 (2017), pp. 102–118. arXiv: `1609.04339 [hep-ph]`.

[62] E. Annala et al. "Quark-matter cores in neutron stars". In: *arXiv e-prints* (2019). arXiv: `1903.09121 [astro-ph.HE]`.

[63] C. Wetterich. "Exact evolution equation for the effective potential". In: *Phys. Lett.* B301 (1993), pp. 90–94.

[64] T. R. Morris. "The Exact renormalization group and approximate solutions". In: *Int. J. Mod. Phys.* A9 (1994), pp. 2411–2450. arXiv: `hep-ph/9308265`.

[65] A. Schwenk and J. Polonyi. "Towards Density Functional Calculations from Nuclear Forces". In: *nucl-th/0403011* (2004). arXiv: `nucl-th/0403011`.

[66] J. Polonyi and K. Sailer. "Effective action and density-functional theory". In: *Phys. Rev.* B66, 155113 (2002), p. 155113. arXiv: `cond-mat/0108179 [cond-mat.str-el]`.

[67] B. Borasoy et al. "Lattice Simulations for Light Nuclei: Chiral Effective Field Theory at Leading Order". In: *Eur. Phys. J.* A31 (2007), pp. 105–123. arXiv: `nucl-th/0611087 [nucl-th]`.

[68] E. Epelbaum, H.-W. Hammer, and U.-G. Meissner. "Modern Theory of Nuclear Forces". In: *Rev. Mod. Phys.* 81 (2009), pp. 1773–1825. arXiv: `0811.1338 [nucl-th]`.

[69] P. Navratil et al. "Recent developments in no-core shell-model calculations". In: *J. Phys.* G36 (2009), p. 083101. arXiv: `0904.0463 [nucl-th]`.

[70] R. Machleidt and D. R. Entem. "Chiral effective field theory and nuclear forces". In: *Phys. Rept.* 503 (2011), pp. 1–75. arXiv: `1105.2919 [nucl-th]`.

[71] S. Quaglioni et al. "No-Core Shell Model Analysis of Light Nuclei". In: *Few Body Syst.* 54 (2013), pp. 877–884. arXiv: `1210.2020 [nucl-th]`.

[72] H.-W. Hammer, A. Nogga, and A. Schwenk. "Three-body forces: From cold atoms to nuclei". In: *Rev. Mod. Phys.* 85 (2013), p. 197. arXiv: `1210.4273 [nucl-th]`.

[73] T. A. Lähde et al. "Lattice Effective Field Theory for Medium-Mass Nuclei". In: *Phys. Lett.* B732 (2014), pp. 110–115. arXiv: `1311.0477 [nucl-th]`.

[74] V. Somà, C. Barbieri, and T. Duguet. "Ab initio self-consistent Gorkov-Green's function calculations of semi-magic nuclei: Numerical implementation at second order with a two-nucleon interaction". In: *Phys. Rev.* C89.2 (2014), p. 024323. arXiv: `1311.1989 [nucl-th]`.

[75] G. Hagen et al. "Coupled-cluster computations of atomic nuclei". In: *Rept. Prog. Phys.* 77.9 (2014), p. 096302. arXiv: `1312.7872 [nucl-th]`.

[76] K. Hebeler et al. "Nuclear forces and their impact on neutron-rich nuclei and neutron-rich matter". In: *Ann. Rev. Nucl. Part. Sci.* 65 (2015), pp. 457–484. arXiv: `1508.06893 [nucl-th]`.

[77] J. E. Lynn et al. "Chiral Three-Nucleon Interactions in Light Nuclei, Neutron-α Scattering, and Neutron Matter". In: *Phys. Rev. Lett.* 116.6 (2016), p. 062501. arXiv: `1509.03470 [nucl-th]`.

[78] E. Epelbaum et al. "Few- and many-nucleon systems with semilocal coordinate-space regularized chiral two- and three-body forces". In: *Phys. Rev.* C99.2, 024313 (2019), p. 024313. arXiv: `1807.02848 [nucl-th]`.

[79] F. Wegner. "Flow-equations for Hamiltonians". In: *Ann. Phys.* 506.2 (1994), pp. 77–91. eprint: `https://onlinelibrary.wiley.com/doi/pdf/10.1002/andp.19945060203`.

[80] K. Tsukiyama, S. Bogner, and A. Schwenk. "In-Medium Similarity Renormalization Group for Nuclei". In: *Phys. Rev. Lett.* 106 (2011), p. 222502. arXiv: `1006.3639 [nucl-th]`.

[81] T. D. Morris, N. M. Parzuchowski, and S. K. Bogner. "Magnus expansion and in-medium similarity renormalization group". In: *Phys. Rev.* C92 (3 2015), p. 034331.

[82] H. Hergert et al. "In-medium similarity renormalization group with chiral two- plus three-nucleon interactions". In: *Phys. Rev.* C87.3 (2013). arXiv: 1212.1190 [nucl-th].

[83] H. Hergert et al. "The In-Medium Similarity Renormalization Group: A Novel Ab Initio Method for Nuclei". In: *Phys. Rept.* 621 (2016), pp. 165–222. arXiv: 1512.06956 [nucl-th].

[84] H. Hergert. "In-medium similarity renormalization group for closed and open-shell nuclei". In: *Phys. Scr.* 92.2 (2017). arXiv: 1607.06882 [nucl-th].

[85] A. Tichai et al. "Hartree–Fock many-body perturbation theory for nuclear ground-states". In: *Phys. Lett.* B756 (2016), pp. 283 –288. ISSN: 0370-2693.

[86] A. Tichai et al. "Open-shell nuclei from No-Core Shell Model with perturbative improvement". In: *Phys. Lett.* B786 (2018), pp. 448 –452. ISSN: 0370-2693.

[87] B. S. Hu et al. "Ab initio nuclear many-body perturbation calculations in the Hartree-Fock basis". In: *Phys. Rev.* C94 (1 2016), p. 014303.

[88] A. Tichai et al. "Bogoliubov many-body perturbation theory for open-shell nuclei". In: *Phys. Lett.* B786 (2018), pp. 195–200. arXiv: 1806.10931 [nucl-th].

[89] V. Somà et al. "Chiral two- and three-nucleon forces along medium-mass isotope chains". In: *Phys. Rev. C* 89 (6 2014), p. 061301.

[90] C. Barbieri and A. Carbone. "Self-Consistent Green's Function Approaches". In: *An Advanced Course in Computational Nuclear Physics, Lecture Notes in Physics, p. 571*. Ed. by M. Hjorth-Jensen, M. P. Lombardo, and U. van Kolck. Vol. 936. Springer International Publishing AG, 2017, p. 571. ISBN: 978-3-319-53335-3.

[91] A. Cipollone, C. Barbieri, and P. Navrátil. "Isotopic Chains Around Oxygen from Evolved Chiral Two- and Three-Nucleon Interactions". In: *Phys. Rev. Lett.* 111 (6 2013), p. 062501.

[92] K. Kowalski et al. "Coupled Cluster Calculations of Ground and Excited States of Nuclei". In: *Phys. Rev. Lett.* 92 (13 2004), p. 132501.

[93] G. Hagen et al. "Benchmark calculations for 3H, 4He, 16O and 40Ca with ab- initio coupled-cluster theory". In: *Phys. Rev.* C76 (2007), p. 044305. arXiv: 0707.1516 [nucl-th].

[94] G. Hagen et al. "Ab initio coupled-cluster approach to nuclear structure with modern nucleon-nucleon interactions". In: *Phys. Rev.* C82 (3 2010), p. 034330.

[95] S. Binder et al. "Ab initio path to heavy nuclei". In: *Phys. Lett.* B736 (2014), pp. 119 –123. ISSN: 0370-2693.

[96] R. J. Bartlett and M. Musial. "Coupled-cluster theory in quantum chemistry". In: *Rev. Mod. Phys.* 79 (2007), pp. 291–352.

[97] R. Roth, J. R. Gour, and P. Piecuch. "Ab initio coupled-cluster and configuration interaction calculations for O16 using the V_{UCOM} interaction". In: *Phys. Rev.* C79.5, 054325 (2009), p. 054325. arXiv: 0806.0333 [nucl-th].

[98] M. Bender, P.-H. Heenen, and P.-G. Reinhard. "Self-consistent mean-field models for nuclear structure". In: *Rev. Mod. Phys.* 75 (2003), pp. 121–180.

[99] R. Furnstahl. "The UNEDF Project". In: *Nucl. Phys. News* 21.2 (2011), pp. 18–24.

[100] H. Nam et al. "UNEDF: Advanced Scientific Computing Collaboration Transforms the Low-Energy Nuclear Many-Body Problem". In: *J. Phys. Conf. Ser.* 402 (2012), p. 012033. arXiv: 1205.0227 [nucl-th].

[101] M. Kortelainen et al. "Nuclear Energy Density Optimization: UNEDF2". In: *JPS Conf. Proc.* 6 (2015), 020018. arXiv: 1410.8303 [nucl-th].

[102] M. Kortelainen et al. "Nuclear energy density optimization: Shell structure". In: *Phys. Rev.* C89, 054314 (2014), p. 054314. arXiv: 1312.1746 [nucl-th].

[103]   P. Hohenberg and W. Kohn. "Inhomogeneous Electron Gas". In: *Phys. Rev.* 136.3B (1964), B864–B871.

[104]   W. Kohn and L. J. Sham. "Self-Consistent Equations Including Exchange and Correlation Effects". In: *Phys. Rev.* 140.4A (1965), A1133–A1138.

[105]   R. Furnstahl. "Eft for DFT". In: *Lect. Notes Phys.* 852 (2012), pp. 133–191. arXiv: `nucl - th / 0702040` `[nucl-th]`.

[106]   J. Drut, R. Furnstahl, and L. Platter. "Toward ab initio density functional theory for nuclei". In: *Prog. Part. Nucl. Phys.* 64 (2010), pp. 120–168. arXiv: `0906.1463` `[nucl-th]`.

[107]   R. J. Furnstahl. "Turning the nuclear energy density functional method into a proper effective field theory: reflections". In: *arXiv e-prints* (2019). arXiv: `1906.00833` `[nucl-th]`.

[108]   S. K. Kemler. "From Microscopic Interactions to Density Functionals". PhD thesis. Darmstadt: Technische Universität, 2017.

[109]   S. Kemler and J. Braun. "Towards a renormalization group approach to density functional theory – general formalism and case studies–". In: *J. Phys.* G40 (2013), p. 085105. arXiv: `1304.1161` `[nucl-th]`.

[110]   S. Kemler, M. Pospiech, and J. Braun. "Formation of selfbound states in a one-dimensional nuclear model— a renormalization group based density functional study". In: *J. Phys.* G44, 015101 (2017), p. 015101. arXiv: `1606.04388` `[nucl-th]`.

[111]   T. Yokota, K. Yoshida, and T. Kunihiro. "Functional renormalization-group calculation of the equation of state of one-dimensional uniform matter inspired by the Hohenberg-Kohn theorem". In: *Phys. Rev.* C99 (2 2019), p. 024302.

[112]   T. Yokota, K. Yoshida, and T. Kunihiro. "Ab initio description of excited states of 1D uniform matter with the Hohenberg-Kohn-theorem-inspired functional-renormalization-group method". In: *Prog. Theor. Exp. Phys.* 2019, 011D01 (2019), p. 011D01. arXiv: `1810.00422` `[nucl-th]`.

[113]   H. Liang, Y. Niu, and T. Hatsuda. "Functional renormalization group and Kohn–Sham scheme in density functional theory". In: *Phys. Lett.* B779 (2018), pp. 436 –440. ISSN: 0370-2693.

[114]   T. Yokota and T. Naito. "Functional-renormalization-group aided density functional analysis for the correlation energy of the two-dimensional homogeneous electron gas". In: *Phys. Rev.* B99, 115106 (2019), p. 115106. arXiv: `1812.00588` `[cond-mat.str-el]`.

[115]   A. Tichai, J. Ripoche, and T. Duguet. "Pre-processing the nuclear many-body problem". In: *Eur. Phys. J.* A55.6 (2019), p. 90. ISSN: 1434-601X.

[116]   J. Braun, M. Leonhardt, and M. Pospiech. "Fierz-complete NJL model study: Fixed points and phase structure at finite temperature and density". In: *Phys. Rev.* D96.7 (2017), p. 076003. arXiv: `1705.00074` `[hep-ph]`.

[117]   J. Braun, M. Leonhardt, and M. Pospiech. "Fierz-complete NJL model study. II. Toward the fixed-point and phase structure of hot and dense two-flavor QCD". In: *Phys. Rev.* D97 (7 2018), p. 076010.

[118]   J. Braun, M. Leonhardt, and M. Pospiech. "Fierz-complete NJL model study III: Emergence from quark-gluon dynamics". In: *arXiv e-prints* (2019). arXiv: `1909.06298` `[hep-ph]`.

[119]   J. I. Kapusta. "Quantum chromodynamics at high temperature". In: *Nucl. Phys.* B148 (1979), pp. 461–498.

[120]   J. Zinn-Justin. "Quantum Field Theory at Finite Temperature: An Introduction". In: *arXiv e-prints* (2000). arXiv: `0005272` `[hep-ph]`.

[121]   A. Altland and B. Simons. *Condensed matter field theory*. Cambridge, UK: Univ. Pr., 2006.

[122]   R. MacKenzie. "Path Integral Methods and Applications". In: *arXiv e-prints* (2000). arXiv: `0004090` `[quant-ph]`.

[123]   H. Gies. "Introduction to the functional RG and applications to gauge theories". In: *Lect. Notes Phys.* 852 (2012), pp. 287–348. arXiv: `hep-ph/0611146` `[hep-ph]`.

[124] J. I. Kapusta and C. Gale. *Finite-Temperature Field Theory: Principles and Applications*. 2nd ed. Cambridge Monographs on Mathematical Physics. Cambridge University Press, 2006.

[125] C. Wetterich. "Spinors in euclidean field theory, complex structures and discrete symmetries". In: *Nucl. Phys.* B852 (Nov. 2011), pp. 174–234. arXiv: `1002.3556 [hep-th]`.

[126] M. E. Peskin and D. V. Schroeder. *An Introduction to quantum field theory*. Reading, USA: Addison-Wesley (1995) 842 p.

[127] B. Delamotte. "An introduction to the nonperturbative renormalization group". In: *cond-mat/0702365* (2007). arXiv: `cond-mat/0702365`.

[128] A. Ringwald and C. Wetterich. "Average action for the N-component φ4 theory". In: *Nucl. Phys.* B334.2 (1990), pp. 506 –526. ISSN: 0550-3213.

[129] N. Tetradis and C. Wetterich. "Scale dependence of the average potential around the maximum in φ4 theories". In: *Nucl. Phys.* B383.1 (1992), pp. 197 –217. ISSN: 0550-3213.

[130] W.-j. Fu, J. M. Pawlowski, and F. Rennecke. "Strangeness Neutrality and QCD Thermodynamics". In: *arXiv e-prints* (2018). arXiv: `1808.00410 [hep-ph]`.

[131] G. Baym et al. "New Neutron Star Equation of State with Quark-Hadron Crossover". In: *arXiv e-prints* (2019). arXiv: `1903.08963 [astro-ph.HE]`.

[132] L. P. Kadanoff. "Scaling laws for ising models near T_c". In: *Physics Physique Fizika* 2 (6 1966), pp. 263–272.

[133] C. G. Callan. "Broken Scale Invariance in Scalar Field Theory". In: *Phys. Rev. D* 2 (8 1970), pp. 1541–1547.

[134] K. Symanzik. "Small distance behaviour in field theory and power counting". In: *Comm. Math. Phys.* 18.3 (1970), pp. 227–246.

[135] J. Alexandre and J. Polonyi. "Functional Callan-Symanzik Equations". In: *Ann. Phys.* 288.1 (2001), pp. 37–51. arXiv: `hep-th/0010128 [hep-th]`.

[136] K. G. Wilson. "Renormalization Group and Critical Phenomena. I. Renormalization Group and the Kadanoff Scaling Picture". In: *Phys. Rev. B* 4 (9 1971), pp. 3174–3183.

[137] K. G. Wilson. "Renormalization Group and Critical Phenomena. II. Phase-Space Cell Analysis of Critical Behavior". In: *Phys. Rev. B* 4 (9 1971), pp. 3184–3205.

[138] M. E. Peskin. "Ken Wilson: Solving the Strong Interactions". In: *J. Stat. Phys.* 157 (2014), p. 651. arXiv: `1405.7086 [physics.hist-ph]`.

[139] L. Canet, B. Delamotte, and N. Wschebor. "Fully developed isotropic turbulence: nonperturbative renormalization group formalism and fixed point solution". In: *arXiv e-prints* (2014). arXiv: `1411.7780 [cond-mat.stat-mech]`.

[140] P. Tomassini. "An Exact Renormalization Group analysis of 3-d Well Developed turbulence". In: *arXiv e-prints* (1997). arXiv: `9706013 [nlin.CD]`.

[141] A. A. Fedorenko, P. L. Doussal, and K. J. Wiese. "Functional renormalization-group approach to decaying turbulence". In: *J. Stat. Mech.: Theory Exp.* 2013.04 (2013), P04014.

[142] C. Mejía-Monasterio and P. Muratore-Ginanneschi. "Nonperturbative renormalization group study of the stochastic Navier-Stokes equation". In: *Phys. Rev. E* 86 (1 2012), p. 016315.

[143] S. Mathey, T. Gasenzer, and J. M. Pawlowski. "Anomalous scaling at nonthermal fixed points of Burgers' and Gross-Pitaevskii turbulence". In: *Phys. Rev.* A92 (2 2015), p. 023635.

[144] C. Pagani. "Functional renormalization group approach to the Kraichnan model". In: *Phys. Rev.* E 92.3, 033016 (2015), p. 033016. arXiv: `1505.01293 [cond-mat.stat-mech]`.

[145]   M. Tarpin et al. "Stationary, isotropic and homogeneous two-dimensional turbulence: a first non-perturbative renormalization group approach". In: *J. Phys.* A52.8, 085501 (2019), p. 085501. arXiv: `1809.00909` [`cond-mat.stat-mech`].

[146]   M. Reuter. "Nonperturbative Evolution Equation for Quantum Gravity". In: *Phys. Rev.* D57 (1998), pp. 971–985. arXiv: `hep-th/9605030`.

[147]   O. Lauscher and M. Reuter. "Ultraviolet fixed point and generalized flow equation of quantum gravity". In: *Phys. Rev.* D65 (2002), p. 025013. arXiv: `hep-th/0108040`.

[148]   D. F. Litim. "Fixed points of quantum gravity". In: *Phys. Rev. Lett.* 92 (2004), p. 201301. arXiv: `hep-th/0312114`.

[149]   A. Codello, R. Percacci, and C. Rahmede. "Investigating the ultraviolet properties of gravity with a Wilsonian renormalization group equation". In: *Ann. Phys.* 324.2 (2009), pp. 414–469. arXiv: `0805.2909` [`hep-th`].

[150]   D. Benedetti, P. F. Machado, and F. Saueressig. "Asymptotic Safety in Higher-Derivative Gravity". In: *Mod. Phys. Lett.* A24.28 (2009), pp. 2233–2241. arXiv: `0901.2984` [`hep-th`].

[151]   E. Manrique, S. Rechenberger, and F. Saueressig. "Asymptotically Safe Lorentzian Gravity". In: *Phys. Rev. Lett.* 106.25, 251302 (2011), p. 251302. arXiv: `1102.5012` [`hep-th`].

[152]   D. Becker and M. Reuter. "En route to Background Independence: Broken split-symmetry, and how to restore it with bi-metric average actions". In: *Ann. Phys.* 350 (2014), pp. 225–301. arXiv: `1404.4537` [`hep-th`].

[153]   A. Eichhorn, S. Lippoldt, and M. Schiffer. "Zooming in on fermions and quantum gravity". In: *Phys. Rev.* D 99.8, 086002 (2019), p. 086002. arXiv: `1812.08782` [`hep-th`].

[154]   M. Demmel, F. Saueressig, and O. Zanusso. "A proper fixed functional for four-dimensional Quantum Einstein Gravity". In: *J. High Energy Phys.* 2015, 113 (2015), p. 113. arXiv: `1504.07656` [`hep-th`].

[155]   H. Gies et al. "Gravitational Two-Loop Counterterm Is Asymptotically Safe". In: *Phys. Rev. Lett.* 116.21, 211302 (2016), p. 211302. arXiv: `1601.01800` [`hep-th`].

[156]   T. Denz, J. M. Pawlowski, and M. Reichert. "Towards apparent convergence in asymptotically safe quantum gravity". In: *Eur. Phys. J.* C78.4, 336 (2018), p. 336. arXiv: `1612.07315` [`hep-th`].

[157]   K. G. Falls, D. F. Litim, and J. Schröder. "Aspects of asymptotic safety for quantum gravity". In: *arXiv e-prints* (2018). arXiv: `1810.08550` [`gr-qc`].

[158]   S. Weinberg. "Critical Phenomena for Field Theorist". In: *Lectures presented at Int. School of Subnuclear Physics, Ettore Majorana, Erice, Sicily* (1976).

[159]   J. M. Pawlowski. "Aspects of the functional renormalisation group". In: *Ann. Phys.* 322 (2007), pp. 2831–2915. arXiv: `hep-th/0512261` [`hep-th`].

[160]   L. D. Faddeev and V. N. Popov. "Feynman diagrams for the Yang-Mills field". In: *Phys. Lett.* B25 (July 1967), pp. 29–30.

[161]   H. Gies and C. Wetterich. "Renormalization flow from UV to IR degrees of freedom". In: *Acta Phys. Slov.* 52 (2002), pp. 215–220. eprint: `hep-ph/0205226`.

[162]   J. Jaeckel and C. Wetterich. "Flow equations without mean field ambiguity". In: *Phys. Rev.* D68 (2003), p. 025020. eprint: `hep-ph/0207094`.

[163]   S. Floerchinger. "Exact flow equation for bound states". In: *Eur. Phys. J.* C69 (2010), pp. 119–132. arXiv: `1001.4497` [`hep-th`].

[164]   S. Floerchinger and C. Wetterich. "Exact flow equation for composite operators". In: *Phys. Lett.* B680 (2009), pp. 371–376. arXiv: `0905.0915` [`hep-th`].

[165]   D. F. Litim and J. M. Pawlowski. "Completeness and consistency of renormalisation group flows". In: *Phys. Rev.* D66 (2002), p. 025030. eprint: `hep-th/0202188`.

[166] M. Q. Huber and J. Braun. "Algorithmic derivation of functional renormalization group equations and Dyson-Schwinger equations". In: *Comput. Phys. Commun.* 183 (2012), pp. 1290–1320. arXiv: `1102.5307` `[hep-th]`.

[167] A. K. Cyrol, M. Mitter, and N. Strodthoff. "FormTracer - A Mathematica Tracing Package Using FORM". In: *Comput. Phys. Commun.* 219 (2017), pp. 346–352. arXiv: `1610.09331` `[hep-ph]`.

[168] J. A. M. Vermaseren. "New features of FORM". In: *arXiv e-prints* (Oct. 2000). arXiv: `0010025` `[math-ph]`.

[169] E. Braaten and R. D. Pisarski. "Simple effective Lagrangian for hard thermal loops". In: *Phys. Rev.* D45 (1992), pp. 1827–1830.

[170] E. Braaten and R. D. Pisarski. "Soft amplitudes in hot gauge theories: A general analysis". In: *Nucl. Phys.* A337.3 (1990), pp. 569 –634. ISSN: 0550-3213.

[171] E. Braaten and R. D. Pisarski. "Resummation and gauge invariance of the gluon damping rate in hot QCD". In: *Phys. Rev. Lett.* 64 (12 1990), pp. 1338–1341.

[172] N. Su. "A Brief Overview of Hard-Thermal-Loop Perturbation Theory". In: *Commun. Theor. Phys.* 57.3 (2012), pp. 409–421. arXiv: `1204.0260` `[hep-ph]`.

[173] N. Su. "Recent progress in hard-thermal-loop QCD thermodynamics and collective excitations". In: *Int. J. Mod. Phys.* A30.9, 1530025 (2015), p. 1530025. arXiv: `1502.04589` `[hep-ph]`.

[174] J. Berges, N. Tetradis, and C. Wetterich. "Nonperturbative renormalization flow in quantum field theory and statistical physics". In: *Phys. Rept.* 363 (2002), pp. 223–386. arXiv: `hep-ph/0005122` `[hep-ph]`.

[175] T. R. Morris. "Derivative expansion of the exact renormalization group". In: *Phys. Lett.* B329 (June 1994), pp. 241–248. arXiv: `hep-ph/9403340` `[hep-ph]`.

[176] T. R. Morris and J. F. Tighe. "Convergence of derivative expansions of the renormalization group". In: *J. High Energy Phys.* 08 (1999), p. 007. arXiv: `hep-th/9906166` `[hep-th]`.

[177] R. J. Myerson. "Renormalization-group calculation of critical exponents for three-dimensional Ising-like systems". In: *Phys. Rev. B* 12 (7 1975), pp. 2789–2793.

[178] G. R. Golner. "Nonperturbative renormalization-group calculations for continuum spin systems". In: *Phys. Rev. B* 33 (11 1986), pp. 7863–7866.

[179] J. P. Blaizot, R. Mendez Galain, and N. Wschebor. "A new method to solve the non perturbative renormalization group equations". In: *Phys. Lett.* B632 (2006), pp. 571–578. arXiv: `hep-th/0503103`.

[180] J.-P. Blaizot, R. Méndez-Galain, and N. Wschebor. "Nonperturbative renormalization group and momentum dependence of n-point functions. I". In: *Phys. Rev. E* 74 (5 2006), p. 051116.

[181] M. Tanabashi et. al. "Review of Particle Physics". In: *Phys. Rev.* D98 (3 2018), p. 030001.

[182] Y. Nambu. "Quasi-Particles and Gauge Invariance in the Theory of Superconductivity". In: *Phys. Rev.* 117 (Feb. 1960), pp. 648–663.

[183] J. Goldstone. "Field Theories with Superconductor Solutions". In: *Nuovo Cim.* 19 (1961), pp. 154–164.

[184] J. Goldstone, A. Salam, and S. Weinberg. "Broken Symmetries". In: *Phys. Rev.* 127 (1962), pp. 965–970.

[185] S. Weinberg. *The quantum theory of fields. Vol. 2: Modern applications.* Cambridge University Press, 2013. ISBN: 9781139632478, 9780521670548, 9780521550024.

[186] M. D. Schwartz. *Quantum Field Theory and the Standard Model.* Cambridge University Press, 2014. ISBN: 1107034736, 9781107034730.

[187] S. Scherer. *Symmetrien und Gruppen in der Teilchenphysik.* Springer-Verlag Berlin Heidelberg, 2016.

[188] C. DeTar et al. "String breaking in lattice quantum chromodynamics". In: *Phys. Rev.* D59 (3 1998), p. 031501.

[189] J. Bulava et al. "String breaking by light and strange quarks in QCD". In: *Phys. Lett.* B793 (2019), pp. 493 –498. ISSN: 0370-2693.

[190] V. Baluni. "CP-nonconserving effects in quantum chromodynamics". In: *Phys. Rev.* D19 (7 1979), pp. 2227– 2230.

[191] R. J. Crewther et al. "Chiral Estimate of the Electric Dipole Moment of the Neutron in Quantum Chromo-dynamics". In: *Phys. Lett.* 88B (1979). [Erratum: Phys. Lett.91B,487(1980)], p. 123.

[192] A. A. Belavin et al. "Pseudoparticle Solutions of the Yang-Mills Equations". In: *Phys. Lett.* B59 (1975), pp. 85– 87.

[193] G. 't Hooft. "Symmetry Breaking Through Bell-Jackiw Anomalies". In: *Phys. Rev. Lett.* 37 (1976), pp. 8–11.

[194] G. 't Hooft. "Computation of the Quantum Effects Due to a Four-Dimensional Pseudoparticle". In: *Phys. Rev.* D14 (1976). [Erratum: Phys. Rev. **D18**, 2199 (1978)], pp. 3432–3450.

[195] R. D. Peccei and H. R. Quinn. "CP Conservation in the Presence of Pseudoparticles". In: *Phys. Rev. Lett.* 38 (25 1977), pp. 1440–1443.

[196] R. D. Peccei. "The Strong CP Problem and Axions". In: *Axions, Lecture Notes in Physics, Volume 741, p. 3.* Ed. by M. Kuster, G. Raffelt, and B. Beltrán. Springer-Verlag Berlin Heidelberg, 2008, p. 3. ISBN: 978-3-540-73517-5.

[197] H. C. van de Hulst, E. Raimond, and H. van Woerden. "Rotation and density distribution of the Andromeda nebula derived from observations of the 21-cm line". In: *bain* 14 (Nov. 1957), p. 1.

[198] M. Schmidt. "The distribution of mass in M 31". In: *bain* 14 (Nov. 1957), p. 17.

[199] L. D. Duffy and K. van Bibber. "Axions as dark matter particles". In: *New J. Phys.* 11.10 (2009), p. 105008.

[200] P. Sikivie. "Experimental Tests of the "Invisible" Axion". In: *Phys. Rev. Lett.* 51 (16 1983), pp. 1415–1417.

[201] P. W. Graham et al. "Experimental Searches for the Axion and Axion-Like Particles". In: *Annu. Rev. Nucl. Part. S.* 65.1 (2015), pp. 485–514. eprint: https://doi.org/10.1146/annurev-nucl-102014-022120.

[202] V. N. Gribov. "Quantization of non-Abelian gauge theories". In: *Nucl. Phys.* B139 (1978), p. 1.

[203] N. Vandersickel and D. Zwanziger. "The Gribov problem and QCD dynamics". In: *Phys. Rep.* 520.4 (2012), pp. 175–251. arXiv: 1202.1491 [hep-th].

[204] R. Alkofer and L. von Smekal. "The infrared behavior of QCD Green's functions: Confinement, dynamical symmetry breaking, and hadrons as relativistic bound states". In: *Phys. Rept.* 353 (2001), p. 281. eprint: hep-ph/0007355.

[205] C. Becchi, A. Rouet, and R. Stora. "Renormalization of the abelian Higgs-Kibble model". In: *Comm. Math. Phys.* 42.2 (1975), pp. 127–162.

[206] C Becchi, A Rouet, and R Stora. "Renormalization of gauge theories". In: *Ann. Phys.* 98.2 (1976), pp. 287 –321. ISSN: 0003-4916.

[207] I. V. Tyutin. "Gauge Invariance in Field Theory and Statistical Physics in Operator Formalism". In: *arXiv e-prints* (2008). arXiv: 0812.0580 [hep-th].

[208] J. C. Taylor. "Ward identities and charge renormalization of the Yang-Mills field". In: *Nucl. Phys.* B33 (Nov. 1971), pp. 436–444.

[209] A. A. Slavnov. "Ward identities in gauge theories". In: *Theor. Math. Phys.* 10 (Feb. 1972), pp. 99–104.

[210] S. L. Adler. "Axial-Vector Vertex in Spinor Electrodynamics". In: *Phys. Rev.* 177 (Jan. 1969), pp. 2426–2438.

[211] J. S. Bell and R. Jackiw. "A PCAC puzzle: $\pi^0 \to \gamma\gamma$ in the σ-model". In: *Nuovo Cimento A Serie* 60 (Mar. 1969), pp. 47–61.

[212]   S. Elitzur. "Impossibility of spontaneously breaking local symmetries". In: *Phys. Rev. D* 12 (12 1975), pp. 3978–3982.

[213]   E. J. Weinberg. *Classical Solutions in Quantum Field Theory: Solitons and Instantons in High Energy Physics*. Caambridge Monographs on Mathematical Physics. Cambridge University Press, 2012.

[214]   T. P. Cheng and L. F. Li. *Gauge theory of elementary particle physics*. Oxford Science Publications, 1984.

[215]   T. Schäfer and E. V. Shuryak. "Instantons in QCD". In: *Rev. Mod. Phys.* 70 (1998), pp. 323–426. arXiv: `hep-ph/9610451`.

[216]   K. Fujikawa. "Path-Integral Measure for Gauge-Invariant Fermion Theories". In: *Phys. Rev. Lett.* 42 (18 1979), pp. 1195–1198.

[217]   K. Fukushima. "Chiral effective model with the Polyakov loop". In: *Phys. Lett.* B591 (2004), pp. 277–284. eprint: `hep-ph/0310121`.

[218]   K. Fukushima. "Phase diagrams in the three-flavor Nambu–Jona-Lasinio model with the Polyakov loop". In: *Phys. Rev.* D77 (2008), p. 114028. arXiv: `0803.3318 [hep-ph]`.

[219]   C. Sasaki, B. Friman, and K. Redlich. "Susceptibilities and the phase structure of a chiral model with Polyakov loops". In: *Phys. Rev.* D75 (2007), p. 074013. arXiv: `hep-ph/0611147`.

[220]   Y. Sakai et al. "Polyakov loop extended NJL model with imaginary chemical potential". In: *Phys. Rev.* D77 (2008), p. 051901. arXiv: `0801.0034 [hep-ph]`.

[221]   T. K. Mukherjee, H. Chen, and M. Huang. "Chiral condensate and dressed Polyakov loop in the Nambu–Jona-Lasinio model". In: *Phys. Rev.* D82 (2010), p. 034015. arXiv: `1005.2482 [hep-ph]`.

[222]   V. Skokov et al. "Meson fluctuations and thermodynamics of the Polyakov loop extended quark-meson model". In: *Phys. Rev.* C82 (2010), p. 015206. arXiv: `1004.2665 [hep-ph]`.

[223]   T. K. Herbst, J. M. Pawlowski, and B.-J. Schaefer. "The phase structure of the Polyakov–quark-meson model beyond mean field". In: *Phys. Lett.* B696 (2011), pp. 58–67. arXiv: `1008.0081 [hep-ph]`.

[224]   N. Strodthoff and L. von Smekal. "Polyakov-Quark-Meson-Diquark Model for two-color QCD". In: *Phys. Lett.* B731 (2014), pp. 350–357. arXiv: `1306.2897 [hep-ph]`.

[225]   B.-J. Schaefer, J. M. Pawlowski, and J. Wambach. "The Phase Structure of the Polyakov–Quark-Meson Model". In: *Phys. Rev.* D76 (2007), p. 074023. arXiv: `0704.3234 [hep-ph]`.

[226]   T. Hell et al. "Thermodynamics of a three-flavor nonlocal Polyakov–Nambu- -Jona-Lasinio model". In: *Phys. Rev.* D81 (2010), p. 074034. arXiv: `0911.3510 [hep-ph]`.

[227]   P. Costa et al. "The QCD critical end point in the PNJL model". In: *EPL* 86.3 (2009), p. 31001. arXiv: `0801.3616 [hep-ph]`.

[228]   J. Braun. "Fermion Interactions and Universal Behavior in Strongly Interacting Theories". In: *J. Phys.* G39 (2012), p. 033001. arXiv: `1108.4449 [hep-ph]`.

[229]   J. Braun and T. K. Herbst. "On the Relation of the Deconfinement and the Chiral Phase Transition in Gauge Theories with Fundamental and Adjoint Matter". In: (2012). arXiv: `1205.0779 [hep-ph]`.

[230]   J. Hubbard. "Calculation of partition functions". In: *Phys. Rev. Lett.* 3 (1959), pp. 77–80.

[231]   R. Stratonovich. "A method for the. computation of quantum distribution functions". In: *Dokl. Akad. Nauk.* 115 (1957), p. 1097.

[232]   R. D. Pisarski and F. Wilczek. "Remarks on the chiral phase transition in chromodynamics". In: *Phys. Rev.* D29 (1984), pp. 338–341.

[233]   B.-J. Schaefer and J. Wambach. "The phase diagram of the quark meson model". In: *Nucl. Phys.* A757 (2005), pp. 479–492. eprint: `nucl-th/0403039`.

[234]   V. L. Ginzburg and L. D. Landau. "On the Theory of superconductivity". In: *Zh. Eksp. Teor. Fiz.* 20 (1950), pp. 1064–1082.

[235]   H. Gies and C. Wetterich. "Universality of spontaneous chiral symmetry breaking in gauge theories". In: *Phys. Rev.* D69 (2004), p. 025001. eprint: `hep-th/0209183`.

[236]   H. Gies. "Running coupling in Yang-Mills theory: A flow equation study". In: *Phys. Rev.* D66 (2002), p. 025006. arXiv: `hep-th/0202207`.

[237]   A. K. Cyrol et al. "Nonperturbative finite-temperature Yang-Mills theory". In: *Phys. Rev.* D97, 054015 (2018), p. 054015. arXiv: `1708.03482 [hep-ph]`.

[238]   J. F. Nieves and P. B. Pal. "Generalized Fierz identities". In: *Am. J. Phys.* 72 (Aug. 2004), pp. 1100–1108. eprint: `hep-ph/0306087`.

[239]   J. Jaeckel. "Understanding the Fierz Ambiguity of Partially Bosonized Theories". In: *arXiv e-prints* (2002). arXiv: `0205154 [hep-ph]`.

[240]   J. Braun et al. "From Quarks and Gluons to Hadrons: Chiral Symmetry Breaking in Dynamical QCD". In: *Phys. Rev.* D94.3 (2016), p. 034016. arXiv: `1412.1045 [hep-ph]`.

[241]   F. Rennecke. "Vacuum structure of vector mesons in QCD". In: *Phys. Rev.* D92.7 (2015), p. 076012. arXiv: `1504.03585 [hep-ph]`.

[242]   R. Alkofer et al. "Bound state properties from the functional renormalization group". In: *Phys. Rev. D* 99 (5 2019), p. 054029.

[243]   P. de Forcrand and O. Philipsen. "The QCD phase diagram for small densities from imaginary chemical potential". In: *Nucl. Phys.* B642 (2002), pp. 290–306. eprint: `hep-lat/0205016`.

[244]   M. D'Elia and M.-P. Lombardo. "Finite density QCD via an imaginary chemical potential". In: *Phys. Rev. D* 67 (1 2003), p. 014505.

[245]   L. Rammelmüller et al. "Surmounting the sign problem in nonrelativistic calculations: A case study with mass-imbalanced fermions". In: *Phys. Rev.* D96.9, 094506 (2017), p. 094506. arXiv: `1708.03149 [cond-mat.quant-gas]`.

[246]   E. Nelson. "Derivation of the Schrödinger Equation from Newtonian Mechanics". In: *Phys. Rev.* 150 (4 1966), pp. 1079–1085.

[247]   G Parisi and Y. S. Wu. "Perturbation theory without gauge fixing". In: *Sci. China, A* 24.ASITP-80-004. 4 (1980), 483–496. 29 p.

[248]   G. Aarts et al. "Simulating QCD at nonzero baryon density to all orders in the hopping parameter expansion". In: *Phys. Rev. D* 90 (11 2014), p. 114505.

[249]   G. Aarts et al. "Insights into the heavy dense QCD phase diagram using Complex Langevin simulations". In: *arXiv e-prints* (2015). arXiv: `1510.09100 [hep-lat]`.

[250]   G. Aarts et al. "Complex Langevin in Lattice QCD: dynamic stabilisation and the phase diagram". In: *arXiv e-prints* (2016). arXiv: `1607.05642 [hep-lat]`.

[251]   M. Scherzer et al. "Complex Langevin: Boundary terms and application to QCD". In: *arXiv e-prints* (2018). arXiv: `1810.09713 [hep-lat]`.

[252]   L. Rammelmüller, J. E. Drut, and J. Braun. "A complex Langevin approach to ultracold fermions". In: *J. Phys. Conf. Ser.* Vol. 1041. J. Phys. Conf. Ser. 2018, p. 012006. arXiv: `1710.11421 [cond-mat.quant-gas]`.

[253]   E. Seiler. "Status of Complex Langevin". In: *Eur. Phys. J. Web Conf.* Vol. 175. EPJ Web Conf. 2018, p. 01019. arXiv: `1708.08254 [hep-lat]`.

[254]   K. Rajagopal. "Mapping the QCD phase diagram". In: *Nucl. Phys.* A661 (1999), pp. 150–161. arXiv: `hep-ph/9908360 [hep-ph]`.

[255]   P. Braun-Munzinger and J. Wambach. "The Phase Diagram of Strongly-Interacting Matter". In: *arXiv e-prints* (2008). arXiv: 0801.4256 [hep-ph].

[256]   M. Stephanov. "QCD phase diagram: an overview". In: *XXIVth International Symposium on Lattice Field Theory*. 2006, p. 24.1. arXiv: hep-lat/0701002 [hep-lat].

[257]   S. A. Bass et al. "TOPICAL REVIEW: Signatures of quark-gluon plasma formation in high energy heavy-ion collisions: a critical review". In: *J. Phys.* G25.3 (1999), R1–R57. arXiv: hep-ph/9810281 [hep-ph].

[258]   R. Pasechnik and M. Šumbera. "Phenomenological Review on Quark-Gluon Plasma: Concepts vs. Observations". In: *Universe* 3.1 (2017), p. 7. arXiv: 1611.01533 [hep-ph].

[259]   E. V. Shuryak. "What RHIC experiments and theory tell us about properties of quark-gluon plasma?" In: *Nucl. Phys.* A750 (2005), pp. 64–83. eprint: hep-ph/0405066.

[260]   V. Laliena. "Searching for the critical endpoint in QCD with two quark flavors". In: *arXiv e-prints* (2005). arXiv: hep-lat/0509153 [hep-lat].

[261]   C. S. Fischer, J. Luecker, and C. A. Welzbacher. "Locating the critical end point of QCD". In: *Nucl. Phys.* A931 (2014), pp. 774–779. arXiv: 1410.0124 [hep-ph].

[262]   R. Gavai and S. Gupta. "The critical end point of quantum chromodynamics". In: *arXiv e-prints* (2005). arXiv: hep-lat/0509151 [hep-lat].

[263]   J. Goswami et al. "Critical end points in (2+1)-flavor QCD with imaginary chemical potential". In: *arXiv e-prints* (2019). arXiv: 1905.03625 [hep-lat].

[264]   L. F. Palhares, E. S. Fraga, and T. Kodama. "Chiral transition in a finite system and possible use of finite-size scaling in relativistic heavy ion collisions". In: *J. Phys.* G38.8 (2011). arXiv: 0904.4830 [nucl-th].

[265]   M. Stephanov, K. Rajagopal, and E. Shuryak. "Signatures of the Tricritical Point in QCD". In: *Phys. Rev. Lett.* 81 (22 1998), pp. 4816–4819.

[266]   M. A. Stephanov. "QCD Phase Diagram and The Critical Point". In: *Int. J. Mod. Phys.* A 20.19 (2005), pp. 4387–4392. eprint: https://doi.org/10.1142/S0217751X05027965.

[267]   The STAR Collaboration and The CBM Collaboration eTOF Group. "Physics Program for the STAR/CBM eTOF Upgrade". In: *arXiv e-prints* (2016). arXiv: 1609.05102 [nucl-ex].

[268]   H. R. Jaqaman, A. Z. Mekjian, and L. Zamick. "Liquid-gas phase transitions in finite nuclear matter". In: *Phys. Rev. C* 29 (6 1984), pp. 2067–2074.

[269]   P. J. Siemens. "Liquid-gas phase transition in nuclear matter". In: *Nature* 305 (Sept. 1983), pp. 410–412.

[270]   A. D. Panagiotou et al. "Experimental Evidence for a Liquid-Gas Phase Transition in Nuclear Systems". In: *Phys. Rev. Lett.* 52 (7 1984), pp. 496–499.

[271]   J. Pochodzalla et al. "Probing the Nuclear Liquid-Gas Phase Transition". In: *Phys. Rev. Lett.* 75 (6 1995), pp. 1040–1043.

[272]   C. Bonati et al. "Chiral phase transition in two-flavor QCD from an imaginary chemical potential". In: *Phys. Rev.* D 90 (7 2014), p. 074030.

[273]   F. Cuteri, O. Philipsen, and A. Sciarra. "QCD chiral phase transition from noninteger numbers of flavors". In: *Phys. Rev.* D 97 (11 2018), p. 114511.

[274]   M. D'Elia, A. di Giacomo, and C. Pica. "Two flavor QCD and confinement". In: *Phys. Rev.* D72.11, 114510 (2005), p. 114510. arXiv: hep-lat/0503030 [hep-lat].

[275]   G. Cossu et al. "Two flavor QCD and confinement - II". In: *arXiv e-prints* (2007). arXiv: 0706.4470 [hep-lat].

[276] J. Braun, M. Leonhardt, and J. M. Pawlowski. "Renormalization group consistency and low-energy effective theories". In: *arXiv e-prints* (2018). arXiv: `1806.04432 [hep-ph]`.

[277] I. A. Shovkovy. "Two lectures on color superconductivity". In: *Found. Phys.* 35 (2005), pp. 1309–1358. arXiv: `nucl-th/0410091 [nucl-th]`.

[278] R. Rapp et al. "Diquark Bose condensates in high density matter and instantons". In: *Phys. Rev. Lett.* 81 (1998), pp. 53–56. arXiv: `hep-ph/9711396 [hep-ph]`.

[279] P. de Forcrand and M. D'Elia. "Continuum limit and universality of the Columbia plot". In: *arXiv e-prints* (2017). arXiv: `1702.00330 [hep-lat]`.

[280] P. Fulde and R. A. Ferrell. "Superconductivity in a Strong Spin-Exchange Field". In: *Phys. Rev.* 135.3A (1964), A550–A563.

[281] A. I. Larkin and Y. N. Ovchinnikov. In: *Zh. Eksp. Teor. Fiz.* 47 (1964), p. 1136.

[282] J. A. Bowers and K. Rajagopal. "Crystallography of color superconductivity". In: *Phys. Rev. D* 66 (6 2002), p. 065002.

[283] R. Casalbuoni and G. Nardulli. "Inhomogeneous superconductivity in condensed matter and QCD". In: *Rev. Mod. Phys.* 76 (1 2004), pp. 263–320.

[284] K.-I. Aoki and M. Yamada. "The RG flow of Nambu–Jona-Lasinio model at finite temperature and density". In: *Int. J. Mod. Phys.* A30.27 (2015), p. 1550180. arXiv: `1504.00749 [hep-ph]`.

[285] T. D. Cohen. "Functional integrals for QCD at nonzero chemical potential and zero density". In: *Phys. Rev. Lett.* 91 (2003), p. 222001. arXiv: `hep-ph/0307089 [hep-ph]`.

[286] G. Markó, U. Reinosa, and Z. Szep. "Bose-Einstein condensation and Silver Blaze property from the two-loop Φ-derivable approximation". In: *Phys. Rev.* D90.12 (2014), p. 125021. arXiv: `1410.6998 [hep-ph]`.

[287] N. Khan et al. "The Phase Diagram of QC2D from Functional Methods". In: *arXiv e-prints* (2015). arXiv: `1512.03673 [hep-ph]`.

[288] W.-j. Fu and J. M. Pawlowski. "Relevance of matter and glue dynamics for baryon number fluctuations". In: *Phys. Rev.* D92.11 (2015), p. 116006. arXiv: `1508.06504 [hep-ph]`.

[289] D. U. Jungnickel and C. Wetterich. "Effective action for the chiral quark-meson model". In: *Phys. Rev.* D53 (1996), pp. 5142–5175. eprint: `hep-ph/9505267`.

[290] J. Berges, D. U. Jungnickel, and C. Wetterich. "Two flavor chiral phase transition from nonperturbative flow equations". In: *Phys. Rev.* D59 (1999), p. 034010. eprint: `hep-ph/9705474`.

[291] M. A. Shifman, A. I. Vainshtein, and V. I. Zakharov. "Instanton Density in a Theory with Massless Quarks". In: *Nucl. Phys.* B163 (1980), p. 46.

[292] E. V. Shuryak. "The Role of Instantons in Quantum Chromodynamics. 1. Physical Vacuum". In: *Nucl. Phys.* B203 (1982), p. 93.

[293] J. M. Pawlowski. "Exact Flow Equations and the $U(1)$-Problem". In: *Phys. Rev.* D58 (1998), p. 045011. arXiv: `hep-th/9605037`.

[294] L. Fister and J. M. Pawlowski. "Yang-Mills correlation functions at finite temperature". In: *arXiv e-prints* (2011). arXiv: `1112.5440 [hep-ph]`.

[295] M. Reuter and C. Wetterich. "Effective average action for gauge theories and exact evolution equations". In: *Nucl. Phys.* B417 (1994), pp. 181–214.

[296] F. Freire, D. F. Litim, and J. M. Pawlowski. "Gauge invariance and background field formalism in the exact renormalisation group". In: *Phys. Lett.* B495 (2000), pp. 256–262. eprint: `hep-th/0009110`.

[297] U. Ellwanger. "Flow equations and BRS invariance for Yang-Mills theories". In: *Phys. Lett.* B335 (1994), pp. 364–370. eprint: `hep-th/9402077`.

[298] M. Bonini, M. D'Attanasio, and G. Marchesini. "BRS symmetry for Yang-Mills theory with exact renormalization group". In: *Nucl. Phys.* B437 (1995), pp. 163–186. eprint: `hep-th/9410138`.

[299] M. Bonini, M. D'Attanasio, and G. Marchesini. "Ward identities and Wilson renormalization group for QED". In: *Nucl. Phys.* A418.1 (1994), pp. 81 –112. ISSN: 0550-3213.

[300] M. D'Attanasio and T. R. Morris. "Gauge invariance, the quantum action principle, and the renormalization group". In: *Phys. Lett.* B378 (Feb. 1996), pp. 213–221. eprint: `hep-th/9602156`.

[301] H. Gies, J. Jaeckel, and C. Wetterich. "Towards a renormalizable standard model without fundamental Higgs scalar". In: *Phys. Rev.* D69 (2004), p. 105008. eprint: `hep-ph/0312034`.

[302] J. M. Pawlowski. "On Wilsonian flows in gauge theories". In: *Int. J. Mod. Phys.* A16 (2001), pp. 2105–2110.

[303] P. Springer. "Constraining low-energy models of QCD from fundamental interactions". Dissertation. München: Technische Universität München, 2016.

[304] K. Rajagopal and F. Wilczek. "The Condensed Matter Physics of QCD". In: *At the Frontier of Particle Physics: Handbook of QCD (in 3 Vols)*. Ed. by M. Shifman. World Scientific Publishing Co. Pte. Ltd., 2001, pp. 2061–2151. ISBN: 9789812810458.

[305] N. Strodthoff, B.-J. Schaefer, and L. von Smekal. "Quark-meson-diquark model for two-color QCD". In: *Phys. Rev.* D85 (2012), p. 074007. arXiv: `1112.5401 [hep-ph]`.

[306] S. K. Greif et al. "Equation of state sensitivities when inferring neutron star and dense matter properties". In: *Mon. Notices Royal Astron. Soc.* 485.4 (2019), pp. 5363–5376. arXiv: `1812.08188 [astro-ph.HE]`.

[307] J. Braun. "The QCD Phase Boundary from Quark-Gluon Dynamics". In: *Eur. Phys. J.* C64 (2009), pp. 459–482. arXiv: `0810.1727 [hep-ph]`.

[308] E. Engel and R. M. Dreizler. *Density Functional Theory: An Advanced Course*. Springer, Berlin, 2011.

[309] W. Ritz. "Über eine neue Methode zur Lösung gewisser Variationsprobleme der mathematischen Physik." ger. In: *J. Reine Angew. Math.* 135 (1909), pp. 1–61.

[310] M. Levy. "Electron densities in search of Hamiltonians". In: *Phys. Rev. A* 26 (3 1982), pp. 1200–1208.

[311] M. Levy. "Universal Variational Functionals of Electron Densities, First-Order Density Matrices, and Natural Spin-Orbitals and Solution of the v-Representability Problem". In: *Proc. Natl. Acad. Sci. U.S.A.* 76.12 (1979), pp. 6062–6065. ISSN: 00278424.

[312] E. H. Lieb. "Density functionals for coulomb systems". In: *Int. J. Quantum Chem.* 24.3 (1983), pp. 243–277. eprint: `https://onlinelibrary.wiley.com/doi/pdf/10.1002/qua.560240302`.

[313] M. Born and R. Oppenheimer. "Zur Quantentheorie der Molekeln". In: *Ann. Phys.* 389.20 (1927), pp. 457–484. eprint: `https://onlinelibrary.wiley.com/doi/pdf/10.1002/andp.19273892002`.

[314] A. D. Daniels and G. E. Scuseria. "Converging difficult SCF cases with conjugate gradient density matrix search". In: *Phys. Chem. Chem. Phys.* 2 (10 2000), pp. 2173–2176.

[315] C.-O. Almbladh and U. von Barth. "Exact results for the charge and spin densities, exchange-correlation potentials, and density-functional eigenvalues". In: *Phys. Rev.* B31 (6 1985), pp. 3231–3244.

[316] J Harris and R. O. Jones. "The surface energy of a bounded electron gas". In: *J. Phys.* F4.8 (1974), pp. 1170–1186.

[317] L. J. Sham. "Exchange and correlation in density-functional theory". In: *Phys. Rev.* B32 (6 1985), pp. 3876–3882.

[318]   D. C. Langreth and J. P. Perdew. "The exchange-correlation energy of a metallic surface". In: *Solid State Commun.* 17 (Dec. 1975), pp. 1425–1429.

[319]   O. Gunnarsson and B. I. Lundqvist. "Exchange and correlation in atoms, molecules, and solids by the spin-density-functional formalism". In: *Phys. Rev.* B13 (10 1976), pp. 4274–4298.

[320]   U. von Barth. "Basic Density-Functional Theory an Overview". In: *Phys. Scr.* T109 (2004), p. 9.

[321]   S. J. Puglia, A. Bhattacharyya, and R. J. Furnstahl. "Density functional theory for a confined Fermi system with short-range interaction". In: *Nucl. Phys. A* 723.1-2 (2003), pp. 145 –180.

[322]   R. Fukuda et al. "Density Functional Theory through Legendre Transformation". In: *Prog. Theor. Phys.* 92.4 (1994), pp. 833–862.

[323]   M. Valiev and G. W. Fernando. "Generalized Kohn-Sham Density-Functional Theory via Effective Action Formalism". In: *arXiv e-prints* (1997). arXiv: `cond-mat/9702247` `[cond-mat.str-el]`.

[324]   H. Eschrig. *The Fundamentals of Density Functional Theory*. Teubner, Stuttgart, 1996.

[325]   W. Kutzelnigg. "Density functional theory in terms of a Legendre transformation for beginners". In: *J. Mol. Struct.* 768.13 (2006), pp. 163 –173.

[326]   C. Alexandrou, J. Myczkowski, and J. W. Negele. "Comparison of mean-field and exact Monte Carlo solutions of a one-dimensional nuclear model". In: *Phys. Rev.* C39 (1989), pp. 1076–1087.

[327]   S. Sinha and L. Santos. "Cold Dipolar Gases in Quasi-One-Dimensional Geometries". In: *Phys. Rev. Lett.* 99 (14 2007), p. 140406.

[328]   F. Deuretzbacher, J. C. Cremon, and S. M. Reimann. "Ground-state properties of few dipolar bosons in a quasi-one-dimensional harmonic trap". In: *Phys. Rev.* A81 (6 2010), p. 063616.

[329]   N. Bartolo et al. "Dipolar-induced resonance for ultracold bosons in a quasi-one-dimensional optical lattice". In: *Phys. Rev. A* 88 (2 2013), p. 023603.

[330]   F. Deuretzbacher et al. "Self-bound many-body states of quasi-one-dimensional dipolar Fermi gases: Exploiting Bose-Fermi mappings for generalized contact interactions". In: *Phys. Rev.* A88.3, 033611 (Sept. 2013), p. 033611. arXiv: `1306.0405` `[cond-mat.quant-gas]`.

[331]   J. Bjerlin. "Dipole-Dipole Interaction in Quasi One-Dimensional Harmonic Traps". MA thesis. Lund University, 2012.

[332]   Inguscio, Massimo and Ketterle, Wolfgang and Salomon, C. *Ultra-cold Fermi gases : proceedings of the International School of Physics "Enrico Fermi", course CLXIV, Varenna on Lake Como, Villa Monastero, 20 - 30 June 2006*. 2007.

[333]   S. Giorgini, L. P. Pitaevskii, and S. Stringari. "Theory of ultracold atomic Fermi gases". In: *Rev. Mod. Phys.* 80 (Oct. 2008), pp. 1215–1274. arXiv: `0706.3360` `[cond-mat.other]`.

[334]   I. Bloch, J. Dalibard, and W. Zwerger. "Many-body physics with ultracold gases". In: *Rev. Mod. Phys.* 80.3 (2008), pp. 885–964.

[335]   T. Kinoshita, T. Wenger, and D. S. Weiss. "Observation of a One-Dimensional Tonks-Girardeau Gas". In: *Science* 305.5687 (2004), pp. 1125–1128. ISSN: 0036-8075. eprint: `https://science.sciencemag.org/content/305/5687/1125.full.pdf`.

[336]   B. Paredes et al. "Tonks-Girardeau gas of ultracold atoms in an optical lattice". In: *Nature* 429.6989 (2004), pp. 277—281. ISSN: 0028-0836.

[337]   G. Zürn. "Few-fermion systems in one dimension". PhD thesis. Combined Faculties of the Natural Sciences and Mathematics of the Ruperto-Carola-University of Heidelberg, 2012.

[338]   G. Zürn et al. "Fermionization of Two Distinguishable Fermions". In: *Phys. Rev. Lett.* 108 (7 2012), p. 075303.

[339] G. Zürn et al. "Pairing in Few-Fermion Systems with Attractive Interactions". In: *Phys. Rev. Lett.* 111.17, 175302 (Oct. 2013), p. 175302. arXiv: 1307.5153 [cond-mat.quant-gas].

[340] X.-W. Guan, M. T. Batchelor, and C. Lee. "Fermi gases in one dimension: From Bethe ansatz to experiments". In: *Rev. Mod. Phys.* 85.4 (2013), pp. 1633–1691. arXiv: 1301.6446 [cond-mat.quant-gas].

[341] F. Serwane et al. "Deterministic Preparation of a Tunable Few-Fermion System". In: *Science* 332.6027 (2011), pp. 336–338. ISSN: 0036-8075. eprint: https://science.sciencemag.org/content/332/6027/336.full.pdf.

[342] D. Roscher et al. "Cluster functional renormalization group and absence of a bilinear spin liquid in the J_1-J_2-Heisenberg model". In: *arXiv e-prints* (2019). arXiv: 1905.01060 [cond-mat.str-el].

[343] F. Rennecke and B.-J. Schaefer. "Fluctuation-induced modifications of the phase structure in (2 +1)-flavor QCD". In: *Phys. Rev.* D96.1, 016009 (2017), p. 016009. arXiv: 1610.08748 [hep-ph].

[344] M. Mitter and B.-J. Schaefer. "Fluctuations and the axial anomaly with three quark flavors". In: *Phys. Rev.* D89.5, 054027 (2014), p. 054027. arXiv: 1308.3176 [hep-ph].

[345] S. Resch, F. Rennecke, and B.-J. Schaefer. "Mass sensitivity of the three-flavor chiral phase transition". In: *arXiv e-prints* (2017). arXiv: 1712.07961 [hep-ph].

[346] M. Q. Huber, A. K. Cyrol, and J. M. Pawlowski. "DoFun 3.0: Functional equations in Mathematica". In: *arXiv e-prints* (2019). arXiv: 1908.02760 [hep-ph].

[347] S. Diehl et al. "Flow Equations for the BCS-BEC Crossover". In: *Phys. Rev.* A76 (2007), p. 021602. arXiv: cond-mat/0701198.

[348] I. Boettcher et al. "Phase structure of spin-imbalanced unitary Fermi gases". In: *Phys. Rev.* A91.1 (2015), p. 013610. arXiv: 1409.5070 [cond-mat.quant-gas].

[349] D. Roscher, J. Braun, and J. E. Drut. "Phase structure of mass- and spin-imbalanced unitary Fermi gases". In: *Phys. Rev.* A91.5 (2015), p. 053611. arXiv: 1501.05544 [cond-mat.quant-gas].

[350] D. F. Litim. "Optimisation of the exact renormalisation group". In: *Phys. Lett.* B486 (2000), pp. 92–99. eprint: hep-th/0005245.

[351] D. F. Litim. "Mind the gap". In: *Int. J. Mod. Phys.* A16 (2001), pp. 2081–2088. arXiv: hep-th/0104221.

[352] D. F. Litim. "Optimised renormalisation group flows". In: *Phys. Rev.* D64 (2001), p. 105007. arXiv: hep-th/0103195.

[353] J. Braun, K. Schwenzer, and H.-J. Pirner. "Linking the quark meson model with QCD at high temperature". In: *Phys. Rev.* D70 (2004), p. 085016. arXiv: hep-ph/0312277.

[354] J.-P. Blaizot et al. "Perturbation theory and non-perturbative renormalization flow in scalar field theory at finite temperature". In: *Nucl. Phys.* A784 (2007), pp. 376–406. arXiv: hep-ph/0610004.

[355] D. F. Litim and J. M. Pawlowski. "Non-perturbative thermal flows and resummations". In: *J. High Energy Phys.* 11 (2006), p. 026. arXiv: hep-th/0609122.

Danksagung

Nach langen Schreibtagen (und Nächten) möchte ich mich an dieser Stelle bei all jenen bedanken, ohne die diese Arbeit unmöglich gewesen wäre. Tatsächlich erscheint es gerade hier und jetzt am schwierigsten die richtigen Worte zu finden, um meiner unfassbaren Dankbarkeit angemessen Ausdruck zu verleihen.

An allererster Stelle steht mein Doktorvater Jens Braun, dem mein ganz besonderer Dank gebührt. Seine stets offene Tür (weit über jede gewöhnliche Bürozeit hinaus), seine persönliche Art und seine uneingeschränkte Bereitschaft jede Fragestellung mit seinem unschätzbaren physikalischen Sachverstand im Detail zu erfassen, sind eine unermessliche Unterstützung und Bereicherung in den vergangenen Jahren für mich gewesen. Unerwähnt sollten auch nicht die gemeinsamen Veröffentlichungen, die gemeinsame Lehre sowie die unzähligen fachlichen und weniger fachlichen Diskussionen bleiben, die eine sehr angenehme und produktive Arbeitsatmosphäre zu erzeugen wussten. Auch möchte ich mich für die Geduld und das unvorstellbare Verständnis bei der Fertigstellung dieser Arbeit bedanken, die sich kaum in Worte fassen lässt. Ich kann einfach nur sagen: *Vielen, vielen Dank*!

Bedanken möchte ich mich weiterhin bei Christian Drischler, Kai Hebeler, Marc Leonhardt, Benedikt Schallmo und Achim Schwenk für eine fruchtbare Zusammenarbeit, die auch in der ein oder anderen Publikation mündete. Weiterhin möchte ich mich bei der Deutschen Forschungsgemeinschaft für die Ermöglichung des Sonderforschungsbereichs 1245 bedanken, der mir die finanziellen Möglichkeiten für meine wissenschaftliche Tätigkeit gegeben hat. Ebenso möchte ich ein Dankeschön auch allen Mitgliedern der *fQCD* Kollaboration für viele hilfreiche Gespräche und Diskussionen aussprechen. An dieser Stelle möchte ich mich auch noch einmal für die Einladung zu einem Vortrag im Rahmen des „Cold Quantum Coffee" in Heidelberg bedanken.

Explizit möchte ich mich auch bei meinen Lektoren für Ihre Unterstützung bei der Erstellung dieses Manuskripts bedanken! Im Besonderen möchte ich ein großes Dankeschön Kai Hebeler für hilfreiche Kommentare und Diskussionen aussprechen, die in vielerlei Hinsicht sehr erleuchtend waren. Weiterhin gebührt ein riesengroßes Dankeschön meinen weiteren Lektoren Daniel Rosenblüh und Benedikt Schallmo, die diese Arbeit in Gänze nach Fehlern durchsucht haben.

Des Weiteren möchte ich den aktuellen und ehemaligen Mitgliedern meiner Arbeitsgruppe Niklas Dittmann, Florian Ehmann, Sandra Kemler, Marc Leonhardt, Walid Mian, Lukas Rammelmüller, Stefan Rechenberger, Daniel Rosenblüh, Dietrich Roscher und Sebastian Töpfel für ausgiebige Gespräche diesseits und jenseits von Physik danken, die den Arbeitsalltag sehr bereichert haben. Insbesondere danke ich auch allen Mitbewohnern aus Büro drei für eine großartige Zeit! Im Speziellen möchte ich mich auch noch einmal bei Marc Leonhardt und Lukas Rammelmüller für angeregte fachliche Diskussionen und spannende Konferenzreisen bedanken, die nicht nur wissenschaftlich, sondern auch persönlich eine Bereicherung in jeder Hinsicht waren. Ein großer Dank gilt ebenso allen Angehörigen des Theoriezentrums, die meine Zeit am Institut sehr angenehm gestaltet und die ein oder andere Kaffeepause sehr bereichert haben.

Bei meiner Familie möchte ich mich für Ihre Unterstützung während der letzten Jahre bedanken. Ebenso wäre ein Physikstudium ohne sie nicht möglich gewesen. Daher kann ich einfach nur Dankeschön sagen! Bei meiner Frau Melanie möchte ich mich ganz besonders für ihren unermüdlichen Einsatz, ihre bedingungslose Unterstützung und ihren Rückhalt bei der Anfertigung der vorliegenden Dissertation bedanken. Die Arbeit wäre ohne sie nicht schaffbar gewesen. *Vielen, vielen Dank*!

Wissenschaftlicher Werdegang

Name	Martin Pospiech	
Geburtsort	Frankfurt am Main	
Geburtsdatum	23.12.1989	
Staatsangehörigkeit	deutsch	

Feb. 2016 –	Wissenschaftlicher Mitarbeiter Doktorand	Technische Universität Darmstadt
Apr. 2014 – Dec. 2015	Masterstudium	Technische Universität Darmstadt Abschluss: Master of Science
Okt. 2010 – Jan. 2014	Bachelorstudium	Technische Universität Darmstadt Abschluss: Bachelor of Science
Sep. 2009 – Jun. 2010	Zivildienst	Jugendwohngruppe Karben-Kloppenheim
Jun. 2009	Abitur	Georg-Büchner-Gymnasium Bad Vilbel

Erklärung

Hiermit versichere ich, dass ich die vorliegende Dissertation selbstständig angefertigt und keine anderen als die angegebenen Quellen und Hilfsmittel verwendet habe. Alle wörtlichen und paraphrasierten Zitate wurden angemessen kenntlich gemacht. Die Arbeit hat bisher noch nicht zu Prüfungszwecken gedient.

_____

Datum und Unterschrift